THE UNIVERSITY *of* EDINBURGH

This thesis has been submitted in fulfilment of the requirements for a Doctor of Philosophy at the University of Edinburgh. Please note the following terms and conditions of use:

• This work is protected by copyright and other intellectual property rights, which are retained by the thesis author, unless otherwise stated.

• A copy can be downloaded for personal non-commercial research or study, without prior permission or charge.

• This thesis cannot be reproduced or quoted extensively from without first obtaining permission in writing from the author.

• The content must not be changed in any way or sold commercially in any format or medium without the formal permission of the author.

• When referring to this work, full bibliographic details including the author, title, awarding institution and date of the thesis must be given.

Evaluation of Thermal Ratings and Loading Limits of Power System Components and Joint Circuits

Chengyan Duan

THE UNIVERSITY *of* EDINBURGH

Doctor of Philosophy

THE UNIVERSITY OF EDINBURGH

2025

Abstract

Met Office has reported that the top 10 warmest years in the UK from 1884 have occurred since 2002, clearly indicating an emerging pattern of higher temperatures due to climate change. These high temperatures ("heatwaves") have drawn increased attention to the impact of climate change on the thermal ratings and loading limits of power system components and joint circuits in which these components operate.

Thermal rating of a given component is based on the component's maximum allowed design/operational temperature, typically representing its maximum loading capacity, which, however, changes with both ambient/weather conditions and operating conditions. Violating or exceeding component's maximum temperature limit can, and usually will, result in a number of negative consequences, including, but not limited to: accelerated ageing, reduced safety clearances and degradation of electrical insulation, which in turn can cause equipment failures, fires and electric shocks, leading not only to the possible permanent damage of the component, but also to potentially wider power system blackouts. When two or more power system components operate in a joint circuit, as is usually the case, thermal ratings and loading limits of the joint circuit are generally determined by the component in the circuit which has the lowest maximum loading capacity for given ambient and operating conditions for the considered period of interest. As the ambient and operating conditions change, the specific component with the lowest maximum loading capacity in the joint circuit may also change, which further complicates accurate evaluation of circuit and system loading capacities.

In order to more accurately evaluate thermal ratings and loading limits of power system components, this PhD research applies thermal modelling, based on the physical models and characteristics of the modelled components at 400kV to 132kV levels (Scotland high-voltage transmission level). Thermal ratings were calculated and assessed using the developed thermal models and considering different operating and ambient conditions, as well as time periods, for the three main power system components: oil-immersed power transformers, cables, and overhead lines. Cables are further divided into directly buried cables, cables in filled troughs, and cables exposed in the air. Thermal modelling processes and thermal-electrical models are formulated for unified ambient and operational conditions, allowing for the evaluation of: static

thermal rating, based on and calculated from the assumed constant (seasonal or monthly) ambient conditions; dynamic thermal rating, calculated for actual ambient conditions; short-term and medium-term overloading rating, calculated for a set of given ambient conditions, pre-fault loading levels and specific durations; cyclic thermal rating, calculated for the given ambient condition, but considering daily cyclic variations of loading profile, with periods of high and low loading conditions, and, finally, exceedance level based ratings, calculated by acknowledging acceptable risk levels for component's operational temperature exceeding its maximum temperature limit (the exceedance ratings directly apply only to overhead lines).

A detailed review of existing standards and literature identified several limitations in current models. These include incomplete treatment of transformer losses that depend on winding temperature and tap position, simplified representation of cooling-mode transitions between oil-natural air-natural and oil-forced air-forced, and limited inclusion of weather effects such as wind speed and solar irradiance. To address these gaps, the transformer model was enhanced to include temperature- and voltage-dependent losses, cooling-mode transitions, exposure differences between tank and cooling plant, tertiary windings, and effective cooling areas. Cable models were extended to cover directly buried, filled-trough, and air-exposed configurations, with explicit consideration of solar irradiance and wind speed effects.

In terms of the improvements of existing models and development of new models: The inconsistencies and gaps described previously are all being addressed accordingly. The previously developed cable thermal model for directly buried cables and cables in conduits is now extended to include cables in filled troughs. Thermal models for the cables exposed to air and solar irradiance are developed, also enabling the consideration of wind speed.

Finally, there is currently no comprehensive approach in existing literature for modelling and evaluating the thermal ratings of joint circuits, while only some guidance is provided for selecting and coordinating ratings for joint circuits with multiple components. However, such guidance is very simple in order to meet the ease-of-use requirements. Building on the improved component-level models, a new methodology

was developed to evaluate the thermal ratings of joint circuits that contain combinations of the mentioned multiple power network components. This method couples the steady-state and transient thermal behaviour of each component under common weather and loading conditions, identifying the limiting element at each time step. Using simulation-based analysis, the presented approach determines time-varying static thermal rating, dynamic thermal rating, cyclic thermal rating, short-term and medium-term overloading rating, and exceedance level-based ratings at the circuit level, and identifies when the circuit thermal loading limit shifts between components for different ambient operating conditions, including heatwave scenarios.

This thesis develops and refines methodologies for accurately evaluating the thermal ratings and loading limits of transformers, cables, and overhead lines under changing climatic conditions. This thesis improves existing thermal models by including weather-dependent and operational factors, such as wind speed, solar irradiance, tap position, cooling-mode transitions, etc., and extending these methods to joint circuits. The work enables a consistent and realistic assessment of circuit/system capability across varying ambient scenarios. The results provide power system operators and planners with a reliable means to quantify the impact of climate change and heatwave events on the network performance, identify thermally constrained assets, and inform asset reinforcement.

Lay Summary

The electricity system that powers our homes, businesses, and industries relies on many interconnected components, such as transformers, underground cables, and overhead power lines, to deliver energy safely and reliably. Each of these components can only carry a certain amount of electrical load before it becomes too hot to operate safely. This safe limit, known as the thermal rating, depends not only on how much electricity is flowing, but also on the surrounding weather conditions.

As the UK experiences more frequent heatwaves and rising temperatures due to climate change, these components face increasing thermal stress. When temperatures rise, equipment can overheat more easily, reducing its lifespan, lowering safety margins, or even causing failures that may lead to power cuts. Understanding how changing weather conditions affect the safe operating limits of these components has therefore become essential for keeping the power system reliable and efficient.

This research focuses on improving the way we calculate and predict how hot these components get under different weather and loading conditions. This study provides improved existing models for transformers, cables, and overhead lines by including real-world factors, such as air temperature, wind speed, sunlight, and equipment settings. These improved models were then used to study how multiple components in a joint circuit behave together, since the weakest (or hottest) part determines how much electricity the whole circuit can carry.

By simulating different climate and operating scenarios, including extreme heat events, the research shows how the performance of power system components and circuits may change in the coming decades. The findings can help electricity network operators to identify which parts of the system are most vulnerable to overheating and plan upgrades or operational adjustments, ensuring that the UK electricity networks remain safe, resilient, and efficient as the climate continues to warm.

Acknowledgements

Firstly, I would like to thank my supervisor, Professor Saša Djokic, for his guidance and support during my PhD studies and research, and for supervising both my PhD studies and the REWARD project within THERMAL programme. I would like to acknowledge the support from the THERMAL programme and NGET for their guidance, measurements and data, which are vital to the development of my methodology.

Then, I would like to thank my colleague, Dr. As'ad Zakaira, for the collaborative work and research on the REWARD project, for processing and sharing the meteorological data, and for all other assistance needed for this research.

I would also like to thank Mr. Gordon Wilson, Mr. David Scott and Mr. Tinashe Chikohora in NGET for providing a large part of the data and feedback used in this thesis. Also, thanks to the ABB Zhongshan Transformer Co. for sharing knowledge and measurements for this thesis.

Thanks to all partners in the project with THERMAL programme for sharing knowledge from other fields and specialities that proved to be of great use in this study.

A very special acknowledgement goes to my family for providing me with all the possible support during my studies and research. There are no words or sentences enough to express my gratitude to my grandmothers, grandfathers, Mum, Dad, and all my relatives for their help, support and belief in my journey to achieve this PhD study.

Declaration

I declare that this thesis was composed by myself, that the work contained herein is my own or as a research assistant contributed in the project REWARD with THERMAL programme P3, except where explicitly stated otherwise in the text, and that this work has not been submitted for any other degree or professional qualification except as specified.

Chengyan Duan

Contents

Abstract ..... **III**

Lay Summary ..... **VI**

Acknowledgements ..... **VII**

Declaration ..... **VIII**

Contents ..... **IX**

List of Figures ..... **XIV**

List of Tables ..... **XXV**

List of Abbreviations ..... **xxviii**

Nomenclature ..... **xxxi**

Chapter 1 Introduction **1**

1.1 Scope of Research 2

1.1.1 Thermal Modelling of Three Main Power System Components 3

1.1.2 Meteorological Data and Loading Profile 3

1.1.3 Thermal Ratings of Individual Components 3

1.1.4 Thermal Ratings of Components in a Joint Circuit 4

1.2 Research Objectives, Outcomes and Publications 6

1.3 Thesis Structure 7

Chapter 2 Overview of Thermal Modelling for Three Main Power System Components **8**

2.1 Existing Models of Components 9

2.1.1 Standard Thermal Models for Power Transformers 9

2.1.2 Other Publications Related to the Thermal Modelling of the Transformer 25
2.1.3 Thermal Models for Cables 35
2.1.4 Models for Overhead Line Conductors 47
2.1.5 Modelling of Components in a Joint Circuit 58
2.1.6 National Grid Technical Guidance Note for the Definition of Thermal Ratings 61
2.2 Problem Statement and Case Study for Thermal Modelling of Components in Power Systems 63
2.2.1 Thermal Time Constants of Components 63
2.2.2 Units for Ratings 68
2.2.3 Impact of Voltage Variation and Load Types 68
2.2.4 Additional Consideration of Pre-Fault and Post-Fault Ratings 69
2.2.5 Inconsistent Ambient Air Temperature for Traditional Rating Seasons 69
2.3 Conclusions 70

Chapter 3 Meteorological Data and Loading Profiles for Different Types of Thermal Ratings 72

3.1 Types of Thermal Ratings 73
3.1.1 Static Thermal Ratings 73
3.1.2 Dynamic Thermal Ratings 74
3.1.3 Cyclic Thermal Ratings 74
3.1.4 Short-Term and Medium-Term Overloading Ratings 74
3.1.5 Exceedance Level-Based Ratings 74
3.1.6 Summary of Thermal Rating Types 75
3.2 Meteorological Data for Thermal Modelling and Rating of Components Considering Heat Wave Impact 75
3.2.1 Ambient Air Temperature 76
3.2.2 Ambient Soil Temperature 77
3.2.3 Wind Speed 80
3.2.4 Wind Attacking Angle 83
3.2.5 Solar Irradiance 83
3.2.6 Impact of Climate Change and Heat Waves 84

3.3 Loading Profiles for Thermal Modelling and Rating of Components 90
3.3.1 Constant Loading Profile 90
3.3.2 Cyclic Loading Profile 91
3.3.3 Ongoing and Future Changes in Loading Profiles 91
3.4 Conclusions 93

Chapter 4 Oil-Immersed Power Transformers 95

4.1 Methodology of Thermal Modelling for Oil-Filled Power Transformers 96
4.1.1 Calculation of Thermal Resistances 98
4.1.2 Calculation of Other Thermal Parameters 104
4.1.3 Efficiency due to the Inhomogeneous Temperature Distribution for Natural Radiation, Convection and Conduction 107
4.1.4 Estimation of the Thermal Parameters for Oil Convection 112
4.1.5 Calculation of the Heat Input from Solar Irradiance 113
4.1.6 Calculation of the Heat Input from Losses 114
4.1.7 Estimation of Load Losses for Different Tap Positions 118
4.1.8 Thermal Capacitances of Transformers 120
4.1.9 Model Validation and Comparison to Standard Models 123
4.2 Thermal Ratings of Power Transformers 128
4.2.1 Steady-State Temperatures of Power Transformers 128
4.2.2 Dynamic and Nameplate Thermal Ratings of Power Transformers 131
4.2.3 Thermal Time Constants of Power Transformers 133
4.2.4 Short-Term and Medium-Term Overloading Ratings of Power Transformers 135
4.2.5 Cyclic Thermal Ratings of Power Transformers 142
4.3 Conclusions 143

Chapter 5 AC Power Cables 145

5.1 Methodology of Thermal Modelling for Cables 146
5.1.1 Thermal Model of Directly Buried Cables 147
5.1.2 Thermal Model of Filled Trough Cables 151
5.1.3 Thermal Model of Exposed Cables 152
5.2 Thermal Ratings of Cables 153

5.2.1 Steady-State Conductor Temperatures for Cables 153
5.2.2 Dynamic and Static Thermal Ratings of Cables 171
5.2.3 Thermal Time Constants of Cables 173
5.2.4 Short-Term and Medium-Term Overloading Ratings of Cables 177
5.2.5 Cyclic Thermal Ratings of Cables 189
5.3 Conclusions 191

Chapter 6 Bare Overhead Line Conductors 192

6.1 Methodology of Thermal Modelling for Overhead Lines 193
6.1.1 Heat Balance Equation of Overhead Lines 193
6.1.2 Calculation of the Heat Loss from Convection 194
6.1.3 Calculation of the Heat Loss from Radiation 195
6.1.4 Calculation of the Heat Input from Solar Irradiance 195
6.1.5 Calculation of the Resistance of the Conductor 195
6.1.6 Calculation of the Maximum Current Carrying Capacity 196
6.1.7 Calculation of Thermal Capacitance of Overhead Lines 196
6.1.8 Case Study 196
6.2 Thermal Ratings of Overhead Lines 201
6.2.1 Steady-State Conductor Temperatures of Overhead Lines 202
6.2.2 Dynamic and Static Thermal Ratings of Overhead Line Conductors 205
6.2.3 Thermal Time Constants of Overhead Lines 207
6.2.4 Short-Term and Medium-Term Overloading Ratings of Overhead Lines 211
6.2.5 Exceedance Level-Based Ratings of OHLs 217
6.3 Conclusions 242

Chapter 7 Thermal Ratings and Loading Limits of Joint Circuits 245

7.1 Selection of Components in Joint Circuits 246
7.2 Rating Unit Selection and the Impact of Voltage Variations and Load Types 247
7.2.1 Impact of Voltage Variations 248
7.2.2 Impact of Load Types and Voltage Variations 248
7.2.3 Load Unit Variation with Fixed Current in Branch 251

7.2.4 Summary 258
7.3 Evaluation of Thermal Ratings and Loading Limits of Joint Circuits 259
7.3.1 Joint Circuit Ratings of Overhead Line and Cable Composite Circuit 260
7.3.2 Joint Circuit Thermal Ratings with Transformers (Substations) 275
Chapter 8 Conclusions and Future Work 298
References 301

List of Figures

Figure 1.1: Single-line diagram of the IEEE-33 bus network [12]. 5
Figure 2.1: Transformer model according to the IEEE and IEC standards [1], [2]. 10
Figure 2.2: Block diagram of the IEEE method [1]. 10
Figure 2.3: Example of the equivalent load cycle compared to the actual load cycle and the peak load [1]. 13
Figure 2.4: Block diagram of the IEC method [2]. 13
Figure 2.5: Illustration of the HST/WTI profile and the S/MTOR of the transformer, amended from [14]. 24
Figure 2.6: Illustration of the HST/WTI profile for cyclic load and the profile of the loading cycle of the transformer, amended from [14]. 25
Figure 2.7: Diagram of the thermal model in [16], [17]. 26
Figure 2.8: Flow chart from method in [16], [17]. 26
Figure 2.9: Diagram of the single-phase equivalent circuit of a transformer with a tertiary winding in star-star-delta configuration [51]. 34
Figure 2.10: Diagram of the thermal model of cable in standard IEC 60287 [4], [5], [55]. 36
Figure 2.11: Diagram of the cable thermal model in IEEE 835 [53]. 41
Figure 2.12: Illustration of short-term and medium-term thermal rating of cables, amended from [14]. 44
Figure 2.13: Illustration of CTR and the standard cyclic loading profile of cables, amended from [14]. 45
Figure 2.14: The 7-phase (A-G) thermal model of the buried cable in conduit. 46
Figure 2.15: Geometry of a covered trough housing three HV cables in a flat formation, amended from [59]. 46
Figure 2.16: Illustration of the heat balance in the physical model for OHLs. 48
Figure 2.17: Illustration of the short-term, medium-term (post-fault) ratings and their respective conductor temperature variation for OHL, amended from [14]. 58

Figure 2.18: Variation of the example OHL conductor temperature with time under the condition of rated current under different ambient conditions. 64
Figure 2.19: Variation of the example cable conductor temperature with time under the condition of rated current and 30°C AT. 65
Figure 2.20: Variation of the example ONAN distribution transformer HST with time from the un-energised start at the condition of rated current [1]. 66
Figure 2.21: Variation of the example OFAF transmission transformer HST with time from the un-energised start at the condition of rated current and 30°C AT [75], [76]. 67
Figure 2.22: Current vs. Power limits for a 390A rating OHL in a three-phase system. 68
Figure 3.1: An example of different types of thermal ratings for an arbitrary network component. 73
Figure 3.2: UKCP18 probabilistic projections for Heathrow, London. 77
Figure 3.3: The hysteresis loop between the measured temperature of air and soil at 1m depth in Kew Gardens, London. 78
Figure 3.4: The hysteresis loop between the measured temperature of air and the soil at 0.3m depth in Kew Gardens, London. 78
Figure 3.5: Polynomial fit for the measured temperature of air and soil at 1m depth in Kew Gardens, London. 79
Figure 3.6: Polynomial fit for the measured temperature of air and the soil at 0.3m depth in Kew Gardens, London. 79
Figure 3.7: Conditional PDF in m/s for Heathrow. 80
Figure 3.8: Scatter Plots in m/s for Heathrow. 81
Figure 3.9: Heatwave ambient in Heathrow, London. 82
Figure 3.10: Per-unitised non-coincidental daily solar irradiance profile used in this thesis. 84
Figure 3.11: Example of 5 minutes and hourly DTR against a constant applied current. 85
Figure 3.12: Air temperature 1981 vs 2022 [83] 86
Figure 3.13: Soil Temperature (1m depth) 1981 vs 2022 [83] 86

Figure 3.14: Wind speed 1981 vs 2022 [83]. 87
Figure 3.15: Solar Irradiance 1981 vs 2022 [83]. 88
Figure 3.16: Pre-fault Zebra transient thermal response at 50 °C conductor limit. 88
Figure 3.17: 2022 Heatwave ambient conditions in Heathrow. 89
Figure 3.18: 1981 Heatwave ambient conditions in Heathrow. 90
Figure 3.19: Standard cyclic loading profile, amended from [14]. 91
Figure 3.20: Transmission demand profile from ELEXON [84]. 91
Figure 3.21: Transmission demand profile normalised by daily maximum demand. 92
Figure 3.22: Measured power transformer loading profile, with the tap position and cooling status marked. 92
Figure 4.1: Representation of the physical model: Partly enclosed (tank) and partly exposed (cooler) transformer. 97
Figure 4.2: Thermal network diagram of the transformer thermal model. 98
Figure 4.3: Example of the thermal conduction process from the top-oil to the outer wall surface of the transformer. 102
Figure 4.4: The variation of the thermal resistance of radiation for the cooler with the variation of temperature rise from the wall to the ambient. 109
Figure 4.5: The variation of the heat transfer coefficient of convection on ONAN and OFAF modes with the variation of temperature rise from wall to ambient. 109
Figure 4.6: The variation of the thermal resistance of convection for the cooler on ONAN and OFAF modes with the variation of temperature rise from wall to ambient. 110
Figure 4.7: Variation of the calculated TOT with the change in the efficiency due to the inhomogeneous temperature distribution. 111
Figure 4.8: Result of the estimated no-load losses with the variation of the supplied voltage. 115
Figure 4.9: Comparison between measurement load losses and estimated load losses under OFAF mode. 120
Figure 4.10: Thermal capacitance modelling for the switching between OFAF and ONAN cooling modes. 122

Figure 4.11: Comparison of the calculated value of HST using improved mode, IEC standard-based models [2] and IEEE Annex G model [1] to the recorded value. 126
Figure 4.12: Comparison of the calculated value of TOT using the improved model, IEC standard-based model [2] and the IEEE Annex G model [1] to the recorded value. 126
Figure 4.13: Variation of steady-state HST at 0.5m/s WS (a) and 1m/s WS (b) of the power transformer in OFAF mode at tap position 11 with the variation of AAT and SI when loaded with respective 1PU, 0.85PU, 0.75PU, and 0.65PU constant NTR current. 129
Figure 4.14: Variation of steady-state HST at 0.5m/s WS (a) and 1m/s WS (b) of the power transformer in OFAF mode at tap position 15 with the variation of AAT and SI when loaded with respective 1PU, 0.85PU, 0.75PU and 0.65PU constant NTR current. 130
Figure 4.15: The calculated DTR in PU of base MVA of the power transformer under OFAF cooling mode for tap positions 11 and 15 with the variation of AAT and SI..131
Figure 4.16: The calculated DTR in the current of the power transformer under OFAF cooling mode for tap positions 11 and 15 with the variation of AAT and SI.....132
Figure 4.17: Variation of the TOT with time for the power transformer at tap positions 11 and 15 when supplied with 1PU voltage on the HV side, loaded with 1PU, 0.85PU, 0.75PU and 0.6PU of NTR current under summer ambient conditions. 134
Figure 4.18: Variation of the HST with time for the power transformer at tap positions 11 and 15 when supplied with 1PU voltage on the HV side, loaded with 1PU, 0.85PU, 0.75PU and 0.6PU of NTR current under summer ambient conditions. 134
Figure 4.19: Example of the HST variation of the power transformer under OFAF cooling mode when loaded with S/MTOR using different overloading periods (up to 60min), pre-fault loading percentage in accordance with the NTR and different AAT. 136
Figure 4.20: Example of the HST variation and the standard cyclic loading profile for the example power transformer under nominal tap position (11) at 30°C AAT.....142

Figure 4.21: The calculated CTR in PU of base MVA of the power transformer under OFAF cooling mode for tap positions 11 and 15 with the variation of AAT and SI..143
Figure 5.1: Cable examples and their ambient summary used in this thesis. 146
Figure 5.2: Thermal model for directly buried cables. 148
Figure 5.3: Thermal model for filled trough cables. 151
Figure 5.4: Thermal model for exposed cables. 152
Figure 5.5: Variation of conductor temperature with the variation of AAT for a single 138kV 2000$mm2$ (a) DBC and 400kV 1000$mm2$ (b) DBC when loaded with respective 1PU, 0.85PU, 0.75PU and 0.65PU constant summer STR current. 156
Figure 5.6: Variation of soil temperature near the cable surface with the variation of AAT for a single 138kV 2000$mm2$ (a) DBC and 400kV 1000$mm2$ (b) DBC when loaded with respective 1PU, 0.85PU, 0.75PU and 0.65PU constant summer STR current. 157
Figure 5.7: Variation of cable conductor temperature under dry-out conditions with variation of AAT for a single 138kV 2000$mm2$ (a) DBC and 400kV 1000$mm2$ (b) DBC when loaded with respective 1PU, 0.85PU, 0.75PU and 0.65PU constant summer STR current. 159
Figure 5.8: Variation of conductor temperature with the variation of AAT and SI for a single 138kV 2000$mm2$ (a) FTC and 400kV 1000$mm2$ (b) FTC when loaded with respective 1PU, 0.85PU, 0.75PU and 0.65PU summer STR current., using 0.9 absorptivity 161
Figure 5.9: Variation of fill temperature with the variation of AAT and SI for a single 138kV 2000$mm2$ (a) FTC and 400kV 1000$mm2$ (b) FTC using 0.9 absorptivity when loaded with respective 1PU, 0.85PU, 0.75PU and 0.65PU summer STR current. 162
Figure 5.10: Variation of conductor temperature with the variation of AAT and SI for a single 138kV 2000$mm2$ (a) FTC and 400kV 1000$mm2$ (b) FTC using 0.5 absorptivity when loaded with respective 1PU, 0.85PU, 0.75PU and 0.65PU summer STR current. 164

Figure 5.11: Variation of fill temperature with the variation of AAT and SI for a single 138kV 2000$mm2$ (a) FTC and 400kV 1000$mm2$ (b) FTC using 0.5 absorptivity when loaded with respective 1PU, 0.85PU, 0.75PU and 0.65PU summer STR current. 166
Figure 5.12: Variation of conductor temperature with the variation of AAT and SI for a single 138kV 2000$mm2$ (a) FTC and 400kV 1000$mm2$ (b) FTC using 0.5 absorptivity and considering dry-out of the fill when loaded with respective 1PU, 0.85PU, 0.75PU and 0.65PU summer STR current. 167
Figure 5.13: Variation of conductor temperature at 0.5m/s WS with the variation of AAT and SI for a single exposed 138kV 2000$mm2$ cable (a) and exposed 400kV 1000$mm2$ cable (b) when loaded with respective 1PU, 0.85PU 0.75PU and 0.65PU constant summer STR current. 169
Figure 5.14: Variation of conductor temperature at 1m/s WS with the variation of AAT and SI for a single exposed 138kV 2000$mm2$ cable (a) and exposed 400kV 1000$mm2$ cable (b) when loaded with respective 1PU, 0.85PU 0.75PU and 0.65PU constant summer STR current. 170
Figure 5.15: Comparison of the DTR for 138kV 2000$mm2$ cable in different constructions and the respective AST with the variation of the AAT when considering both 0.5m/s and 1m/s WS. 172
Figure 5.16: Comparison of the DTR for 400kV 1000mm2 cable in different constructions and the respective AST with the variation of the AAT. 172
Figure 5.17: Variation of the conductor temperature with time SI for a single 138kV 2000$mm2$ DBC (a) and 400kV 1000$mm2$ DBC (b) when loaded with 1PU, 0.85PU, 0.75PU and 0.6PU of respective constant summer STR current under summer STR ambient conditions. 175
Figure 5.18: Variation of the conductor temperature with time for a single 138kV 2000$mm2$ FTC (a) and 400kV 1000$mm2$ FTC (b) when loaded with 1PU, 0.85PU, 0.75PU and 0.6PU of respective constant summer STR current under summer STR ambient condition. 176

Figure 5.19: Variation of the conductor temperature with time SI for a single exposed 138kV 2000$mm2$ cable (a) and exposed 400kV 1000$mm2$ cable (b) when loaded with 1PU, 0.85PU, 0.75PU and 0.6PU of respective constant summer STR current under summer STR ambient condition. 178
Figure 5.20: Example of the temperature variation and cyclic current for the 400kV 1000mm2 DBC at 30℃ AAT, which is equivalent to 21.8℃ AST1m. 189
Figure 5.21: Comparison of the CTR for 138kV 2000mm2 cable in different constructions and the respective AST with the variation of the AAT. 190
Figure 5.22: Comparison of the CTR for 400kV 1000mm2 cable in different constructions and the respective AST with the variation of the AAT. 190
Figure 6.1: Thermal model for the overhead lines. 193
Figure 6.2: Comparison of the DTR variation using three convection equations in [9] of an example OHL conductor under different attacking angles and wind speeds, with the final result marked. 197
Figure 6.3: Variation of a single ACSR Zebra OHL conductor temperature with the variation of AAT and SI for 0.5m/s and 1 m/s WS values when loaded with the respective 1PU, 0.85PU, 0.75PU and 0.65PU summer STR current. 203
Figure 6.4: Variation of a single AAAC Sorbus OHL conductor temperature with the variation of AAT and SI for 0.5m/s and 1 m/s WS values when loaded with the respective 1PU, 0.85PU, 0.75PU and 0.65PU summer STR current. 204
Figure 6.5: Variation of the maximum DTR with different AAT, WS and SI for a single ACSR Zebra 50℃ limit OHL conductor. 206
Figure 6.6: Variation of the maximum DTR with the variation of AAT, WS and SI for a single AAAC Sorbus 75℃ limit OHL conductor. 207
Figure 6.7: Variation of the conductor temperature with time for ACSR Zebra at OHL Summer STR condition when loaded with 1, 0.85, 0.75 and 0.6 PU of constant summer STR current. 208
Figure 6.8: Variation of the conductor temperature with time for AAAC Sorbus at OHL Summer STR condition when loaded with 1, 0.85, 0.75 and 0.6 PU of constant summer STR current. 209

Figure 6.9: Variation of the conductor temperature with time for ACSR Zebra at OHL during Heatwave UK summer when loaded with 1, 0.85, 0.75 and 0.6 PU of constant summer STR current. 210
Figure 6.10: Variation of the conductor temperature with time for AAAC Sorbus at OHL during Heatwave UK summer when loaded with 1, 0.85, 0.75 and 0.6 PU of constant summer STR current. 211
Figure 6.11: An example of the OHL conductor temperature variation when loaded with the respective S/MTOR current. 212
Figure 6.12: Recorded ambient weather data at St. Johns Wood substation. 219
Figure 6.13: Example of 5 minutes and hourly DTR against a constant applied current. 219
Figure 6.14: Location of available weather data for the exceedance analysis. 220
Figure 6.15: 2019 CT curve at St. Johns Wood 225
Figure 6.16: 1977 CT curve at Heathrow vs original experiment (Leatherhead) 226
Figure 6.17: Probabilistic loading current for exceedance level at Heathrow (1977 vs 2019) 227
Figure 6.18: Braintree Substation and Andrewsfield Weather Station (9.35 km) 229
Figure 6.19: Representative ambient weather conditions at Braintree. 230
Figure 6.20: Braintree Zebra OHL Exceedance Ratings at 1 PU and 0.85 PU STR Summer Current in 2022 230
Figure 6.21: Zoomed in Figure 6.20 during a heatwave. 231
Figure 6.22: Pentir-Trawsfynydd, Garth OHL-Cable Compound and Porthmadog Weather Station. 231
Figure 6.23: Representative ambient weather conditions at Pentir-Trawsfynydd in 2022 232
Figure 6.24: Pentir-Trawsfynydd, Sorbus OHL Exceedance Ratings at 1 PU and 0.85 PU STR Summer Current in 2022. 232
Figure 6.25: Braintree exceedances throughout the years. 233
Figure 6.26: Loading current vs exceedance for highest and lowest exceedance years at Braintree 2022 and 2012. 234

Figure 6.27: Braintree, different operating design limits and their corresponding exceedances for the year 2022. 235
Figure 6.28: Pentir-Trawsfynydd exceedances throughout the years. 236
Figure 6.29: Loading current vs exceedance for highest and lowest exceedance years at Pentir-Trawsfynydd 2022 and 2017. 237
Figure 6.30: Pentir-Trawsfynydd, different operating design limits and their corresponding exceedances for the year 2022. 237
Figure 6.31: Pre-fault exceedance level under summer STR design conditions for Braintree, 85% of 663 A(20℃ AAT, 12° AA, 0.5 m/s WS, and 0 $W/m2$ SI), Zebra at 50 ℃ limit, from 2008 to 2023. 239
Figure 6.32: Post-fault exceedance level under summer STR design conditions for Braintree, 100% of 663A (20℃ AAT, 0.5 m/s WS, and 0 $W/m2$ SI), Zebra at 50 ℃ limit, from 2008 to 2023. 240
Figure 6.33: Pre-fault exceedance level under summer STR design conditions for Pentir-Trawsfynydd, 85% of 943A (20℃ AAT, 0.5 m/s WS, and 0 $W/m2$ SI), Sorbus at 75 ℃ limit, from 2011 to 2024. 241
Figure 6.34: Post-fault exceedance level under summer STR design conditions 100% of 943A for Pentir-Trawsfynydd (20℃ AAT, 0.5 m/s WS, and 0 $W/m2$ SI), Sorbus at 75 ℃ limit, from 2011 to 2024. 241
Figure 7.1: Diagram of the 2-bus test system without impedance in branch 0.....249
Figure 7.2: Comparison of the apparent power demand to the load with the voltage variation for different load types.....250
Figure 7.3: Comparison of the current flow to the load with the voltage variation for different load types. 251
Figure 7.4: Variation of the ratio of the load unit with voltage to keep the current in the branch constant. 252
Figure 7.5: Variation of apparent power flow with voltage variation from a constant current. 253
Figure 7.6: Diagram of the 2-bus test system with impedance added between bus0 and bus1. 254

Figure 7.7: Variation of the load unit ratio with voltage to keep the current in the branch constant when considering only the current limit and considering both voltage and current limit. 257
Figure 7.8: Pentir-Trawsfynydd, Garth cable compound, OHL – Cables..... 260
Figure 7.9: Variation of the joint circuit post-fault DTR with the variation of AAT, SI under 0.5m/s WS (a) and 1m/s WS (b) for the example OHL and cable composite circuit. 261
Figure 7.10: Variation of the joint circuit pre-fault DTR with the variation of AAT, SI under 0.5m/s WS (a) and 1m/s WS (b) for the example OHL and cable composite circuit. 264
Figure 7.11: Variation of the S/MTOR of individual components in a joint circuit with the variation of AAT under high SI and 0.5m/s WS assumption. 269
Figure 7.12: Variation of the joint circuit CTR using standard cyclic loading profile with the variation of AAT, SI under 0.5m/s WS (a) and 1m/s WS (b) for the example OHL and cable composite circuit. 271
Figure 7.13 Variation of the joint circuit CTR using standard cyclic loading profile with the variation of AAT, SI under 0.5m/s WS (a) and 1m/s WS (b) for the example OHL and cable composite circuit when considering the 20% spare capacity of OHL during pre-fault condition. 273
Figure 7.14: Example of a transmission power transformer, with its LV side connected by cable, indicating parts of the cable are exposed to ambient air and solar irradiance [104]. 275
Figure 7.15: Joint Circuit DTR of substation under pre-fault condition, tap position 11, 0.5m/s WS, full view (a) and detailed (b). 277
Figure 7.16: Joint DTR of substation under pre-fault condition, tap position 11, 1m/s WS, full view and detailed. 279
Figure 7.17: Joint circuit DTR of substation under pre-fault condition, tap position 15, 0.5m/s WS, full view and detailed. 281
Figure 7.18: Joint circuit DTR of substation under pre-fault condition, tap position 15, 1m/s WS, full view and detailed. 282

Figure 7.19: Joint circuit DTR of substation under post-fault condition, tap position 11, 0.5m/s WS, full view and detailed. 285
Figure 7.20: Joint circuit DTR of substation under post-fault condition, tap position 11, 1m/s WS, full view and detailed. 286
Figure 7.21: Joint circuit DTR of substation under post-fault condition, tap position 15, 0.5m/s WS, full view and detailed. 287
Figure 7.22: Joint circuit DTR of substation under post-fault condition, tap position 15, 1m/s WS, full view and detailed. 288
Figure 7.23: Comparison of joint circuit CTR of substation with the variation of AAT and SI under 0.5m/s WS at tap position 11, full background CTR view (a), detailed (b). 293
Figure 7.24 Comparison of joint circuit CTR of substation with the variation of AAT and SI under 1m/s WS at tap position 11, full background CTR view (a), detailed (b). 295
Figure 7.25: Comparison of joint circuit CTR of substation with the variation of AAT and SI under 0.5m/s WS at tap position 15, full background CTR view (upper), detailed (lower). 296
Figure 7.26: Comparison of joint circuit CTR of substation with the variation of AAT and SI under 1m/s WS at tap position 15, full background CTR view (a), detailed (b). 297

List of Tables

Table 2.1: Ambient Temperature of the Rating Months [14]. 69
Table 3.1: Summary of heatwave values in Heathrow for three heatwave events. 82
Table 3.2: Available weather data overview in 1981 [83]. 85
Table 3.3: Input Static Ambient Conditions using Summer Assumptions for the Joint Rating of the Components used for the Following Assessments. 94
Table 4.1: Data and Parameters of the Example Power Transformer from [17]. 123
Table 4.2: Transformer Tap Position Dependent Data and Parameters of the Example Power Transformer [76]. 123
Table 4.3: Transformer Technical Specifications [76], [97], [98]. 124
Table 4.4: Parameters Outside of Specifications [1], [2], [23], [93], [99]. 124
Table 4.5: Temperature error metrics for different models (whole day). 127
Table 4.6: Temperature errors at key points. 127
Table 4.7. Short-Term and Medium-Term Overloading Ratings of the Example Power Transformers at Tap Position 11 with variation of Ambient Air Temperatures, Pre-Fault loading Percentage in accordance with Nameplate Rating 137
Table 4.8. Short-Term and Medium-Term Overloading Ratings of the Example Power Transformer at Tap Position 15 with variation of Ambient Air Temperatures, Pre-Fault Loading Percentage in accordance with Nameplate Rating 138
Table 4.9: Values of Different Pre-Fault Loadings in accordance with the Dynamic Thermal Ratings of the Example Power Transformer 139
Table 4.10: Short-Term and Medium-Term Overloading Ratings of Power Transformer at Tap Position 11 with variation of Ambient Air Temperatures, Pre-Fault Loading Percentage in accordance with Dynamic Thermal Ratings 140
Table 4.11: Short-Term and Medium-Term Overloading Ratings of Power Transformer at Tap Position 15 with variation of Ambient Air Temperatures, Pre-Fault Loading Percentage in accordance with Dynamic Thermal Ratings 141

Table 5.1: Specifications of cables used in the assessment [4], [5], [6], [59], [100], [101]. 154
Table 5.2: Short-Term and Medium-Term Overloading Ratings of Directly Buried 138kV 2000$mm2$ Cable. 179
Table 5.3: Short-Term and Medium-Term Overloading Ratings of Directly Buried 400kV 1000$mm2$ Cable 180
Table 5.4: Short-Term and Medium-Term Overloading Ratings of Filled Trough 138kV 2000$mm2$ Cable 182
Table 5.5: Short-Term and Medium-Term Overloading Ratings of Filled Trough 400kV 1000$mm2$ Cable 183
Table 5.6: Short-Term and Medium-Term Overloading Ratings of Exposed 138kV 2000$mm2$ Cable considering both 0.5m/s Wind Speed and no Solar Irradiance 184
Table 5.7: Short-Term and Medium-Term Overloading Ratings of Exposed 138kV 2000$mm2$ cable considering 1m/s Wind Speed and no Solar Irradiance 185
Table 5.8: Short-Term and Medium-Term Overloading Ratings of Exposed 400kV 1000$mm2$ Cable considering both 0.5m/s Wind Speed and no Solar Irradiance 187
Table 5.9: Short-Term and Medium-Term Overloading Ratings of Exposed 400kV 1000$mm2$ cable considering 1m/s Wind Speed and no Solar Irradiance 188
Table 6.1: Equivalent heating from solar irradiance to eliminate the cooling from wind speed. 198
Table 6.2: Equivalent cooling from wind speed to eliminate the heating from solar irradiance 199
Table 6.3: Equivalent WS under no SI condition for the variation of WS with 1k SI. 200
Table 6.4: Specification of the example OHL conductors [71], [103]. 201
Table 6.5: Short-Term and Medium-Term Overloading Ratings of ACSR Zebra 50°C Limit Considering 0.5m/s Wind Speed and 0 Solar Irradiance 213
Table 6.6: Short-Term and Medium-Term Overloading Ratings of ACSR Zebra 50°C Limit Considering 1m/s Wind Speed 0 Solar Irradiance 214

Table 6.7: Short-Term and Medium-Term Overloading Ratings of AAAC Sorbus 75°C Limit Considering 0.5m/s Wind Speed 0 Solar Irradiance 215
Table 6.8: Short-Term and Medium-Term Overloading Ratings of AAAC Sorbus 75°C Limit Considering 1m/s Wind Speed 0 Solar Irradiance 216
Table 6.9: Weather data overview (nearby original experiment location) [79], [83].221
Table 6.10: Summary of TGN26 guidelines for OHLs' exceedances.....223
Table 7.1: Ambient conditions under the summer STR assumption in practice [3], [8], [11], [14], [56], [77].....246
Table 7.2: New ambient conditions for summer STR considered global warming and heat waves.....247
Table 7.3: Short-Term and Medium-Term Overloading Ratings of Overhead Line Sorbus and 400kV 1000$mm2$ Cable Composite 0.5m/s WS and 0 SI 267
Table 7.4: Short-Term and Medium-Term Overloading Ratings of Overhead Line Sorbus and 400kV 1000$mm2$ Cable Composite 0.5m/s WS and 1000 SI 268
Table 7.5: Joint Circuit Short-Term and Medium-Term Overloading Ratings of Substation, 0.5m/s WS, 0 SI and Tap Position 11.....291
Table 7.6: Joint Circuit Short-Term and Medium-Term Overloading Ratings of Substation, 0.5m/s WS, 0 SI and Tap Position 15.....292

List of Abbreviations

AA	Attacking angle
AAT	Ambient air temperature
AAAC	All aluminium alloy conductor
AC	Alternating current
ACSR	Aluminium conductor steel reinforced
AST	Ambient soil temperature
AST0.3m	Ambient soil temperature at 0.3m depth
AST1m	Ambient soil temperature at 1m depth
AT	Ambient temperature
CCC	Current carrying capacity
CDF	Cumulative distribution function
CFD	Computational fluid dynamics
ConstI	Constant current
ConstPQ	Constant power
ConstZ	Constant impedance
CRF	Cyclic rating factor
CTR	Cyclic thermal rating
DBC	Directly buried cable
DC	Direct current
DNO	Distributed network operator
DTR	Dynamic thermal rating
ExpoC	Exposed cable
FEM	Finite element method
FTC	Filled trough cable
HST	Hot-spot temperature
HSTR	Hot-spot temperature rise

HV	High voltage
LV	Low voltage
MAE	Mean absolute error
NTOT	Non-top oil temperature
NTR	Normal/nameplate thermal rating
NWP	numerical weather prediction
SI	Solar irradiance
SP/A	Spring and Autumn
SST	Steady-state temperature
STR	Static thermal rating
S/MTOR	Short-term and medium-term thermal rating
S/NH	Summer and normal hot
TGN	Technical guidance note
THN	Thermal-hydraulic network
TOT	Top-oil temperature
TOTR	Top-oil temperature rise
TS	Technical specifications
TTC	Thermal time constant
ODAF	Oil directed air forced
OFAF	Oil forced air forced
OHL	Overhead line
ONAN	Oil natural air natural
ONAF	Oil natural air forced
PDF	Probability distribution function
PU	Per unit
RCC	Radiation, convection and conduction
RMSE	Root mean square error
RTTR	Real-time thermal rating
WS	Wind speed
WTI	Winding temperature indicator

W/NC	Winter and normal cold

Nomenclature

α	Solar absorptivity
α_{air}	Thermal diffusivity of air
α_{lid}	Absorptivity of the trough lid
$\alpha(t)$	Attainment factor of the temperature difference between the cable surface and conductor at time i prior to the time of maximum conductor temperature
A'	Projected area of conductor per unit length
A_{cc}	Cable conductor area
$A_{cond,cooler}$	Total area for the conduction of the respective object
$A_{conv,cooler}$	Total area for air convection of the transformer cooler
$A_{conv,object}$	Total area for air convection of the respective object
$A_{conv,tank}$	Total area for air convection of the transformer tank
A_{inner}	The surface area of the inside wall of the conduit
A_{nat}	Coefficients for calculating the natural convective heat transfer process
A_o	The surface area of the cable in the conduit
A_{plate}	Surface area of a single cooling plate in the transformer cooler
$A_{solar,cooler}$	Projected area for the solar irradiance of the transformer cooler
$A_{solar,tank}$	Projected area for the solar irradiance of the transformer tank
a_0	temperature coefficient of resistance of the winding material
β	Inclination degree
β_{air}	Thermal expansion coefficient of the air
$\beta(t)$	Attainment factor of the temperature difference between ambient and cable surface at time i prior to the time of maximum conductor temperature
B_{max}	Maximum magnetic flux density

C_{av}	Heat capacity of the air flow
C_{coeff}	Coefficient of solar heating
C_{mode}	Efficiency due to inhomogeneous temperature distribution for radiation, convection and conduction under respective cooling modes
C_{OFAF}	Efficiency due to inhomogeneous temperature for radiation, convection and conduction under OFAF cooling mode
C_{ONAN}	Efficiency due to inhomogeneous temperature for radiation, convection and conduction under ONAN cooling mode
C_T	Correlation term
Cp	Specific heat capacity of the conductor
Cp_{Al}	Specific heat capacity of the aluminium
Cp_{steel}	Specific heat capacity of the steel
δ	Attacking angle
δ_s	Thermal diffusivity of the homogeneous environment
δ_1	Thickness of the metallic tape core screen
$\partial(gr_{WTI})$	Fixed offset in the WTI gradient
σ	Setfan-Boltzmann constant
Δt	Time increment for the calculation
$\Delta\theta_{BO}$	Temperature rise of the fluid in the bottom over the ambient
$\Delta\theta_{BO,r}{}'$	Fluid temperature at the bottom at the rated load on a different tapping
$\Delta\theta_{DO/BO,r}{}'$	Temperature rise of fluid at the top of the duct over the bottom of the duct at a different tapping
$\Delta\theta_d$	Temperature rise due to the presence of dielectric losses in the cable system
$\Delta\theta_{H,A,r}$	Max winding temperature rise above ambient at rated load and rated AT
$\Delta\theta_{H1}(t)$	First gradient for the hot-spot temperature rise over the top-oil at time t

$\Delta\theta_{H1,i}$	Initial first gradient for the hot-spot temperature rise over the top-oil
$\Delta\theta_{H2}(t)$	Second gradient for the hot-spot temperature rise over the top-oil at time t
$\Delta\theta_{H1,i}$	Initial second gradient for the hot-spot temperature rise over the top-oil
$\Delta\theta_{HS,A,r}$	Hot-spot temperature rise over ambient
$\Delta\theta_{HS,TO}$	Current hot-spot temperature rises over top-oil
$\Delta\theta_{HS,TO}(t)$	Hot-spot temperature rises over top-oil at time t
$\Delta\theta_{HS,TO,i}$	Initial hot-spot temperature rises over top-oil
$\Delta\theta_{HS,TO,r}$	Rated hot-spot temperature rises over top-oil
$\Delta\theta_{HS,TO,u}$	Ultimate hot-spot temperature rises over top-oil
$\Delta\theta_{H/WO}$	Temperature rise of the HST over the fluid at the winding HST location at the bottom
$\Delta\theta_{max}$	Maximum conductor temperature rise above ambient
$\Delta\theta_{s}$	Cable surface temperature rise above the ambient
$\Delta\theta_{TO,A}$	Current top-oil temperature rise over ambient
$\Delta\theta_{TO,A,i}$	Initial top-oil temperature rise over ambient
$\Delta\theta_{TO,A,r}$	Rated top-oil temperature rise over ambient
$\Delta\theta_{TO,A,u}$	Ultimate top-oil temperature rise over ambient
$\Delta\theta_{T/B}$	Temperature rise of the fluid at the top of the radiator over the bottom
$\Delta\theta_{WO/BO}$	Temperature rise of the fluid at the winding HST location over the fluid in the bottom
$\Delta\theta_{W/A,r}$	Rated average temperature rise of the winding over ambient
$\Delta\theta_{w}$	Winding temperature gradient
$\Delta\theta_{x}$	Critical temperature rise of the soil to the ambient
D	Diameter of the conductor
D_a	External diameter of the armour

D_c	Diameter of the core over its metallic screen tapes
D_e	External diameter of the cable
D_e^*	External diameter of the cable for corrugated sheaths
D_{earth}	Earth diameter
D_i	Internal diameter of a tubular conductor or the diameter of a steel core
D_{inner}	Inner diameter of the cylinder-shaped cable-conduit complex
D_o	Outer diameter of the cylinder-shaped cable-conduit complex
D_s	External diameter of the sheath
d_c	Diameter of the conductor of the cable
ε	Emissivity
ε_{inner}	Emissivity of the inside wall of the conduit
ε_o	Emissivity of the cable in the conduit
ε_s	Emissivity of the surface of the conductor
E_{HS}	Eddy loss at the winding hot spot location
E_{store}	Heat stored in the conductor
$E_{store,short-circuit}$	Heat stored in the conductor under short-circuit conditions
F	Mutual heating effect factor
$F_{AA,day}$	Ageing acceleration factor of the day (24 hours)
$F_{AA}(\theta_{heavy})$	Ageing acceleration factor in the heavy loading period
$F_{AA}(\theta_{heavy}')$	Ageing acceleration factor in the heavy loading period after applying the cyclic rating factor
$F_{AA}(\theta_{light})$	Ageing acceleration factor in the light loading period
$F_{AA}(\theta_{light}')$	Ageing acceleration factor in the light loading period after applying cyclic rating factor
F_{cyl}	Geometric factor of concentric cylinders
F_{c-g}	Fraction of the radiated energy from the conductor that reaches the ground and the surroundings

F_{c-sky}	Fraction of the radiated energy from the conductor that goes to the sky
F_{sw}	Shape factor
f	Frequency
γ	Coefficient of the absorption of solar radiation
G	Geometric factor
$\bar{G}$	Geometric factor based on the thickness of the material between the copper tape screen and the outer covering
Gb	Geometric factor
Gr	Grashof number
g	Constant of gravitational acceleration
g_r	Average winding to average oil (in the tank) temperature gradient at rated current
gr_{obs}	Observed winding temperature indicator gradient
gr_{WTI}	Winding temperature indicator gradient set in the instrument
θ	Effective sun's ray incidence angle
$\theta_{A,r}$	Ambient temperature at the rated condition
$\theta_{A,1}$	Ambient temperature at the prior
θ_{AO}	Average fluid temperature in the tank and the radiator
$\theta_{AO,r}$	Average fluid temperature in the tank and radiator at rated load
$\theta_{AO,1}$	Average fluid temperature in the tank and radiator at the prior
θ_a	Ambient temperature
$\theta_{a,object}$	Ambient air temperature of the respective object
θ_{av}	Mean value of the temperature
$\theta_{a,NP}$	Air temperature specified for nameplate rating
θ_{BO}	Temperature of the fluid at the bottom at the current time
$\theta_{BO,r}$	Fluid temperature at the bottom at the rated load
θ_c	Conductor temperature
$\theta_c'(i)$	Conductor temperature at time i

$\theta_c'(\infty)$	Conductor temperature at steady-state
$\theta_c'(t)$	Conductor temperature at time t
$\theta_{DAO,r}$	Average temperature of the fluid in the cooling ducts at rated load
$\theta_{DAO,1}$	Average temperature of the fluid in the cooling ducts at the prior
θ_{flim}	Temperature at the boundary layer of the conductor and the air
θ_g	Temperature of the ground beneath the conductor
$\theta_{HS,r}$	Hot-spot temperature at rated load prior
$\theta_{HS,1}$	Hot-spot temperature at rated condition
θ_{HST}	Hot-spot temperature
$\theta_{HST,r}$	Hot-spot temperature at rated condition
θ_{high}	Higher conductor temperature
θ_{inner}	Temperature of the inside wall of the conduit
θ_K	Temperature factor for the resistance correction
θ_{low}	Lower conductor temperature
θ_{max}	Maximum equipment temperature
$\theta_{max,NP}$	Maximum equipment temperature specified in nameplate rating
θ_{NTO}	Non-top-oil temperature
θ_o	Temperature of the cable in the conduit
θ_{paper}	Absolute temperature of the insulation paper
θ_{sky}	The temperature of the sky above the conductor
θ_{TDO}	Winding duct-oil temperature
θ_{TO}	Temperature of the fluid at the top
$\theta_{TO,r}$	Temperature of the fluid at the top at the rated condition
$\theta_{TO,r}{}'$	Temperature of the fluid at the top at rated condition on a different tapping
θ_{WO}	Temperature of oil (fluid) adjacent to the winding hot-spot at a given time
$\theta_{WO,r}$	Temperature of oil (fluid) adjacent to the winding hot-spot at rated load

θ_{WTI}	Measurement temperature by winding temperature indicator
$\theta_{wall,object}$	Wall outer surface temperature of the respective object
$\theta_{w,r}$	Average winding temperature at rated load
$\theta_{w,1}$	Average winding temperature at prior and
H	Hot-spot factor
$Hours$	Hour of the day
H_c	Altitude of the sun
H_{cooler}	Overall height of the transformer cooler
H_e	Altitude of the conductor relative to the sea level
H_{HS}	Per unit of winding height to the hot spot location
H_{tank}	Overall height of the transformer tank
h	Heat dissipation coefficient
$h_{conv,air,cooler}$	Heat transfer coefficient for air convection of the transformer cooler
$h_{conv,air,object}$	Heat transfer coefficient for air convection of the object
$h_{conv,air,tank}$	Heat transfer coefficient for air convection of the transformer tank
$h_{F,air,object}$	Heat transfer coefficient for forced air convection of the object
$h_{N,air,object}$	Heat transfer coefficient for naturl air convection of the object
K	Loading ratio
K_{angle}	Factor of the direction of the wind
K_e	Emissivity coefficient with respect to the black body
K_{ed}	Eddy current coefficient
K_{HS}	Temperature correction for losses at hot-spot location
K_{hys}	Hysteresis coefficient
K_i	Initial loading ratio
K_r	Radiation shape factor taking into account the radiation areas
K_u	Ultimate loading ratio
K_w	Temperature correction for the losses of winding

k	Ratio of the temperature rise of the cable surface to the temperature rise of the conductor of the cable above ambient at steady-state
$k_{ageing,h,o}$	Average ageing rate constant reflecting hydrolytic and oxidative reactions simultaneously
k_{air}	Thermal conductivity of the air in the conduit
$k_{c,DTR}$	Load factor limit for dynamic thermal rating
k_{eff}	Effective thermal conductivity of air
k_f	Thermal conductivity of the air at the film
k_{oil}	Thermal conductivity of transformer oil
k_{sk}	Skin effect factor
k_{solar}	Factor of solar irradiance in SI units
k_{tf}	Scaling factor that adds the effect of the adjacent cables
k_{11}	Thermal model constant
k_{21}	Thermal model constant
k_{22}	Thermal model constant
λ	Effective radial thermal conductivity
$\lambda_{air,object}$	Thermal conductivity of the air for the respective object
λ_f	Thermal conductivity of the air film in contact with the conductor
λ_1	Ratio of the total losses in the metallic sheath due to the conductor losses (sheath loss factor)
λ_2	Ratio of the total losses in metallic armour due to the conductor losses
L	Distance from the surface of the ground to the cable axis (burial depth)
L_c	Characteristic length of the cylinder-shaped cable-conduit complex
L_{cooler}	Overall length of the transformer cooler
$L_{cond,wall,object}$	Characteristic length of conduction for the respective object

$L_{c,cooler}$	Characteristic length of the transformer cooler
$L_{c,tank}$	Characteristic length of the transformer tank
L_{CTR}	Cyclic thermal rating of the transformer
L_{DE}	Equivalent load of a day
$L_{DE}{}'$	Equivalent loading after applying cyclic rating factor
$L_{F,fan,cooler}$	Characteristic length of forced convection by wind generated from the cooling fan of the transformer cooler
$L_{F,wind,cooler}$	Characteristic length of forced convection by natural wind of the transformer cooler
$L_{F,air,tank}$	characteristic length of forced air convection of the transformer tank
$L_{N,air,cooler}$	Characteristic length of the transformer cooler for natural convection
$L_{N,air,tank}$	Characteristic length of the transformer cooler for forced convection
L_{rated}	Rated load (power) of the transformer
L_{tank}	Overall length of the transformer tank
Lat	Latitude
LF	Daily loss-load factor for the cables
$(L/A)_{oil,mode}$	Characteristic length over the effective cooling area of the transformer oil convection under the respective cooling mode
$(L/A)_{oil,OFAF}$	Characteristic length over the effective cooling area of the transformer oil convection under OFAF cooling mode
$(L/A)_{oil,ONAN}$	Characteristic length over the effective cooling area of the transformer oil convection under ONAN cooling mode
I	Electrical current
I_{adj}	Adjusted current rating of the equipment in question
$I_{applied}$	Load currents were chosen so that statistically significant excursions were obtained over the range of design temperatures

I_{cable}	Electrical current through the cable conductor
$I_{cable,CTR}$	Cyclic thermal rating of the cable
I_{design}	Corresponding current for these sets of temperature intervals with the fixed ambient conditions
I_f	Normalized current for the passive fire-protected cable system
I_{HV}	Current in high-voltage winding
I_i	average hourly current load
I_{LV}	Current in low voltage winding
$I_{LV,0}$	Zero sequence current of the low voltage winding
I_{max}	Maximum allowed current of the conductor
I_{NP}	Nameplate rating of the equipment in question
I_o	Normalized current for the baseline condition
$I_{pu}(tap)$	Current loading in per-unit to rated current at the current tap position
I_r	Rated current at the rated load
$I_r{}'$	The rated load on a different tapping
I_{TV}	Current in tertiary winding
I_{10}	No-load current in the primary winding
I_2	Rated current of the secondary winding
$I_2{}'$	Given current on the secondary winding
μ	Load loss factor
μ_f	Dynamic viscosity of air at the film
$\mu_{HS,r}$	Viscosity of the fluid for hot-spot calculation at and rated load
$\mu_{HS,1}$	Viscosity of the fluid for hot-spot calculation at the prior
$\mu_{w,r}$	Viscosity of the fluid for average winding temperature rises rated load
$\mu_{w,1}$	Viscosity of the fluid for average winding temperature rises at the prior
$M_{cable,CTR}$	Cyclic rating factor of the cable

m	Mass of the conductor per unit length
m_{Al}	Mass of the aluminium
m_{cc}	Mass of core and coil
m_{ex}	Winding exponent
m_{nat}	Coefficients of calculating the natural convective heat transfer process
m_{steel}	Mass of the steel
mCp_A	Thermal capacity of phase A
$mCp_{A,db}$	Thermal capacity of phase A for directly buried cable
mC_{AB}	Thermal capacity of phase B
$mCp_{B,db}$	Thermal capacity of phase B for directly buried cable
mCp_C	Thermal capacity of phase C
$mCp_{C,db}$	Thermal capacity of phase C for directly buried cable
mCp_c	Heat capacity of conductor
mCp_{cc}	Heat capacitance of core and coil assembly
mCp_{cooler}	Heat capacitance of transformer cooler
$mCp_{cooler,extra}$	Extra heat capacitance of transformer cooler due to switch from ONAN to OFAF cooling mode
$mCp_{condu,inner}$	Capacity of the inner part of the conduit
$mCp_{condu,outer}$	Heat capacity of the outer part of the conduit
mCp_D	Thermal capacity of phase D
$mCp_{D,db}$	Thermal capacity of phase D for directly buried cable
mCp_E	Thermal capacity of the phase E
mCp_F	Thermal capacity of the phase F
mCp_G	Thermal capacity of the phase G
mCp_{HS}	Thermal capacitance representing the hot-spot
mCp_i	Thermal capacity of the insulation
mCp_j	Thermal capacity of the jacket

$mCp_{oil\&cc}$	Heat capacitance of transformer oil, core and coil assembly without hot-spot
$mCp_{oil\&cc,extra}$	Extra heat capacitance of transformer oil, core and coil due to switch from ONAN to OFAF cooling mode
mCp_s	Thermal capacity of the sheath
mCp_{tank}	Heat capacitance of transformer tank
$mCp_{tank,extra}$	Extra heat capacitance of transformer tank due to switch from ONAN to OFAF cooling mode
N_{HV}	Turn numbers of the high-voltage winding
N_{LV}	Turn numbers of the low-voltage winding
N_{TV}	Turn numbers of the tertiary winding
N_{day}	Number of the day
Nu	Nusselt number
Nu_{δ}	Nusselt number with AA of δ degree
$Nu_{N,object}$	Nusselt number of natural convection of the respective object
$Nu_{N,object}$	Nusselt number of forced convection of the respective object
Nu_{nat}	Nusselt number with no wind
$Nu_{nat,0}$	Nusselt number with no horizontal inclination
$Nu_{nat,\beta}$	Nusselt number of the conductor with inclination to the horizontal of β degree
Nu_{90}	Nusselt number with AA of 90°
Num_{plate}	Total number of cooling plate in the transformer cooler
n	Number of load-carrying conductors in a cable
n_{ex}	Oil exponent
ω	Solar hour angle
ϕ	Wind attacking angle between wind direction and the conductor axis
Pr	Prandtl number
$Pr_{air,object}$	Prandtl number of air convection for the respective object

Q_s	Total heat flux density
Q_{se}	Total solar and sky-radiated heat flux rate elevation corrected
q_c	Rate of heat loss by convection
q_{cn}	Rate of natural convection heat loss
q_{c1}	Rate of forced convection heat loss at low wind speeds
q_{c2}	Rate of forced convection heat loss at high wind speeds
q_d	Dielectric losses
$q_{gen,c}$	Heat generated by the core per minute
$q_{loss,c,OE}$	Loss of the core when overexcitation occurs
$q_{gen,HS,ed,r}$	Corrected Eddy loss at rated load and rated HST
$q_{gen,HS,Joule,r}$	Corrected Joule loss generated at rate load and rated HST
$q_{gen,stray}$	Heat generated by the stray loss
$q_{gen,w,ed,r}$	Heat generated by eddy loss in the winding at rated load
$q_{gen,w,Joule,r}$	Heat generated by the Joule losses in the winding at the rated load
q_i	Corona heating
$q_{in,load}$	Heat input from load losses
$q_{in,loss,t}$	Heat input from total losses
$q_{in,loss,dielectic}$	Heat input from the dielectric loss
$q_{in,loss,t}$	Total heat input from all sources of losses
$q_{in,solar}$	Heat input from solar irradiance
$q_{in,total}$	Total heat input
$q_{in,total,r}$	Total heat input at rated condition
q_J	Rate of heat input from the Joule effect
$q_{loss,copper,rated}$	Rated copper losses on the secondary winding
$q_{loss,c,r}$	Loss of the core
$q_{loss,load,TV}$	Heat losses in the tertiary winding
$q_{loss,no-load}$	No-load losses
$q_{loss,no-load,copper}$	No-load copper losses

$q_{loss,no-load,di}$	No-load dielectric losses
$q_{loss,no-load,ed}$	No-load eddy current losses
$q_{loss,no-load,hys}$	No-load hysteresis losses
$q_{loss,no-load,iron}$	No-load iron losses
$q_{loss,no-load,Joule}$	No-load Joule losses
$q_{loss,no-load,stray}$	No-load stray losses
$q_{loss,t,r}$	Total losses at rated load
$q_{lost,HS}$	Heat lost per minute by the hot-spot
$q_{lost,O}$	Heat lost by the oil
$q_{lost,w}$	Heat loss per minute by the winding
q_M	Magnetic heating
$q_{out,air}$	Heat loss from air convection
$q_{out,rad}$	Heat loss from radiation
q_r	Rate of heat loss by radiation of the conductor
q_s	Rate of heat input from the solar irradiance in the conductor surface
$q_{stray,r}$	Stray loss at rated load
q_w	Evaporative cooling
ρ_{air}	The density of the air
ρ_f	Density of air at the film of the conductor and the ambient
ρ_{th}	Thermal resistivity of the material in question
$\rho_{th,fill}$	Thermal resistivity of the backfill
$\rho_{th,fiiler}$	Thermal resistivity of the filler material
$\rho_{th,i}$	Thermal resistivity of the insulation
$\rho_{th,Native}$	Thermal resistivity of the earth
$\rho_{th,s}$	Thermal resistivity of the homogeneous environment
$\rho_{th,soil}$	Thermal resistivity of the soil
$R_{AC}(\theta_c)$	AC resistance of the conductor at the temperature θ_c

$R_{AC,max}$	AC resistance of the conductor at the maximum prolonged operation temperature
$R_{DC}(\theta_c)$	DC resistance of the conductor at temperature θ_c
$R_{MR,A}$	Thermal resistance of mixed radiation and air convection
$R_{N,O}$	Thermal resistance of natural oil convection
$R_{th,A}$	Thermal resistance of phase A
$R_{th,A,db}$	Thermal resistance of phase A for directly buried cable
$R_{th,B}$	Thermal resistance of phase B
$R_{th,B,db}$	Thermal resistance of phase B for directly buried cable
$R_{th,C}$	Thermal resistance of phase C
$\bar{R}_{th,ca}{}'$	Total thermal resistance between the conductor and the ambient
$R_{th,condu}$	Thermal resistance of the conduit
$R_{th,cond,wall,cooler}$	Thermal resistance of conduction for the transformer cooler wall
$R_{th,cond,wall,objet}$	Thermal resistance of conduction for the wall of the obeject
$R_{th,cond,wall,tank}$	Thermal resistance of conduction for the transformer tank wall
$R_{th,conv,air}$	Thermal resistance of air convection
$R_{th,conv,air,cooler}$	Thermal resistance of air convection for the transformer cooler
$R_{th,conv,air,object}$	Thermal resistance of air convection for the respective object
$R_{th,conv,air,tank}$	Thermal resistance of air convection for the transformer tank
$R_{th,conv,C}$	Thermal resistance of convection in the air gap
$R_{th,conv,oil}$	Thermal resistance of oil convection
$\bar{R}_{th,da}{}'$	Total thermal resistance between the insulation and the ambient
$R_{th,C,db}$	Thermal resistance of phase C for directly buried cable
$R_{th,D}$	Thermal resistance of phase D
$R_{th,D,db}$	Thermal resistance of phase D for directly buried cable
$R_{th,E}$	Thermal resistance of phase E
$R_{th,e}$	Thermal resistance of the earth or external thermal circuit
$R_{th,F}$	Thermal resistance of phase F

$R_{th,G}$	Thermal resistance of phase G
$R_{th,i}$	Thermal resistance of the insulation
$R_{th,j}$	Thermal resistance of the jacket
$R_{th,rad}$	Thermal resistance of radiation
$R_{th,rad,cooler}$	Thermal resistance of radiation for the transformer cooler
$R_{th,rad,object}$	Thermal resistance of radiation for the respective object
$R_{th,rad,tank}$	Thermal resistance of radiation for the transformer tank
$R_{th,1}$	Thermal resistance per core between conductor and sheath/Thermal resistance of insulation
$R_{th,2}$	Thermal resistance between sheath and armour
$R_{th,3}$	Thermal resistance of external serving (jacket)
$R_{th,4}$	Thermal resistance of the surrounding
$R_{th,4}{}'$	Thermal resistance of the air gap between the cable and the ducts/conduit
$R_{th,4}{}''$	Thermal resistance of the wall of the ducts/conduit
$R_{th,4}{}'''$	Thermal resistance of the surrounding medium of the duct/conduit
R_{TV}	Equivalent electrical resistance of the tertiary winding
$R_{\theta_{high}}$	AC resistance of the conductor at a higher temperature
$R_{\theta_{low}}$	AC resistance of the conductor at the lower temperature
$R(\theta_c)$	Electrical resistance of the conductor at the temperature θ_c, which can be DC or AC
Ra	Rayleigh number
$Ra_{L,air,object}$	Rayleigh number of the air convection for the respective object
$Ra_{L,oil}$	Rayleigh number of natural convection of oil
Re	Reynolds number
$Re_{L,air,object}$	Reynolds numberof the air convection for the respective object
$r_{B,db}$	Depth of the B phase of the environment for directly buried cable

r_c	Radius of the conductor
r_E	Radius of the E phase of the environment around the cable
r_e	Overall radius of the cable or the cable-conduit complex
r_{env}	Radius of the equivalent cylindrical environment
r_F	Radius of the F phase of the environment around the cable
r_i	Radius of the main insulation
r_{inner}	Inside radius of the section
r_o	Outer radius of the section
r_s	Outer radius of sheath
S_i	Intensity of the solar radiation
S_{OFAF}	Rated MVA on OFAF mode
S_{ONAN}	Rated MVA on ONAN mode
S_2	Rated apparent power on the secondary winding
$S_2{}'$	Given apparent power on the secondary winding
τ_{TO}	Rated oil time constant
$\tau_{TO,r}$	Current oil time constant
τ_w	Winding time constant
t	Loading duration
t_g	Average nominal clearance between the core metallic screentape and the average inside diameter of the sheath
t_i	Thickness of the core insulation, including carbon black and metallized paper tapes
t_{heavy}	Length of the heavy loading period
t_{light}	Length of the light loading period
t_1	Thickness of the insulation between the conductor and sheath
t_2	Thickness of the bedding
t_3	Thickness of the serving
U	Constants depending on the actual construction of the cable
U_{HV}	Voltage of the high-voltage winding

U_{LV}	Voltage of the low-voltage winding
U_{TV}	Voltage of the tertiary winding
U_1	Rated primary voltage
$U_1{}'$	Given voltage at the primary winding
V	Constants depending on the actual construction of the cable
V_{wind}	Wind speed from the natural wind
$V_{wind,AF}$	Wind speed from the cooling fan under AF cooling mode
$V_{wind,comb,object}$	Combined wind speed of the respective object
χ	The solar azimuth variable
x	Exponent for duct oil rise over bottom oil
x_{ex}	Winding exponent
x_{disp}	Capillary axial displacement
Y	Constants depending on the actual construction of the cable
Y_c	Ratio of the losses from skin and proximity effects to the Joule losses
Y_i	Fraction of the cable losses to its maximum value at time i prior to the time of maximum conductor temperature
y	Exponent of average fluid rise with heat loss
y_{ex}	Winding exponent
y_{WTI}	WTI exponent
$VG_{I,HV}$	Effect of the vector group on the phase current of the HV winding
$VG_{I,LV}$	Effect of the vector group on the phase current of the LV winding
$VG_{turn,HV}$	Effect of the vector group on the turn number of the HV winding
$VG_{turn,LV}$	Effect of the vector group on the turn number of the LV winding
W_{cooler}	Overall width of the transformer cooler
W_d	Dielectric loss per unit length
$W_{HV}(tap)$	Normalized weightages of the load losses of the LV winding to the total load losses at the tap position in question

$W'_{HV}(tap)$	Weightages of the load losses of the HV winding to the total load losses at the tap position in question before normalizing
$W_{LV}(tap)$	Normalized weightages of the load losses of the LV winding to the total load losses at the tap position in question
$W'_{LV}(tap)$	Weightages of the load losses of the LV winding to the total load losses at the tap position in question before normalizing
W_{tank}	Overall width of the transformer tank
Z_c	Azimuth of the sun
Z_l	Azimuth of the line
$Z_{pu}(tap)$	Per-unit impedance depends on the respective tap positions
z_{ttb}	Exponent for the top-to-bottom fluid temperature difference

Chapter 1

Introduction

Growing concerns about climate change have brought renewed focus to the resilience and reliability of power systems worldwide, which depend on the proper design and rating of the individual components that make up the network. Most power system components are limited by their maximum permissible operating temperature. Exceeding these temperature limits can lead to several serious consequences, including accelerated ageing, reduced electrical insulation levels and safety clearances that increase the risk of electrical faults and shocks, and, in extreme cases, fires or explosions. Such failures can result in permanent damage to assets, destruction of nearby equipment, and even widespread power outages.

The allowable temperature thresholds that define safe operating limits are expressed through thermal ratings. Accurate and comprehensive evaluation of these ratings is essential for maintaining the reliability, safety, and longevity of the power system.

Thermal ratings are determined using electrical-thermal models, which describe how components heat up and cool down under different electrical and environmental conditions. Developing and applying accurate thermal models is therefore a key step in establishing reliable thermal ratings. In this PhD study, three main power system components are being evaluated: power transformers, cables, and overhead lines (OHLs). The research presents detailed thermal modelling methodologies for each component, supported by meteorological data that represent realistic ambient conditions, as well as typical loading profiles.

Thermal ratings were calculated and assessed for various operating states and time periods. These include pre-fault and post-fault conditions, steady-state continuous

operation, cyclic daily loading, and short- or medium-term overloading periods ranging from a few minutes to several hours. Different assumptions about loading duration and environmental conditions naturally lead to different thermal ratings for each component.

However, components in a power system rarely operate in isolation. In most cases, two or more components form joint circuits, where the overall circuit rating is limited by the component in the circuit which has the lowest maximum loading capacity for given ambient and operating conditions for the considered period of interest. Under the influence of climate change and more frequent heatwave events, it has become increasingly important to evaluate these joint-circuit ratings using measured weather data. Such evaluations help determine which component becomes limiting under specific conditions and how the thermal behaviour of one component affects the others.

To maintain consistency, all components in a joint circuit must be evaluated under the same loading profile assumptions, whether static (constant), cyclic, or time-varying, so that their ratings are unified. Proper evaluation of the joint circuit's thermal ratings helps preserve the resilience, reliability, and safety of the existing power system. They also help identify the weaknesses of the existing system, enabling the planning of a new power system or an upgrade to the existing system more efficiently and effectively, both operationally and economically, in a changing climate.

1.1 Scope of Research

This thesis presents a comprehensive assessment of the operational thermal characteristics of three main components in the power system: the oil-immersed power transformer, cable, and OHL. Unless otherwise specified, all transformers discussed herein refer to oil-immersed units. In addition to individual component studies, two representative joint circuit configurations, composite circuits (combining OHL and cable sections) and substation circuits (linking transformers with connected OHLs and/or cables), are also analysed. Other components, such as circuit breakers, are also essential in the power system, but due to limited time, they are not included in this thesis.

This work establishes consistent methodologies for STR, DTR, S/MTOR, exceedance rating and CTR. The methodologies are applied uniformly across all

component types, allowing the accurate assessment of each component and the overall joint circuit capacity under both normal operating and emergency conditions.

1.1.1 Thermal Modelling of Three Main Power System Components

This thesis presents the methodology used to develop thermal models for the three main power system components: power transformers, cables, and OHLs. Each model is derived from the component's physical characteristics and incorporates key thermal parameters, including ambient conditions, heat inputs, thermal capacitances, and thermal resistances.

1.1.2 Meteorological Data and Loading Profile

Ambient weather conditions are a key input to the thermal rating models, as they directly influence the heat transfer and loading capacity of network components. These conditions include ambient air temperature (AAT), ambient soil temperature (AST), wind speed (WS), wind direction (or attacking angle, AA), and solar irradiance (SI). In addition, the component's or circuit's loading profile must be included when assessing ratings under non-continuous or time-varying operating conditions.

1.1.3 Thermal Ratings of Individual Components

Before assessing the joint circuit rating, the thermal performance and ratings of the individual components must first be evaluated.

Transformer Ratings: The steady-state hot-spot temperature (HST) was calculated using the proposed thermal models for an example 120/240MVA 400/132 kV auto-transformer operating in oil-natural air natural (ONAN) and oil-forced air-forced (OFAF) cooling mode. Both the nominal tap position and the tap position associated with maximum losses were analysed to determine steady-state top-oil and HST under various ambient and loading conditions. Transient thermal time constants (TTC) were evaluated to model temperature evolution after load steps. STR and DTR are assessed based on the calculated steady-state hot-spot temperature. S/MTOR are derived based on allowable hot-spot temperature rise and winding temperature indicator (WTI) trip limit, determining maximum loading for short-term (3, 5, 10, 20 minutes) and medium-

term (60 and 360 minutes) overloads. CTR is evaluated by modelling the thermal response of top-oil and winding hot-spot temperatures to daily load cycles, ensuring that the transformer returns to thermal equilibrium over 24 hours while respecting the temperature-rise limits are not exceeded [1]-[3].

Cable Ratings: three types of cable construction are considered in this thesis: directly buried cable (DBC), cable in a filled trough (or filled trough cable, FTC), and cable exposed in air and to solar irradiance (or exposed cable, ExpoC). The calculated ratings are applied to the 400 kV XLPE power cables (ExpoC, FTC, and DBC sections) and to the 132 kV XLPE power cables. Soil thermal resistivity, soil temperatures, and moisture conditions are incorporated to provide a realistic, site-specific assessment. STR and DTR calculated from steady-state temperatures (SSTs). S/MTOR are assessed using the cable's TTCs to determine the permissible overload duration before conductor temperature reaches its maximum limit. CTR are calculated by applying 24-hour cyclic load profiles and solar irradiance patterns, ensuring thermal recovery during light-load periods and calculating the maximum sustainable cyclic current without exceeding design temperature limits [4]-[8].

OHL Ratings: STR and DTR are calculated using IEEE 738 [9] and BS EN [10] for the considered ACSR Zebra and AAAC Sorbus conductors. For S/MTOR maximum permissible loading above DTR is determined for defined emergency durations, considering conductor thermal inertia, pre-fault loading and allowable maximum temperatures. Exceedance levels analysis of OHLs: Sub-hourly (5-minute) ambient data derived from hourly weather records via linear interpolation. Dynamic simulation of exceedance level analysis was performed using 5-minute interpolated ambient data derived from hourly weather records, and the results were compared with Technical Guidance Note (TGN) 026 thresholds: ≤ 12 % for post-fault, ≤ 0.1 % for pre-fault, and ≤ 0.01 % for 5 °C over-temperature exceedance [11].

1.1.4 Thermal Ratings of Components in a Joint Circuit

Circuits in the transmission power system are composed of various of different components. These components include, but are not limited to, OHL, cables,

transformers, joints and terminations. The overall capacity of a circuit is limited by the component with the lowest rating, which is also denoted as the joint circuit rating. The components in different circuits may vary, so the combination of components that form a circuit may differ.

When assessing the hosting capacity of a network containing both OHL and transformers, it was found that the violation of the thermal limit occurs at the head of the network, e.g., the branch from bus 0 to bus 1 in the IEEE 33-bus network, as shown in Figure 1.1. This finding suggests a high risk of congestion at this location. Such a location usually represents the network substation, where it can be assumed that all the components for an open substation share the same ambient temperature and likely other ambient conditions.

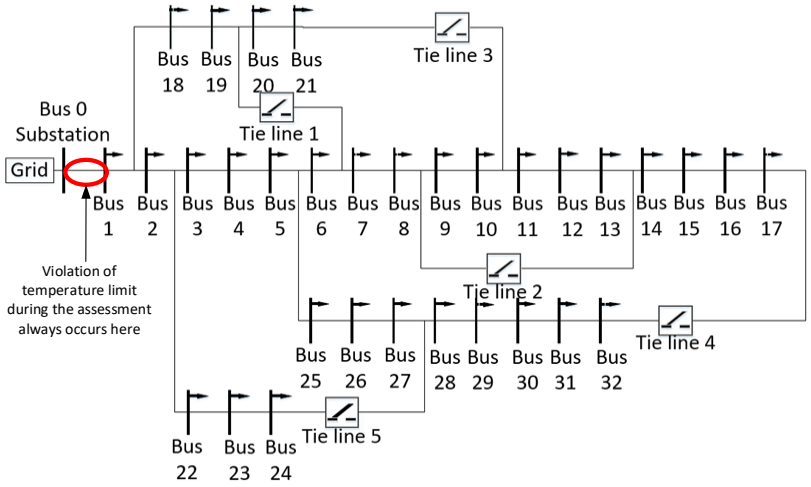

Figure 1.1: Single-line diagram of the IEEE-33 bus network [12].

In this study, a joint circuit is defined as a configuration that includes at least two of the main power network components: OHL, cable, and transformer. Two representative joint circuit types are analysed:

1. OHL–cable composite circuit, representing a busbar connection, and
2. OHL–transformer–cable circuit, representing a typical grid entry point or substation connection.

Joints, terminations, and protection systems are not included in the present analysis but should be addressed in future work.

1.2 Research Objectives, Outcomes and Publications

The main objectives of this PhD study are:

- To develop consistent rating methodologies for OHL, cable, and transformer components and circuits under steady-state, dynamic, emergency, and cyclic loading conditions, and to introduce the exceedance rating concept for OHL.
- To identify the limiting element within joint circuits and assess its influence on the overall circuit capacity.
- To quantify the impact of environmental factors, including air temperature, solar irradiance, wind speed, and soil temperature, on the thermal ratings of individual components and circuits.
- To provide network planners/operators with practical headroom estimates under both continuous and emergency conditions

This work published conference proceeding:

- *Probabilistic Evaluation of Static, Dynamic and Cyclic Thermal Rating Constraints for Hosting Capacity Analysis*

Journal articles published and in preparation of publish:

- *Hosting capacity of distribution networks for controlled and uncontrolled residential EV charging with static and dynamic thermal ratings of network components*
- *Improved Transformer Thermal Model: Inclusion of Weather Factors, Cooling and Tap Changer Controls and Typical Test Results* (in preparation)
- *Transformer in a Joint Circuit* (in preparation)
- *Full Evaluation (Exceedance and Security Limits/Levels) of the Transformer in a Joint Circuit* (in preparation)

This work also forms part of the *THERMAL* programme (Project P3: REWARD) in collaboration with National Grid Electricity Transmission. Project report of:

- *Review of Relevant Literature and Previous Work/Projects*
- *Review of Existing Transformer, OHL and Cable Models*

- *Improved Models at Individual Asset/Component Level*
- *Improved Models at Joint Circuit Level*
- *Report on Substation Level Integration*
- *Report on Network Level Integration*
- *Report on System Level Integration*
- *Report on the Accelerated Component Ageing*
- *Report on the Increase of Component Failure Rates*
- *Report on Integration in a Common Toolset for System Performance Analysis*

has been delivered to the programme. Together with project model repositories:

- *Repository of Existing Models*
- *Repository of Improved Models*

1.3 Thesis Structure

Chapter 2 reviews existing literature and previous work on thermal modelling, and the capacity limits of the three main components individually. It also summarises the established approaches to determining the thermal ratings of these components.

Chapter 3 presents the meteorological data and loading profile used in this thesis, including both historical and projected data. It also outlines the key assumptions applied and the development of new ambient condition scenarios used to assess component performance under heatwave conditions.

Chapters 4, 5, and 6 focus individually on power transformers, AC power cables and OHLs, respectively. Each chapter presents the corresponding individual thermal modelling processes, thermal models, and thermal ratings, followed by assessments and discussion of the findings.

Chapter 7 evaluates the joint circuit ratings of the three main components. Ratings for two example joint circuits are provided, along with the thermal ratings for each joint circuit, and discuss additional factors influencing joint-circuit performance before concluding the study.

Chapter 2

Overview of Thermal Modelling for Three Main Power System Components

This chapter presents a detailed review of existing thermal models, standards, and research relevant to the evaluation of thermal capacity limits for the three principal components of the power transmission system: OHLs, underground cables, and power transformers. The review highlights both established methodologies and recent developments in assessing static, dynamic, and cyclic thermal ratings, drawing upon international standards as well as technical reports.

Particular attention is given to identifying the assumptions, simplifications, and boundary conditions applied in traditional rating approaches, and to highlighting recent efforts aimed at improving the physical representation of heat transfer processes within each component.

The chapter begins by outlining the standard models for transformers, cables, and overhead lines, as defined in key international standards and commonly adopted within industry practice. This is followed by a review of supplementary academic and industrial studies that have advanced or extended these models to better capture transient thermal behaviour, environmental dependencies, and the influence of operational factors such as voltage variation and loading profiles. Subsequently, the modelling of components operating jointly within the same circuit is reviewed, such as OHL–cable–transformer configurations in transmission substations. This is examined to understand how their individual thermal limits interact and influence overall circuit performance.

The latter part of the chapter discusses the definitions of thermal ratings within technical guidance documents such as TGN 26, with emphasis on the limitations of fixed

seasonal assumptions and inconsistent ambient air temperatures used in traditional steady-state rating methodologies. Finally, a problem statement is formulated to justify the need for improved modelling approaches that consider thermal time constants, load types, pre-fault and post-fault operating conditions, and consistent ambient assumptions across all components. This review provides the necessary context and foundation for the development of unified thermal rating methodologies presented in the subsequent chapters.

2.1 Existing Models of Components

This section reviews existing literature and previous work, aimed at evaluating the thermal capacity limits of network components. The main aim is to provide a comprehensive overview of the previous efforts in evaluating thermal ratings and capacity limits of the three most common components: overhead lines (OHLs), underground cables and power transformers, as well as the literature and previous work on the joint or combined capacity limits of these components operating together in the same circuit, as in, e.g., transmission system substations. The report provides details on the thermal models, as presented in related standards, as well as in some other related studies investigating the development of improved modelling frameworks for evaluating their static and dynamic (or real-time) thermal ratings, as well as cyclic thermal ratings.

2.1.1 Standard Thermal Models for Power Transformers

The standard models for the rating of the transformers are given by [1], [2], [13]:

- [1] IEEE Std C57.91: IEEE Guide for Loading Mineral-Oil-Immersed Transformers and Step-Voltage Regulators
- [2] IEC 60076-7: Loading guide for mineral-oil-immersed power transformers
- [1] IEEE Std C57.91 Annex G: Alternate temperature calculation method
- [13] CIGRE 659: Transformer Thermal Modelling
- [14] TGN(E) 303: Co-ordination of Plant Thermal Ratings
- [3] TGN(T) 029: Transformer Loading Guide

2.1.1.1 Existing Standards for Thermal Modelling of the Transformer: IEEE Std C57.91: IEEE Guide for Loading Mineral-Oil-Immersed Transformers and Step-Voltage Regulators

The standard [1] provides a method of calculation for the oil-immersed transformer HST θ_{HST} using winding and oil exponents, considering only the variation of ambient temperature θ_a and transformer loading ratio K. The transformer DTR can be calculated by assuming the transformer is loaded indefinitely at a constant ambient temperature.

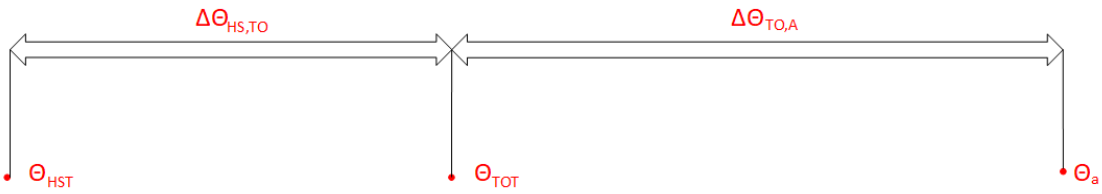

Figure 2.1: Transformer model according to the IEEE and IEC standards [1], [2].

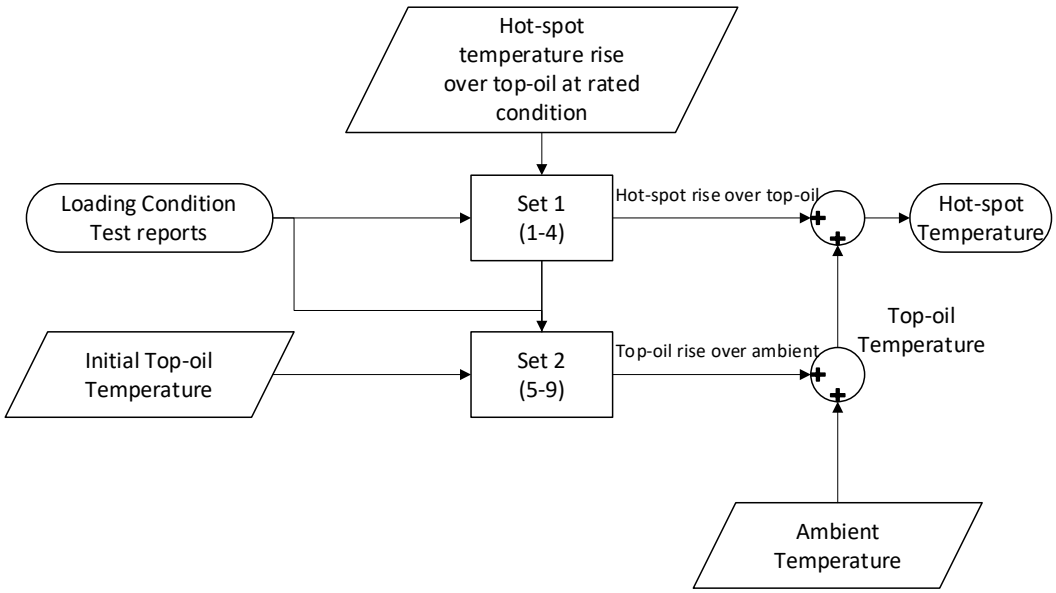

Figure 2.2: Block diagram of the IEEE method [1].

The general model and the calculation of HST according to IEEE standards are summarised in Figure 2.1 and Figure 2.2, respectively. For clarity, the equations are divided into two sets. Namely, the Set 1 equation, which governs the hot-spot rise over top oil, and Set 2, which governs the top-oil rise over ambient. Set 1 is expressed as follows:

$$\Delta\theta_{HS,TO} = (\Delta\theta_{HS,TO,u} - \Delta\theta_{HS,TO,i})(1 - e^{(-t)/\tau_w}) + \Delta\theta_{HS,TO,i} \quad (1)$$

$$\Delta\theta_{HS,TO,i} = \Delta\theta_{HS,TO,r} \cdot {K_i}^{2m_{ex}} \quad (2)$$

$$\Delta\theta_{HS,TO,u} = \Delta\theta_{HS,TO,r} \cdot {K_u}^{2m_{ex}} \quad (3)$$

$$\Delta\theta_{HS,TO,r} = \Delta\theta_{HS,A,r} - \Delta\theta_{TO,A,r} \quad (4)$$

where: $\Delta\theta_{HS,TO}$, $\Delta\theta_{HS,TO,u}$, $\Delta\theta_{HS,TO,i}$ and $\Delta\theta_{HS,TO,r}$ are the current, ultimate, initial and rated hot-spot temperature rise over top-oil in K, respectively; t is the loading duration in min; τ_w is the winding time constant in min; K_i and K_u are initial and ultimate loading ratios, respectively; m is the winding exponent; $\Delta\theta_{HS,A,r}$ and $\Delta\theta_{TO,A,r}$ are the hot-spot and top-oil temperature rise over ambient in K, respectively.

For Set 2 equations, (5)-(9) represent the top-oil rise over ambient and are expressed as:

$$\Delta\theta_{TO,A} = (\Delta\theta_{TO,A,u} - \Delta\theta_{TO,A,i})(1 - e^{(-t)/\tau_{TO}}) + \Delta\theta_{TO,A,i} \quad (5)$$

$$\Delta\theta_{TO,A,i} = \Delta\theta_{TO,A,r} \cdot \left(\frac{\left({K_i}^2 \cdot Ratio\right) + 1}{Ratio + 1}\right)^{n_{ex}} \quad (6)$$

$$\Delta\theta_{TO,A,u} = \Delta\theta_{TO,A,r} \cdot \left(\frac{\left({K_u}^2 \cdot Ratio\right) + 1}{Ratio + 1}\right)^{n_{ex}} \quad (7)$$

$$\tau_{TO,r} = \frac{mCp \cdot \Delta\theta_{TO,A,r}}{q_{in,total,r}} \quad (8)$$

$$\tau_{TO} = \tau_{TO,r} \frac{\left(\frac{\Delta\theta_{TO,A,u}}{\Delta\theta_{TO,A,r}}\right) - \left(\frac{\Delta\theta_{TO,A,i}}{\Delta\theta_{TO,A,r}}\right)}{\left(\frac{\Delta\theta_{TO,A,u}}{\Delta\theta_{TO,A,r}}\right)^{\frac{1}{n_{ex}}} - \left(\frac{\Delta\theta_{TO,A,i}}{\Delta\theta_{TO,A,r}}\right)^{\frac{1}{n_{ex}}}} \quad (9)$$

where: $\Delta\theta_{TO,A}$, $\Delta\theta_{TO,A,u}$ and $\Delta\theta_{TO,A,i}$ are the current, ultimate and initial top-oil rise to ambient in $Kelvin$, respectively; $Ratio$ is the ratio of the load losses to no-load losses

of the tap position in question. n_{ex} is the oil exponent in min; $\tau_{TO,r}$ and τ_{TO} are the rated and current oil time constant in min, respectively; mCp is the heat capacity in $J \cdot kg/K$; $q_{in,total,r}$ represents the total losses at the rated condition.

2.1.1.2 Cyclic Thermal Rating in IEEE Std C57.91

Next, this standard presents a method to convert the transformer loading for the day prior and the 24-hour fluctuating transformer load profile, or the peak of the 24-hour transformer loading profile, to constant load profiles, denoted as equivalent load, shown in Figure 2.3.

The equivalent load of a day L_{DE} is calculated by:

$$L_{DE} = \left[\frac{{L_1}^2 t_1 + {L_2}^2 t_2 + {L_3}^2 t_3 + \cdots + {L_n}^2 t_n}{t_1 + t_2 + t_3 + \cdots + t_n}\right]^{0.5} \tag{10}$$

where: L_1,L_2,… are the hourly power outputs for t_1, t_2 ... hours. From the equivalent load of a day and the peak of the same day, the HST at the end of the day can be calculated using (1)-(9). When the determined HST is lower than the limit, a cyclic rating factor (CRF) can be applied as a multiplier to the equivalent daily loading to reach the HST limit, expressed as:

$$L_{DE}{}' = L_{DE} \cdot CRF \tag{11}$$

where: $L_{DE}{}'$ is the equivalent loading after applying CRF. The CTR is then determined by the lower of the HST limit reaching CRF of the equivalent load of the day and the equivalent load of the peak load period of the day as follows:

$$L_{CTR} = \min\left(CRF_{daily}, CRF_{peak}\right) * L_{rated} \tag{12}$$

where: L_{rated} is the rated power of the transformer, CRF_{daily} and CRF_{peak} are the CRF for equivalent daily loading and peak loading that reach the HST limit.

The limitation of this approach is that the method for calculating the daily equivalent loading and the equivalent loading during peak hours does not accurately reflect the real-time temperature change of the transformer due to changes in loading during a load cycle. In other words, it cannot capture the real-time fluctuating load. As

shown in Figure 2.3, the dashed line represents the equivalent load used in the calculation, compared to the actual load shown as the solid line.

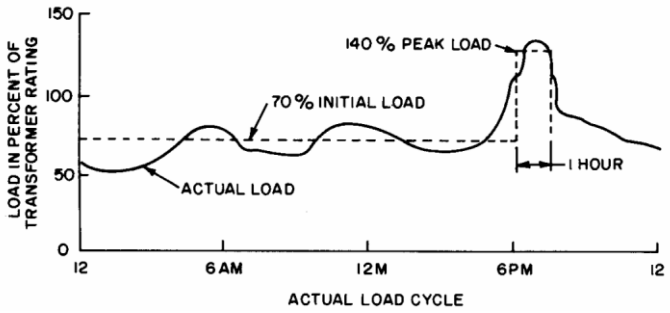

Figure 2.3: Example of the equivalent load cycle compared to the actual load cycle and the peak load [1].

2.1.1.3 Previous Standard for Transformer IEC 60076-7: Loading Guide for Mineral-oil-immersed Power Transformers

The IEC standards [2] provide a similar method that follows the same calculation order for the transformer HST: first calculating the TOT from AT and the loading ratio, and then calculating the HST from TOT. The difference is in the use of the hot-spot factor (HSF) instead of the winding exponent when calculating the HST from TOT.

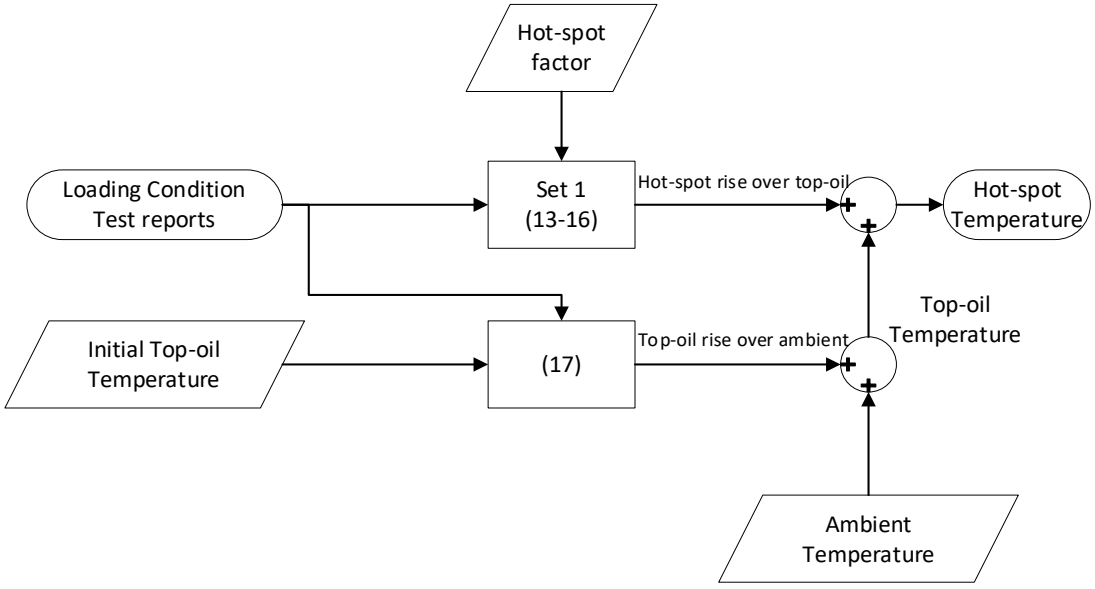

Figure 2.4: Block diagram of the IEC method [2].

The general model used by the IEC standard is the same as that shown in Figure 2.1 for the IEEE standard. Similar to the IEEE standard, the equations governing the IEC method are divided into two sets of equations, where Set 1 equations (13)-(16) define the hot-spot rise over top-oil and are expressed as:

$$\Delta\theta_{HS,TO}(t) = \Delta\theta_{H1}(t) - \Delta\theta_{H2}(t) \tag{13}$$

$$\Delta\theta_{H1}(t) = \Delta\theta_{H1,i} + (k_{21} \cdot \Delta\theta_{HS,TO,r} \cdot K^{y_{ex}} - \Delta\theta_{H1,i})(1 - e^{-t/(k_{22}\cdot\tau_w)}) \tag{14}$$

$$\Delta\theta_{H2}(t) = \Delta\theta_{H2,i} + ((k_{21} - 1) \cdot \Delta\theta_{HS,TO,r} \cdot K^{y_{ex}} - \Delta\theta_{H2,i})(1 - e^{-t/(k_{22}\cdot\tau_o)}) \tag{15}$$

$$\Delta\theta_{HS,TO,r} = H \cdot gr \tag{16}$$

where: $\Delta\theta_{HS,TO}(t)$ is the hot-spot temperature rise over top-oil at time t in $Kelvin$; $\Delta\theta_{H1}(t)$ and $\Delta\theta_{H2}(t)$ are two gradients for the hot-spot temperature rise over the top-oil at time t increase to a level corresponding to a loading ratio; $\Delta\theta_{H1,i}$ and $\Delta\theta_{H2,i}$ are two initial gradients for the hot-spot temperature rise over the top-oil increase to a level corresponding to a loading ratio; $\Delta\theta_{HS,TO,r}$ is the hot-spot temperature rise over top-oil at the rated condition in $Kelvin$; K is the loading ratio in PU; y_{ex} is the winding exponent; t is the duration of loading in min; τ_w and τ_o are winding time constant and oil time constant in min, respectively; gr is the average winding to average oil (in the tank) temperature gradient at rated current in $Kelvin$; H is the hot-spot factor; k_{21}, k_{22} are thermal model constants, the recommended value is given by [2].

For Set 2 equations, the top-oil rise over ambient can be expressed as follows:

$$\Delta\theta_{TO,A}(t) = \Delta\theta_{TO,A,i} + (\Delta\theta_{TO,A,r} \cdot (\left(\frac{1 + Ratio \cdot (K^2)}{1 + Ratio}\right)^{x_{ex}} - \Delta\theta_{TO,A,i}) \cdot (1 - e^{-t/(k_{11}\cdot\tau_o)}) \tag{17}$$

where: x_{ex} is the winding exponent; k_{11} is thermal model constant, the recommended value is given by [2].

2.1.1.4 Existing Standards for Thermal Modelling of the Transformer: IEEE Std C57.91 Annex G: Alternate Temperature Calculation Method

The IEEE Std C57.91, Annex G, [1], provides another method of calculating the HST for the transformer based on the fluid flow condition. The general equation for calculating the HST θ_{HST} is given as:

$$\theta_{HST} = \theta_A + \Delta\theta_{BO} + \Delta\theta_{WO/BO} + \Delta\theta_{H/WO} \tag{18}$$

where: θ_A is the average ambient temperature during the period in ℃; $\Delta\theta_{BO}$ is the temperature rise of the fluid in the bottom over the ambient in ℃; $\Delta\theta_{WO/BO}$ is the temperature rise of the fluid at the winding HST location over the fluid in the bottom in ℃; and $\Delta\theta_{H/WO}$ is the temperature rise of the HST over the fluid at the winding HST location at the bottom in ℃. The temperature of the fluid at the bottom θ_{BO} and the top θ_{TO} are calculated by:

$$\theta_{BO} = \theta_{AO} - \frac{\Delta\theta_{T/B}}{2} \tag{19}$$

$$\theta_{TO} = \theta_{AO} + \frac{\Delta\theta_{T/B}}{2} \tag{20}$$

where: θ_{AO} is the average fluid temperature in the tank and the radiator in ℃; and $\Delta\theta_{T/B}$ is the temperature rise of the fluid at the top of the radiator over the bottom in ℃.

2.1.1.4.1 Calculation of the Average Winding Temperature in IEEE Std C57.91 Annex G

The heat generated from the winding per minute $q_{in,w}$ is calculated by:

$$q_{gen,w} = K^2 \cdot \left(q_{gen,w,Joule,r} \cdot K_w + \frac{q_{gen,w,ed,r}}{K_w} \right) \cdot \Delta t \tag{21}$$

where: K is the ratio of load to rated load; K_w is the temperature correction for the losses of winding; $q_{gen,w,Joule,r}$ is the heat generated by the Joule losses in the winding at rated load in W; $q_{gen,w,ed,r}$ is the heat generated by eddy loss in the winding at rated load in W; Δt is the time increment for the calculation in min.

The temperature correction for the losses in winding K_w is expressed as:

$$K_w = \frac{\theta_{w,1} + \theta_K}{\theta_{w,r} + \theta_K} \tag{22}$$

where: θ_K is the temperature factor for the resistance correction in ℃; $\theta_{w,1}$ and $\theta_{w,r}$ are the average winding temperatures at prior and rated load, respectively, in ℃. The heat loss per minute by the winding $q_{lost,w}$ for oil-natural air-natural (ONAN), oil-natural air-forced (ONAF) and OFAF cooling modes is calculated by:

$$q_{lost,w} = \left(\frac{\theta_{w,1} - \theta_{DAO,1}}{\theta_{w,r} - \theta_{DAO,r}}\right)^{\frac{5}{4}} \cdot \left(\frac{\mu_{w,r}}{\mu_{w,1}}\right)^{\frac{1}{4}} \cdot (q_{gen,w,Joule,r} + q_{gen,w,ed,r}) \cdot \Delta t \tag{23}$$

where: $\theta_{DAO,1}$ and $\theta_{DAO,r}$ are the average temperatures of the fluid in the cooling ducts at prior and at rated load in ℃, respectively; $\mu_{w,1}$ and $\mu_{w,r}$ are the viscosity of the fluid for average winding temperature rise at prior and rated load in cP; For oil-directed air-forced (ODAF) cooling mode, the heat lost per minute by the winding is calculated as follows:

$$q_{lost,w} = \left(\frac{\theta_{w,1} - \theta_{DAO,1}}{\theta_{w,r} - \theta_{DAO,r}}\right) \cdot (q_{gen,w,Joule,r} + q_{gen,w,ed,r}) \cdot \Delta t \tag{24}$$

The viscosity correction is not included because the fluid is pumped. The thermal capacity of the winding mCp_w can be estimated by:

$$mCp_w = \frac{(q_{gen,w,Joule,r} + q_{gen,w,ed,r}) \cdot \tau_w}{\theta_{w,r} - \theta_{DAO,r}} \tag{25}$$

where: τ_w is the winding time constant in min. The average winding temperature at the time t_2 can be expressed as:

$$\theta_{w,2} = \frac{q_{gen,w} + q_{lost,w} + mCp_w \cdot \theta_{w,1}}{mCp_w} \tag{26}$$

2.1.1.4.2 Calculation of the Temperature Rise of the Oil in the Winding Duct over the Bottom

The temperature rise of the oil (fluid) in the winding duct over the bottom $\Delta\theta_{DO/BO}$ can be calculated by:

$$\Delta\theta_{DO/BO} = \theta_{TDO} - \theta_{BO} = \left(\frac{q_{lost,w}}{(q_{gen,w,Joule,r} + q_{gen,w,ed,r}) \cdot \Delta t}\right)^{x} \cdot (\theta_{TDO,r} - \theta_{BO,r}) \quad (27)$$

where: x is the exponent for duct oil rise over bottom oil. Its value is 0.5 for ONAN, ONAF and OFAF cooling modes, 1 for ODAF cooling mode; θ_{TDO} and $\theta_{TDO,r}$ are the fluid temperature at the top of the duct at the current time in question and rated load in ℃, respectively; θ_{BO} and $\theta_{BO,r}$ are the fluid temperature at the bottom at the current time in question and the rated load in ℃, respectively.

The hot-spot may not be located at the top of the winding. The oil temperature at the hot-spot elevation is calculated by:

$$\Delta\theta_{WO/BO} = H_{HS} \cdot (\theta_{TDO} - \theta_{BO}) \quad (28)$$

$$\theta_{WO} = \theta_{BO} + \Delta\theta_{WO/BO} \quad (29)$$

where: H_{HS} is the per unit of winding height to the hot spot location. If the winding duct-oil temperature θ_{TDO} is less than the TOT in the tank, then the oil temperature adjacent to the hot-spot is assumed to be equal to the top-oil temperature and defined as:

$$If\ \theta_{TDO} < \theta_{TO}\ is\ true: \theta_{WO} = \theta_{TO} \quad (30)$$

The corrected Joule loss generated at the rated load and rated HST $q_{gen,HS,Joule,r}$ and corrected Eddy loss at rated load and rated HST $q_{gen,HS,ed,r}$ are calculated by:

$$q_{gen,HS,Joule,r} = \frac{\theta_{HST,r} + \theta_K}{\theta_{w,r} + \theta_K} \cdot q_{gen,w,Joule,r} \quad (31)$$

$$q_{gen,HS,ed,r} = E_{HS} \cdot q_{gen,HS,Joule,r} \quad (32)$$

where: E_{HS} is the eddy loss at the winding hot spot location, per unit of the Joule loss; $\theta_{HST,r}$ is the rated hot-spot temperature in ℃; θ_K is the temperature factor for resistance correction in ℃.

The heat generated per minute at HST is expressed as:

$$q_{gen,HS} = K^2 \cdot \left(q_{gen,HS,joule,r} \cdot K_{HS} + \frac{q_{gen,HS,ed,r}}{K_{HS}}\right) \cdot \Delta t \tag{33}$$

where: K_{HS} is the temperature correction for losses at the hot-spot location, determined by:

$$K_{HS} = \frac{\theta_{HS,1} + \theta_K}{\theta_{HS,r} + \theta_K} \tag{34}$$

where: $\theta_{HS,1}$ and $\theta_{HS,r}$ are the HST at rated load prior and at rated condition in ℃, respectively. The heat lost per minute by the hot-spot $q_{lost,HS}$ for ONAN, ONAF and OFAF cooling modes is calculated as:

$$q_{lost,HS} = \left(\frac{\theta_{HS,1} - \theta_{WO}}{\theta_{HS,r} - \theta_{WO,r}}\right)^{\frac{5}{4}} \cdot \left(\frac{\mu_{HS,r}}{\mu_{HS,1}}\right)^{\frac{1}{4}} \cdot (q_{gen,HS,Joule,r} + q_{gen,HS,ed,r}) \cdot \Delta t \tag{35}$$

where: θ_{WO} and $\theta_{WO,r}$ are the temperature of the oil (fluid) adjacent to the winding hot-spot at the time in question and at rated load in ℃, respectively; $\mu_{HS,1}$ and $\mu_{HS,r}$ are the viscosity of the fluid for hot-spot calculation at prior and rated load in cP; For ODAF cooling mode, the heat lost per minute by the winding is expressed as:

$$q_{lost,w} = \left(\frac{\theta_{HS,1} - \theta_{WO}}{\theta_{HS,r} - \theta_{WO,r}}\right) \cdot \left(q_{gen,w,Joule,r} + q_{gen,w,ed,r}\right) \cdot \Delta t \tag{36}$$

The HST at the time t_2 can be calculated by:

$$\theta_{HS,2} = \frac{q_{gen,HS} + q_{lost,HS} + mCp_w \cdot \theta_{HS,1}}{mCp_w} \tag{37}$$

2.1.1.4.3 Calculation of Average Oil Temperature in IEEE C57.91 Annex G

The heat generated by the core per minute $q_{gen,c}$ is calculated by:

$$q_{gen,c} = q_{loss,c,r} \cdot \Delta t \tag{38}$$

where: $q_{loss,c,r}$ is the loss of the core in W. For overexcitation conditions, the heat generated by the core per minute $q_{gen,c}$ is determined by using:

$$q_{gen,c} = q_{loss,c,OE} \cdot \Delta t \tag{39}$$

where: $q_{loss,c,OE}$ is the loss of the core when overexcitation occurs in W. The heat generated by the stray loss $q_{gen,stray}$ is expressed as:

$$q_{gen,stray} = \left(\frac{K^2 \cdot q_{loss,stray,r}}{K_w}\right) \cdot \Delta t \tag{40}$$

where: $q_{stray,r}$ is the stray loss at rated load in W. The heat lost by oil $q_{lost,O}$ is calculated by:

$$q_{lost,O} = \left(\frac{\theta_{AO,1} - \theta_{A,1}}{\theta_{AO,r} - \theta_{A,r}}\right)^{\frac{1}{y}} \cdot q_{loss,t,r} \cdot \Delta t \tag{41}$$

where: $\theta_{AO,1}$ and $\theta_{AO,r}$ are the average fluid temperatures in the tank and radiator at the prior and rated load in ℃; $\theta_{A,1}$ and $\theta_{A,r}$ are the ambient temperature at the prior and rated condition in ℃; y is the exponent of average fluid rise with heat loss, with a value of 0.8 for ONAN cooling mode, 0.9 for ONAF and OFAF cooling modes, 1 for ODAF; and $q_{loss,t,r}$ is the total losses at rated load in W, calculated by:

$$q_{t,r} = q_{w,Joule,r} + q_{w,ed,r} + q_{stray,r} + q_{core,r} \tag{42}$$

The total heat capacity mCp_{total} is expressed as follows:

$$mCp_{total} = m_{tank} \cdot Cp_{tank} + m_{core} \cdot Cp_{core} + m_{oil} \cdot Cp_{oil} \tag{43}$$

The average oil temperature at the time t_2 is calculated by:

$$\theta_{AO,2} = \frac{q_{lost,w} + q_{gen,stary} + q_{gen,c} - q_{lost,O} + mCp_{total} \cdot \theta_{AO,1}}{mCp_{total}} \tag{44}$$

2.1.1.4.4 Calculation of Top and Bottom Oil Temperatures in IEEE C57.91 Annex G

The top oil temperature θ_{TO} and bottom oil temperature θ_{BO} are calculated by:

$$\theta_{BO} = \theta_{AO} - \frac{\Delta\theta_{T/B}}{2} \tag{45}$$

$$\theta_{TO} = \theta_{AO} + \frac{\Delta\theta_{T/B}}{2} \tag{46}$$

where: $\Delta\theta_{T/B}$ is the temperature rise of oil (fluid) at the top of the radiator over the bottom of the radiator in ℃, calculated by:

$$\Delta\theta_{T/B} = \theta_{TO} - \theta_{BO} = \left(\frac{q_{lost,o}}{q_{loss,r} \cdot \Delta t}\right)^{z_{ttb}} \cdot (\theta_{TO,r} - \theta_{BO,r}) \tag{47}$$

where: $\theta_{TO,r}$ and $\theta_{BO,r}$ are rated top oil temperature and rated bottom oil temperature in ℃, respectively.

2.1.1.4.5 Calculation of Top-oil and Bottom-oil Rise Over Ambient

The temperature of the top oil (fluid) rises over ambient at the rated load $\Delta\theta_{AO,r}$ is given by:

$$\Delta\theta_{AO,r} = \frac{\Delta\theta_{TO,r} + \Delta\theta_{BO,r}}{2} \tag{48}$$

where: $\Delta\theta_{TO,r}$ and $\Delta\theta_{BO,r}$ are the temperatures of the top and bottom oil (fluid) rise over the ambient at rated load in ℃. The temperature of the top and the bottom fluid rises over ambient at rated load on a different tapping $\Delta\theta_{TO,r}{}'$ and $\Delta\theta_{BO,r}{}'$ are calculated by:

$$\Delta\theta_{TO,r}{}' = \Delta\theta_{AO,r}\left(\frac{q_{t,r}{}'}{q_{t,r}}\right)^{y} + \left(\frac{\Delta\theta_{TO,r} - \Delta\theta_{BO,r}}{2}\right)\left(\frac{q_{t,r}{}'}{q_{t,r}}\right)^{z} \tag{49}$$

$$\Delta\theta_{BO,r}{}' = \Delta\theta_{AO,r}\left(\frac{q_{t,r}{}'}{q_{t,r}}\right)^{y} - \left(\frac{\Delta\theta_{TO,r} - \Delta\theta_{BO,r}}{2}\right)\left(\frac{q_{t,r}{}'}{q_{t,r}}\right)^{z_{ttb}} \tag{50}$$

where: z_{ttb} is the exponent for the top-to-bottom fluid temperature difference. It has a value of 0.5 for ONAN and ONAF cooling modes and 1 for OFAF and ODAF cooling modes.

2.1.1.4.6 Calculation of the Average Winding Temperature Rise over Ambient in IEEE Std C57.96 Annex G

The temperature rise of the fluid at the top of the duct over the bottom of the duct at the rated load for ONAN, ONAF and ODAF cooling mode is expressed as:

$$\Delta\theta_{DO/BO,r} = \Delta\theta_{TO,r} - \Delta\theta_{BO,r} \tag{51}$$

For OFAF cooling mode:

$$\Delta\theta_{DO/BO,r} = \Delta\theta_{W/A,r} - \Delta\theta_{BO,r} \tag{52}$$

where: $\Delta\theta_{W/A,r}$ is the rated average temperature rise of the winding over ambient in ℃. For the temperature rise of the fluid at the top of the duct over the bottom of the duct at a different tapping $\Delta\theta_{DO/BO,r}{}'$ is calculated by:

$$\Delta\theta_{DO/BO,r}{}' = \Delta\theta_{DO/BO,r}\left(\frac{I_r{}'}{I_r}\right)^{2x} \tag{53}$$

where: I_r and $I_r{}'$ are the rated current at the rated load and the rated load on a different tapping in A, respectively.

The rated average winding temperature rise over ambient at different tapping positions for ONAN, ONAF and OFAF cooling modes is expressed as:

$$\Delta\theta_{W/A,r}{}' = (\Delta\theta_{W/A,r} - \Delta\theta_{BO,r} - \frac{\Delta\theta_{DO/BO,r}}{2}) \cdot \left(\frac{I_r{}'}{I_r}\right)^{1.6} + \Delta\theta_{BO,r}{}' + \frac{\Delta\theta_{DO/BO,r}{}'}{2} \tag{54}$$

For ODAF cooling mode:

$$\Delta\theta_{W/A,r}{}' = (\Delta\theta_{W/A,r} - \Delta\theta_{BO,r} - \frac{\Delta\theta_{DO/BO,r}}{2}) \cdot \left(\frac{I_r{}'}{I_r}\right)^2 + \Delta\theta_{BO,r}{}' + \frac{\Delta\theta_{DO/BO,r}{}'}{2} \quad (55)$$

2.1.1.4.7 Calculation of the Hottest-spot Rise over Ambient in IEEE Std C57.91 AnnexG

The winding HST rise over ambient temperature at rated load at a different tapping for ONAN, ONAF and OFAF cooling modes is calculated by:

$$\Delta\theta_{H/A,r}{}' = (\Delta\theta_{H/A,r} - \Delta\theta_{BO,r} - \Delta\theta_{DO/BO,r}) \cdot \left(\frac{I_r{}'}{I_r}\right)^{1.6} + \Delta\theta_{BO,r}{}' + \Delta\theta_{DO/BO,r}{}' \quad (56)$$

For ODAF cooling mode:

$$\Delta\theta_{H/A,r}{}' = (\Delta\theta_{H/A,r} - \Delta\theta_{BO,r} - \Delta\theta_{DO/BO,r}) \cdot \left(\frac{I_r{}'}{I_r}\right)^2 + \Delta\theta_{BO,r}{}' + \Delta\theta_{DO/BO,r}{}' \quad (57)$$

2.1.1.5 Existing Standard for Thermal Modelling of the Transformer: CIGRE 659: Transformer Thermal Modelling

Standard [13] does not provide a new model and uses the existing standard model in [1], [2], [15]. The modelling approaches are categorised into three main methods: correlation methods (e.g., [1], [2], [15]), CFD models, and THN models.

The CFD method requires detailed information on the geometry of the active parts (e.g., LV/HV/TV winding and core). The computational cost is much higher and requires extensive knowledge of FEM and fluid dynamics to be applied [13]. Therefore, the CFD models are not suitable for use as generic transformer models.

The THN models are more commonly used in the transformer design phase. Correlation models require the least amount of information from the transformer [13]. The differences in the levels of detail required across methods imply that correlation models are better suited for rating purposes in studies at the level of an entire power system.

Standard [13] defines the DTR as a group of loadings, namely: normal cyclic loading (normal life expectancy loading), planned loading beyond nameplate rating, long-time emergency loading and short-time emergency loading. The loading factor limit criterion depends on the following factors: the HST limit, the daily loss-of-life, and the bubbling inception temperature.

The transformer DTRs are determined using the load factor limit $k_{c,DTR}$ at which the transformer can operate without violating the pre-defined HST limit for given ambient conditions. Using the model in [2] as an example, the relationship of the HST, θ_{HST} and the load factor limit $k_{c,DTR}$ is given by:

$$\theta_{HST} = \theta_a + \theta_{TOT}\left(\frac{1 + K \cdot {k_{c,DTR}}^2}{1 + K}\right) + H \cdot g_r \cdot {k_{c,DTR}}^{y_{ex}} \tag{58}$$

where: θ_a and θ_{TOT} are the ambient temperature and top-oil temperature, respectively, and H is the hot-spot factor of the transformer. For a given HST limit, the load factor limit $k_{c,DTR}$ is only dependent on the ambient temperature θ_a and it can be calculated using the fitting function as:

$$k_{c,DTR} = \alpha \cdot \theta_a + \beta \tag{59}$$

Similar to standard models, this model is very empirical. Empirical data are needed depending on the transformer's voltage level and construction.

2.1.1.6 National Grid Technical Guidance Note for Short-Term Thermal Ratings and Cyclic Rating of Transformers

National Grid TGN 29 [3] presents that from an operational perspective, the HST of the transformer is measured and calculated by the WTI, and the temperature limit of the transformer is the pre-set value of the temperature (max. emergency temperature) measured and calculated by the WTI in HV, LV and TV windings. This temperature limit varies with different WTI settings, but the typical values are 120°C and 125°C. The WTI will send the trip signal, and the protection equipment will disconnect the transformer once the temperature limit is exceeded. It is also worth noting that the typical error of the WTI is ±3°C.

2.1.1.6.1 National Grid Technical Guidance Note for Short-Term and Medium-Term Overloading Ratings of Transformers

The TGN 303 [14] presents the STTR of the transformer. During an emergency, e.g., a post-fault scenario, the transformer can use the maximum emergency temperature limit set by the WTI settings. The emergency temperature limit is higher than the transformer temperature limit during normal operation or pre-fault. The pre-fault temperature limit is usually the maximum nameplate temperature limit of the transformer. The HST/WTI temperature profile and the STTR loading profile are shown in Figure 2.5.

2.1.1.6.2 National Grid Technical Guidance Note for Cyclic Thermal Rating of Transformer

The CTR of the transformer uses the maximum emergency temperature limit determined by the WTI setting as the temperature limit. The same indefinite cycle of 6 hours of peak loading and 18 hours at 0.6PU of the peak is applied without violating the maximum emergency temperature limit, as shown in Figure 2.6.

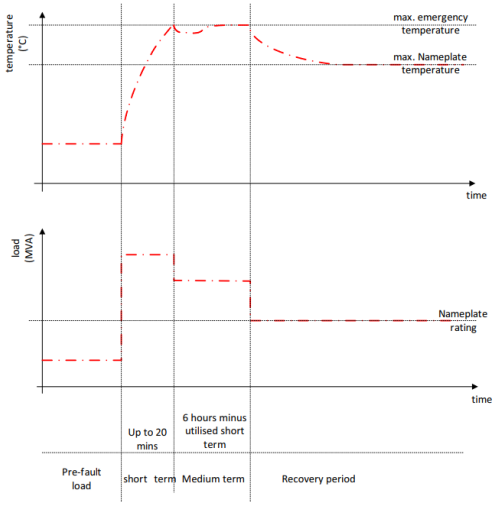

Figure 2.5: Illustration of the HST/WTI profile and the S/MTOR of the transformer, amended from [14].

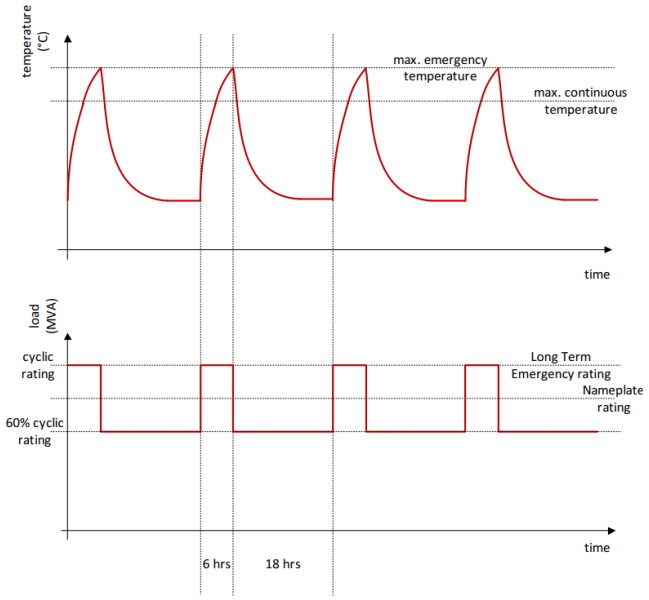

Figure 2.6: Illustration of the HST/WTI profile for cyclic load and the profile of the loading cycle of the transformer, amended from [14].

No values are shown in figures, as they are for illustration purposes only and those are common practice in National Grid.

2.1.2 Other Publications Related to the Thermal Modelling of the Transformer

Other publications related to the thermal modelling of the transformer are shown in this sub-section. The transformer model presented in the thesis [16] and paper [17] considers the individual effect of wind speed and solar irradiance on the calculated transformer HST. The calculated result considered the effect of solar irradiance on a 120 MVA transformer in ONAN mode, compared with the winding temperature indicator measurement. A 90 MVA transformer in ONAN mode is used to compare the calculated result with the effect of wind speed and the WTI measurement result.

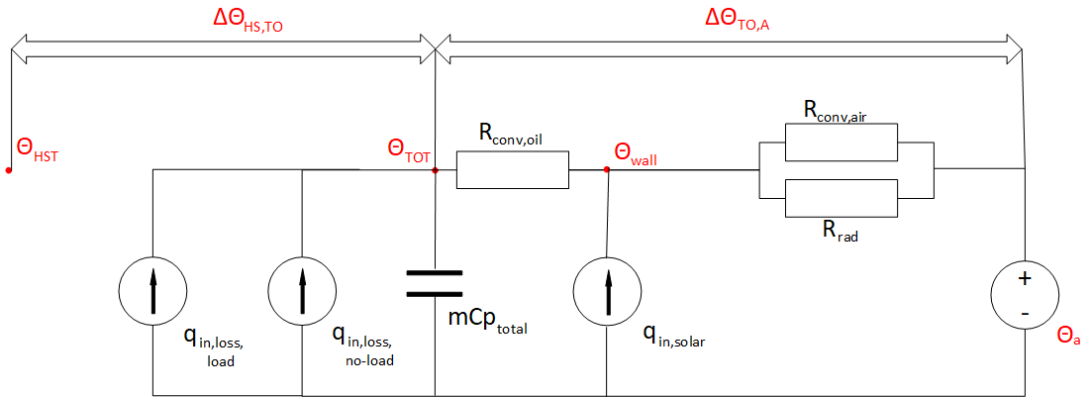

Figure 2.7: Diagram of the thermal model in [16], [17].

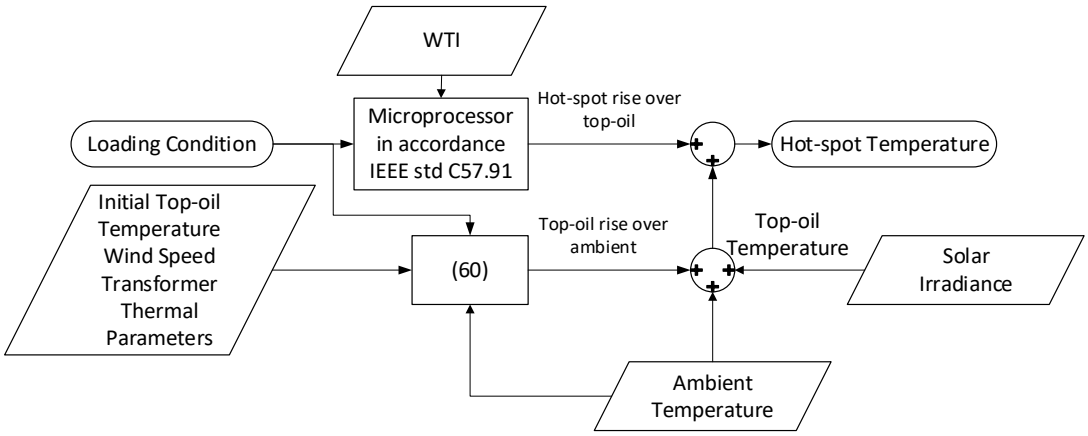

Figure 2.8: Flow chart from method in [16], [17].

The general steps in this method are outlined as follows:

1. Using transformer dimensions, a physical model of the tank and radiator is built.

2. Using the data from the transformer specification, empirical values, loading ratio and ambient conditions through the thermal model, the TOT of the transformer is calculated.

3. The HST rise over TOT $\Delta\theta_{HS,TO}$ is calculated using standard equations (IEC/IEEE) and added to the TOT to determine the HST. The HST rise over TOT can be calculated using the suggested value of the equation from IEC 60076 or IEEE Std C57.91 [1], [2]. The equation used in this step is from IEEE Std C57.91, Figure 2.8. This

method's Set 1 equations are the same as IEEE Std C57.91 [1]. Then, the top-oil rise over ambient is defined by:

$$q_{in,load} + q_{in,no-load} = mCp_o \frac{d\theta_{TOT}}{dt} + \frac{\theta_{TOT} - \theta_A - R_{MR,A} \cdot q_{in,solar}}{R_{N,O} + R_{MR,A}} \quad (60)$$

where: $q_{in,load}$ and $q_{in,\mathrm{no}-load}$ are heat input from load losses and no-load losses in W, respectively; mCp_o is the thermal capacitance of transformer oil in $K/kg * J$; θ_{TOT} and θ_A are top-oil temperature and ambient temperature, respectively; $R_{MR,A}$ and $R_{N,O}$ are thermal resistance of mixed radiation and convection and thermal resistance of natural oil convection in K/W, respectively; $q_{in,solar}$ is the heat input from solar irradiance in W.

This method acknowledges the non-linear behaviour of top-oil temperature rise over ambient (TOTR) with variation in ambient temperature by introducing calculations of thermal resistances for air convection, radiation, and oil convection.

Then, this model accounts for the effects of wind speed and solar irradiance during the phases when calculating TOTR. It introduces wind speed into the calculation of thermal resistance for heat loss by air convection. The model also includes solar irradiance as a heat input.

Paper [18] predicts the HST of the transformer using a learning algorithm. This process involves ambient temperature, wind speed, solar irradiance, and loading profile at hourly intervals. It uses recurrent neural networks followed by a support vector machine for regression, which is beyond the scope of this review. Using the measured temperature as a reference, the results of machine learning-based temperature estimation showed improved accuracy compared to the standard IEC model [2]. The effect of rainfall on the transformer HST calculation is mentioned but not detailed.

Paper [19] presented a method of calculating the winding temperature (from low-voltage winding) of the transformer using a model that takes the test certificate of the transformer and measurements from the WTI. The required temperature inputs are top-oil temperature, cooler temperature, LV winding temperature, HV winding temperature,

LV winding temperature gradient, and HV winding temperature gradient. The oil temperature time constant and oil exponent are also considered.

The focus point of the improvement is the WTI gradient, or the top-oil to winding gradient. The gradients are corrected by the measured values using three models:

$$gr_{obs} = gr_{WTI} \cdot {I_{LV}}^2 \tag{61}$$

$$gr_{obs} = gr_{WTI} \cdot {I_{LV}}^{2y_{WTI}} \tag{62}$$

$$gr_{obs} = \partial(gr_{WTI}) + gr_{WTI} \cdot {I_{LV}}^2 \tag{63}$$

where: gr_{WTI} is the WTI gradient set in the instrument; $\partial(gr_{WTI})$ is the fixed offset in the WTI gradient; I_{LV} is the current in the LV winding; y_{WTI} is the WTI exponent; gr_{obs} is the observed WTI gradient, calculated by:

$$gr_{obs} = \theta_{WTI} - \theta_{TO} \tag{64}$$

where: θ_{WTI} and θ_{TO} are measured temperatures of WTI and top-oil, respectively.

According to publicly available information, the TeRMiTE and its transformer model TRALC are based on the IEC standard [15] from 1991, which has since been replaced by [2]. This method utilised the temperature measured by the WTI, which is helpful for current substation control and management, but not for ageing assessment or rating determination based on transformer ageing assessment results.

2.1.2.1 Other Related Publications for Transformer Thermal Modelling

The model in [20] acknowledges the non-linear change in the thermal resistance of transformer oil and introduces an improved method for transformer hot-spot calculation based on existing standard models. Papers [19] and [20] introduced multi-stage thermal models, including the he-exchange processes of winding-to-oil and oil-to-air. The result of this multi-stage model is compared to the measured temperature data from a 31.5MVA ONAN transformer and a 40MVA ONAF transformer. Paper [23] extends the multi-stage model to include heat conduction and considers different temperatures at the top, middle, and bottom of the transformer, leading to different rates

of heat dissipation to the ambient. Thus, different thermal resistances are considered within the same phase of the heat exchange process at different positions in the transformer. Paper [24] proposes optimising the existing transformer DTR modelling method by adopting hydraulic modelling of the transformer duct. The optimised model is compared with existing standards, and the model is supported by measured HST data from a 20 MVA ONAN transformer. Paper [25] introduces a geometrical approach to modelling the temperature of oil in the tank and the top-oil, and the temperature gradient of the oil.

2.1.2.2 Other Publications Related to the Determination of the Cyclic Thermal Rating of the Transformer

Paper [26] presents a method that divides the loading period into heavy and light loading of the transformer. The heavy-load period may cause a higher ageing rate than the unity ageing rate, and vice versa. The CRF can be calculated by balancing the heavy-loading and light-loading ageing rates to the unity ageing rate over 24 hours. This paper defines the CTR for continuous loading of the transformer as the ability to run the transformer above its nameplate rating for limited periods without accelerating its ageing, and states that the method has been tested using the TRALC 1 method.

No equations are provided in [26]. However, based on the method described, it is calculated by:

$$F_{AA}\left(\theta_{light}\right) \cdot t_{light} + F_{AA}\left(\theta_{heavy}\right) \cdot t_{heavy} = F_{AA,day} \tag{65}$$

where: $F_{AA}\left(\theta_{light}\right)$ and $F_{AA}\left(\theta_{heavy}\right)$ are the ageing acceleration factors in the light loading period and heavy loading period, respectively; t_{light} and t_{heavy} are the lengths of the light loading period and heavy loading period, respectively; $F_{AA,day}$ is the ageing acceleration factor of the day (24 hours).

Next, the ageing acceleration factor of a day is compared to the nominal ageing acceleration factor. If the calculated ageing acceleration factor of a day is smaller than the nominal value (which it should be from the start), CRF is applied as a multiplier to the loading profile of the respective transformer on the respective day. From the new

loading profile, a new temperature $\theta_{h,CTR}$ of the transformer for the same 24-hour period is obtained, and ageing acceleration factor after applying the CRF of the transformer for 24 hours should be equal to unity.

The term CRF is taken from the process of determining the cable CTR. In the case of the transformer CTR, standard [13] use the term "load factor limit" for similar purposes.

$$\frac{F_{AA}(\theta_{light}{}') \cdot t_{light} + F_{AA}(\theta_{heavy}{}') \cdot t_{heavy}}{24} = 1 \tag{66}$$

where: $F_{AA}(\theta_{light}{}')$ and $F_{AA}(\theta_{heavy}{}')$ are the ageing acceleration factors in the light loading period and the heavy loading period after applying the CRF to the loading profile of the transformer, respectively.

Thus, the CTR of the transformer L_{CTR} can be expressed as:

$$L_{CTR} = L_{rated} * CRF \tag{67}$$

This method agrees with the definition of the *planned loading beyond nameplate* in [13]. Company directive [27] defines CTR as the maximum current that the component may carry during the operation of a succession of identical 24-hour load cycles without violating the temperature limit.

2.1.2.3 Other Publications Related to the Effect on the Transformer from Network or Other Network Components

Paper [28] studied and evaluated the performance of the system by applying dynamic rating to a medium power transformer that is used for connecting the wind farm to the grid. Paper [29] evaluated the effect of distributed photovoltaic generation on the HST of the transformer and the ageing process of the transformer. Paper [30] presents a method of calculating the rate of ageing of the transformer using the calculated HST of the transformer from the measured state of power consumption.

The connection of wind farms and distributed photovoltaic generation to the grid will change the transformer loading profile. The change in the loading profile of the

transformer will change the HST profile of the transformer, thus affecting the ageing acceleration factor of the transformer and the CTR of the transformer.

2.1.2.4 Heat Input from No-Load Losses of the Transformer

Paper [31] the load and no-load losses of the transformer with loading ratio and voltage. The no-load (idle) losses $q_{loss,no-load}$ is given by the no-load iron losses $q_{loss,no-load,iron}$ and no-load copper losses $q_{loss,no-load,copper}$ (or no-load Joule losses $q_{loss,no-load,Joule}$) in the primary winding:

$$q_{loss,no-load} = q_{loss,no-load,iron} + q_{loss,no-load,copper} \tag{68}$$

$$q_{loss,no-load,copper} = R_1 {I_{10}}^2 \tag{69}$$

where: R_1 is the resistance of the primary winding and I_{10} is the no-load current in the primary winding. The no-load copper losses are negligible [31], so it can be rewritten to:

$$q_{loss,no-load} = q_{loss,no-load,iron} \tag{70}$$

The iron losses $q_{loss,no-load,iron}$ are further divided into hysteresis losses $q_{loss,no-load,hys}$ and 'fuco losses', which are the eddy current losses, $q_{loss,no-load,ed}$, calculated by:

$$q_{loss,no-load,hys} = K_{hys} \cdot f \cdot {B_{max}}^{1.6} \tag{71}$$

$$q_{loss,no-load,ed} = K_{ed} \cdot f^2 \cdot {B_{max}}^2 \tag{72}$$

where: K_{hy} and K_{ed} are the hysteresis and eddy current coefficient; f is the frequency in Hz; B_{max} is the maximum magnetic flux density.

The variation of the iron losses at a given voltage ${U_1}'$ is given by:

$$q_{loss,no-load} = \frac{{U_1}'}{U_1} \cdot q_{loss,no-load,rated} \tag{73}$$

where: U_1 is the rated primary voltage and $q_{loss,no-load,rated}$ is the no-load losses at the rated condition. The variation of the copper losses and a given apparent power on the secondary winding $S_2{}'$ or a given current on the secondary winding $I_2{}'$ is given by:

$$q_{loss,copper} = \left(\frac{S_2{}'}{S_2}\right)^2 q_{loss,copper,rated} = \left(\frac{I_2{}'}{I_2}\right)^2 q_{loss,copper,rated} \quad (74)$$

where: S_2 is the rated apparent power on the secondary winding; I_2 is the rated current of the secondary winding; $q_{loss,copper,rated}$ is the rated copper losses on the secondary winding.

A limitation of the experiment in this paper is that load losses are measured only on the secondary side, and resistance is assumed constant (74). However, the variation of no-load losses of the transformer with the voltage in the primary winding can be better understood.

Paper [32] shows a method of calculating the load and no-load losses of the transformer using FEM. Papers [33]-[41] investigate how different aspects affect the no-load losses of the transformer and estimate the no-load losses of the transformer using FEM analysis. Paper [42] investigated the stray losses, which are part of the no-load losses of the transformer but can occur outside of the core and winding using FEM analysis. Paper [43] investigated the relationship between the magnetic and magneto-strictive properties of the materials and no-load losses in the large power transformer. Paper [44] presents a method of calculating the no-load losses of the transformer based on the properties, mass and shape of the core material. The extra loss factors are used to reflect the effect of the extra losses caused by the design of the core, i.e., corners in the core. Paper [45] presents the calculation of the no-load losses of the transformer considering the properties of the core material and the phase asymmetry of the no-load current. Paper [46] presents a method of estimating the percentage of eddy current losses in the no-load losses, stating that the eddy current losses are around 60 % of the total no-load losses.

Given all these analyses, the following sources forming the no-load losses of the transformer have been identified, namely, hysteresis losses $q_{loss,no-load,hys}$, eddy current losses $q_{loss,no-load,ed}$, stray losses $q_{loss,no-load,stray}$, dielectric losses $q_{loss,no-load,di}$ and Joule losses of the no-load current $q_{loss,no-load,Joule}$, which can be expressed as:

$$q_{loss,no-load} = q_{loss,no-load,hys} + q_{loss,no-load,ed} + q_{loss,no-load,stray} + q_{loss,no-load,di} + q_{loss,no-load,Joule} \quad (75)$$

There is no test method to separate transformer stray losses from eddy losses, according to [13]. However, based on common practice, it is advised that the hysteresis losses $q_{loss,no-load,hys}$ and eddy current losses $q_{loss,no-load,ed}$ are treated as the dominant sources of the no-load losses, contributing up to 98 per cent to the no-load losses [33], [46]. The stray losses $q_{loss,no-load,stray}$, the dielectric losses $q_{loss,no-load,di}$ and Joule losses of the no-load current $q_{loss,no-load,Joule}$ are almost always neglected, as mentioned in these studies [31], [33], [41], [46], [47].

2.1.2.4.1 Heat Losses of the Transformer to the Ambient

In paper [48], CFD simulation of the radiator for an ONAN transformer is presented, including a complete CFD model of a 4-panel, 1-meter-high stamped transformer radiator. Two improvements are made over the existing model by accounting for radiative and convective heat transfer. The thermal process considered conduction, convection, and radiation. The convection effect is natural air convection because it is considered a constant. By considering the radiation and (natural) air convection, this paper provided a radiator model with better accuracy than existing standards [1], [2].

Paper [49] developed a simplified CFD model for the radiator of an ONAN transformer. The results of the new CFD model are compared with an experiment-verified model and existing empirical equations, helping to better understand the operation and temperature distribution of the transformer radiator.

2.1.2.5 Tertiary Winding of the Transformer

Some work in the literature studied transformers equipped with tertiary windings, as in [50] and [51], presented methods for calculating the apparent power rating of the tertiary winding. Furthermore, it is noted that there is a potential hazard for a transformer without a tertiary stabilisation winding during a fault. Standard [50] explained the aspects of tertiary winding, especially tertiary stabilisation winding, in the power transformer.

Paper [51] presents an equivalent model for a distribution transformer equipped with a tertiary winding in a star-star-delta configuration, as shown in Figure 2.9.

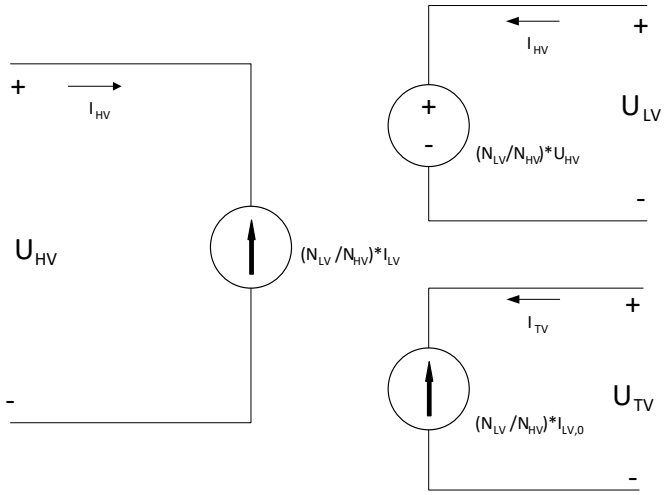

Figure 2.9: Diagram of the single-phase equivalent circuit of a transformer with a tertiary winding in star-star-delta configuration [51].

The U_{HV}, $U_{LV}$and U_{TV} are the voltages of the HV, LV and TV windings, respectively; I_{HV}, $I_{LV}$and I_{TV} are the corresponding currents; $I_{LV,0}$ is the zero sequence current of the LV winding; N_{HV}, N_{LV} and N_{TV} are the turn numbers of the HV, LV and TV windings, respectively. The heat losses in the tertiary winding can be considered as Joule losses, calculated by:

$$q_{loss,load,TV} = {I_{TV}}^2 \cdot R_{TV} \tag{76}$$

where: R_{TV} is the equivalent electrical resistance of the tertiary winding.

2.1.2.6 Summary of Transformer Thermal Modelling

For the extensive reviews mentioned, the transformer thermal modelling generally follows the route from ambient temperature, then to the top-oil temperature, and finally to the hot-spot temperature. This work made improvements on temperature-dependent load losses and voltage-dependent no-load losses; cooling-mode transitions; exposure differences between tank and cooling plant; heat input from losses in tertiary windings; and effective cooling areas.

2.1.3 Thermal Models for Cables

This subsection reviews cables, which are electrically insulated conductors typically buried underground but that can also be exposed to air when installed on pylons/towers (as overhead cables, normally found in distribution networks) or partially exposed to air, e.g., at cable transition towers in transmission networks. The buried cables can be installed directly buried or within a duct/tunnel/conduit/or trough. While buried (or fully underground), cables are not directly and quickly affected by meteorological conditions and therefore have longer time constants. Cables that are fully or partially exposed to the air are affected by meteorological conditions. Offshore cables, such as submarine cables, operate in a very different environment compared to onshore buried cables and may have different thermal limits (and are exposed to various temperature changes in the surrounding environment), so they are considered out of scope for this report. The models used to evaluate cable thermal ratings are derived from equations that reflect cable properties and construction, as well as the thermal model of the surroundings.

The standard models for the evaluation of thermal rating of cables are given by:

- [4]-[6], [52] IEC 60287 Family: Electric cables - Calculation of the current rating
- [7] IEC 60853 Family: Calculation of the cyclic and emergency current rating of cables
- [53], [54] IEEE 835 & 848: IEEE Standard Power Cable Ampacity Tables & IEEE Standard Procedure for the Determination of the Ampacity Derating Factor for Fire-Protected Cable Systems

- [55] CIGRE 640: A Guide for Rating Calculations of Insulated Cables
- [56] TS 2.05: Cable Systems
- [8] TGN(E) 067: Current Ratings for AC Cables
- [14] TGN(E) 303: Co-ordination of Plant Thermal Ratings

2.1.3.1 Existing Standard Model for the Rating of Cables: IEC 60287: Electric cables - Calculation of the Current Rating

The IEC standards [4], [5] present the method for calculating the thermal resistance per core between the conductor and the sheath $R_{th,1}$, thermal resistance between the sheath and armour $R_{th,2}$, the thermal resistance of the external serving $R_{th,3}$ and the thermal resistance of the surrounding $R_{th,4}$.

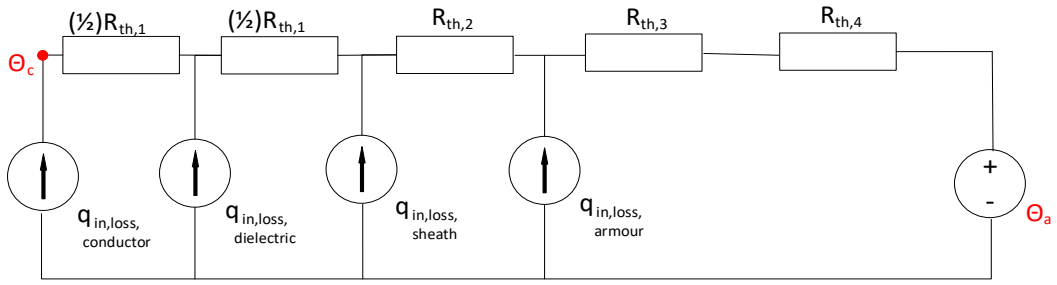

Figure 2.10: Diagram of the thermal model of cable in standard IEC 60287 [4], [5], [55].

The general equation for the calculation of the continuous rating of the cable is given by [4]:

$$I_{cable} = \left[\frac{\Delta\theta_{max} - W_d(0.5R_{th,1} + n(R_{th,2} + R_{th,3} + R_{th,4}))}{R_{AC,max} \cdot R_{th,1} + nR_{AC,max} \cdot (1+\lambda_1)R_{th,2} + nR_{AC,max} \cdot (1+\lambda_1+\lambda_2)(R_{th,3} + R_{th,4})}\right]^{0.5} \quad (77)$$

where: $\Delta\theta_{max}$ is the maximum conductor temperature rise above ambient; W_d is the dielectric loss per unit length of the cable at the maximum operating temperature in W; n is the number of load-carrying conductors in one cable, e.g., a single-core cable has one load-carrying conductor in one cable; $R_{AC,max}$ is the AC resistance of the conductor at the maximum prolonged operation temperature per meter in Ω/m; λ_1 is the ratio of

the total losses in the metallic sheath due to the conductor losses; λ_2 is the ratio of the total losses in metallic armour due to the conductor losses. The calculation of the individual parameters is given in [5].

2.1.3.1.1 Calculation of the Thermal Resistance Between Conductor and Sheath in IEC 60287

For single-core cables, the thermal resistance between the conductor and sheath is given as:

$$R_{th,1} = \frac{\rho_{th,i}}{2\pi} \ln\left(1 + \frac{2 \cdot t_1}{d_c}\right) \cdot \frac{1}{C_{LL}} \tag{78}$$

where: $\rho_{th,i}$ is the thermal resistivity of the insulation in $K \cdot m/W$; d_c is the diameter of the conductor in mm; t_1 is the thickness of the insulation between the conductor and sheath in mm; C_{LL} is the length correction factor for the laying-up cores considered.

2.1.3.1.2 Calculation of the Thermal Resistance between Sheath and Armour in IEC 60287

For $R_{Th,2}$, the thermal resistance between sheath and armour for single, two and three core cables with a common sheath is calculated by:

$$R_{th,2} = \frac{\rho_{th}}{2\pi} \ln\left(1 + \frac{2 \cdot t_2}{D_s}\right) \tag{79}$$

where: t_2 is the thickness of the bedding and D_s is the external diameter of the sheath, both in mm; ρ_{th} is the thermal resistivity of the material in question in $K \cdot m/W$.

2.1.3.1.3 Calculation of the Thermal Resistance of the Outer Covering in IEC 60287

The general thermal resistance of the external covering or servings can be expressed as:

$$R_{th,3} = \frac{\rho_{th}}{2\pi} \ln\left(1 + \frac{2 \cdot t_3}{D_a}\right) \tag{80}$$

where: t_3 is the thickness of the serving in mm; D_a is the external diameter of the armour in mm.

2.1.3.1.4 Calculation of the Thermal Resistance of the Surrounding Medium for Cable Exposed to Air in IEC 60287

For a cable fully exposed to air or for a cable partially exposed to air, the thermal resistance of the surrounding air $R_{Th,4}$ is calculated by:

$$R_{th,4} = \frac{1}{\pi D_e^* \cdot h \cdot (\Delta\theta_s)^{1/4}} \tag{81}$$

where: D_e^* is the external diameter of the cable for corrugated sheaths in mm; h is the heat dissipation coefficient in $W/m^2(K)^{5/4}$, the unit of this coefficient is for balancing the unit on both sides of the equation so they are equal; $\Delta\theta_s$ is the cable surface temperature rise above the ambient in K.

2.1.3.1.5 Calculation of the Thermal Resistance of the Surrounding Medium for a Single Isolated Buried Cable in IEC 60287

For the single isolated cable buried in the ground, the thermal resistance of the surrounding medium $R_{Th,4}$ can be expressed as:

$$R_{th,4} = \frac{1}{2\pi}\rho_{th,soil} \cdot \ln\left(\mu_1 + \sqrt{{u_1}^2 - 1}\right) \tag{82}$$

$$\mu_1 = \frac{2L}{D_e} \tag{83}$$

where: $\rho_{th,soil}$ is the thermal resistivity of the soil in $K \cdot m/W$; L is the distance from the surface of the ground to the cable axis in mm; D_e is the external diameter of the cable in mm.

2.1.3.1.6 Calculation of the Thermal Resistance of the Surrounding Medium for Three Single-core Buried Cables in IEC 60287

For three single-core metallic sheathed cables in the flat formation, the thermal resistance of the surrounding medium is expressed as:

$$R_{th,4} = \rho_{th,soil} \cdot (0.475 \cdot \ln\left(\mu_1 + \sqrt{{u_1}^2 - 1}\right) - 0.346) \quad (84)$$

For three single-core non-metallic sheathed cables in flat formation, the thermal resistance of the surrounding medium is calculated as:

$$R_{th,4} = \rho_{th,soil} \cdot (0.475 \cdot \ln\left(\mu_1 + \sqrt{{u_1}^2 - 1}\right) - 0.142) \quad (85)$$

For three single-core metallic sheathed cables in trefoil formation, the thermal resistance of the surrounding medium is calculated by:

$$R_{th,4} = \frac{1.5}{\pi} \rho_{th,soil} \cdot (\ln\left(\mu_1 + \sqrt{{u_1}^2 - 1}\right) - 0.63) \quad (86)$$

For three single-core non-metallic sheathed cables in trefoil formation, the thermal resistance of the surrounding medium is expressed as:

$$R_{th,4} = \frac{1}{2\pi} \rho_{th,soil} \cdot \ln\left(\mu_1 + \sqrt{{u_1}^2 - 1} + 2\ln\left(\mu_1\right)\right) \quad (87)$$

2.1.3.1.7 Calculation of the Thermal Resistance of the Surrounding Medium for Buried Cables in Ducts or Conduits in IEC 60287

The thermal resistance of the surrounding medium for the buried cables in ducts is divided into three parts, namely, the thermal resistance of the air gap between the cable and the ducts/conduit ${R_{Th,4}}'$, the thermal resistance of the wall of the ducts/conduit ${R_{Th,4}}''$ and the thermal resistance of the surrounding medium of the duct/conduit ${R_{Th,4}}'''$. The total thermal resistance of the surrounding medium of the cable is then calculated using:

$$R_{th,4} = R_{th,4}{}' + R_{th,4}{}'' + R_{th,4}{}''' \tag{88}$$

$$R_{th,4}{}' = \frac{U}{1 + 0.1 \cdot (V + Y\theta_m) \cdot D_e} \tag{89}$$

$$R_{th,4}{}'' = \frac{1}{2\pi}\rho_{th}\ln\left(\frac{D_o}{D_d}\right) \tag{90}$$

where: U, V, Y are constants given in [5] depending on the actual construction of the cable; θ_m is the mean temperature of the medium filling the space between the cable and the duct/conduit; D_o and D_d are the outer and inner diameters of the duct in mm, respectively; ρ_T is the thermal resistivity of the duct material in $K \cdot m/W$.

The thermal resistance of the surrounding medium of the duct/conduit $R_{Th,4}{}'''$ can be treated as the thermal resistance of the surrounding medium of the cable without the duct/conduit, which can then be calculated accordingly.

2.1.3.2 Existing Standard Model for the Rating of Cables: IEC 60853-3: *Calculation of the Cyclic and Emergency Current Rating of Cables*.

Standard [7] presents the method of calculating cyclic thermal rating (CTR) for the cables. Based on the continuous rating of the cable calculated in [5], the CTR of the cable $I_{cable,CTR}$ can be determined by multiplying the value of the continuous rating of the cable and the calculated CTR factor of the cable $M_{cable,CTR}$, expressed as:

$$I_{cable,CTR} = I_{cable,DTR} \cdot M_{cable,CTR} \tag{91}$$

where: CTR factor of the cable $M_{cable,CTR}$ is calculated by:

$$M_{cable,CTR} = \frac{1}{(A + B)^{0.5}} \tag{92}$$

$$A = \sum_{i=0}^{5} Y_i\left(\frac{\theta_c'(i+1)}{\theta_c'(\infty)} - \frac{\theta_c'(i)}{\theta_c'(\infty)}\right) \tag{93}$$

$$B = \mu \cdot (1 - \frac{\theta_c'(6)}{\theta_c'(\infty)}) \tag{94}$$

$$\frac{\theta_c'(t)}{\theta_c'(\infty)} = (1 - k + k \cdot \beta(t)) \cdot \alpha(t) \tag{95}$$

where: Y_i is the fraction of the cable losses to its maximum value at time i prior to the time when the maximum conductor temperature occurs in hours; $\theta_c'(\infty)$, $\theta_c'(t)$ and $\theta_c'(i)$ are conductor temperature at steady-state, at time t, and at time i, respectively; μ is the load loss factor; k is the ratio of the temperature rise of the cable surface to the temperature rise of the conductor of the cable above ambient at steady-state; $\alpha(t)$ is the attainment factor of the temperature difference between the cable surface and the conductor at time i prior to the time of maximum conductor temperature; and $\beta(t)$ is the attainment factor of the temperature difference between the ambient and the cable surface at time i prior to the time of maximum conductor temperature.

2.1.3.3 Existing Standard Model for the Rating of Cables, IEEE 835 & 848: IEEE Standard Power Cable Ampacity Tables & IEEE Standard Procedure for the Determination of the Ampacity Derating Factor for Fire-Protected Cable Systems

The standard [53] introduces a 3-phase model shown in Figure 2.11, considering the thermal resistance of the insulation $R_{th,i}$, the thermal resistance of the jacket $R_{th,j}$, and the thermal resistance of the earth or the external thermal circuit $R_{th,e}$. The heat source considered is the heat input from the conductor and sheath losses.

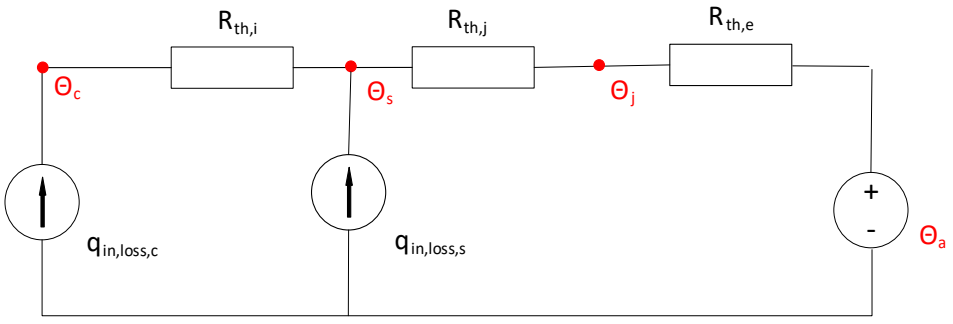

Figure 2.11: Diagram of the cable thermal model in IEEE 835 [53].

2.1.3.3.1 Thermal Model of Calculation of Current Carrying Capacity for Cables in IEEE 835

The general equation for calculating the maximum CCC of the cable is then expressed as:

$$I_{max} = \sqrt{\frac{\theta_c - (\theta_a + \Delta\theta_d)}{R_{DC}(1 + Y_c) \cdot \bar{R}_{th,ca}{}'}} \cdot 10^3 \tag{96}$$

where: θ_c and θ_a are the conductor temperature and the ambient temperature, respectively; $\Delta\theta_d$ is the temperature rise due to the presence of dielectric losses in the cable system in K; R_{DC} is the DC resistance of the conductor in Ω/m; Y_c is the ratio of the losses from skin and proximity effects to the Joule losses; $\bar{R}_{th,ca}{}'$ is the total thermal resistance between the conductor and the ambient.

The temperature rises due to the presence of dielectric losses in the cable system $\Delta\theta_d$ is calculated by:

$$\Delta\theta_d = q_d \cdot \bar{R}_{da}{}' \tag{97}$$

where: q_d is the dielectric losses in W; and $\bar{R}_{da}{}'$ is the total thermal resistance between the insulation and the ambient.

2.1.3.3.2 Calculation of the Derating Factor for the Current Rating of the Fire-Protected Cable in IEEE 848

The standard [54] presents the following relations to calculate the derating factor of the current rating of the cable, or the ampacity derating factor ADF, or ampacity correction factor ACF of the cable in the case of a fire-protected cable:

$$ADF = \frac{I_o - I_f}{I_o} \tag{98}$$

$$ACF = \frac{I_f}{I_o} \tag{99}$$

where: I_o is the normalised current for the baseline condition in A; I_f is the normalised current for the passive fire-protected cable system in A.

2.1.3.4 Existing Standard Model for the Rating of Cables: CIGRE 640: A Guide for Rating Calculations of Insulated Cables

The CIGRE 640 [55] utilises the same model from IEC 60287-1-1 [4] with modifications in parameters for the calculation of the CTR of cables. The CIGRE 640 introduces an improved method of calculating the CTR of the cable using the term load factor LF, where:

$$LF = \frac{\sum_{i=1}^{24} I_i}{24 I_{max}} \tag{100}$$

where: I_i is the average hourly load in A, and the I_{max} is the maximum hourly load in A. Next, from the $Load\ Factor$, the ratio of average losses to peak losses, denoted as the loss factor μ can be determined. The value of the loss factor is defined as:

$$\mu = \frac{1}{W_{max} \cdot \tau} \cdot \int_{t=0}^{\tau} W(t) \cdot dt \tag{101}$$

which can be approximated as:

$$\mu = \frac{\sum_{i=0}^{23} {I_i}^2}{24 \cdot {I_{max}}^2} \tag{102}$$

The new thermal resistance of the surroundings of the cable, considering the cyclic loading on the cable, can be determined as follows:

$$R_{th,4} = \frac{n}{2\pi}(\rho_{th,fill}\left(\ln\left(\frac{D_x}{D_{earth}}\right) + LF\left(\ln\left(\frac{2L + \sqrt{4L^2 - {D_x}^2}}{D_x}\right) + \ln(F)\right)\right) \tag{103}$$
$$+ (\rho_{th,Native} - \rho_{th,fill}) \cdot N \cdot Gb)$$

where: $\rho_{th,Native}$ and $\rho_{th,fill}$ are the thermal resistivity of the native soil or backfill in $K \cdot m/W$; D_{earth} is the earth (soil) diameter in m; D_x is the diameter where the average heat output is seen in m; F is the mutual heating effect factor; LF is the daily loss-load factor for the cables; Gb is the geometric factor.

2.1.3.5 National Grid Technical Guidance Note of Short-Term Emergency Ratings and Cyclic Rating for Cables

National Grid TGN 67 [8] given the maximum operation temperature of 90°C for XLPE insulated cable for all installations. TGN 303 [14] suggested that the maximum temperature limit of cables should not be violated, as the cable is highly likely to suffer irreparable damage from overheating.

2.1.3.5.1 National Grid Technical Guidance Note of Short-Term Emergency Ratings for Cables

TGN [8] and [14] define the short-term rating, also known as short-term thermal rating (STTR) or overloading rating [11]. The STTR utilises the slow temperature response of the cable (or large thermal time constant) when the cable is initially loaded below its rated current, i.e., a pre-load below 1PU. In such circumstances, the cable conductor temperature is below its temperature limit and can be overloaded for a given time without violating the cable conductor temperature limit, as shown in Figure 2.12.

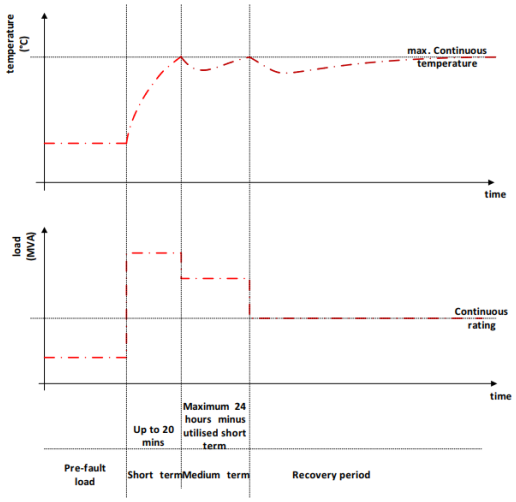

Figure 2.12: Illustration of short-term and medium-term thermal rating of cables, amended from [14].

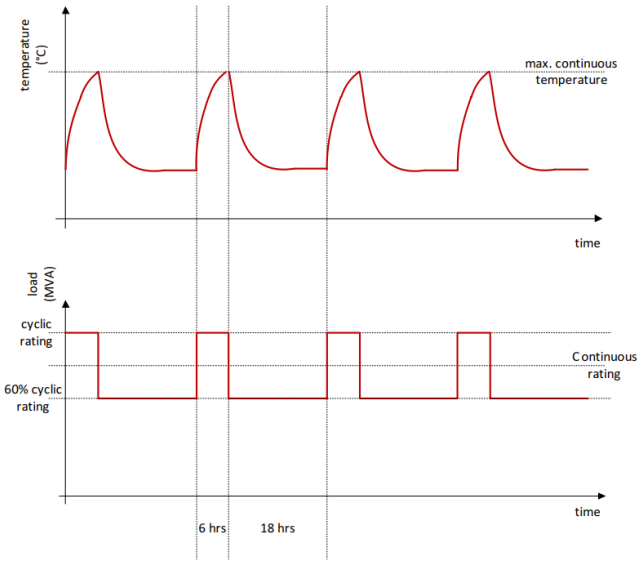

Figure 2.13: Illustration of CTR and the standard cyclic loading profile of cables, amended from [14].

2.1.3.5.2 National Grid Technical Guidance Note of Cyclic Thermal Rating for Cables

National Grid TGN 303 [14] also presents the definition of the CTR of a cable. The CTR of cable follows a given loading profile that cycles daily (24 hours) for an indefinite period without exceeding its temperature limit. The standard cyclic loading profile consists of 6 hours of peak load and 18 hours of low load, with the low load equal to 0.6PU of the peak load. The temperature profile of the cable and the standard cyclic loading profile are shown in Figure 2.13.

2.1.3.6 Other Models in Publications for Cables

Reference [57] presents a thermal model of the DBC, Existing Models for Cables in Literature: Real-time Thermal State and Component Loading Estimation in Active Distribution Networks. Then, based on the 4-phase model in [57], the thesis [58] introduced an improved 7-phase model for the cable in conduit by splitting the insulation from the group of insulation, sheath and jacket. Next, it added the air-gap phase of the conduit and the conduit itself.

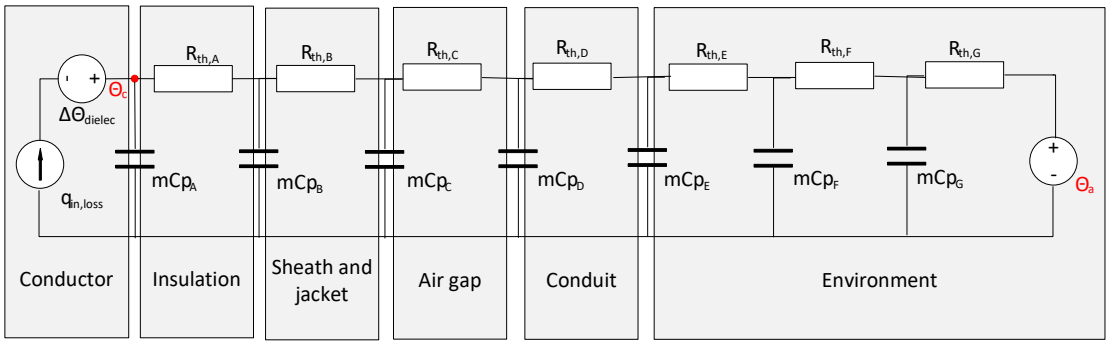

Figure 2.14: The 7-phase (A-G) thermal model of the buried cable in conduit.

2.1.3.7 Existing Model for Cable in Trough

Publications [59], [60] present the thermal model for the cable in an unfilled trough. On top of that, the geometry of the trough housing HV cables is also present, shown in Figure 2.15. Based on this geometry of the HV cable trough, the model for the filled trough can be developed accordingly.

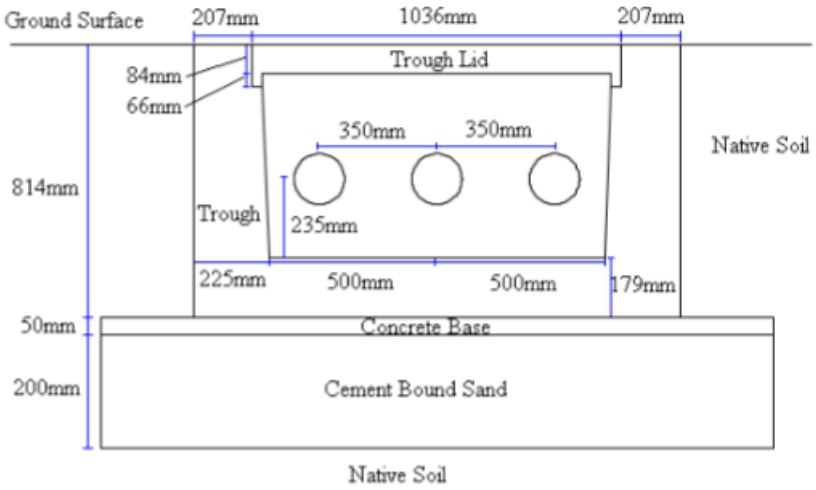

Figure 2.15: Geometry of a covered trough housing three HV cables in a flat formation, amended from [59].

2.1.3.8 Summary of Cable Thermal Modelling

For the extensive reviews mentioned, the cable thermal modelling generally follows the route from cable conductor, then to the cable's insulation, sheath and jacket, finally to its ambient, where the ambient could further divided into direct exposure to ambient soil; in a conduit or trough then to the ambient soil; or exposure to the ambient

air. This work made improvement on temperature dependent Joule losses in the cable conductor and improved thermal model for cable exposed in air and solar irradiance to consider the variation of WS.

2.1.4 Models for Overhead Line Conductors

This sub-section reviews OHLs, which have simple construction (bare conductors) and are operated in the environment/surroundings. These surroundings are usually represented as homogeneous ambient air. The operating temperature of bare conductor OHLs is directly and quickly affected by ambient conditions (also denoted as weather or meteorological conditions), which AAT, WS, AA and SI typically represent. The OHLs have short time constants, which are typically in the range of a few tens of minutes. The most frequently used model for evaluating the thermal rating and loading capacity of OHLs is a set of thermal balance equations, as presented in standards [9], [10], [61].

The standard models for the rating of the OHL conductors are given in [9], [10], [61]:

[1] IEC TR 61597: Overhead Electrical Conductors – Calculation Methods for Stranded Bare Conductors.

[2] IEEE Std 738: IEEE Standard for Calculating the Current-Temperature Relationship of Bare Overhead Conductors.

[3] CIGRE 207: Thermal behavior of overhead conductors.

The standard models use the thermal/heat balance equation to calculate the current-carrying capacity (CCC) of the OHL conductor as the maximum steady-state current for the given maximum conductor temperature under the given ambient conditions. An example illustration of the heat balance model for OHL is shown in Figure 2.16.

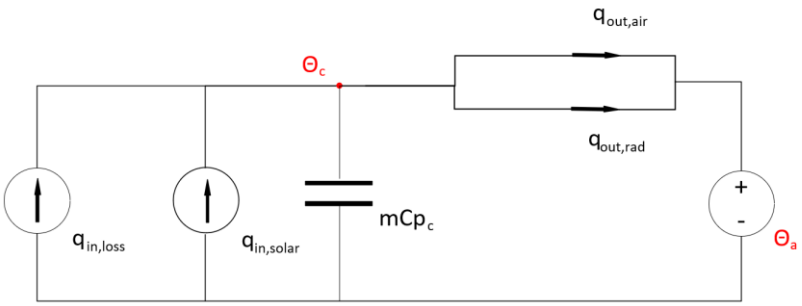

Figure 2.16: Illustration of the heat balance in the physical model for OHLs.

2.1.4.1 Existing Standards for the Rating of Overhead Lines: IEC TR 61597:2021: Overhead Electrical Conductors – Calculation Methods for Stranded Bare Conductors

The general heat balance equations in the IEC standard [10] is given by:

$$q_J + q_s = q_r + q_c \tag{104}$$

where: q_J is the heat input (generated) from the Joule effect; q_s is the heat input (gain) from the solar irradiance reaching the conductor surface; q_r is the heat loss by radiation from the conductor; q_c is the heat loss by convection over the conductor surface.

2.1.4.1.1 Calculation of the Heat Input from Joule Losses in IEC TR 61597

The heat input from the Joule losses is calculated by:

$$q_J = R(\theta_c) \cdot I^2 \tag{105}$$

where: $R(\theta_c)$ is the electrical resistance of the conductor operating at a temperature θ_c in Ω/m; I is the conductor current in A.

2.1.4.1.2 Calculation of Heat Input from Solar Irradiance in IEC TR 61597

The heat input from solar irradiance is calculated by:

$$q_s = \gamma \cdot D \cdot S_i \tag{106}$$

where: γ is the coefficient of the absorption of solar radiation; D is the diameter of the conductor in m; S_i is the intensity of the solar radiation in W/m^2.

2.1.4.1.3 Calculation of the Heat Loss from Radiation in IEC TR 61597

The heat loss from radiation is calculated by:

$$q_{sol} = \sigma \cdot \pi \cdot D \cdot K_e \cdot ((\theta_c + 273.15)^4 - (\theta_a + 273.15)^4) \quad (107)$$

where: σ is the Stefan-Boltzmann constant equal to $5.67 \cdot 10^{-8}\ W/(m^2 \cdot K^4)$; K_e is the emissivity coefficient with respect to the black body; θ_a is the ambient temperature in K; θ_c is the conductor temperature at the final equilibrium state in ℃.

2.1.4.1.4 Calculation of the Heat Loss from Convection in IEC TR 61597

The heat loss from convection in [10] only considers forced convection and is calculated by:

$$q_c = \lambda_f \cdot Nu \cdot (\theta_c - \theta_a)\pi \quad (108)$$

where: λ_f is the thermal conductivity of the air film in contact with the conductor can be assumed as a constant equal to $0.02585\ W/(m \cdot K)$; Nu is the Nusselt number calculated as:

$$Nu = 0.65 \cdot Re^{0.2} + 0.23 \cdot Re^{0.61} \quad (109)$$

where: Re is the Reynolds number calculated by:

$$Re = 1.644 \cdot 10^9 \cdot V_w \cdot D \cdot ((\theta_a + 273.15) + 0.5(\theta_c - \theta_a))^{-1.78} \quad (110)$$

where: V_w is the wind speed in m/s.

2.1.4.1.5 Calculation of the Maximum Current Carrying Capacity in IEC TR 61597

The final maximum CCC of the conductor at steady-state, I_{max}, can be calculated by:

$$I_{max} = \sqrt{\frac{q_r + q_c - q_s}{R(\theta_c)}} \quad (111)$$

2.1.4.2 Existing Standards for the Rating of the Overhead Lines: CIGRE 601: Guide for Thermal Rating Calculations of Overhead Lines

The thermal balance equation gives the CIGRE thermal model of the OHL conductor steady-state operating conditions, similar to [9] and [61], and expressed as:

$$q_J + q_S + q_M + q_i = q_c + q_r + q_w \tag{112}$$

where: q_J is the heating from Joule losses; q_s is the heating from solar irradiance; q_M is the magnetic heating; q_i is the corona heating; q_c is the convective cooling; q_r is the rate of the radiative cooling; q_w is the evaporative cooling.

Magnetic heating is often included in joule heating because it increases the resistance of the conductor. The magnitude of the corona heating is far less than the convective effects under the condition of high humidity and high wind speed. Therefore, it is considered irrelevant for the purpose of rating OHLs in [61].

The evaporation effect is difficult to quantify for the assessment process. Magnetic heating, corona heating and evaporative cooling are simplified or ignored in [61]. The thermal balance equation can then be rewritten as:

$$q_J + q_S = q_c + q_r \tag{113}$$

which is identical to (104).

The transient thermal balance equation is provided in [61] and expressed as:

$$E_{store} = q_J + q_S - q_c - q_r \tag{114}$$

where: E_{store} is the heat stored in the conductor in joules. By using the transient thermal balance equation, the temperature and the change of the temperature can be calculated to determine emergency ratings and/or cyclic ratings. The emergency ratings can be calculated as the time it takes the conductor to reach its target temperature after the change in the current of the OHL.

Standard [61] also provides an assumption for the modelling of the temperature of the conductor under short-circuit conditions, denoted as an adiabatic state, where the cooling effect is ignored for a short duration and, therefore, the heat equation in this state can be written as:

$$E_{store,short-circuit} = q_J + q_S \tag{115}$$

2.1.4.2.1 Calculation of the Heat Input from Joule Losses in CIGRE 601

The calculation of the heat input from the Joule losses divides the Joule losses into AC and DC-related ones, where the calculation for the DC is the same as (105), but it specifies the impact of the skin effect from DC to AC as:

$$q_J = k_{sk} \cdot I^2 \cdot R_{DC}(\theta_c) \tag{116}$$

where: $R_{DC}(\theta_c)$ is the DC resistance of the conductor at temperature θ_c; k_{sk} is the skin effect factor, determined using the outer and inner radius of the conductor [61]. The calculation of the heat from solar heating is identical to (106).

2.1.4.2.2 Calculation of the Temperature Distribution of Conductor in CIGRE 601

Different from [10] and [9], the temperature of the surface of the OHL conductor is different from the temperature of the core of the conductor in [61] and is calculated by:

$$\theta_c - \theta_s = \frac{q_{in,total}}{2\pi\lambda}\left(\frac{1}{2} - \frac{{D_i}^2}{D^2 - {D_i}^2} \cdot \ln\left(\frac{D}{D_i}\right)\right) \tag{117}$$

where: λ is the effective radial thermal conductivity in $W/(m \cdot K)$; $q_{in,total}$ is the total heat input per unit length in W/m; D is the overall diameter of the conductor in m; D_i is the internal diameter of a tubular conductor or the diameter of a steel core if present in m.

2.1.4.2.3 Calculation of the Heat Loss from Convection in CIGRE 601

The general equation for the calculation of the heat loss rate from convection in [61] is identical to (108). The thermal conductivity of the air is calculated by:

$$\lambda_f = 2.368 \cdot 10^{-2} + 7.23 \cdot 10^{-5} \cdot c - 2.763 \cdot 10^{-8} \cdot {\theta_f}^2 \tag{118}$$

where the film temperature θ_f is assumed to be:

$$\theta_f = 0.5 \cdot (\theta_s + \theta_a) \tag{119}$$

The calculation of the effect of the forced convection is also different in [61], where its Nusselt number is first expressed as the Nusselt number with AA of 90° as:

$$Nu_{90} = B \cdot Re^n \tag{120}$$

where: B and n are coefficients given in [61]. The Reynolds Number is calculated as:

$$Re = V_w \cdot D / v_f \tag{121}$$

where: V_w is the wind speed in m/s; v_f is the kinematic viscosity of the air in the film in m^2/s. The kinematic viscosity is calculated by:

$$v_f = \mu_f / \rho_{air} \tag{122}$$

where: μ_f is the dynamic viscosity of the air in the film; ρ_{air} is the density of the air in kg/m^3. The dynamic viscosity of the air can be calculated as a function of the temperature of the air at the film θ_f:

$$\mu_f = (17.239 + 4.635 \cdot 10^{-2} \cdot \theta_f - 2.03 \cdot 10^{-5} \cdot {\theta_f}^2) \cdot 10^{-6} \tag{123}$$

The temperature is valid for air at the film, up to 300°C, as expressed in (42). In the case of AA less than 90 degrees, the relation between the Nusselt number of the respective AA, Nu_δ is the Nusselt number at 90 degrees of AA for smooth conductors is expressed as:

$$\frac{Nu_\delta}{Nu_{90}} = (\sin^2(\delta) + 0.0169 \cdot cos^2(\delta))^{0.225} \tag{124}$$

For stranded conductors with AA smaller or equal to 24 degrees, (44) describes the adjusted Nusselt number as expressed below:

$$\frac{Nu_{\delta}}{Nu_{90}} = 0.42 + 0.68(\sin(\delta))^{1.08} \tag{125}$$

Furthermore, for stranded conductors with AA greater than 24 degrees, its Nusselt number is expressed as follows:

$$\frac{Nu_{\delta}}{Nu_{90}} = 0.42 + 0.58(\sin(\delta))^{0.9} \tag{126}$$

For Re smaller than 4000, (124)-(126) are valid. In the case of no wind or zero wind speed, the respective Nusselt number Nu_{nat} is calculated by:

$$Nu_{nat} = A_{nat} \cdot (Gr \cdot Pr)^{m_{nat}} \tag{127}$$

where: Gr and Pr are Grashof and Prandtl numbers, respectively. A_{nat} and m_{nat} are coefficients of calculating the natural convective heat transfer process, and their value is given in the standard [61].

The reduction in heat loss from natural convection due to the inclination of the conductor from the horizontal plane is also considered. The Nusselt number relation with no horizontal inclination $Nu_{nat,0}$ to the Nusselt number of the conductor with inclination to the horizontal plane of β degrees $Nu_{nat,\beta}$ for smooth conductors, with an inclination to the horizontal plane less than 60 degrees, is expressed as:

$$\frac{Nu_{nat,\beta}}{Nu_{nat,0}} = 1 - 1.58 \cdot 10^{-4} \cdot \beta^{1.5} \tag{128}$$

For stranded conductors with an inclination to the horizontal plane less than 80 degrees, the Nusselt number is expressed as:

$$\frac{Nu_{nat,\beta}}{Nu_{nat,0}} = 1 - 1.76 \cdot 10^{-6} \cdot \beta^{2.5} \tag{129}$$

2.1.4.2.4 Calculation of Heat Loss from Radiation in CIGRE 601

The heat loss from radiation is given in a detailed form in [61] by splitting the heat radiated to the ground and the heat radiated to the sky:

$$q_r = \pi \cdot \mathrm{D} \cdot \sigma_B \cdot F_{c-g} \cdot \varepsilon_s \cdot \left((\theta_s + 273.15)^4 - \left(\theta_g + 273.15\right)^4\right) + \pi \cdot \mathrm{D} \cdot \sigma_B \cdot F_{c-sky} \cdot \varepsilon_s \cdot \left((\theta_s + 273.15)^4 - \left(\theta_{sky} + 273.15\right)^4\right) \quad (130)$$

where: ε_s is the emissivity of the surface of the conductor; F_{c-g} is the fraction of the radiated energy from the conductor that reaches the ground and the surroundings; F_{c-sky} is the fraction of the radiated energy from the conductor that goes to the sky; θ_g and θ_{sky} are the ground temperature beneath the conductor and the temperature of the sky above the conductor, respectively.

However, by assuming the temperature of the ground beneath the conductor θ_g and the temperature of the sky, θ_{sky} above the conductor to be equal to the ambient temperature θ_a. Standard [3] confirms that utilising (107) and (110) in standards [1] and [2] will be sufficiently accurate to determine the conductor rating.

2.1.4.2.5 Calculation of the Change of Temperature in Transient State in CIGRE 601

The general equation for the calculation of the change of temperature in the transient state is given by:

$$m \cdot Cp \cdot \frac{d\theta_{av}}{dt} = q_J + q_M + q_S - q_c - q_r \quad (131)$$

where: m is the mass of the conductor per unit length in kg/m; Cp is the specific heat capacity of the conductor in $J/(kg \cdot K)$; θ_{av} is the mean value of the temperature. The heat capacity of the conductor per unit length mCp is calculated by:

$$mCp = m_{Al} \cdot Cp_{Al} + m_{steel} \cdot Cp_{steel} \quad (132)$$

where: m_{Al} and m_{steel} are the masses of the aluminium and steel of the conductor per unit length in kg, respectively; Cp_{Al} and Cp_{steel} are the specific heat capacities of

aluminium and steel in $J/(kg \cdot K)$, respectively. This example is given for the OHL conductor, which uses aluminium and steel, as in ACSR conductors. Should other materials be used (e.g. copper), this can be changed accordingly.

2.1.4.2.6 Calculation of the Fault Rating in CIGRE 601

The fault rating in the adiabatic state is given by the general equation in the standard [61] as:

$$mCp \cdot \frac{d\theta_{av}}{dt} = q_J \tag{133}$$

In accordance with (116), the fault rating I_{fault} can be rewritten to:

$$I_{fault} = \sqrt{mCp \cdot \frac{d\theta_{av}}{dt} / (R_{DC}(\theta_c) \cdot k_{sk})} \tag{134}$$

2.1.4.3 Existing Standards Regarding the Rating of Overhead Lines: IEEE Std 738: IEEE Standard for Calculating the Current-Temperature Relationship of Bare Overhead Conductors

Standard [9] presents the same thermal balance equation as in [10]. However, the elements are calculated differently, which will be present in the chapter for the individual component of OHL. This standard provides a method for estimating the SI based on Earth's orbit around the Sun and Earth's self-rotation when the measurement of SI is unavailable.

2.1.4.3.1 Calculation of the Total Solar and Sky Radiated Heat Flux Rate when Unknown in IEEE Std 738

When the data of Q_{se} is not available, it can be calculated by:

$$Q_{se} = k_{solar} \cdot Q_s \tag{135}$$

where: Q_s is the total heat flux density; k_{solar} is a factor of solar irradiance calculated as:

$$k_{solar} = 1 + (1.148E-4) \cdot H_e + (1.108E-8) \cdot {H_e}^2 \quad (136)$$

The total heat flux density Q_s can be calculated by:

$$\begin{aligned} Q_s = & -42.2391 + 63.8044 \cdot H_c - 1.922 \cdot {H_c}^2 + (3.46921E-2) \cdot {H_c}^3 \\ & - (3.61118E-4) \cdot {H_c}^4 + (1.94318E-6) \cdot {H_c}^5 \\ & + (4.07608E-9) \cdot {H_c}^6 \end{aligned} \quad (137)$$

where: H_c is the altitude of the Sun in degrees. The effective Sun's ray incidence angle θ can be calculated by:

$$\theta = \arccos\left[\cos(H_c) \cdot \cos(Z_c - Z_l)\right] \quad (138)$$

where: Z_c is the Azimuth of the sun (degrees) and Z_l is the Azimuth of the line (degrees).

The H_c can be calculated as:

$$H_c = \arcsin\left(\cos(Lat) \cdot \cos(\delta) \cdot \cos(\omega) + \sin(Lat) \cdot \sin(\delta)\right) \quad (139)$$

where: ω is the hour angle; the Lat is the latitude; δ and ω can be calculated by:

$$\delta = 23.4583 \cdot \sin\left(360 \cdot \frac{284 + N_{day}}{365}\right) \quad (140)$$

$$\omega = 15 \cdot (Hours - 12) \quad (141)$$

where: N_{day} is the number of the day; $Hours$ is the hour of the day.

The azimuth angle of the Sun, Z_c, in (23) can be calculated by:

$$Z_c = C_{coeff} + \arctan(\chi) \quad (142)$$

where: χ is the solar azimuth variable, which can be expressed as:

$$\chi = \frac{\sin(\omega)}{\sin(Lat) \cdot \cos(\omega) - \cos(Lat) \cdot \tan(\delta)} \quad (143)$$

The value of C_{coeff} depends on the value of χ and the value of ω. For the values of ω between 0 and -180, and when the value of χ is equal to or greater than 0, the value

of the C_{coeff} is 0. Otherwise, the value of C_{coeff} is 180. For values of ω between 0 and 180, and when the value of χ is smaller than 0, the value of C_{coeff} is 360. Else, the value of C_{coeff} is 180. The solar heat gain rate cannot be smaller than 0. If the calculated value is negative, it is set to 0.

2.1.4.4 National Grid Technical Guidance Note for Calculation of Short-Term Ratings for Overhead Lines

In National Grid TGN [11] and [14], the calculation of the short-term ratings for the OHL is presented. The study by Price [62] served as a basis for the development of TGN 026 [11]. The values presented indicate that an acceptable 'excursion time' of 10% was adopted at post-fault ratings, meaning the line is permitted to exceed its maximum rating for 10% of the time. In practice, the OHL must maintain 20% spare CCC for post-fault situations. That is, the maximum temperature is reached only under the post-fault rating, where the OHL can use its full CCC, whereas under the pre-fault rating, it is 84% of that. So, at any time, if the OHL is operated below 0.85PU during normal (pre-fault) operation, it can be overloaded for a short period. The short-term rating is the rating the OHL can use during the given period, during which the OHL conductor temperature reaches the maximum allowed temperature at the end of the overloading period. The OHL must reduce its loading to the post-load rating to avoid exceeding the temperature limit after short-term overloading. An example illustration of the OHL conductor temperature variation with respect to its loading is given by TGN [14], shown in Figure 2.17.

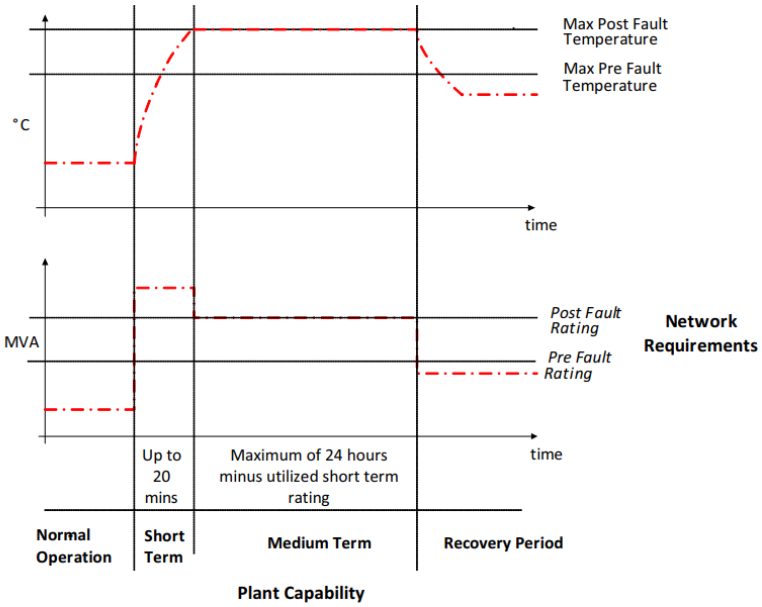

Figure 2.17: Illustration of the short-term, medium-term (post-fault) ratings and their respective conductor temperature variation for OHL, amended from [14].

2.1.4.5 Summary of Overhead Line Thermal Modelling

For the extensive reviews mentioned, the cable thermal modelling generally follows the same heat balance equation as shown in (104). The difference between standards [9], [10], [61] is the difference in the calculation of the heat losses from air convection. This work follows the approach present in [9].

2.1.5 Modelling of Components in a Joint Circuit

The OHLs, cables, and transformers are network components that are typically operated together, forming a circuit, e.g., in a substation, which will have at least a transformer and an OHL and/or cable, or all three components. A revised rating of one of the three components should not result in a violation (or underutilization) of the limits of the other components. This revised rating should take into account other essential components that must be considered in practice, such as circuit breakers, disconnectors, and physical joints of different components, which are, however, considered out of the scope of this review (the uprating method of these other components can be found in [63]).

To develop a joint rating for a circuit consisting of a transformer and OHL, cable, or both OHL and cable, reference [64], which provides an EPRI background, states that a DTR circuit rating method should simultaneously apply thermal rating models for the major types of equipment. Together with paper [65] and reports [66], [67], definitions of power ratings of transmission circuits were given as follows: the STRs are the maximum allowable currents with no time limit in "MVA" or amperes. The emergency (or transient) thermal ratings are these STRs with a time limit. These ratings are based on critical temperatures, exposure time limits, worst-case thermal heat transfer, and historical electrical loading assumptions, e.g., low WS and high AT for OHLs, high average AT for transformers, and the transient ratings are assumed to follow a high preload. The DTRs are variable thermal ratings revised from the STRs, requiring monitoring of ambient conditions and circuit loads. The real-time thermal ratings they present are based on predicted ambient and load profiles generated by prediction algorithms. The recorded ambient and load profiles over 24 hours, with a step size of 2-5 minutes, are fed into these prediction algorithms. The maximum recording length is 24 hours, and the latest recording will cause the oldest previous recording to be discarded. Manual override or adjustment of these profiles is also possible. The real-time ratings of the substation are given for every hour of the day (24 hours) using the lowest value of the real-time rating of the circuits within the substation.

Reference [68] also presents a general method of the adjustment of ratings for some circuits, which are expressed as follows:

$$I_{adj} = I_{NP} * \left(\frac{\theta_{max} - \theta_a}{\theta_{max,NP} - \theta_{a,NP}} \right)^{\frac{1}{n}} \tag{144}$$

where: I_{adj} and I_{NP} are adjusted current rating and nameplate rating of the equipment in question in A, respectively; θ_{max}, $\theta_{max,NP}$, θ_a and $\theta_{a,NP}$ are maximum equipment temperature, maximum equipment temperature specified in nameplate rating, air temperature and air temperature specified for nameplate rating in ℃, respectively; and n is an exponent with a value between 1.6 and 2.0. Note that this equation pertained only to limits in current, where power is not represented in this equation.

The EPRI DTR calculation included this adjustment for OHLs and transformers, but it is not applied to cables. However, it is stated that the thermodynamic algorithms, e.g., (131) for OHLs, are applied to OHLs and cables. The transformer models used by EPRI to date of the paper [68] are not applicable to thermodynamic algorithms. Other EPRI reports related to the joint rating of components (circuits) are unavailable in the public domain.

The code of practice [69] and paper [26] noted that when assessing the CTR of the transformer, all the components of the transformer (e.g., tap changer and bushing) and the associated equipment (for example, cables, switchgear and current transformers) should be capable of carrying a higher load. If it is found that the higher load is not suitable, a lower loading and duration limit should be used.

The CTR, as defined by the company directive [27], can be applied to all components rather than being limited to a specific component. The joint CTR is the maximum current that all components may carry during the operation of the considered load cycle without violating their respective temperature limits. Applying this definition to all components can help unify the methodology for evaluating the CTRs of different components, which is beneficial for assessing the joint/circuit CTR when all components operate together.

2.1.5.1 National Grid Technical Guidance Note for Components in a Joint Circuit

The National Grid TGN 303 [14] presents the S/MTOR, which can be used as short-term emergency ratings of OHL, cables and transformers. An example of a combined OHL-cable circuit (composite circuit) is present. In the composite circuit, the ratings are classified as pre-fault rating, 100% post-fault rating, medium-term thermal rating, and all STTR with different pre-fault percentages for different ambient conditions and months.

Another mention in [13] of component rating in a joint circuit is that, if any component in the joint circuit is applied a cyclic thermal rating, the pre-fault rating of the OHL should match the cyclic thermal rating of the component in question.

2.1.5.2 Summary of Joint Circuit Thermal Modelling

For the extensive reviews mentioned, there is little information on how ratings for a joint circuit are defined, calculated, and evaluated. This work presents a comprehensive methodology for the thermal ratings and loading limits of a joint circuit.

2.1.6 National Grid Technical Guidance Note for the Definition of Thermal Ratings

The National Grid TGN 303 [14] provides definitions of the different thermal ratings for the three main components. It can be seen that [14] defines those ratings as either current or load, where the load is power, which shows the issue with the lack of unification of the rating unit.

2.1.6.1 Circuit Rating in Technical Guidance Note

Circuit rating is the maximum current or load assigned to a circuit under specified conditions.

2.1.6.2 Continuous (Pre-Fault) Rating in Technical Guidance Note

Continuous rating, or pre-fault rating, is the maximum current or load that a component can withstand for indefinite operation without exceeding any limit.

2.1.6.3 Nameplate Rating in Technical Guidance Note

The nameplate rating is the continuous rating specified by the manufacturer.

2.1.6.4 Cyclic Rating in Technical Guidance Note

Cyclic rating is the maximum peak current or load assigned to a specific load pattern (or loading profile) that repeats over 24 hours for indefinite operation. Note that the CTR here in TGN considers a constant ambient for the components.

2.1.6.5 Short-Term Rating in Technical Guidance Note

Short-term rating is the rating for a specified period of up to 20 minutes if the circuit has previously been operated at or below the 100% continuous rating. A short-

term rating is not an emergency rating. It can be defined for both pre-fault and post-fault short-term ratings.

2.1.6.6 Medium-Term Rating in Technical Guidance Note

A medium-term rating is like a short-term rating, but for a period of 20 minutes to 24 hours.

2.1.6.7 Emergency Rating in Technical Guidance Note

Emergency rating is the rating that allows transformers to operate above their maximum nameplate rating, with the acceptance of the risk of transformer failure.

2.1.6.8 Exceedance Rating in Technical Guidance Note

Exceedance ratings are for OHLs that acknowledge the random variations of AAT, WS, AA and SI, expressed as a percentage of time that the temperature of the OHL conductor exceeds a given temperature limit under a continuous 1PU post-fault loading. The exceedance-based ratings accepted a certain risk (e.g., 10%) of exceedance that could lead to a violation of the temperature limit for OHLs.

2.1.6.9 Summary of Definitions of Ratings in National Grid Technical Guidance Note

In this thesis, the ratings are denoted as thermal ratings. For instance, short-term ratings are called short-term thermal ratings to distinguish them from static thermal ratings and to highlight that they are based on the thermal characteristics of the components.

It can be seen that the pre-fault rating applies to all three main components. However, the CTR is only applied to cables and transformers. This does not mean the OHL is unaffected by the CTR when connected to the same circuit. The OHL and the other components that use CTR are loaded with the same current. Thus, the OHL should also fulfil the CTR requirement used by other components. The same applies to the short- and medium-term ratings: all components in the same circuit should not exceed their respective limits.

While calculating CTR for the OHL is not recommended in TGN [14], the exceedance rating is unique to the OHL. The cables and transformers have their respective maximum temperature limits, and the OHL can accept the risk of exceeding those limits at the given exceedance level. The exceedance rating for the OHLs should be investigated individually in the study, as it is a risk-based rating, where such risk is unacceptable for the cables and transformers in operation.

2.2 Problem Statement and Case Study for Thermal Modelling of Components in Power Systems

As discussed in section 1.1.4, a joint circuit may contain multiple different components. There exist various issues when going from individual components to joint circuits. For ratings beyond steady-state, thermal time constants are needed for components in a joint circuit. Then, the rating units of the components differ: some are in current, while others are in power. Voltage variations and operational conditions (pre- or post-fault) in the power system, and ambient conditions, all impact various components in different ways.

2.2.1 Thermal Time Constants of Components

Different components show different TTCs, reflecting how quickly each component transitions from its initial state (temperature) to its final steady-state (temperature). In the following sections, the available data or calculations of TTCs from standard models for the three main components are presented. Four thermal time constants are used in this case study, from the first to the fourth TTCs, representing the time required for the temperature in question to change from its initial temperature to reach 63.2%, 86.5%, 95% and 98.2% of the ultimate maximum temperature difference, respectively.

2.2.1.1 Thermal Time Constants for Overhead Lines

The variation of the conductor temperature with time when loaded with close to normal rated current under three different ambient conditions: rated AT (30°C), no WS and no SI; rated AT, $15m/s$ WS and no SI; and rated AT, no WS and $900W/m^2$ SI can

be calculated using a time-step iterative approach from [70] by applying equations from [9], [10], [61], with [9] as the main source. An example of an OHL conductor used is the ACSR conductor type PENGUIN from [71]. The result is shown in Figure 2.18. The AA of 0° is chosen, as it is the most conservative value, and the thermal constants are calculated accordingly.

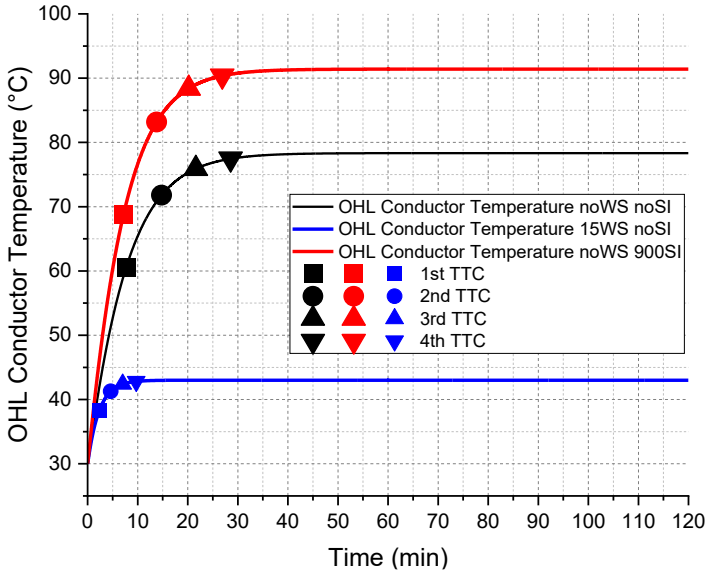

Figure 2.18: Variation of the example OHL conductor temperature with time under the condition of rated current under different ambient conditions.

The first to fourth thermal time constants (TTCs) for the example Type PE ACSR conductor under rated AT, no WS, and no SI conditions are 7.7min, 14.8min, 21.6min, and 28.6min (0.13 h, 0.25 h, 0.36 h, and 0.48 h), respectively. For rated AT, $15 m/s$ WS, and no SI, these are 2.3min, 4.6min, 7.0min and 9.7min (0.04h, 0.08h, 0.12h and 0.16h), respectively. For rated AT, no WS and $900 W/m^2$ SI, they are 7.2min, 13.8min, 20.2min and 26.9min (0.12h, 0.23h, 0.34h and 0.45h), respectively. It can be seen that the fourth thermal constant of the OHL is still below 30 minutes.

2.2.1.2 Thermal Time Constants for Cables

Paper [72] provided a TTC of a crane cable with a current of 72.1A for 72 min at the AT of 30°C. Crane cables are cables exposed to air, as classified in [5]. For buried cables, using the model in [57], the TTC of an example directly buried single-core

$120mm^2$ copper conductor copper screen PVC jacket cable in [73] can be calculated by the mathematical definition of the time constant.

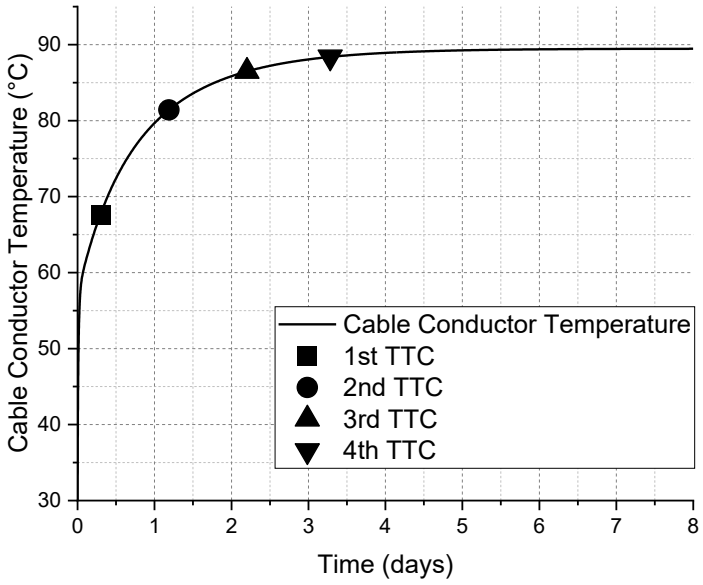

Figure 2.19: Variation of the example cable conductor temperature with time under the condition of rated current and 30°C AT.

The first to fourth TTC, for example, single-core $120mm^2$ copper conductor copper screen PVC jacket cable are 429min, 1919min, 3169min and 4729min (7.15h, 28.65h, 52.82h and 78.82h), respectively. It can be seen that the fourth thermal constant of the cable is over 3 days.

2.2.1.3 Thermal Time Constants for Transformers

When calculating the thermal rating of transformers, the TTCs are included in the calculation process for a non-infinite loading period [1], [2]. Where [1] stated that the time constant of HST is approximately equal to the time constant of TOT. The TTCs of some dry-type and epoxy resin transformers are shown for comparison.

Figure 2.20 shows the variation of the HST of an example distribution transformer modified from [74]. The difference is that the rated HSTR of the modified transformer is 80°C at the rated AT of 30°C instead of 65°C HSTR at the maximum AT of 45°C. The transformer is assumed to be loaded from a non-energised state, then

energised and loaded with the rated load at the first timestep at 30°C AT. Figure 2.21 shows the variation of the HST using a transformer at the transmission level [75], [76].

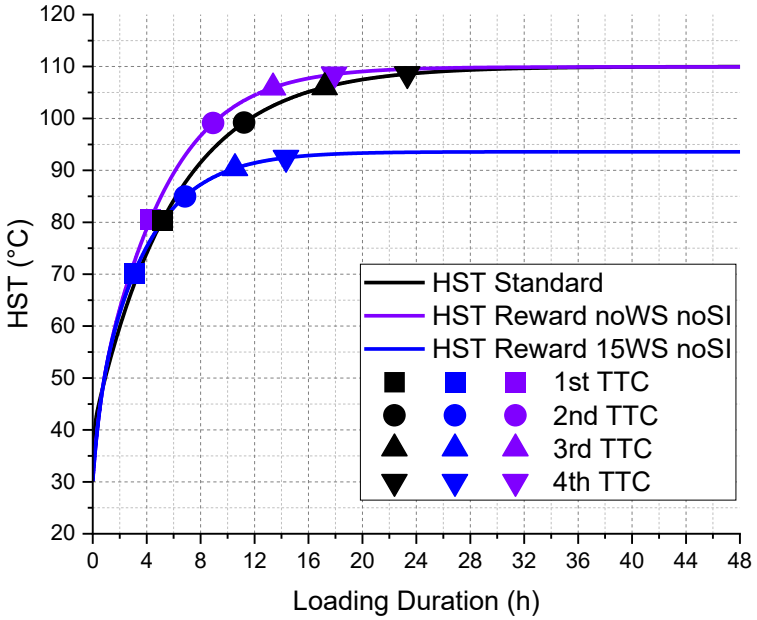

Figure 2.20: Variation of the example ONAN distribution transformer HST with time from the un-energised start at the condition of rated current [1].

The first to fourth TTCs for the example of a modified 6.3MVA ONAN transformer at 30°C using the standard model are 5.18h, 11.23h, 17.20h, and 23.33h, respectively. For the model in this thesis, 30°C AT, no WS, and no SI are 4.28h, 8.93h, 13.38h, and 17.9h, respectively. For the model in this thesis for 30°C AT, 15m/s WS, and no SI, these are 3.06h, 6.85h, 10.55h and 14.33h, respectively. It can be seen that although the thermal constants vary with ambient conditions, the results for the thermal constant in the standard and reward models were all within 24 hours. The introduction of WS will reduce all TTCs relative to the situation in which no WS is applied.

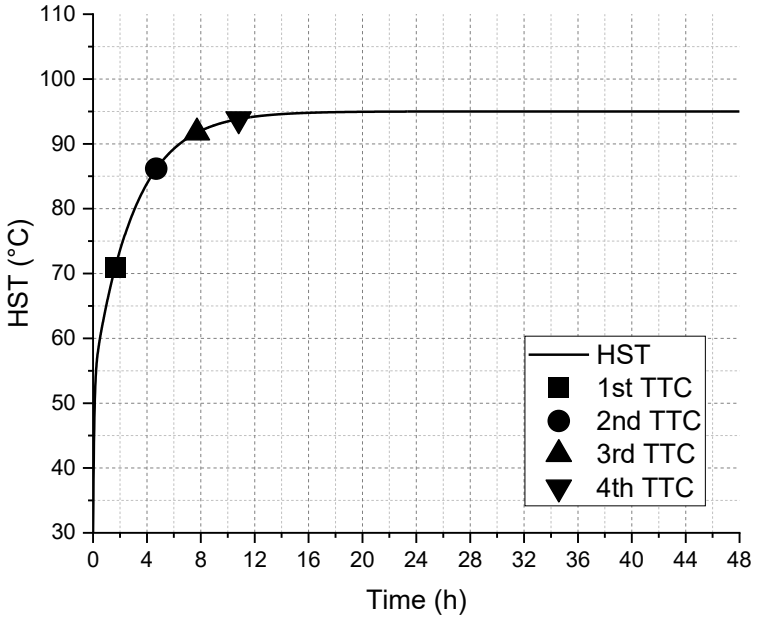

Figure 2.21: Variation of the example OFAF transmission transformer HST with time from the un-energised start at the condition of rated current and 30°C AT [75], [76].

The first to fourth TTC for the example 240MVA OFAF transmission transformer are 1.65h, 4.70h, 7.72h and 10.82h, respectively.

2.2.1.4 Summary of Thermal Constants of Components

The TTCs of the different components differ significantly. The TTC of the example OHL is the shortest, and even the fourth TTC is less than half an hour. The buried cable has the longest TTC, with 7 hours for the first TTC and almost 80 hours for the fourth TTC, which is more than 3 days. The example transformer has the first TTC slightly longer than the first TTC taken from the existing publications, but its fourth TTC is still less than a day.

Different TTCs of different components show that the steady state of all components in the system (substation) is only reachable after the component with the longest TTC enters the steady-state. This calculation assumes that all other external parameters remain unchanged, i.e., the ambient conditions and component loading profiles remain constant (or cyclic). It is assumed that the third (95%) or fourth (98.2%) TTC is the steady-state because, in actual practice, the error of the measurement/monitoring equipment is usually within 5%.

2.2.2 Units for Ratings

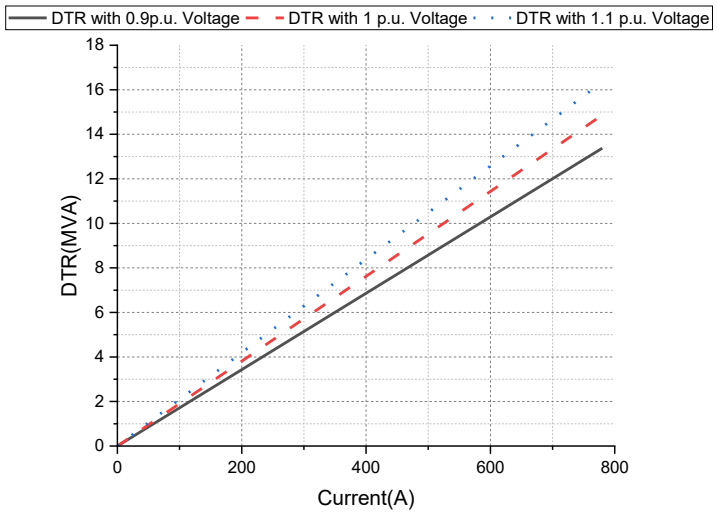

Figure 2.22: Current vs. Power limits for a 390A rating OHL in a three-phase system.

In practice, the unit used to specify transformer ratings differs from that used for OHLs and cable ratings. For transformers, VA (apparent power) is typically used for rating, while amperes (current) are normally used for rating OHLs and cables. To convert the current rating to the DTR rating that uses VA as the unit for a given OHL, the current rating is multiplied by the system's voltage limit, yielding a range of power ratings for that current rating. As an example, the relation between the apparent power, current and voltage of an OHL conductor with 390A normal thermal rating taken from [71] is shown in Figure 2.22, where during the process of assessing the hosting capacity (HC) of the network in [92], the actual DTR limit of the OHL and transformer are given in amps and voltage limit violations are checked for the buses in the network where loads are connected.

2.2.3 Impact of Voltage Variation and Load Types

Three basic types of loads are present in the power system: constant-power, constant-impedance, and constant-current loads. The power demand profile as a function of voltage varies for each type of basic load. For instance, the demand for a constant-power load does not change with voltage, whereas the demand for a constant-impedance

load varies with the square of the voltage. So, it is important to investigate how voltage variation affects the ratings of individual components and the joint circuit.

2.2.4 Additional Consideration of Pre-Fault and Post-Fault Ratings

In TGN [14], it was stated that, for the OHL, it is mandatory to preserve 20% of the continuous pre-fault rating for post-fault continuous conditions without violating the temperature limit. This mandatory reservation of capacity effectively means the maximum pre-fault rating is 85% (or 84%) of the post-fault rating. Then, the pre-fault and post-fault ratings of the cable are the same regardless of its construction type. Lastly, for the power transformer, during post-fault conditions, it can use a higher rating denoted as maximum emergency rating, which is higher than the maximum continuous rating, and it should be able to load at 1.2PU of its nameplate thermal rating (NTR) indefinitely.

2.2.5 Inconsistent Ambient Air Temperature for Traditional Rating Seasons

National Grid TGN 303 [14] presents the rating of a year as divided into 12 months. The rating season for OHLs, buried cables, and transformers is assigned. TGNs [3], [8], [11], TS [56] and engineering recommendations [77] present the value of the ambient temperatures of all the components considered in this thesis for these seasons, shown in Table 2.1.

Table 2.1: Ambient Temperature of the Rating Months [14].

Month	**Jan**	**Feb**	**Mar**	**Apr**	**May**	**Jun**	**Jul**	**Aug**	**Sep**	**Oct**	**Nov**	**Dec**
OHL [°C]	2	2	9	9	20	20	20	20	9	9	9	2
DB Cable (1m soil) [°C]	10	10	10	10	15	15	15	15	15	15	10	10
FTC (0.3m soil) [°C]	10	10	15	15	35	35	35	35	25	25	15	10
ExpoC [°C]	10	10	20	20	30	30	30	30	20	20	20	10
Transformer [°C]	10	10	20	20	30	30	30	30	20	20	20	10

It can be seen that the components exposed to ambient air, namely OHL, have inconsistent ambient temperatures. For instance, the AAT considered by OHL is 20°C,

whilst the AAT for exposed cable and transformer is 30°C. The reason is that the seasonal rating of the OHL is based on exceedance. Still, the transformer and exposed cable cannot accept the risk, so the AAT for them is more conservative. This issue should be discussed in greater detail because components exposed to the same ambient temperature should consider it when evaluating the joint rating.

2.3 Conclusions

This chapter has provided a comprehensive review of the existing methodologies and models used to evaluate the thermal capacity limits of the three primary components within electrical transmission systems, power transformers, underground cables, and overhead lines, as well as their combined operation within joint circuits. The review has highlighted that while the standardised thermal models defined in international and national guidance documents remain the foundation of rating practice, they are often based on simplified assumptions and fixed ambient design conditions that may no longer represent current or emerging operational environments.

In terms of the improvements of existing models and the development of new models:

The oil-immersed transformer thermal model is improved and completed: dependency of transformer load losses on the winding temperature and tap position is added; dependency of no-load losses on the supply voltage variations is added; switching from ONAN to OFAF cooling mode and vise-versa is modelled more accurately; WS and SI are included as the part of the transformer thermal model and the final output is HST instead of TOT; case when the tank and cooling plant of a large transformer are exposed to different ambient conditions is included; heat inputs from transformers equipped with tertiary winding and auxiliaries is included; evaluation of effective cooling area is introduced, to represent the inhomogeneous temperature distribution in different cooling modes.

The previously developed cable thermal model for directly buried cables (DBCs) and cables in conduits is now extended to include cables in filled troughs (FTCs).

Thermal models for the cables exposed to air and solar irradiance (ExpoC) are developed, also enabling the consideration of WS.

The discussion of supplementary publications and recent research initiatives has shown significant progress toward improving model accuracy through enhanced representation of dynamic behaviour, environmental variability, and interdependence between component and system-level performance. However, inconsistencies remain in the treatment of ambient conditions, thermal time constants, and load characteristics, leading to potential discrepancies when determining pre-fault and post-fault ratings or when comparing seasonal and real-time capacities across different asset types.

Importantly, the review of modelling approaches for joint circuits has emphasised that individual component ratings cannot be considered in isolation. As OHLs, cables, and transformers increasingly operate as integrated systems, their collective thermal behaviour and mutual constraints must be understood to ensure safe and reliable network operation. These findings underscore the need to re-evaluate existing rating methodologies, moving toward unified, condition-dependent frameworks that reflect realistic ambient conditions and operational interactions. The insights gained from this review form the technical basis for the subsequent chapters, which focus on developing and applying improved thermal modelling and rating methodologies for individual components and their combined operation within complete transmission circuits.

Chapter 3

Meteorological Data and Loading Profiles for Different Types of Thermal Ratings

This chapter describes the meteorological and operational data used to evaluate the thermal performance and rating of power system components under various rating methodologies. Since thermal ratings are highly sensitive to both ambient and loading conditions, accurate and representative input data are essential to ensure reliable estimation of conductor, cable, and transformer temperatures. The chapter begins by outlining the different types of thermal ratings considered in this thesis, including static, dynamic, cyclic, short-term and medium-term overloading, and the newly introduced exceedance rating concept. Each rating type is defined in the context of its operational purpose and its dependence on environmental and electrical conditions.

The second part of the chapter focuses on the meteorological datasets used to support the thermal modelling of individual components and joint circuits. Detailed analyses are provided for the key weather parameters influencing heat transfer and cooling performance, air temperature, soil temperature, wind speed, attacking angle, and solar irradiance. Particular attention is given to the representation of heatwave conditions, which are increasingly relevant in the context of climate variability and can significantly affect the available thermal capacity of network assets.

The final section discusses the development of realistic loading profiles to represent different operational scenarios, including constant and cyclic load patterns, as well as anticipated future changes driven by system demand growth and renewable integration. By integrating these meteorological and loading datasets, this chapter establishes the foundation for the subsequent modelling and evaluation of component

and circuit thermal ratings under a wide range of operating and environmental conditions.

3.1 Types of Thermal Ratings

Five main thermal ratings are presented in the following chapter of this thesis: static thermal rating (STR) as thick orange line, dynamic thermal rating (DTR) as blue line, cyclic thermal rating (CTR) as dashed dotted yellow line, short-term and medium-term overloading (emergency) rating (S/MTOR) and exceedance rating as red bar, and exceedance ratings as green dashed line, shown in Figure 3.1 below as an arbitrary overview.

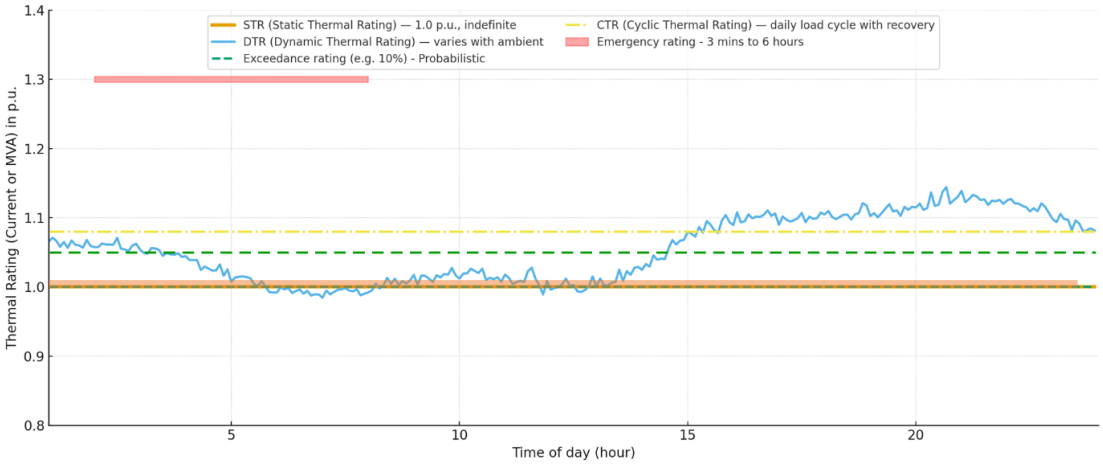

Figure 3.1: An example of different types of thermal ratings for an arbitrary network component.

3.1.1 Static Thermal Ratings

The STR is calculated by using a certain set of probabilistic worst-case scenarios. STR is applicable for an indefinite continuous operation under constant ambient conditions. In practice, for OHL, STR is given in season, summer STR, spring and autumn (SP/A) STR and winter STR. Buried cables are specified for winter and normal cold (W/NC) season, and summer and normal hot (S/NH) season. Each season considers a different ambient soil temperature (AST) and thermal resistivity. However, for consistency, the thermal resistivity is set to the S/NH value ($1.2K \cdot m/W$) in this thesis.

The transformer uses NTR as its STR, where NTR is assumed to be the same across seasons in practice [3], [8], [11], [14], [77], [78]. Because the focus point of this thesis is extreme heat and heat waves, the STR is prioritised on the summer STR unless specified.

3.1.2 Dynamic Thermal Ratings

The DTR in this thesis is calculated by real-time prevailing ambient conditions, assuming an indefinite operation, so it is considered a continuous rating. In this thesis, DTR are calculated as a map for the range of ambient temperatures (could be AAT or AST), WS and SI for different components. For the transformer equipped with an on-load tap changer (OLTC), the DTR are split into nominal tap position and worst tap position in terms of thermal performance.

3.1.3 Cyclic Thermal Ratings

The CTR is calculated by recognising that loading of the component might not always be at peak loading throughout a day, but cycling with a certain period of peak load and a certain period of low load, forming a daily cyclic loading, which reflects more about load pattern effects on thermal response [1], [7], [14].

3.1.4 Short-Term and Medium-Term Overloading Ratings

The S/MTOR allows temporary loading above the maximum continuous rating (could be STR or DTR) under post-fault conditions, as long as the pre-defined maximum temperature limit is not violated for a certain time duration. The loading must be reduced to the maximum post-fault continuous rating to avoid exceeding the temperature limit [14].

3.1.5 Exceedance Level-Based Ratings

Exceedance level-based rating is for OHL and is a subset of DTR, but not of the indefinite operation. The thermal ratings in the exceedance ratings are real-time thermal ratings (RTTRs) that account for thermal inertia. RTTR accounts for the fact that the conductor or equipment temperature does not instantly reach its new steady-state value

after a change in loading or ambient conditions. Instead, the temperature follows a time-dependent response governed by the TTC of the component. Where the rating is set at a given probability of exceedance of the conductor temperature limit, typically over a given year. The STR of OHL is defined in this way (e.g., 10% exceedance level) under RTTR. The exceedance rating introduces a probabilistic definition of the capacity of the OHL, where STR is based on [11].

3.1.6 Summary of Thermal Rating Types

Together, these rating categories distinguish ratings by assuming indefinite operation (STR, DTR), acknowledging the daily cycle (CTR), explicitly introducing time limits (S/MTOR), or incorporating probabilities of exceedance (Exceedance Ratings) using RTTR. CTR in particular highlights that network loading might be inherently cyclic and discontinuous at peak, which can be safely leveraged to achieve higher ratings.

3.2 Meteorological Data for Thermal Modelling and Rating of Components Considering Heat Wave Impact

Different components are exposed in different ambient conditions. In this thesis, the ambient conditions considered are AAT, AST1m, AST0.3m, WS, AA and SI, as these are the primary drivers influencing the thermal behaviour and rating of OHL, cables, and transformers. Ambient conditions, such as precipitation and humidity, that can affect the thermal rating of components are ignored in the current stage due to insufficient data. Instead, common assumptions from TGNs and standards are used. Non-standard assumptions should be included and improved in the future. In this study, we are focusing on the effects of the heatwave. Therefore, comparisons are mainly done based on the summer STR ambient conditions value.

3.2.1 Ambient Air Temperature

The most basic ambient condition is the AAT, in which the OHL, ExpoC, and transformers are directly exposed. In this work, the AAT also determined ASTs, which will be discussed in the next section.

For an OHL carrying a constant current (e.g., its summer STR), the conductor temperature can be calculated as a function of AAT, SI, WS and loading level. Summer STR is the continuous thermal rating of the conductor calculated for typical summer design conditions: 20°C AAT, 0.5 m/s WS, 12° attacking angle (AA), and 0 W/m² SI.

For DBC and filled FTC, the new STR are assessed under the following ambient conditions: 30 °C AAT, 0 m/s WS, and 0 W/m² SI. As for ExpoC, the STR ambient conditions are: 30°C AAT, 0.5 m/s WS, 90° AA, and 0 W/m^2 SI. The 90° AA is assumed, as the wind direction is parallel to the ground and perpendicular to the ExpoC.

For the 400/132 kV power transformer (120/240 MVA, ONAN/OFAF), the summer STR is calculated under 30 °C AAT, 0.5 m/s WS, and 0 W/m² SI, representing standard nameplate summer rating conditions.

The SST of both OHL conductors is calculated across a wide range of AAT, SI, and WS to capture both historical and projected UK extremes. For AAT, a range of −30 °C to +50 °C is used. The lower bound (−30 °C) represents a rounded value slightly below the UK's historical minimum of −27.2 °C [79], ensuring conservative coverage of extreme cold events. The upper bound (+50 °C) reflects climate-change projections, with the highest temperature already reaching 40.2 °C in July 2022 and expected to rise further in future decades under UKCP18 scenarios [80]. The projection in Figure 3.2 suggests that the 95th percentile maximum air temperature in London can reach 50°C in 2099, and the current quadratic interpolation from the trend suggests this might well be reached in 2080.

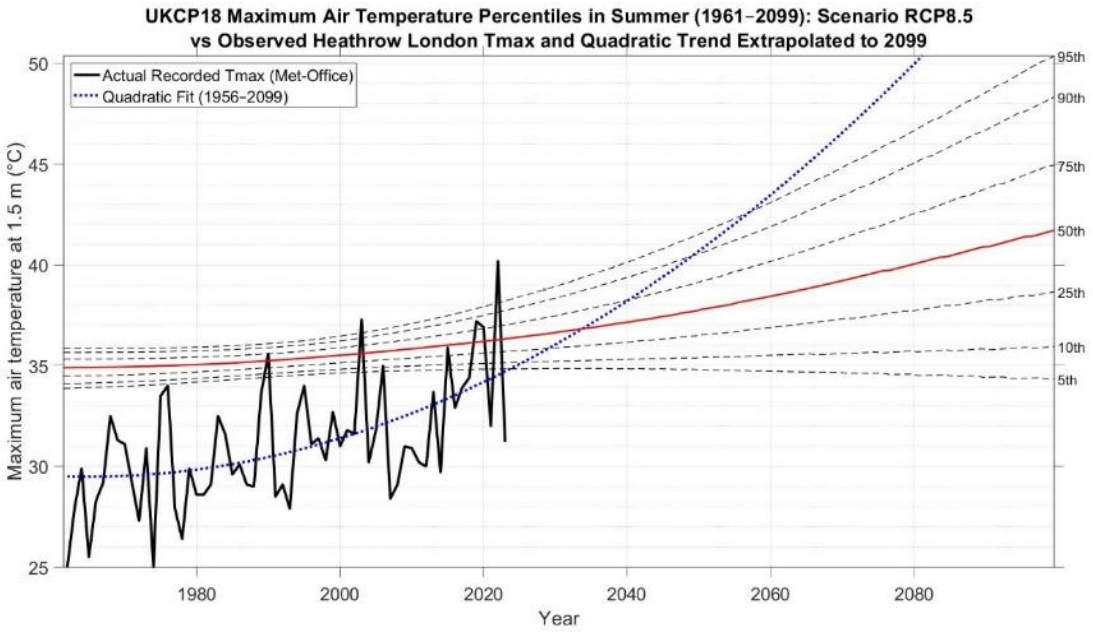

Figure 3.2: UKCP18 probabilistic projections for Heathrow, London.

3.2.2 Ambient Soil Temperature

DBC and FTC are exposed in AST1m and AST0.3m, respectively. The AST is calculated based on its relationship to AAT. However, due to the high thermal inertia at 1m and 0.3m soil depths, the measurements from the Met Office show a hysteresis loop in the relationship between AAT and AST, as shown in Figure 3.3 and Figure 3.4, respectively. The ASTs are taken from 2008 to 2023 in hourly resolutions, data from Kew Gardens are taken as it is near Heathrow, where the hottest heatwave was present (Heathrow does not have soil temperature measurement data).

As mentioned, this thesis background of investigating heat waves and extreme heat and the calculated result from a lower AST, can only achieve a higher rating, which is not conservative and is not the scope of this thesis, so the polynomial fitting result for the summer-to-winter is used for both AST 1m and 0.3m, shown in Figure 3.5 and Figure 3.6, respectively.

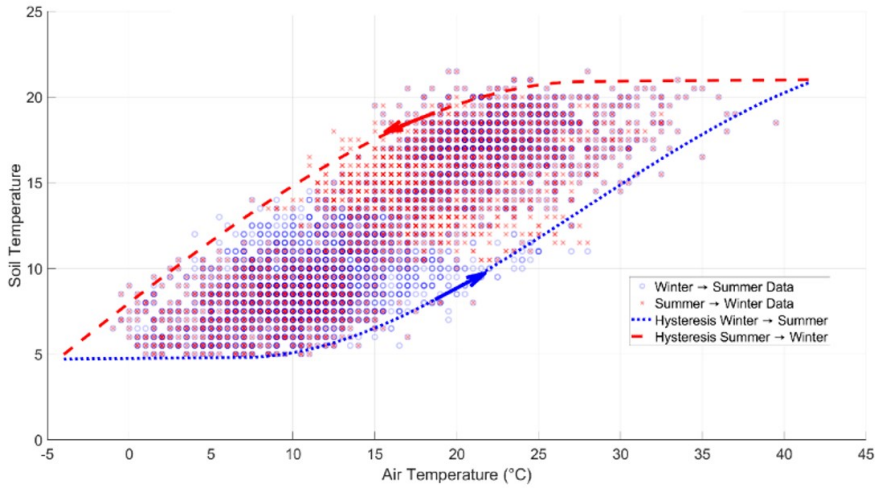

Figure 3.3: The hysteresis loop between the measured temperature of air and soil at 1m depth in Kew Gardens, London.

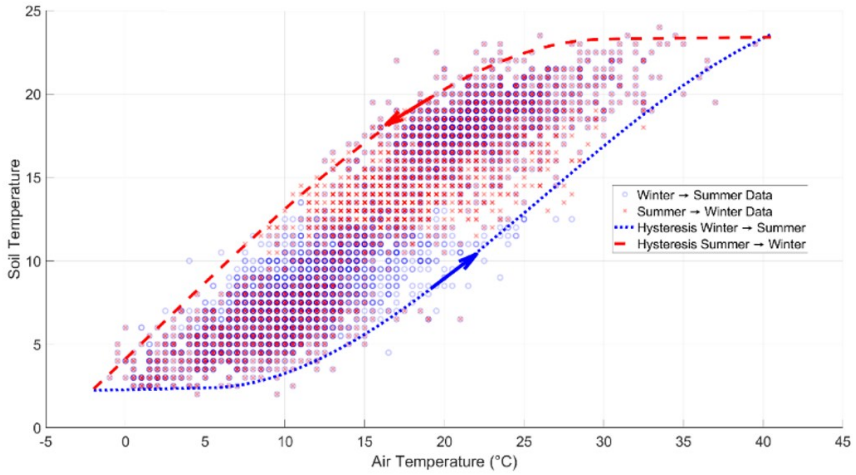

Figure 3.4: The hysteresis loop between the measured temperature of air and the soil at 0.3m depth in Kew Gardens, London.

The fitted ASTs are functions of AAT, calculated by:

$$AST1m = 0.00010849 * \left({\theta_{air}}^{3}\right) + 0.00396891 * \left({\theta_{air}}^{2}\right) + 0.42635952 * (\theta_{air}) + 8.37714634 \quad \text{if } AST1m < 0, AST1m = 0°C \tag{145}$$

$$AST0.3m = -0.00018094 * \left({\theta_{air}}^{3}\right) + 0.00836081 * \left({\theta_{air}}^{2}\right) + 0.54950808 * (\theta_{air}) + 5.26332715 \quad \text{if } AST0.3m < 0, AST0.3m = -0.5°C \tag{146}$$

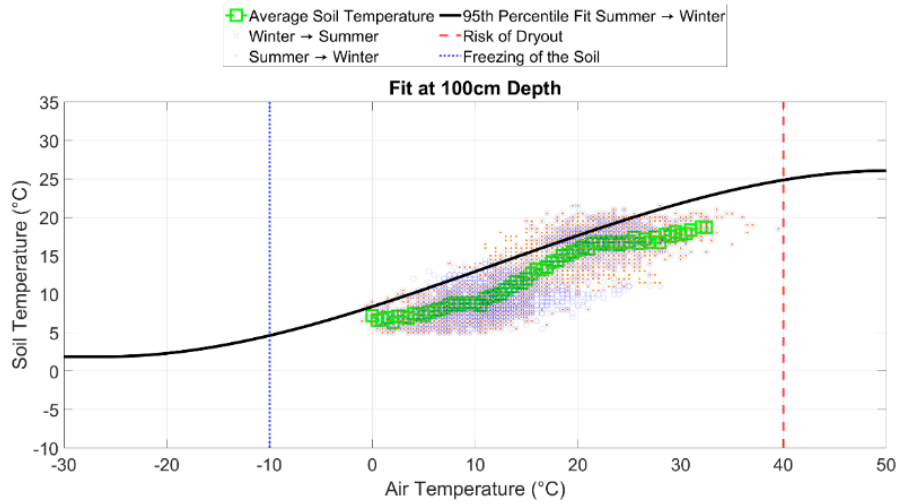

Figure 3.5: Polynomial fit for the measured temperature of air and soil at 1m depth in Kew Gardens, London.

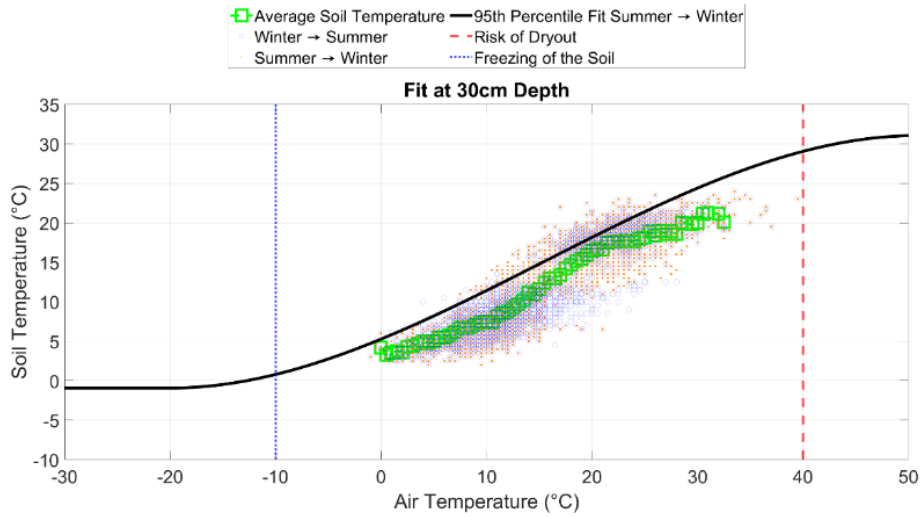

Figure 3.6: Polynomial fit for the measured temperature of air and the soil at 0.3m depth in Kew Gardens, London.

As marked in the results of the relationship between AAT and AST, there exists a risk of dry-out of the soil under high AAT conditions and freezing of the soil under low AAT conditions. These two effects are not taken into consideration during the calculation of the ratings, but the consequences of soil dry-out will be discussed briefly in this thesis.

3.2.3 Wind Speed

According to the current distribution network operator (DNO) guidance and TGNs, the standard wind speed assumption is 0.5 m/s [77], [81]. However, it was found that under heat-wave conditions, the 0.5m/s WS assumption might be too conservative.

This section presents conditional probability density functions (PDFs) in Figure 3.7 and wind-speed scatter plots in Figure 3.8, conditioned on solar irradiance at Heathrow (London). During periods of high solar irradiance (i.e., hottest hours), wind speeds are generally not near zero. The distribution shows that wind speed is typically above 1 m/s when solar irradiance is at its peak. The industry-standard assumption of 0.5 m/s wind speed is overly conservative for summer peak thermal rating calculations. Using 1 m/s already represents a near-worst-case but more realistic scenario for the time of maximum heating.

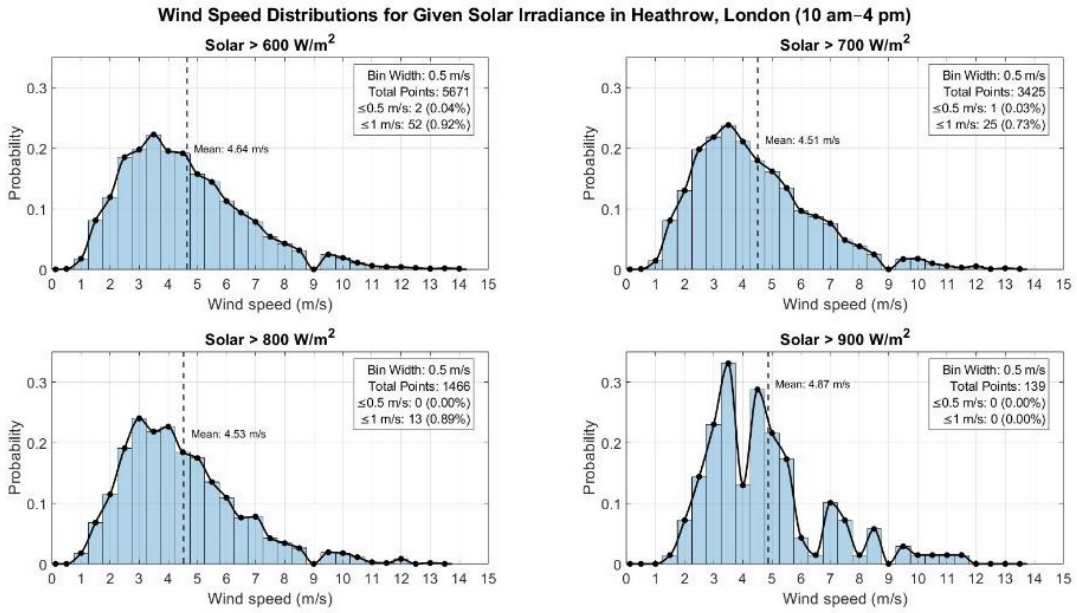

Figure 3.7: Conditional PDF in m/s for Heathrow.

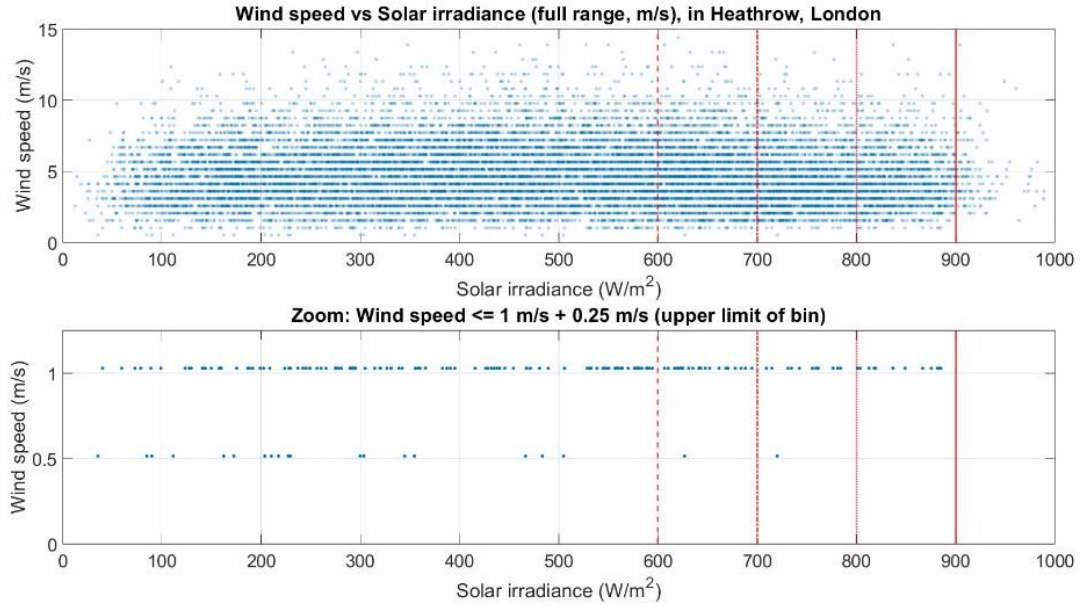

Figure 3.8: Scatter Plots in m/s for Heathrow.

Heatwaves in Heathrow are defined as the hottest day ±1 day, spaced at least 2 weeks apart, as shown in Figure 3.9. For each heatwave, peak hourly values of temperature, solar irradiance, and minimum wind speed are identified within ±3 hours of midday. Peak temperatures during heatwaves coincide with elevated wind speeds, driven by increased atmospheric mixing during the day. Even during extreme events, wind speeds rarely drop below 1 m/s at the time of maximum temperature. Solar irradiance averages remain high (>500 W/m²) during these periods, showing strong radiative heating. Assuming 0 m/s or very low wind speed simultaneously with peak temperature is extremely unlikely. Using 1 m/s as the baseline wind speed better represents true worst-case conditions while avoiding unnecessary underutilization of the capacity of OHL or any exposed component. Therefore, both 0.5 m/s (as standard) and 1 m/s are utilised in this thesis to represent the standard conservative assumption and 1m/s as the more realistic conservative assumption.

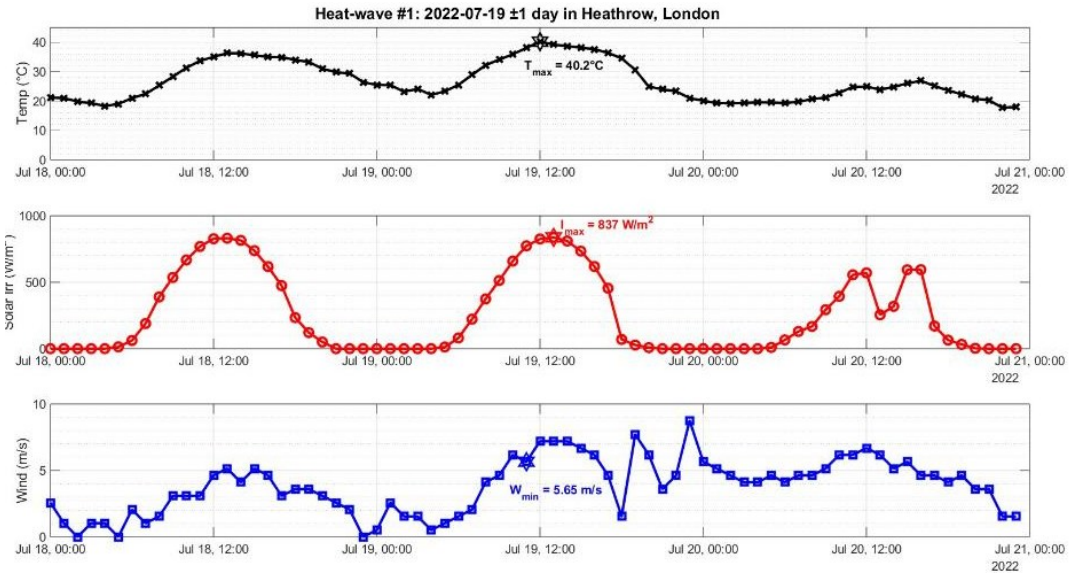

Figure 3.9: Heatwave ambient in Heathrow, London.

Table 3.1: Summary of heatwave values in Heathrow for three heatwave events.

London, Heathrow			
	Average Temperature (°C) on Heatwave Day		
Time	Heatwave 1	Heatwave 2	Heatwave 3
Peak	40.2	37.2	36.9
10 am-4pm	38.3	35.2	34.6
7am-7pm	35.7	33.5	31.1
Day	30.3	28.8	26.0
3 Days	26.7	25.6	23.0

	Average Solar Irradiance on Heatwave Day		
Time	Heatwave 1	Heatwave 2	Heatwave 3
Peak	837	765	824
10 am-4pm	751	623	694
7am-7pm	532	464	489
Day	439	362	401
3 Days	387	330	417

	Average Wind (m/s) on Heatwave Day		
Time	Heatwave 1	Heatwave 2	Heatwave 3
Peak	5.7	3.1	6.7
10 am-4pm	6.6	4.7	8.1
7am-7pm	5.5	4.2	6.7
Day	4.3	3.3	5.1
3 Days	3.8	3.5	4.4

Table 3.1 provides a consolidated table of peak temperatures, solar irradiance, and the lowest wind speeds observed during three heatwave events at Heathrow. The lowest wind speed during heatwaves remains >1 m/s in almost all cases, confirming that

calm conditions (<0.5 m/s) do not typically coincide with maximum heating. Thermal ratings based on 0.5 m/s lead to excessive conservatism, unnecessarily reducing network capacity. 1 m/s can be used as the minimum credible wind speed for design purposes, still maintaining a conservative margin but enabling higher STR/DTR values. However, further analysis of WS is needed for all sites in the UK to confirm, but due to time constraints, it can only be included in future work.

The analysis presented here uses Heathrow as an example, but the same trend is observed at other UK sites such as Coventry and Edinburgh. In all locations, wind speeds during periods of maximum solar irradiance and peak temperature are generally above 1 m/s, confirming that calm conditions (<0.5 m/s) rarely coincide with the hottest periods. In this report, both 0.5 m/s and 1.0 m/s wind speeds are used in the analysis. Where 0.5 m/s represents the current standard assumption, while 1.0 m/s represents a realistic worst-case condition based on observed UK data, this comparison highlights the conservatism of the standard and quantifies the potential capacity gain when adopting a more representative WS.

3.2.4 Wind Attacking Angle

For components exposed in WS, the OHL follows the standard assumption of 12-degree AA [11], [77], [78]. In a power transformer, the AA is always considered the worst-attacking angle, as shown in the following chapter. The ExpoC, because the part investigated in this thesis is the ExpoC in a cable compound, where it emerges vertically from the ground surface and connects the OHL or transformer via a termination. The WS, measured parallel to the ground surface, is always perpendicular to the ExpoC. So, the AA considered by ExpoC is always 90 degrees unless specified otherwise.

3.2.5 Solar Irradiance

In this thesis, three levels of SI are considered: zero SI or no SI, which represent the conditions at night; $500 W/m^2$ which represent the SI for a normal sunny day in any given season, and $1000 W/m^2$ from the highest measured SI in the UK, which represents the SI during summer and especially during an event of a heatwave. However, due to the inclusion of CTR, which considers a cyclic loading profile, the SI between days

behaves like a daily cycle. The following representative SI profiles recorded from hourly non-coincidental maximum SI in the UK are used as a typical daily SI profile, shown in Figure 3.10 [82]. The non-coincidental SI is per unitised. When using the 500 and 1000 W/m^2 SI, the peak represents the 500 and 1000 W/m^2 SI.

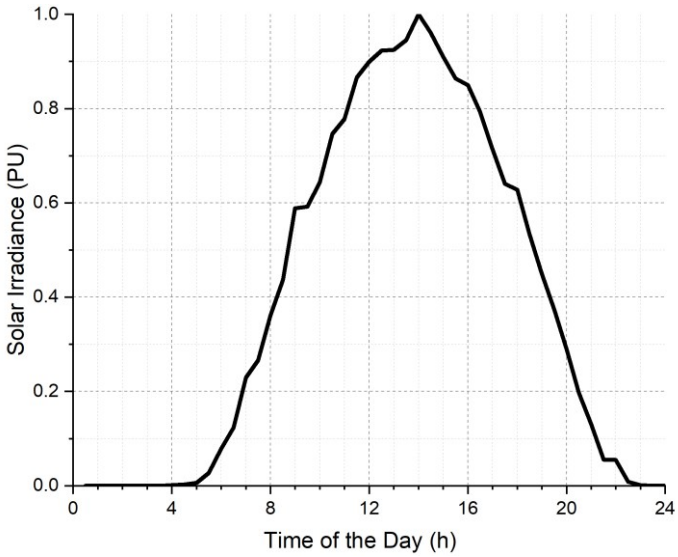

Figure 3.10: Per-unitised non-coincidental daily solar irradiance profile used in this thesis.

3.2.6 Impact of Climate Change and Heat Waves

The ambient weather data in 1981 and 2022 are shown in Figure 3.12 to Figure 3.15, representing the air temperature, soil temperature at 1m, wind speed, and solar irradiance, respectively. To represent changes due to global warming. The hourly weather data are extracted from [83] at Heathrow and its nearby locations, should any missing data from Heathrow not be available. The complete data set of air temperature, wind speed, solar irradiance, and soil temperature spans back to 1981. The year 2022 and Heathrow were chosen as the highest ambient air temperature was recorded here. The summary of available weather data in 1981 is shown below in Table 3.2. Next, weather data from 1981 are compared to the present 2022 conditions, especially in summer as defined by operational practice (May - Aug), when heatwave events occur.

Table 3.2: Available weather data overview in 1981 [83].

Location	Air Temperature	Wind Speed	Solar Irradiance	Soil Temperature
Heathrow	✓	✓	x	x
Kew Gardens	✓	x	x	✓
London Weather Centre (decommissioned)	x	x	✓	x

Additionally, as different thermal responses of components, especially OHLs, can be within an hour, a finer resolution of weather data is needed. In this case, due to the lack of finer resolution measurements of weather data available, a linear interpolation of 12 by 5-minute weather data captures a better thermal response due to its thermal inertia, especially for the components with lower thermal time constants. An example of Zebra OHL against a constant applied current is shown below, where the hourly data underestimates the dynamic ratings by 4% compared to the 5-minute data. However, it is worth noting that the linear interpolation method is used only because real measured 5-minute data are unavailable. The majority of the dataset is publicly provided only in 1-hour intervals. The linearly interpolated data does not capture the true fluctuations in the ambient data, so measured 5-minute interval data should be used if available.

Figure 3.12 to Figure 3.15 show the 5-minute interpolated from hourly data air temperature, soil temperature, wind speed, and solar irradiance in 1981 and 2022. It can be seen in Figure 3.12 that the maximum 5-minute air temperature reached 40 °C in 2022 and 28 °C in 1981. Additionally, the maximum daily mean temperature recorded was 30 °C in 2022 and 23.5 °C in 1981. For all days, except a few days in 1981, the air temperature in 2022 is higher, with an average of 2°C.

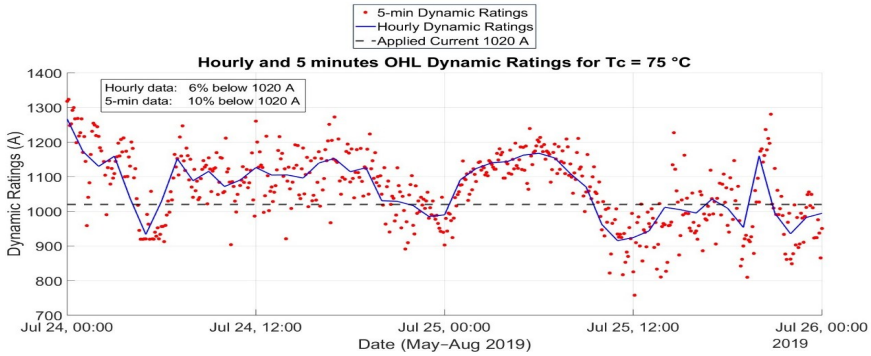

Figure 3.11: Example of 5 minutes and hourly DTR against a constant applied current.

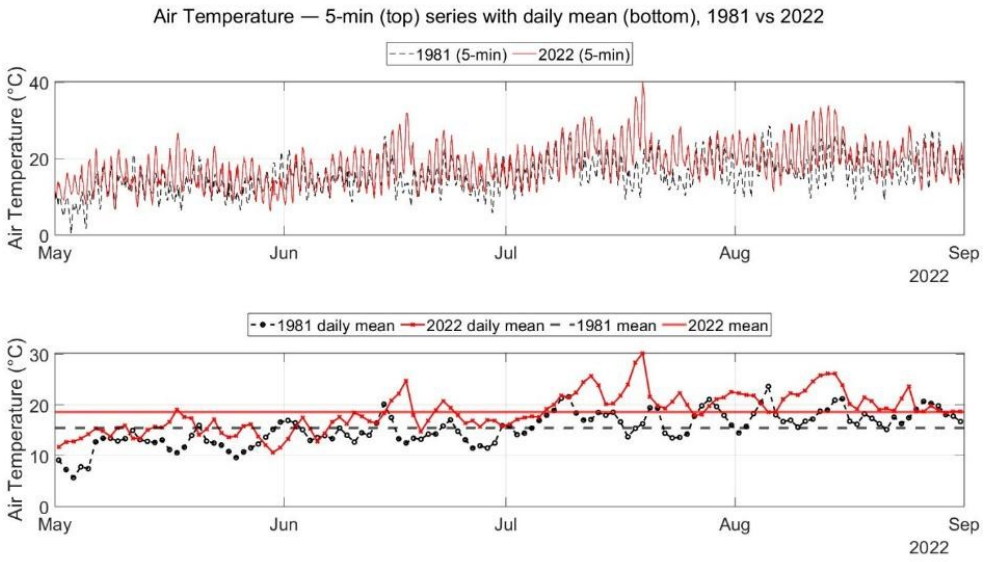

Figure 3.12: Air temperature 1981 vs 2022 [83].

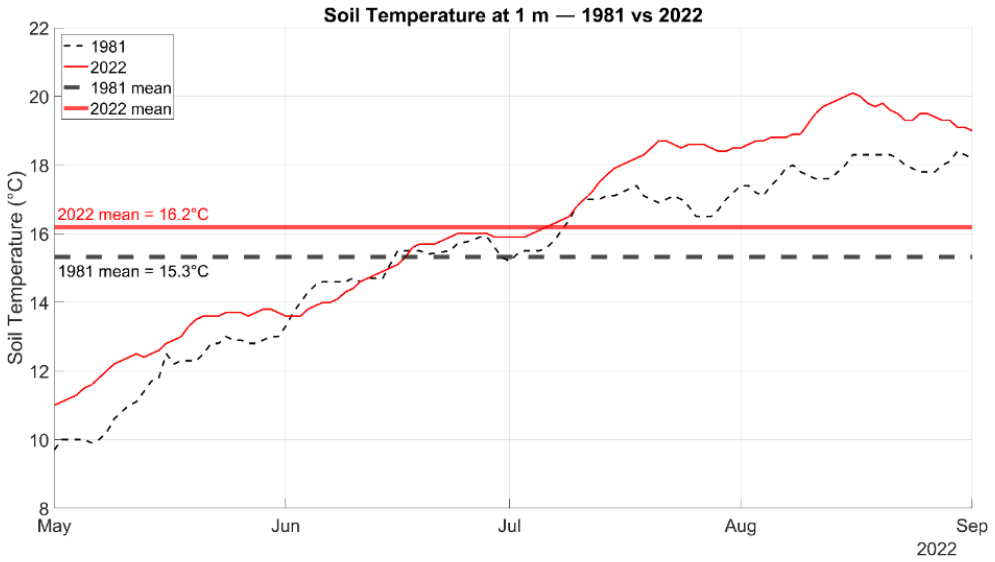

Figure 3.13: Soil Temperature (1m depth) 1981 vs 2022 [83].

The soil temperature at 1 m depth is described in Figure 3.13. The maximum s temperature in 2022 and 1981 was recorded at 20 °C and 18.5 °C, respectively. The mean soil temperature has increased by around 1 °C from 1981 to 2022. Soil temperature can be observed to gradually increase from May to September, and can be seen with further increments when heatwave events occur. The peaks of soil temperatures occurred within two weeks after heatwave events.

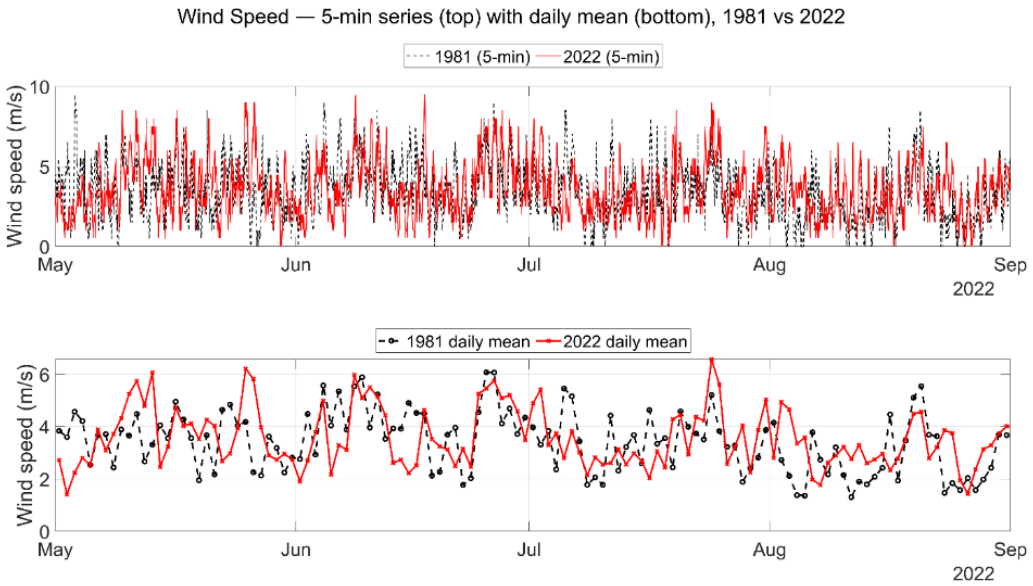

Figure 3.14: Wind speed 1981 vs 2022 [83].

Figure 3.14 shows the wind speed in 1981 and 2022. The patterns of 5-minute and average wind speeds between the two years remain similar. Nonetheless, it can be seen that the wind speed can be zero (or low) at any time. As wind speed is one of the main drivers in cooling the OHL, risks in operating at these low wind speeds are evaluated later in the thermal response.

Figure 3.15 shows the solar irradiance in 1981 vs 2022. It can be seen that the daily energy received from the sun in Wh/m^2 in 2022 is around 20% higher than 1981. An inference can be made that high solar irradiance must be present, especially when discussing heatwave events in the hottest year. Assuming it at zero W/m^2 would not be conservative.

Based on these ambient conditions, an example of Zebra OHL conductor temperature at 50 °C limit (with ambient design conditions 20 °C AAT, 0.5 m/s WS, 12 ° AA, and 0 W/m^2) under normal continuous pre-fault constant loading conditions is shown in Figure 3.16 below. It can be seen clearly that the conductor temperature in 2022 present weather conditions, is around 20% higher than the 1981. The exceedances of conductor temperature events are four times higher, and the risks of operating it at current levels must be reassessed in compliance with operating standards. This will be discussed in further detail later in the exceedance ratings.

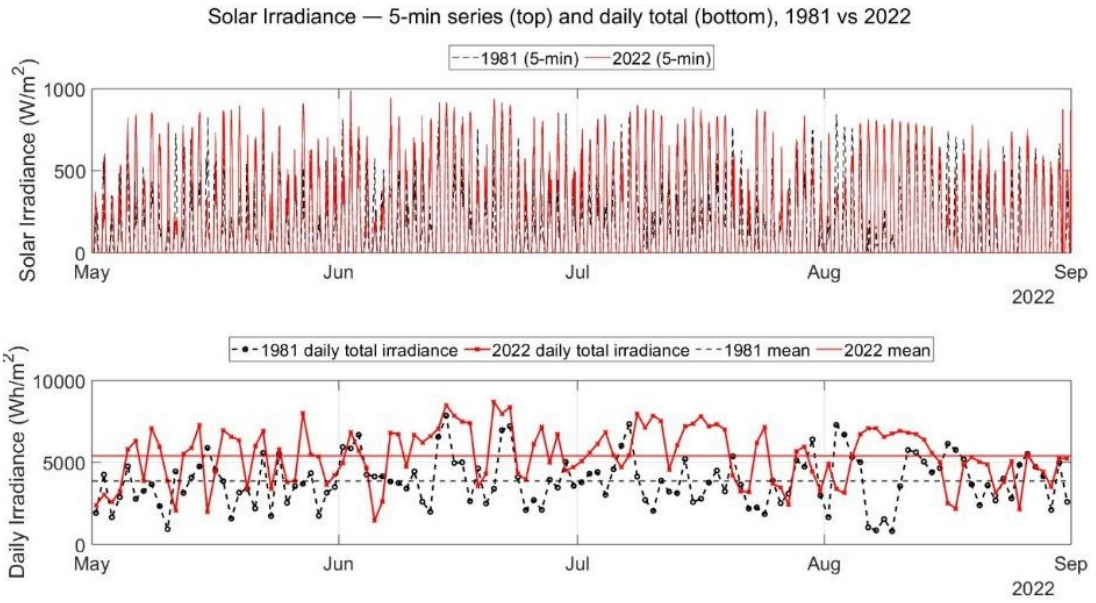

Figure 3.15: Solar Irradiance 1981 vs 2022 [83].

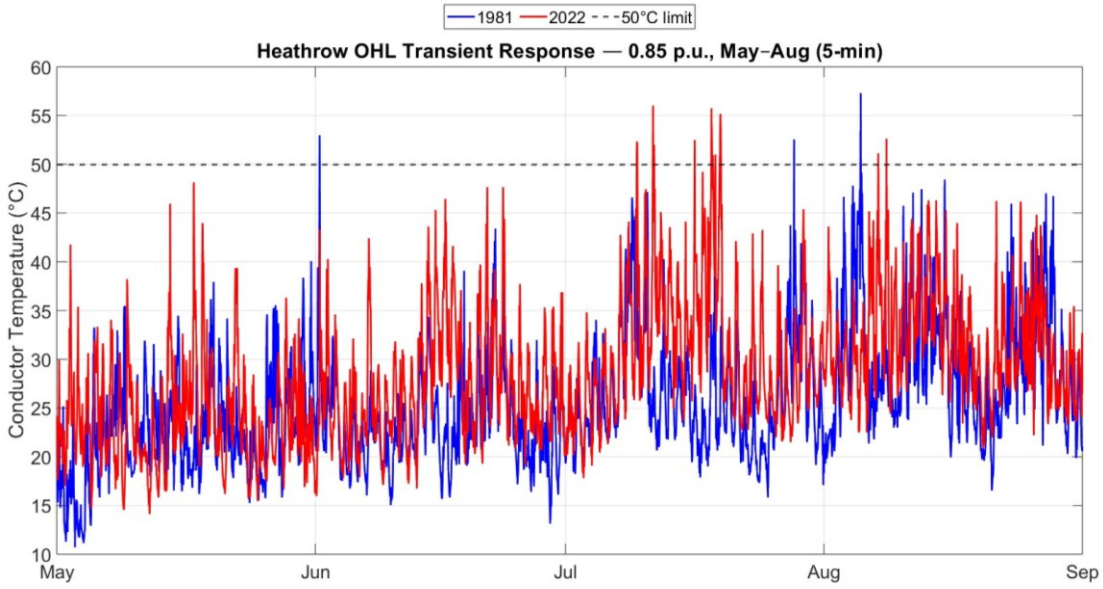

Figure 3.16: Pre-fault Zebra transient thermal response at 50 °C conductor limit.

Additionally, Figure 3.17 shows the ambient conditions of air temperature, soil temperature, wind speed, and solar irradiance during the heatwave in 2022. The air temperature approached 40 °C during the heatwave day, where the example of Zebra OHL would have only 10°C of headroom to operate, considering its 50 °C conductor

temperature limit. Nonetheless, it can be seen that the wind speed is around 7 m/s when the highest temperature is recorded. It can be seen that the tendency of wind speed to follow the shape of air temperature is clear. Further analysis needs to be undertaken for all available sites across the UK to validate the presence of heatwaves and their corresponding wind speed. This should be done in future works to confirm if the assumption of low wind speed occurrence during heatwave events is too conservative or not.

Figure 3.18 shows the heatwave conditions in 1981 at Heathrow. The air temperature reaches around 28°C with a much lower wind speed at around 1 m/s. It can be seen that the wind speed is much lower for the heatwave in 1981 compared to 2022. The peak solar irradiance in both 1981 and 2022 differs by around 10%, albeit solar irradiance with a lesser effect on OHL heating.

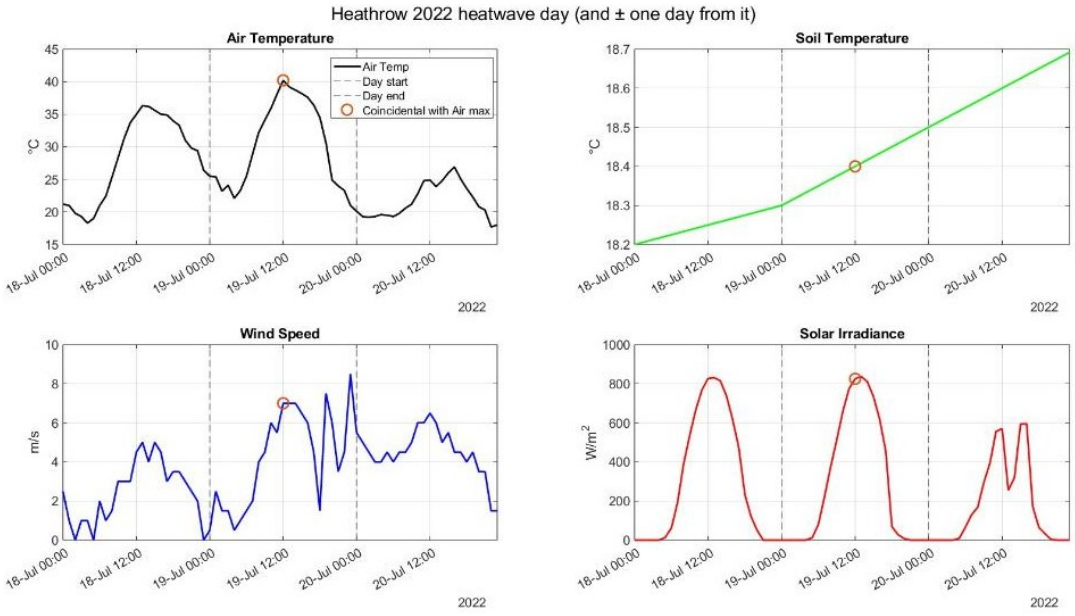

Figure 3.17: 2022 Heatwave ambient conditions in Heathrow.

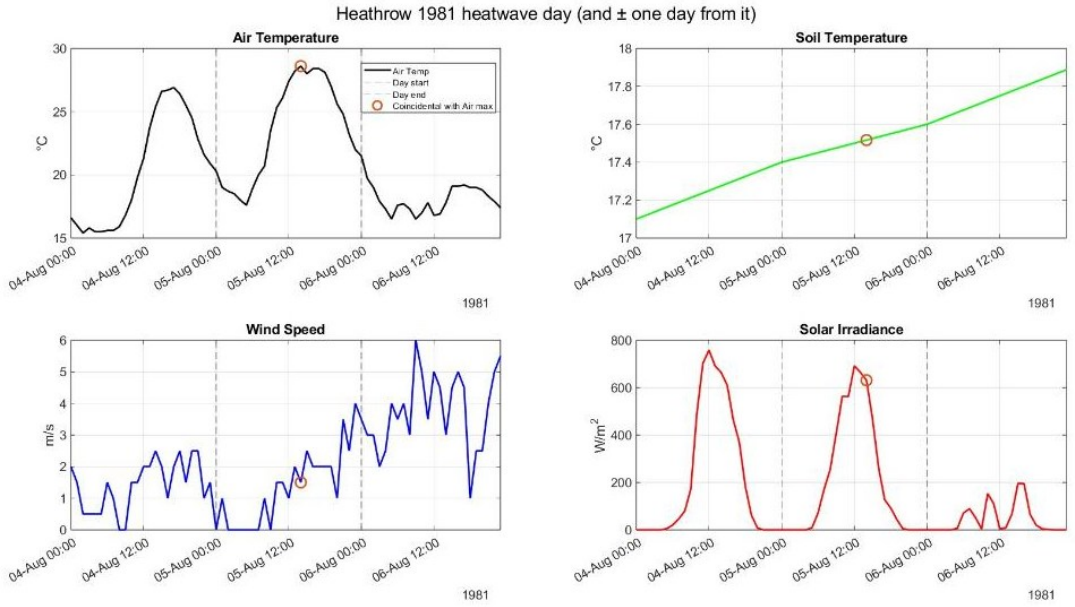

Figure 3.18: 1981 Heatwave ambient conditions in Heathrow.

3.3 Loading Profiles for Thermal Modelling and Rating of Components

Two types of loading profiles are used in this report. The first is a constant loading profile, applied at several loading levels (1.0 PU, 0.85 PU, 0.75 PU, and 0.65 PU) to study steady-state behaviour under fixed loading. The second is a cyclic loading profile, represents a realistic daily load cycle with peak and off-peak periods, allowing assessment of CTR and thermal recovery between load peaks.

3.3.1 Constant Loading Profile

To understand the conductor's thermal behaviour, the load is expressed throughout this report as a per-unit (PU) fraction of the STR current. Four loading levels are studied: 1.0 PU, 0.85 PU, 0.75 PU, and 0.65 PU, which correspond to:

- 1.0 PU: Post-fault CCC, representing maximum permissible current during contingency or emergency operation.
- 0.85 PU: Normal pre-fault current rating with a 20% margin reserved for emergencies.

- 0.75 PU and 0.65 PU: Cases with larger reserved margins, equivalent to using about one-quarter or one-half of the pre-fault CCC as reserve, respectively.

3.3.2 Cyclic Loading Profile

The cyclic loading profile used in this thesis is the standard loading profile given in TGN 303 [14], shown in Figure 3.19. The standard cyclic loading profile consists of a 6-hour peak loading period and an 18-hour 0.6PU low loading period. At this stage, only the standard cyclic loading profile is used to assess the CTR of the components.

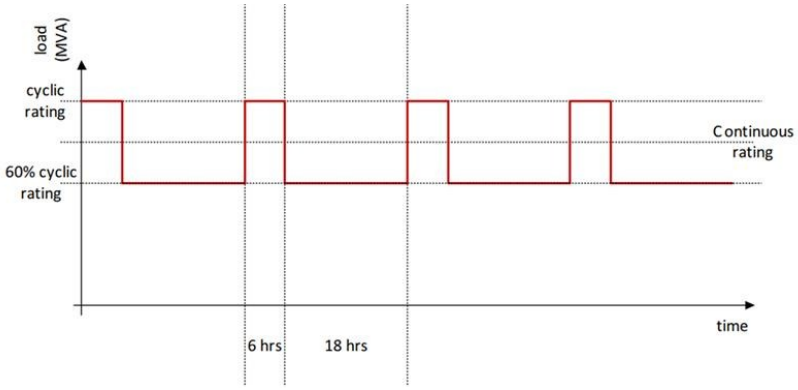

Figure 3.19: Standard cyclic loading profile, amended from [14].

3.3.3 Ongoing and Future Changes in Loading Profiles

It is worth noting that, based on other available data, a revised cyclic loading profile different from the standard loading profile can also be used. A set of national transmission system demand data from [82] is shown in Figure 3.20. This figure provides the demand in the transmission system in the whole UK by measurement and some estimation.

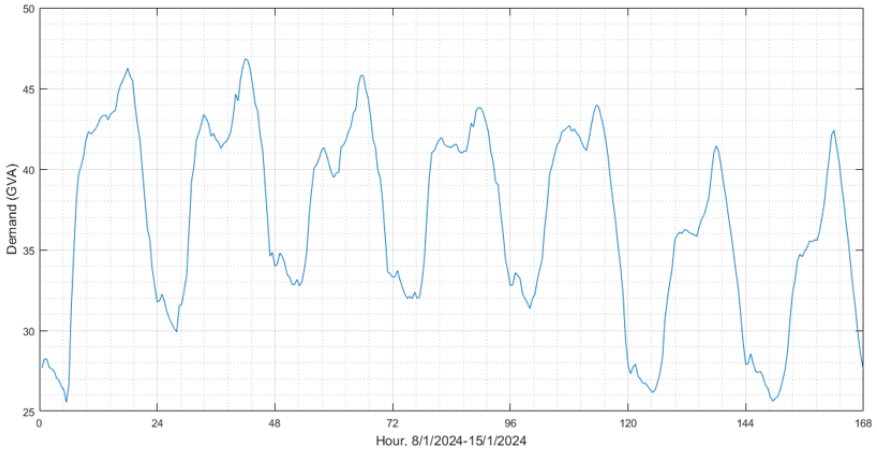

Figure 3.20: Transmission demand profile from ELEXON [84].

A better representation of the daily demand profile from measurement in MVA to the normalised value in PU to the daily maximum demand of a natural day is shown in Figure 3.21.

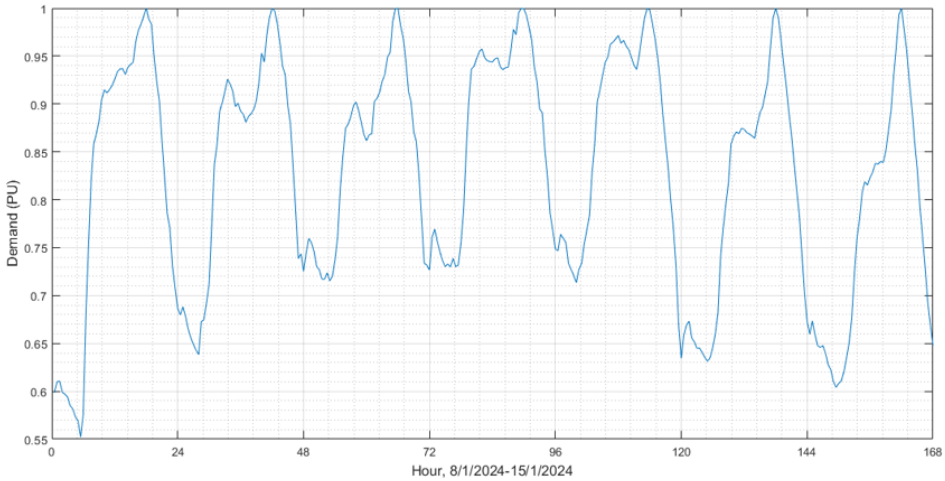

Figure 3.21: Transmission demand profile normalised by daily maximum demand.

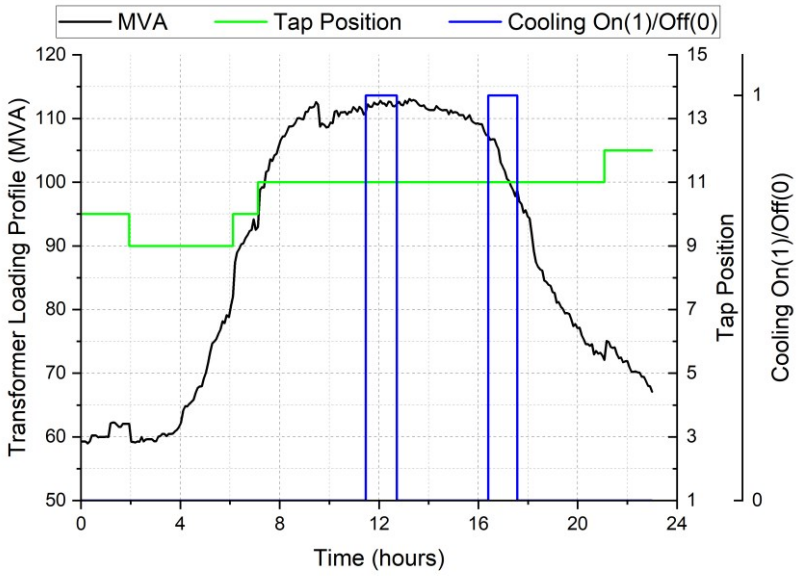

Figure 3.22: Measured power transformer loading profile, with the tap position and cooling status marked.

A measurement of the loading profile of a power transformer operating dual cooling mode (ONAN/OFAF) is shown in Figure 3.22, in which the tap position and cooling status are recorded. The tap position is used to control the output voltage to meet

the network requirement. From the results of both examples of transmission demand profile and loading profile on a power transformer, it can be seen that:

1. When considering 0.95PU to be the same as 1PU peak demand, the duration of daily peak demand increases from 6 hours under the standard loading profile assumption to around 12 hours.
2. The low-demand period can be increased to 0.75PU of the peak, rather than 0.6PU in the standard loading profile assumption.

Such findings indicate that, for various reasons, including demand-side management and the increasing penetration of electric vehicles, the 6-hour peak and 18-hour 0.6PU demand standards may not hold in the following year. However, due to the time limit, the change in the cyclic loading profile used is still the cyclic loading profile by the standard assumption in this work. The impact of the change in the cyclic loading profile from the standard assumption should be investigated in the future.

3.4 Conclusions

To calculate the individual component rating and the joint circuit rating, it is crucial to understand how the rating of each component behaves under its own ambient and loading conditions. Once the independent thermal response of each asset is characterised, the joint circuit rating can be assessed based on the combined thermal behaviour of the OHL–cable–transformer configuration operating as a single system. The ambient conditions summarised in Table 3.3 were therefore defined and applied as the reference conditions for this thesis, representing typical and extreme summer scenarios for all key parameters, including air and soil temperature, wind speed, attacking angle, solar irradiance, and soil thermal resistivity.

This chapter has outlined the ambient conditions used to obtain and process meteorological and loading data that serve as the boundary inputs to the thermal models developed in subsequent analyses. The classification of thermal rating types, static, dynamic, cyclic, short-term and medium-term overloading, and exceedance ratings, has established the operational contexts in which these data are applied. A detailed examination of ambient variables highlighted the significant influence of meteorological

factors, particularly air temperature, wind speed, and solar irradiance, on the available thermal capacity of OHLs and exposed equipment, while soil temperature and resistivity are critical for accurately evaluating underground and trough-installed cables.

Furthermore, representative loading profiles were developed to capture both steady and cyclic operating patterns, enabling the assessment of thermal ratings under realistic and stress-inducing conditions such as heatwaves. These profiles also provide a consistent basis for comparing historical, current, and potential future operating conditions.

Overall, this chapter establishes a consistent and physically representative set of environmental and operational inputs required for reliable calculation of both individual component ratings and joint circuit ratings. These datasets form the foundation for the thermal modelling and exceedance analyses presented in the following chapters, where the interaction between components and the influence of varying ambient conditions on thermal performance are explored in greater depth.

Table 3.3: Input Static Ambient Conditions using Summer Assumptions for the Joint Rating of the Components used for the Following Assessments.

Ambient condition	**Value**
Air temperature (OHL, exposed cable, transformer) [°C]	-30 to 50
1m soil temperature (DBC) [°C]	2.1 to 26.1
0.3m soil (FTC) [°C]	-0.5 to 31
Wind speed [m/s]	0.5 and 1, if unspecified
Attacking angle [degree]	12 for OHL, 90 for ExpoC, if unspecified
Solar irradiance $[W/m^2]$	0 (no SI), 500 (medium SI) and 1000 (high SI)
Soil resistivity $[K \cdot m/W]$	1.2 if unspecified

Chapter 4

Oil-Immersed Power Transformers

Power transformers, being essential and critical components of electrical networks, have garnered particular attention due to their susceptibility to thermal stresses under varying climatic and operational conditions [1], [2], [13]. Climate change directly impacts transformer performance through ambient conditions such as ambient air temperature (AAT), wind speed (WS), and solar irradiance (SI), while indirectly affecting transformers by increasing electricity demand due to widespread electrification of transportation and intensified usage of cooling and heating equipment [17], [85].

As discussed in Section 2.1.1, thermal ratings of transformers are fundamentally determined by their hottest-spot temperature (HST), a key indicator of insulation degradation and operational limits of transformer windings [1], [2], [13]. Accurate thermal modelling thus becomes crucial for assessing transformer capacity, managing long-term insulation life, and better thermal management. Standards IEEE [1] and IEC [2] thermal models provide foundational frameworks for such analyses, but often overlook or inadequately represent dynamic operational and environmental factors critical for precise thermal evaluation in contemporary contexts.

While previous works [17], [21]-[24] have incrementally improved oil-immersed power transformer thermal modelling by incorporating WS, SI, non-linear oil resistance, and multi-stage heat transfer, they generally remain limited in two respects: (i) they do not fully represent the interaction between environmental conditions and operational control actions (such as OLTC tap operations or active cooling mode transitions), and (ii) they lack practical methods for estimating key thermal parameters (e.g., tap-position-dependent losses, effective radiator areas) when measurements are unavailable. The present paper addresses these gaps by considering weather conditions, such as ambient AT, WS, and SI, along with operational factors, including variable

supplied voltage, power loading conditions, and real-time adjustments from operational controls like the OLTC and active cooling transitions (e.g., switching from ONAN to OFAF modes).

The main contributions of this chapter are:

- Develop a comprehensive methodology for calculating and estimating key thermal modelling parameters, extending applicability across a wide range of ambient conditions and operational scenarios.
- Enhance heat input calculations by explicitly incorporating real-time dependencies, including the effect of supply voltage on no-load losses and temperature-dependent variation of load losses.
- Refine the thermal capacitance representation to accurately capture dynamic cooling-mode transitions (e.g., ONAN to OFAF or vice versa) and model the distinct thermal inertia of windings and hot-spot regions.
- Introduce a robust estimation approach to represent the full tap-position dependency of load losses, eliminating the need for direct measurement data while maintaining accuracy.

The methodology of thermal rating of power transformers is followed by thermal modelling. As discussed in Section 3.1, DTR, S/MTOR, and CTR are present. Transformers do not have STR but NTR, as specified. Also, the maximum emergency temperature limit of the transformer cannot be violated/exceeded, so transformers do not have an exceedance level rating.

4.1 Methodology of Thermal Modelling for Oil-Filled Power Transformers

The model represents the transformer as two rigid parallelepipeds joined by top and bottom-mounted pipes: the main tank, which houses the active parts, and the cooler (radiator). Oil heated in the centrally located winding-core assembly rises through the windings, enters the upper pipe, descends through the cooler, and returns via the lower pipe; this loop can operate in natural, directed, or forced-flow mode. Electrically, the unit is treated as a step-down transformer energised on its high-voltage primary, with

the low-voltage secondary delivering current and voltage at the rated ratio; the full set of electrical losses is represented by heat sources located in the windings.

Thermally, temperature increases from the bottom to the top of the windings, with the maximum at the hot-spot of one phase; a balanced three-phase load is assumed. Therefore, any hot-spot migration caused by unbalance is not considered in this work.

Heat follows a four-stage path: it is generated in the coil and core, and into the top-oil by oil convection. Then conducted through the tank and cooler walls, and finally dissipated to the surroundings by air convection and radiation. Top-oil temperature measured inside the tank can be misleading because of incomplete mixing, so the reference value is taken at the cooler header or top pipe, where mixing is complete. Because the tank and cooler can be exposed to different environments, an enclosed tank versus an outdoor cooler model allows each surface its own ambient air temperature, solar gain, and wind speed, with the cooler's ambient taken as the reference for calculations. Figure 4.1 shows an example of a fully enclosed transformer.

Figure 4.2 expands the transformer thermal circuit into a network with multiple heat sources, resistances, and thermal masses. Four heat inputs act on the winding region: losses from load currents in the HV and LV windings $q_{in,load,HV\&LV}$, the no-load losses $q_{in,no-load}$, loss generated in a tertiary winding $q_{in,TV}$, and auxiliary losses $q_{in,Auxilliary}$ such as cooling-fan drives. In addition, solar radiation contributes to two external heat sources $q_{in,solar,tank}$ and $q_{in,solar,cooler}$, one striking the tank and the other the cooler [1], [2], [17], [23].

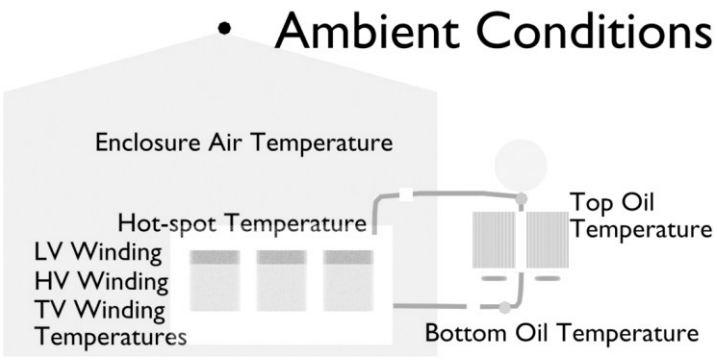

Figure 4.1: Representation of the physical model: Partly enclosed (tank) and partly exposed (cooler) transformer.

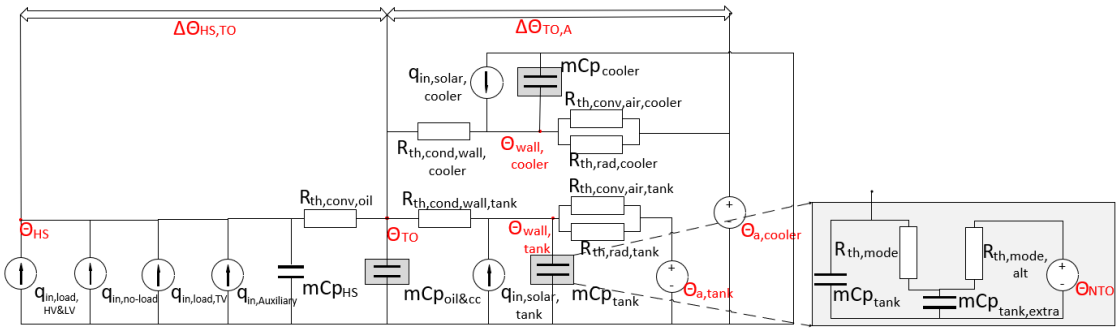

Figure 4.2: Thermal network diagram of the transformer thermal model.

Heat resistances are represented by seven lumped thermal resistances. Air-side convection has separate resistances for the tank, $R_{th,conv,air,tank}$ and for the cooler, $R_{th,conv,air,cooler}$, and each of those surfaces also presents its radiation resistance, $R_{th,rad,tank}$ and $R_{th,rad,cooler}$. Conduction through the steel walls is likewise split between the tank, $R_{th,cond,tank}$ and cooler, $R_{th,cond,cooler}$. Inside the oil circuit, a single convection resistance, $R_{th,conv,oil}$ links the winding oil channel to the bulk top-oil [17], [21]-[23].

Four thermal capacities are considered: the winding hot-spot, mCp_{HS}, the remaining oil-coil-core volume, $mCp_{oil\&cc}$, the tank shell, mCp_{tank}, and the cooler assembly, mCp_{cooler}. Correspondingly, the model has four key temperatures: the hot-spot, θ_{HS}, the top-oil θ_{TO}, the outer wall of the tank, $\theta_{wall,tank}$, and the outer wall of the cooler, $\theta_{wall,cooler}$. Because the tank and cooler can face different environments, distinct ambient temperatures are assigned to the tank enclosure, $\theta_{a,tank}$ and to the cooler's outdoor location, $\theta_{a,cooler}$, allowing the model to resolve spatially varying heat exchange while still using a compact thermal network.

4.1.1 Calculation of Thermal Resistances

Four main types of thermal resistances: air convection, radiation, conduction and oil convection are present in the following sections, without specification, the temperatures in this section's equations are all in $Kelvin$:

4.1.1.1 Calculation of Thermal Resistance of Air Convection

Under the ONAN cooling mode, the thermal resistance of air convection for the transformer tank or cooler is shown in Figure 4.2. The transformer tank and cooler are denoted as $object$ unless specified otherwise; transformer ONAN and OFAF cooling modes are denoted as $mode$ unless specified otherwise; $R_{th,conv,air,object}$ is calculated by:

$$R_{th,conv,air,object} = \frac{1}{C_{mode} \cdot A_{conv,object} \cdot h_{conv,air,object}} \tag{147}$$

where: C_{mode} is a dimensionless factor that represents the efficiency due to the inhomogeneous temperature distribution for the radiation, convection and conduction (RCC) heat transfer process of the transformer under ONAN or OFAF cooling mode, which is the solution for the inhomogeneous surface temperature distribution of the transformer introduced in this paper, and it will be discussed in section 4.1.3; $A_{conv,object}$ is the total area for convective cooling of the respective object in m^2; $h_{conv,air,object}$ is the heat transfer coefficient of the air convection of the transformer tank or cooler in $W/(m^2 \cdot K)$. The calculation of the heat transfer coefficient of the air convection can be found in [17], [22], [23]:

$$h_{conv,air,object} = ({h_{F,air,object}}^{3.2} + {h_{N,air,object}}^{3.2})^{\frac{1}{3.2}} \tag{148}$$

$$h_{F,air,object} = \lambda_{air,object} \cdot Nu_{F,air}/L_{F,air,object} \tag{149}$$

$$Nu_{F,air,object} = {Pr_{air,object}}^{1/3} \cdot {Re_{L,air,object}}^{1/2} \tag{150}$$

$$Pr_{air,object} = \frac{V_{wind,comb,object} \cdot L_{F,air,object} \cdot \rho_{air,object}}{\mu_{air,object}} \tag{151}$$

$$Re_{L,air,object} = \frac{\mu_{air,object}}{\alpha_{air,object} \cdot \rho_{air,object}} \tag{152}$$

$$\alpha_{air,object} = \frac{\mu_{air,object}}{\alpha_{air,object} \cdot \rho_{air,object}} \tag{153}$$

$$h_{N,air,object} = \frac{\lambda_{air,object} \cdot Nu_{N,air,object}}{L_{N,air,object}} \tag{154}$$

$$\lambda_{air,object} = 0.02424 + (7.477 \cdot 10^{-5}) \cdot (\theta_{air,object} - 273.15) - (4.407 \cdot 10^{-9}) \cdot (\theta_{air,object} - 273.15)^2 \tag{155}$$

$$Nu_{N,air,object} = {Ra_{L,air,object}}^{1/4} \tag{156}$$

$$Ra_{L,air,object} = \frac{g \cdot \beta_{air,object} \cdot c_{air,object} \cdot {\rho_{air,object}}^2 \cdot (\theta_{TO} - \theta_{air,object})}{\mu_{air,object} \cdot \lambda_{air,object}} \cdot {L_{N,air,object}}^3 \tag{157}$$

$$\beta_{air,object} = 0.004 - 1.3 \cdot 10^{-5} \cdot (\theta_{air,object} - 273.15) \tag{158}$$

$$\mu_{air,object} = v_{air,object} \cdot \rho_{air,object} \tag{159}$$

$$v_{air,object} = (0.0001 \cdot (\theta_{air,object} - 273.15)^2 + 0.08681 \cdot (\theta_{air,object} - 273.15) + 13.38) \cdot 10^{-6} \tag{160}$$

$$\rho_{air,object} = 1.094 \cdot 10^{-5} \cdot (\theta_{air,object} - 273.15)^2 - 0.004 \cdot (\theta_{air,object} - 273.15) + 1.278 \tag{161}$$

$$c_{air,object} = 4.12 \cdot 10^{-4} \cdot (\theta_{air,object} - 273.15)^2 - 0.02 \cdot (\theta_{air,object} - 273.15) + 1006 \tag{162}$$

where: $Nu_{F,air,object}$ is the Nusselt number of the forced convection of air; $Pr_{air,object}$ is the Prandtl number of the forced convection of air; $V_{w,object}$ is the wind speed in m/s; $\alpha_{air,object}$ is the thermal diffusivity of air in m^2/s; $\lambda_{air,object}$ is the thermal conductivity of air in $W/(m \cdot K)$; $Nu_{N,air,object}$ and $Ra_{L,air,object}$ are the Nusselt number and Rayleigh number of natural convection of air, respectively; $\beta_{air,object}$ is the thermal

expansion coefficient of air in $1/K$; $\mu_{air,object}$ is the dynamic viscosity of the air in $kg/(m \cdot s)$; $v_{air,object}$ is the kinetic viscosity of the air in m^2/s; $\rho_{air,object}$ is the density of the air in kg/m^3; $c_{air,object}$ is the specific heat of the air in $W \cdot s/(kg \cdot K)$; $L_{N,air,object}$ and $L_{F,air,object}$ are the characteristic lengths of natural and forced convection of air in m. As a conclusion, it is calculated by a function of:

$$h_{conv,air,object} = f(\theta_{a,object}, \theta_{wall,object}, L_{N,air,object}, L_{F,wind,object}, L_{F,fan,object}, V_{wind,AF}, V_{wind}) \quad (163)$$

where: $L_{N,air,object}$, $L_{F,wind,object}$ and $L_{F,fan,object}$ are characteristic length of natural air convection, forced air convection from (natural) wind and forced air convection from the cooling fan in m, respectively; $V_{wind,AF}$ and V_{wind} are the wind speeds from the cooling fan and from natural wind in m/s, respectively.

The total wind speed generated by the cooling fans $V_{wind,AF}$ is calculated by:

$$V_{wind,AF} = \frac{Vol_{AF,air}}{0.5 \cdot (W_{cooler} \cdot L_{cooler})} \quad (164)$$

where: $Vol_{AF,air}$ is the total air quantity displaced by the cooling fan in m^3/s. The wind speed generated by the cooling fans is calculated as the displacement air volume of all cooling fans divided by the available area for airflow, i.e., the overall volume of the cooling plant is not fully occupied by the cooling plates. It is assumed that the cooling plate occupies 50% of the overall volume of the cooling plant. The height of the cooling plate equals the cooling plant, so it takes up 50% of the area projected from below, leaving 50% for the air tunnel.

For the transformer cooler in OFAF cooling mode, the forced-convection characteristic length is taken to be the wind generated by the cooling fan. $L_{AF,wind,cooler}$. One limitation of this model is the difficulty in distinguishing the characteristic length of forced air convection when the transformer cooler is affected by both natural wind and cooling fan wind, due to limited measurements. Natural wind is usually considered horizontal, while wind from cooling fans is vertical, flowing from the bottom to the top

of the cooler. As the two flows of wind are perpendicular to each other, thus, the combined wind speed $V_{wind,comb}$ under such circumstances, it is calculated by:

$$V_{wind,comb} = \sqrt{{V_{wind,AF}}^2 + {V_{wind}}^2} \tag{165}$$

Note that (165) is based on an assumption and it has not been verified yet.

4.1.1.2 Calculation of Thermal Resistance of Radiation

The thermal radiation resistance indicates how effectively the transformer wall surface radiates heat, affecting the ambient temperature difference between the wall surface and the ambient. It is calculated by:

$$R_{th,rad,object} = \frac{1}{\sigma \cdot \varepsilon \cdot C_{mode} \cdot A_{rad,object}\left({\theta_{wall,object}}^2 + {\theta_{a,object}}^2\right)} \cdot \frac{1}{(\theta_{wall,object} + \theta_{a,object})} \tag{166}$$

where: $A_{rad,object}$ is the total area for radiative cooling in m^2; σ is the Stefan-Boltzmann constant; ε is the emissivity factor of the transformer tank, which has a value of 0.9, suggested by [17].

4.1.1.3 Calculation of Thermal Resistance of Conduction

Heat conduction is added to separate the thermal capacitance of the transformer tank and cooler from that of the oil. So, the effect of solar irradiance will not be affected by the thermal capacitance of oil, resulting in a more accurate result. Figure 4.3 shows the heat conduction at the transformer wall considered in this model.

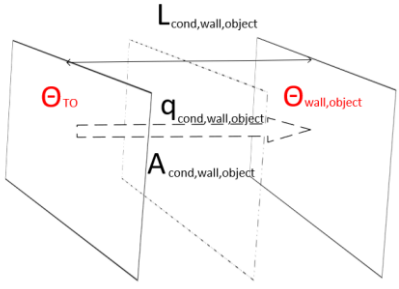

Figure 4.3: Example of the thermal conduction process from the top-oil to the outer wall surface of the transformer.

The thermal resistance of conduction for the transformer shows how effective the heat transfer via conduction from the inner side of the transformer wall to the outer side of the transformer, for a given temperature difference, calculated by:

$$R_{cond,wall,object} = \frac{L_{cond,object}}{C_{mode} \cdot A_{cond,object} \cdot \lambda_{wall,object}(\theta_{wall,object})} \quad (167)$$

where: $L_{cond,object}$ is the characteristic length of heat conduction of the respective object in m, equal to the thickness of the transformer wall or the thickness of the radiator; $\lambda_{wall,object}(\theta_{wall,object})$ is the thermal conductivity of the material used in the transformer wall at the temperature $\theta_{wall,object}$ in $W/(m \cdot K)$; $A_{cond,object}$ is the effective area of heat conduction in m^2 can be estimated as the same as the effective area of air convection of the respective object:

$$A_{cond,object} = A_{conv,object} \quad (168)$$

4.1.1.4 Calculation of Thermal Resistance of Oil Convection

The heat transfer coefficient of the convection of oil is considered pure natural convection under ONAN cooling mode, and pure forced convection under OFAF cooling mode, i.e., mixed convection of oil is not considered under OFAF cooling mode. It is calculated by:

$$R_{th,conv,oil} = \frac{(L/A)_{oil,mode}}{k_{oil} \cdot Nu_{oil,mode}} \quad (169)$$

where: $(L/A)_{oil,mode}$ is the characteristic length over the effective cooling area of the transformer oil convection under the respective cooling mode in m^{-1}; $Nu_{oil,mode}$ is the Nusselt number of the oil convection under the cooling mode in question; k_{oil} is the thermal conductivity of oil in $W/(m \cdot K)$. The calculation Nusselt number and thermal conductivity of oil can be found in [1], [17], [22], [23], given by:

$$\lambda_{oil} = 0.124 + 1.424 \cdot 10^{-4} \cdot (\theta_{TO} - 273.15) \quad (170)$$

$$Nu_{N,oil} = {Ra_{L,oil}}^{1/4} \tag{171}$$

$$Ra_{L,oil} = \frac{g \cdot \beta_{oil} \cdot c_{oil} \cdot {\rho_{oil}}^2 \cdot \Delta\theta_w}{\mu_{oil} \cdot \lambda_{oil}} \cdot {L_{oil}}^3 \tag{172}$$

$$\Delta\theta_w = \frac{\Delta\theta_{HS,TO,r}}{H} \cdot I_{pu}(tap)^{2m_{ex}} \tag{173}$$

$$\beta_{oil} = 8.6 \cdot 10^{-4} \tag{174}$$

$$\mu_{oil} = v_{oil} \cdot \rho_{oil} \tag{175}$$

$$v_{oil} = (\exp\left(\exp(24.736) \cdot {\theta_{TO}}^{-4.163}\right) - 0.7) \cdot 10^{-6} \tag{176}$$

$$\rho_{oil} = 887 - 0.659 \cdot (\theta_{TO} - 273.15) \tag{177}$$

$$c_{oil} = 1960 + 4.005 \cdot (\theta_{TO} - 273.15) \tag{178}$$

where: $\Delta\theta_w$ and $\Delta\theta_{HS,TO,r}$ are the winding temperature gradient and the rated hot-spot temperature rise over top-oil in K; H is the hot-spot factor; $I_{pu}(tap)$ is the current loading in per-unit to rated current at the current tap position; m_{ex} is the winding exponent; L_{oil} is the characteristic length of convection of top-oil in m; h_{oil} is the heat transfer coefficient of natural convection of oil in $W/(m^2 \cdot K)$; λ_{oil} is the thermal conductivity of oil in $W/(m \cdot K)$; $Nu_{N,oil}$ and $Ra_{L,oil}$ are the Nusselt number and Rayleigh number of natural convection of oil, respectively; β_{oil} is the thermal expansion coefficient of oil in $1/K$; μ_{oil} is the dynamic viscosity of the oil in $kg/(m \cdot s)$; v_{oil} is the kinetic viscosity of the oil in m^2/s; ρ_{oil} is the density of the oil in kg/m^3; c_{oil} is the specific heat of oil in $W \cdot s/(kg \cdot K)$.

4.1.2 Calculation of Other Thermal Parameters

The calculation of thermal characteristic parameters is derived from the physical model of the transformer, along with measurements and assumptions, as presented in the following.

4.1.2.1 Thermal Parameters of Transformer Tank

The surface area of the transformer tank in contact with air $A_{conv,tank}$ is considered as the surface area of the transformer tank except for the bottom, calculated by:

$$A_{conv,tank} = 2 \cdot L_{tank} \cdot H_{tank} + 2 \cdot W_{tank} \cdot H_{tank} + L_{tank} \cdot W_{tank} \quad (179)$$

where: L_{tank}, W_{tank} and H_{tank} are the length, width and height of the transformer tank in m, respectively.

The characteristic length of the transformer tank $L_{c,tank}$ is calculated by the volume and the surface area of the overall transformer tank, considering a parallelepiped object:

$$L_{c,tank} = \frac{L_{tank} \cdot W_{tank} \cdot H_{tank}}{2 \cdot (L_{tank}W_{tank} + L_{tank}H_{tank} + W_{tank}H_{tank})} \quad (180)$$

The characteristic length of the natural convection of the transformer tank $L_{N,air,tank}$ is the same as the characteristic length of the transformer tank and the characteristic length of forced air convection $L_{F,air,tank}$ is determined by the smaller value of the total length and the width of the transformer tank [86], [87]:

$$L_{N,air,tank} = L_{c,tank} \quad (181)$$

$$L_{F,air,tank} = \min (L_{tank}, W_{tank}) \quad (182)$$

The effective projected area for the solar irradiance of the transformer tank $A_{solar,tank}$ is calculated by the maximum projected area of a parallelepiped object, so it is conservative:

$$A_{solar,tank} = ((L_{tank} \cdot W_{tank}) + (L_{tank} \cdot H_{tank}) + (W_{tank} \cdot H_{tank})) \cdot \sqrt{3}/3 \quad (183)$$

The surface area of the transformer tank can be used for radiative cooling $A_{rad,tank}$ is also considered as the surface area of the transformer tank, except for the surface area of the bottom of the transformer, calculated by:

$$A_{rad,tank} = 2 \cdot L_{tank} \cdot H_{tank} + 2 \cdot W_{tank} \cdot H_{tank} + L_{tank} \cdot W_{tank} \quad (184)$$

4.1.2.2 Thermal Parameters of the Transformer Cooler

The surface area of the transformer cooler in contact with air $A_{conv,cooler}$ is considered the total surface area of all cooler plates, calculated by:

$$A_{conv,cooler} = Num_{plate} \cdot A_{plate} \quad (185)$$

where: Num_{plate} is the total number of the (active) cooling plates; A_{plate} is the surface area of each cooling plate in m^2.

The effective projected area for the solar irradiance of the transformer tank $A_{solar,cooler}$ follows (183) but uses the geometry data of the transformer cooler.

The character length of the natural convection of the cooler $L_{N,air,cooler}$ is calculated by the volume of the cooler and the total surface area of the cooler. The real occupied volume of the cooler is assumed to be half of the overall volume of the cooler:

$$L_{N,air,cooler} = \frac{L_{cooler} \cdot W_{cooler} \cdot H_{cooler}}{2 \cdot A_{cooler,conv}} \quad (186)$$

where: L_{cooler}, W_{cooler} and H_{cooler} are the overall length, width and height of the transformer cooler in m, respectively.

The character length of forced convection by the (naturally generated) wind of the transformer cooler $L_{F,wind,cooler}$ is also calculated by the smaller value of the overall length and the width of the transformer cooler:

$$L_{F,wind,cooler} = \min (L_{cooler}, W_{cooler}) \quad (187)$$

The characteristic length of forced convection by wind generated from the cooling fan of the transformer cooler $L_{F,fan,cooler}$ is determined by the height of the cooling plate:

$$L_{F,fan,cooler} = H_{cooler} \quad (188)$$

The surface area of the transformer cooler can be used for radiative cooling $A_{rad,cooler}$ is also considered the surface area of the transformer cooler when treated as a parallelepiped. Similar to the transformer tank, the surface area of the bottom of the cooler is ignored. Then, its internal surface area is also ignored because the radiative heat transfer on its internal surfaces does not transfer heat to the ambient. So, the surface area of the transformer cooler can be used for radiative cooling is calculated by:

$$A_{rad,cooler} = 2 \cdot L_{cooler} \cdot H_{cooler} + 2 \cdot W_{cooler} \cdot H_{cooler} + L_{cooler} \cdot W_{cooler} \quad (189)$$

4.1.3 Efficiency due to the Inhomogeneous Temperature Distribution for Natural Radiation, Convection and Conduction

For the standard models [1] and [2], the TOT is calculated from the AT added by TOTR. The mechanism of the TOTR is due to the heat flow from top-oil to the ambient and the total thermal resistance between top-oil and the ambient. As shown in Figure 4.2, the heat in the top-oil or oil as a whole can escape to the ambient via two routes: one is from top-oil to the surface of the transformer tank or cooler through thermal conduction and escape to the ambient via air convection, the other is through the same conduction and escape to the ambient via radiation. Both heat dissipation routes are present simultaneously, given a temperature difference between the top-oil and the ambient, for the three heat transfer effects: radiation, convection, and conduction. The areas considered by the respective processes are known, but the source temperature is given as TOT. Standard [2] shows that the outer wall temperature of the transformer decreases along the vertical axis, from the top of the transformer tank and cooler to the bottom. This suggests that when using the TOT as the higher temperature (with the ambient temperature as the lower), the ability to dissipate heat to the ambient will be overestimated. This can be translated to the effectiveness of the cooling areas considered in the thermal model decreases from top to bottom. A reduction in either the heat transfer coefficients of RCC or the cooling areas considered by RCC processes should be made.

Studies [88], [89] showed that the temperature decrease of the transformer along the vertical axis between the transformer tank surface temperature and the ambient is non-linear, contrary to the standard assumption. Study [90] demonstrated that the

temperature distribution across different cooler plates within the same cooler block also varies. Then, Study [89] reports the decrease in the heat transfer coefficient due to a decrease in the temperature difference. Furthermore, study [91] reveals that the cooling ability of the different cooler banks within the same cooler varies in the AN (33% difference) and AF (25% difference) modes. Therefore, without an extremely detailed and comprehensive measurement campaign of the temperature distribution on the transformer tank and cooler under different conditions, it is unlikely to model different cooler blocks and their cooler fins/plates individually.

Previous work [17] introduced empirical factors based on the geometry and flow regime, adjusted by the measured value of TOTR to the heat transfer coefficient of natural convection and forced convection from natural wind. These empirical factors ignored the fact that the inhomogeneous temperature distribution impacts the thermal resistance of convection. Furthermore, this inhomogeneous temperature distribution on the transformer surface also affects the thermal radiation resistance. The variation of the thermal resistance of radiation with the variation of temperature rise from wall to ambient when neglecting the efficiency due to the inhomogeneous temperature distribution (set to 1) under 20°C ambient temperature is shown in Figure 4.4. It can be seen that for the range of the temperature rise considered, a 10K less temperature range will increase the thermal resistance of radiation by around 1e-4 K/W.

From (147), (166) and (167), it can be seen that the variation of the thermal resistance between TOT and ambient only depends on the wall temperature (or wall temperature rise, as discussed above), efficiency due to inhomogeneous temperature distribution and heat transfer coefficient of convection, where the wall temperature is an intermediary result.

From (163), it can be seen that, for a given ambient condition, the variation in the heat transfer coefficient depends only on the wall temperature, since all other inputs are constants. The variation in the heat transfer coefficient of convection in ONAN and OFAF modes with the temperature rise from wall to ambient at a constant 20°C ambient temperature is shown in Figure 4.5. The respective thermal resistances when cooling

efficiency is neglected (set to 1) at an ambient temperature of 20°C are shown in Figure 4.6.

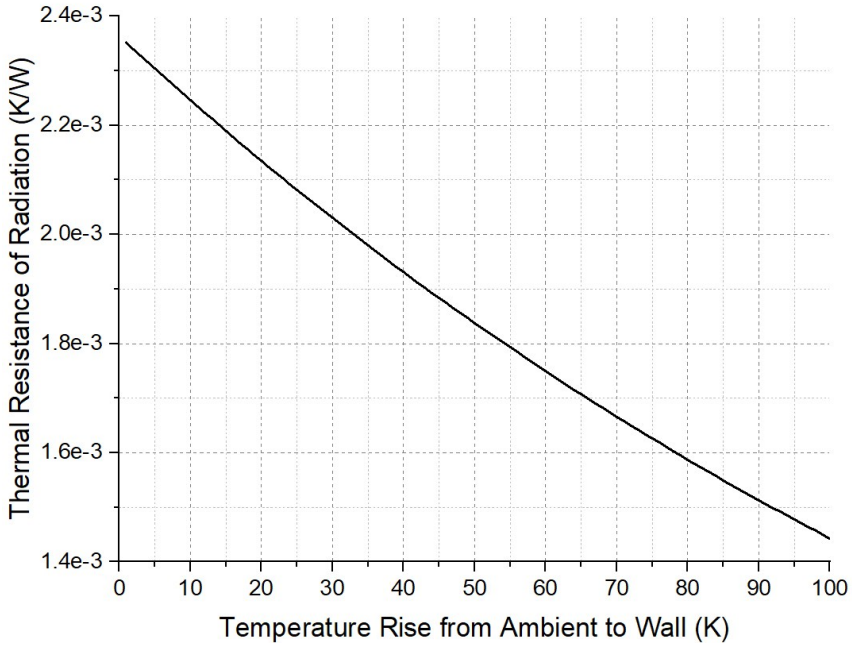

Figure 4.4: The variation of the thermal resistance of radiation for the cooler with the variation of temperature rise from the wall to the ambient.

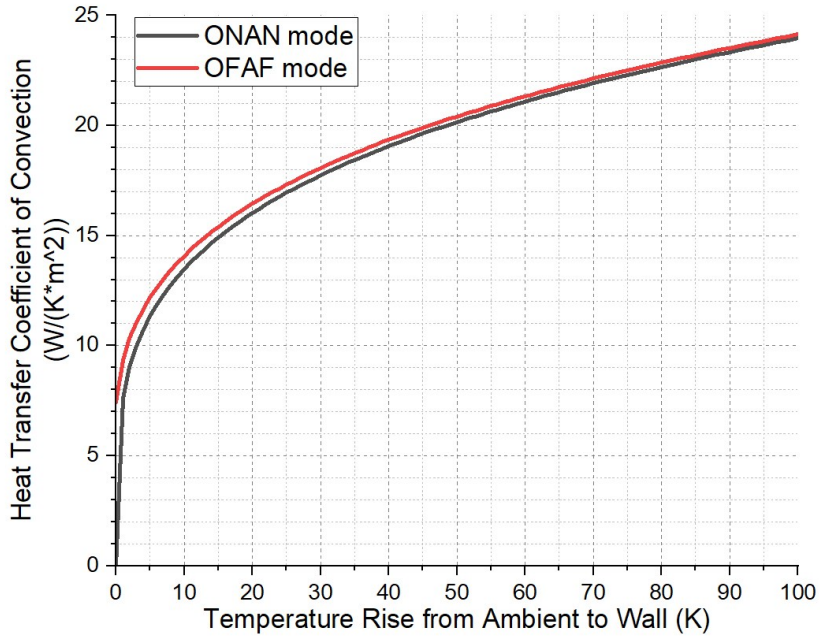

Figure 4.5: The variation of the heat transfer coefficient of convection on ONAN and OFAF modes with the variation of temperature rise from wall to ambient.

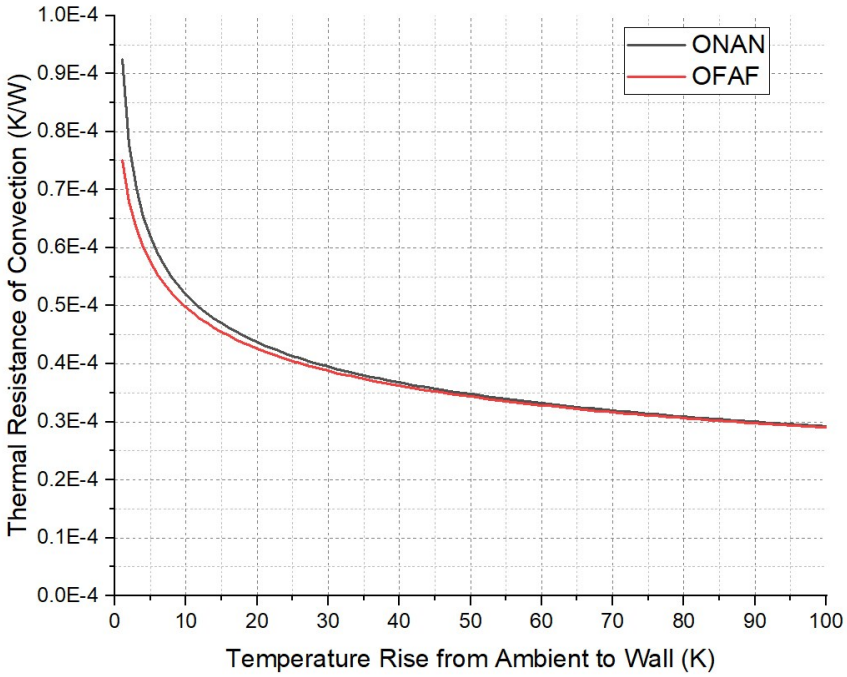

Figure 4.6: The variation of the thermal resistance of convection for the cooler on ONAN and OFAF modes with the variation of temperature rise from wall to ambient.

From the results, it can be seen that the heat transfer coefficient is higher in OFAF mode than in ONAN mode, and the thermal resistance is consistently lower in OFAF mode. However, the difference decreases as the temperature rise increases. Then, within the range of temperature rise from wall to ambient close to the guaranteed TOTR value, i.e., 60K, the heat transfer coefficient and the convection thermal resistance are highly non-linear.

The thermal resistance of conduction is extremely small (1E-6 K/W at 20°C) and will decrease as the temperature increases. At OFAF-rated losses, it contributes to less than 1K of temperature rise and is only present for mathematical purposes.

When neglecting the efficiency due to the inhomogeneous temperature distribution (set to 1), all the cooling areas are considered as a thermal body with a homogeneous temperature distribution. The result of TOTR under ONAN and OFAF cooling mode at respective rated conditions is shown in Figure 4.7, denoted as $if\ homogeneous$.

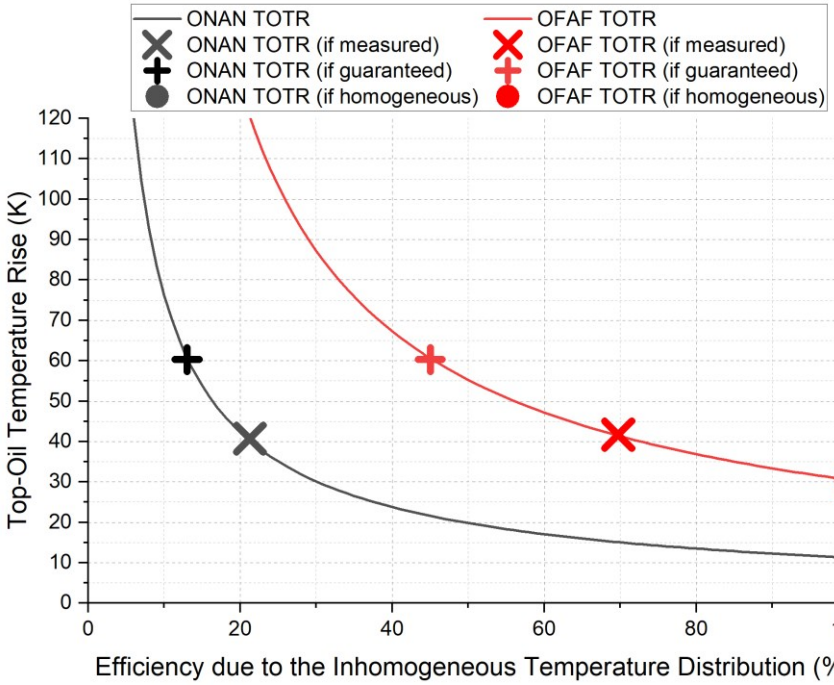

Figure 4.7: Variation of the calculated TOT with the change in the efficiency due to the inhomogeneous temperature distribution.

The results of TOTR in both modes are significantly underestimated due to the underestimation of thermal resistances when assuming a homogeneous temperature distribution. However, as the wall temperature is an intermediate result, the heat transfer coefficient can be calculated from the TOTR assuming a homogeneous temperature distribution. The only explanation left for the underestimation is that the total cooling area of the transformer surface suffers from reduced efficiency due to the inhomogeneous temperature distribution. Considering the availability of transformer specifications, two efficiencies due to the inhomogeneous temperature distribution under ONAN and OFAF cooling modes are suggested for their respective rated conditions, noted as the efficiency due to the inhomogeneous temperature distribution for the RCC heat transfer process, or the efficiency due to the inhomogeneous temperature distribution. The efficiency due to the inhomogeneous temperature distribution represents the general reduction in the cooling ability, assuming that both modes have a homogeneous temperature distribution.

The same efficiency due to the inhomogeneous temperature distribution applies to the heat transfer in the conduction-radiation and conduction-convection processes, provided that the RCC occurs simultaneously, unless measurement from a transformer installed in a vacuum can be obtained. However, such an application is outside the scope of a power transformer in a normal power system, and conducting a measurement campaign for a large power transformer in a vacuum is extremely difficult.

The variation in the calculated TOTR with the efficiency due to the inhomogeneous temperature distribution under ONAN and OFAF modes is shown in Figure 4.7. It illustrates a brute force algorithm for calculating the efficiency due to the inhomogeneous temperature distribution. The values of the efficiency due to the inhomogeneous temperature distribution for both measured and guaranteed TOTR are also marked. The values are calculated from measured TOTR, as the guaranteed TOTR represents the worst-case design that meets the requirements of standards. Ageing of the transformer is usually subject to the ageing of the electrical insulation in the windings [1], [2]. Stagnation and congestion of the transformer oil and air flow path should be considered poor maintenance rather than ageing. Ageing of the transformer cooling surface, which is made of steel, is very unlikely to have a significant impact. However, such an ageing process warrants further investigation. The calculated efficiency due to inhomogeneous temperature distribution under ONAN and OFAF cooling modes is 0.212 and 0.698, respectively.

4.1.4 Estimation of the Thermal Parameters for Oil Convection

The effective cooling area of the winding for oil convection is unknown in either cooling mode, according to any available sources. However, based on the guaranteed hot-spot temperature rise (HSTR) over ambient and the guaranteed TOTR over ambient, we can assume the guaranteed HST over TOT is equal to its guaranteed value in both cooling modes. Thus, we can estimate the characteristic length over the effective cooling area of the winding for oil convection $(L/A)_{oil,ONAN}$ by:

$$(L/A)_{oil,ONAN} = \frac{\Delta\theta_{HS,TO,r} \cdot k_{oil} \cdot Nu_{oil,ONAN}}{q_{in,loss,t}} \tag{190}$$

where: $\Delta\theta_{HS,TO,r}$ is the temperature rise from the hot-spot over the top-oil at the rated condition in K; $q_{in,loss,t}$ is the total heat input from losses in W; $Nu_{oil,ONAN}$ is the Nusselt number of oil convection under the ONAN cooling mode, which can be calculated from [17], [23].

The effective area for forced oil convection under OFAF cooling mode should be bigger than what is considered the effective cooling area under ONAN cooling mode because, from past experience, the temperature difference between top-oil and bottom oil is much smaller under OFAF cooling mode compared to ONAN cooling mode. Then, as the study [89] shows, the oil flow rate near the winding also affects the winding temperature distribution, altering the effective cooling area when a single temperature reference is used for the entire cooling area. This difference in oil flow rate is much more significant for a transformer operating in OFAF mode than in ONAN mode, due to the forced oil circulation provided by the oil pumps. By assuming the characteristic length of oil convection is constant, the characteristic length over the effective area for forced oil convection $(L/A)_{oil,OFAF}$ can be estimated by:

$$(L/A)_{oil,OFAF} = (L/A)_{oil,ONAN} \cdot \frac{C_{ONAN}}{C_{OFAF}} \tag{191}$$

The estimated characteristic length over the effective cooling area of oil convection is 0.050 m^{-1} under ONAN cooling mode. The estimated oil speed in the heat transfer process of the forced oil convection under OFAF cooling mode is 0.23 m/s.

4.1.5 Calculation of the Heat Input from Solar Irradiance

This heat input is derived from the thermal irradiance of the sun and the sky, as projected onto the outer surface of the transformer wall. Two heat sources from solar irradiance are considered: heat input from the solar irradiance in the transformer tank $q_{in,solar,tank}$ and heat input from the solar irradiance in the transformer cooler $q_{in,solar,cooler}$.

The heat input from the solar irradiance is given by:

$$q_{in,solar,object} = \alpha \cdot Q_s \cdot A_{object,SI} \tag{192}$$

The value of the effective projected surface area should also be improved through additional measurements, provided that data on the actual geolocation of the transformer can be obtained, which is not possible for security reasons. However, at this stage, the maximum projected area of the parallelepiped is used for the transformer, providing a conservative estimate.

4.1.6 Calculation of the Heat Input from Losses

The heat input from losses is separated into no-load losses, load losses, tertiary winding losses, and auxiliary losses in the winding, as presented in the following sections.

4.1.6.1 Calculation of the Heat Input from No-Load Losses

Heat from no-load losses is generated in the transformer core as long as the transformer is energised. The no-load losses are independent of the load ratio and core temperature. Instead, the no-load losses mainly depend on the supplied frequency and voltage [33], [46], [47], [92]. The five sources are hysteresis losses, eddy-current losses, dielectric losses, Joule losses from the no-load current, and stray losses. Stray losses occur outside the core and winding, and can currently be evaluated only using FEM simulation [42]. The other no-load losses can be calculated by using [33], [46].

Some limitations of this model include the assumption that the frequency is always set to a constant 50Hz in this paper, which may not hold in real-world transformer operation, especially during post-fault conditions. Nonetheless, in a pre-fault situation where frequency deviation is less than 1%, the no-load losses can be well represented. The saturation of the magnet at high-loading conditions is also not taken into consideration in this model. The variation in no-load losses with respect to core temperature is also neglected. Eddy current losses should be inversely proportional to temperature, as higher temperature increases the core's electrical resistivity, thereby decreasing eddy current losses. The hysteresis losses, dielectric losses and joule losses with variations in temperature are negligible [46], [47]. It is advised that the hysteresis

losses and eddy current losses are the dominant sources of the no-load losses, which contribute up to 98 per cent of the no-load losses [33], [46]. The no-load stray losses, the no-load dielectric losses and the no-load Joule losses due to the no-load current are usually neglected [31], [33], [41], [46], [47].

However, due to the lack of measurement of the magnetic flux, the change in magnetic flux to the voltage of the transformer and the joule losses of no-load current are often neglected by most operators and manufacturers, along with dielectric losses. Nevertheless, based on past experience, the no-load losses per unit at supplied voltages ranging from 0.5 PU to 1.5 PU are shown in Figure 4.8. It can be seen that for a 1.1 PU supplied voltage, the no-load losses increased to 1.27 PU of the rated no-load losses. For the example transformer, it increased from 54.8kW to 72.5kW. For the maximum rated total losses under OFAF cooling mode at tap 15, it increases from 874.8kW to 892.5kW, which is a 2% difference. This suggests that the no-load losses variation due to the supplied voltage variation better not be neglected. The relation between supplied voltages and per-unitised no-load losses is measured from factory testing. The voltage in power systems is limited to a given range, depending on the regulation, and is normally narrower than the voltage range used in factory testing.

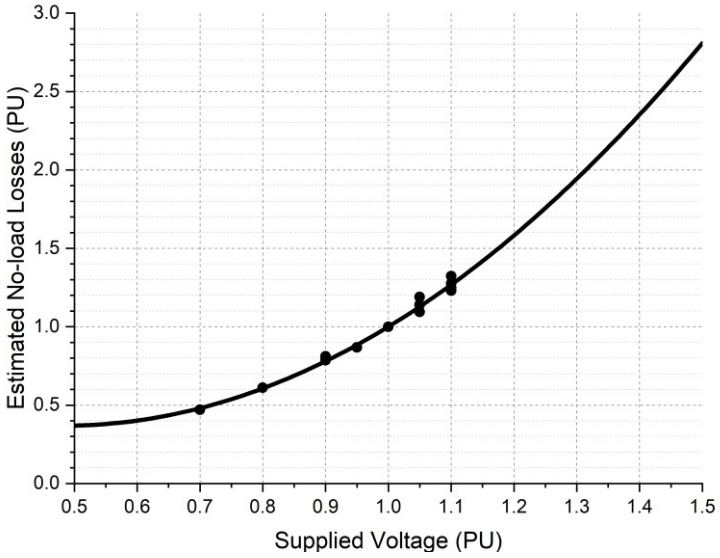

Figure 4.8: Result of the estimated no-load losses with the variation of the supplied voltage.

4.1.6.2 Calculation of the Heat Input from Load Losses

According to the available measurement data, the load losses $q_{in,load,HV\&LV}$ under the respective current in PU, the average winding temperature, tap position and cooling mode are calculated by:

$$q_{in,load,HV\&LV}(I_{pu}, \theta_w, tap, mode) = q_{in,load,r}(tap, mode) \cdot I_{pu}(tap)^2 \cdot R_{pu}(\theta_w) \tag{193}$$

where: $q_{in,load,r}(tap, mode)$ is the heat input from load losses under the rated condition of the respective tap position and cooling mode in W; $I_{pu}(tap)$ is the LV current to the rated LV current of the respective tap position in PU; $R_{pu}(\theta_w)$ is the winding resistance with respect to the winding resistance at the rated temperature in PU, calculated by:

$$R_{pu}(\theta_w) = 0.9 \cdot \frac{1 + \theta_w \cdot \mathrm{a}_0}{1 + 75 \cdot \mathrm{a}_0} + 0.1 \cdot \frac{1 + 75 \cdot \mathrm{a}_0}{1 + \theta_w \cdot \mathrm{a}_0} \tag{194}$$

where: a_0 is the temperature coefficient of resistance of the winding material, assumed to be copper, its value can be found in [93]; θ_w is the average winding temperature, which can be calculated by:

$$\theta_w = (\theta_{HS} - \theta_a) \cdot \frac{\Delta\theta_{w,r,mode}}{\Delta\theta_{HS,r,mode}} + \theta_a \tag{195}$$

where: θ_{HS} and θ_a are the HST and AAT in ℃; $\Delta\theta_{w,r,LV,OFAF}$ and $\Delta\theta_{HS,r,OFAF}$ is the rated average winding temperature rise (WTR) above ambient, and the rated HSTR above ambient under OFAF cooling mode in K. Due to limitations in the winding resistance measurement, the 1 PU average winding resistance is assumed to be at the average winding temperature of 75℃ [1], [2]. This estimation method assumes that 90% of the load losses are proportional to the increase in winding resistance resulting from higher average winding temperature. 10% of the load losses are due to eddy losses. The total load losses are inversely proportional to the increase in winding resistance; the combination of the variation in inducted current and resistance results in an inverse

relationship between the eddy-loss component of the load losses and the average winding temperature.

The per-unit value of the LV current to the rated LV current of the respective tap position is calculated by:

$$I_{pu}(tap) = I_{LV}/I_{LV,r}(tap) \tag{196}$$

where: I_{LV} is the LV current in A; $I_{LV,r}(tap)$ is the rated LV current of the respective tap position in A.

For the ONAN cooling mode, the LV current in PU $I_{LV,pu}$ is calculated by:

$$I_{LV,pu} = \frac{I_{LV}}{I_{LV,r,ONAN}(tap)} \tag{197}$$

$$I_{LV,r,ONAN}(tap) = I_{LV,r} \cdot \frac{S_{ONAN}(tap)}{S_{OFAF}(tap)} \tag{198}$$

where: $I_{LV,r,ONAN}$ is the rated LV current at the ONAN cooling mode in A. $S_{ONAN}(tap)$ and $S_{OFAF}(tap)$ are the MVA ratings of the transformer of the respective tap position under ONAN and OFAF cooling modes, respectively.

One limitation of this model is that load losses across different windings are treated as Joule losses and eddy losses. The stray flux losses are generated due to the current harmonics, which are dependent on the tap position and proportional to the load current squared and the frequency squared [94]. For a transformer at high loading, such losses can be neglected, as shown in standard equations [2].

4.1.6.3 Heat Input from Tertiary Windings and Auxiliary Losses

The transmission transformer is equipped with a tertiary winding. Depending on its usage, the tertiary winding can be a third winding supplying utilities to the transformer and within the substation, or a tertiary stabilisation winding that stabilises the neutral point of the star-connected winding, provides a zero-sequence current path, and suppresses third-harmonic voltages.

The heat input from the tertiary winding is from the stabilisation of unbalance, determined by the zero-sequence current [51]. The thermal impact of unbalance is out of scope at the current stage. It should be done in future work, and the suppression of the harmonic in the no-load exciting current should be considered as part of the no-load losses instead of the load losses from the tertiary winding [50], [51], [95], [96].

The auxiliary may use the tertiary winding to supply, but its losses are taken into account in auxiliary losses, so it is not included in tertiary losses to prevent duplication.

4.1.7 Estimation of Load Losses for Different Tap Positions

When the measurements of the load losses for other tap positions are unavailable, acknowledging that the OLTC is equipped on the LV side, using the lowest tapping (tap position 15), which yields maximum losses of the example transformer as the reference, the following method can be used:

$$q_{in,load,r}(tap, mode) = q_{in,load,r}(15, mode) \cdot Z_{pu}(tap) \cdot \left[\left(\frac{I_{LV,r}(tap)}{I_{LV,r}(15)}\right)^2 \cdot W_{LV}(tap) + W_{HV}(tap)\right] \quad (199)$$

where: $W_{LV}(tap)$ and $W_{HV}(tap)$ are the weightages of the load losses assuming pure joule losses of LV winding and HV winding to the total load losses at the tap position in question in PU, respectively; $Z_{pu}(tap)$ is the impedance of the tap position in question with respect to the reference tap position (15) in PU. Due to the limited measurements available, the impedance changes with respect to the tap position are available for the percentage of voltage in HV with LV short-circuited, which represents the percentage of the supplied voltage in HV when the LV is short-circuited and produces the rated LV current at the specified ap position. The lowest tap position, corresponding to the highest loss (tap position 15, see Table 4.2), is used as the reference. Consequently, the impedance depends on the respective tap positions $Z_{pu}(tap)$ can be calculated by:

$$Z_{pu}(tap) = U_{\%}(tap)/U_{\%}(15) \quad (200)$$

where: $U_{\%}(tap)$ and $U_{\%}(15)$ are the impedance represented by the percentage of voltage at the tap position in question and tap position 15, respectively.

The estimated weightages of LV and HV windings at different tap positions can be calculated by:

$$W_{LV}(tap) = \frac{W'_{LV}(tap)}{W'_{LV}(tap) + W'_{HV}(tap)} \tag{201}$$

$$W_{HV}(tap) = 1 - W_{LV}(tap) \tag{202}$$

$$W'_{LV}(tap) = \frac{TR(tap)}{VG_{I,LV}{}^2} \cdot \frac{1}{VG_{turn,LV}} \tag{203}$$

$$W'_{HV}(tap) = \frac{1}{VG_{I,HV}{}^2} \cdot \frac{1}{VG_{turn,HV}} \tag{204}$$

where: $W'_{LV}(\text{tap})$ and $W'_{HV}(\text{tap})$ are the weightages of the load losses of the LV winding and the HV winding to the total load losses at the tap position in question before normalising, respectively; $TR(tap)$ is the voltage (turn) ratio at the tap position in question; $VG_{I,LV}$, $VG_{turn,LV}$, $VG_{I,HV}$ and $VG_{turn,HV}$. The effect of the vector group on the phase current of the LV winding, the turn number of the LV winding, the phase current of the HV winding and the turn number of the HV winding, respectively. For an HV-LV connected in a star-delta configuration, they are equal to $\sqrt{3}$, 1, 1 and $\sqrt{3}$, respectively. The star-connected winding has less phase voltage, resulting in fewer winding turns and, consequently, lower impedance due to the coil's length. While the delta-connected winding has less phase current but the same phase voltage, the number of turns and their impedance are unaffected.

The estimated results of the load losses for all tap positions are shown in Figure 4.9. It can be observed that the load losses at all other tap positions are overestimated by an average of 2.8% and a maximum error of 5.6%, which should be conservative for transformer thermal modelling. However, suppose measurement data of load losses on those significant tap positions (maximum current, nominal, minimal resistance and

minimal current taps) are available. In that case, the interpolation method can be used to estimate the value of load losses missed by measurement.

This estimation is based on the assumption that the cross-section of the coil in HV and LV is the same. An alternative approach can be achieved by multiplying the current density and the copper mass to calculate the Joule loss component of the load losses, and then applying a factor to account for load losses that are not Joule losses, based on statistical data. However, such an approach is based on significantly more detailed transformer data and is not considered in this paper.

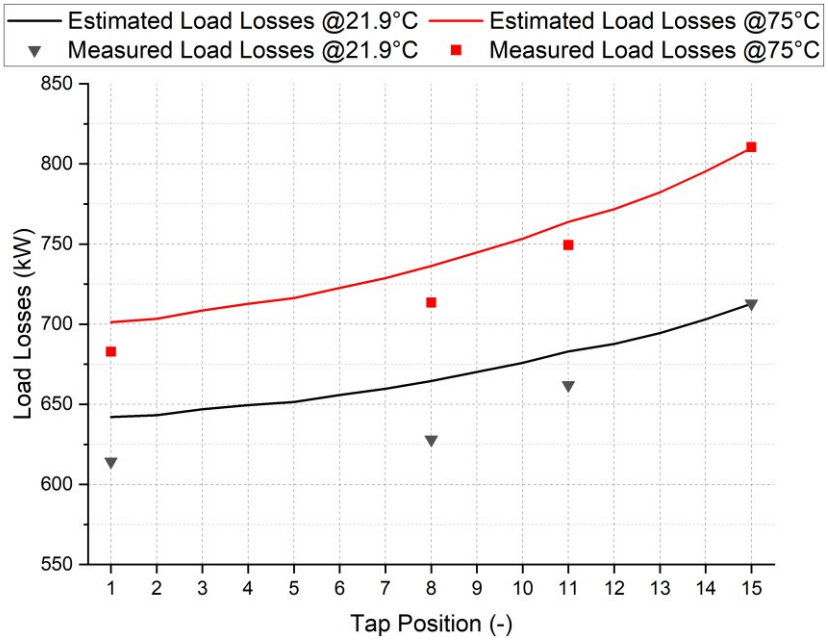

Figure 4.9: Comparison between measurement load losses and estimated load losses under OFAF mode.

4.1.8 Thermal Capacitances of Transformers

The thermal capacitance representing the hot-spot is estimated to be 5% of the thermal capacitance of the core and coil assembly, hot-spot mCp_{HS}:

$$mCp_{HS} = 0.05 \cdot mCp_{cc} \tag{205}$$

where: mCp_{cc} is the thermal capacitance of the core and coil assembly in $W \cdot s/K$. The 5% estimation is based on measurement results and results from the IEC standard-based thermal model [2]. Then, using the ONAN cooling mode as a reference, it is found that

the thermal capacitance of a large power transformer is overestimated in [1] due to the inhomogeneous temperature distribution. It should be revised to account for the efficiency due to inhomogeneous temperature distribution under the respective cooling mode, as well as the effective thermal capacitance, considering the effective thermal capacitance in converting the inhomogeneous temperature distribution on a large thermal capacitance into an effective thermal capacitance with uniform temperature. The same efficiency can be used to convert a large, complex thermal mass with an inhomogeneous temperature distribution into an effective thermal mass with a uniform temperature. The revised thermal capacitance under the ONAN cooling mode can be calculated using:

$$mCp_{tank} = \mathrm{C_{ONAN}} \cdot 0.0882 \cdot m_{tank} \tag{206}$$

$$mCp_{cooler} = \mathrm{C_{ONAN}} \cdot 0.0882 \cdot m_{cooler} \tag{207}$$

$$mCp_{oil\&cc} = \mathrm{C_{ONAN}} \cdot 0.3513 \cdot Litre_{oil} + (\mathrm{C_{ONAN}} - 0.05) \cdot 0.1323 \cdot m_{cc} \tag{208}$$

where: m_{cc}, m_{tank} and m_{cooler} are the mass of the core and coil assembly, the mass of the transformer tank and the mass of the transformer cooler in kg, as defined in Fig.2, respectively; $Litre_{oil}$ is the volume of oil in L.

Under the OFAF cooling mode, the extra thermal capacitance of tank $mCp_{tank,extra}$, cooler $mCp_{cooler,extra}$ and oil $mCp_{oil,extra}$ can be calculated by:

$$mCp_{tank,extra} = (\mathrm{C_{OFAF}} - \mathrm{C_{ONAN}}) \cdot mCp_{tank} \tag{209}$$

$$mCp_{cooler,extra} = (\mathrm{C_{OFAF}} - \mathrm{C_{ONAN}}) \cdot mCp_{cooler} \tag{210}$$

$$mCp_{oil\&cc,extra} = (\mathrm{C_{OFAF}} - \mathrm{C_{ONAN}}) \cdot mCp_{oil} + (\mathrm{C_{OFAF}} - \mathrm{C_{ONAN}}) \cdot mCp_{oil\&cc} \tag{211}$$

The change in thermal capacitance during a cooling mode change can be simulated by the following system, using the thermal capacitance of the transformer tank as an example, as shown in Figure 4.10.

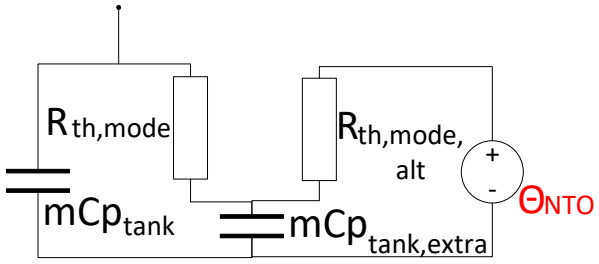

Figure 4.10: Thermal capacitance modelling for the switching between OFAF and ONAN cooling modes.

The thermal resistance $R_{th,mode}$ and $R_{th,mode,alt}$ act as switches. For the solver iteration issue, under the ONAN cooling mode, the value of thermal resistance in $R_{th,mode}$ equal to a very high value, e.g., 1e9, and the value of $R_{th,mode,alt}$ equal to a very low value, e.g., 1e-5. Therefore, this extra thermal capacitance is effectively unusable for the calculation under the ONAN cooling mode. Then, under OFAF cooling mode, the value of the two thermal resistances representing the switches exchange their assigned value so that the thermal model can consider the extra thermal capacitance.

In practice, the switching from ONAN to OFAF cooling mode should involve the direct mixture of colder bottom oil and hotter top-oil due to the activation of pumps. This process is not instant and should take into consideration some thermal resistance. Currently, the thermal resistance only acts as a switch, allowing the change of thermal capacitance in the model. It is worth noting that a high thermal resistance value can prevent an instant mixture between cold and hot oil. However, if set too high, it will lead to a significant temperature difference between the thermal capacitance considered by the ONAN mode and the extra thermal capacitance introduced by forced circulation of oil. In such a case, the additional thermal capacitance could not be properly utilised by the model under OFAF cooling mode. The value of 1e-5 is tested to be sufficient to prevent the instantaneous mixing of cold and hot oil, while maintaining an ignorable temperature difference between the thermal capacitances.

The temperature reference of the extra thermal capacitance is the non-top oil temperature (NTOT), which accounting for the thermal mass of oil not considered by the TOT. Under ONAN mode, this temperature should be slightly lower than the average oil temperature because it excludes the thermal mass of the top-oil. Under the OFAF

cooling mode, this temperature reference should not have any effect. Therefore, due to mathematical reasons, the NTOT is assigned a value lower than the TOT of the time, e.g., 2 °C lower. The NTOT matters during the transient process of switch from ONAN cooling mode to OFAF cooling mode. Given the available measurement of NTOT or bottom oil temperature at the rated condition, the NTOT can be calculated by [1]. However, if such measurements are unavailable, the NTOT under ONAN cooling mode can be estimated by:

$$\theta_{NTO} = \theta_{a,cooler} + \frac{\theta_{TO} - \theta_{a,cooler}}{2} \tag{212}$$

4.1.9 Model Validation and Comparison to Standard Models

ONAN/OFAF at 400/132 kV can be directly obtained by the manual [97] and drawing [76], [98] as shown in Table 4.1-Table 4.3. Other external parameters used are shown in Table 4.4.

Table 4.1: Data and Parameters of the Example Power Transformer from [17].

ONAN/OFAF TOTR (K)	40.7/41.4
ONAN/OFAF load losses at 75℃ (kW)	202/810
No-load losses (kW)	55

Table 4.2: Transformer Tap Position Dependent Data and Parameters of the Example Power Transformer [76].

Tap Position	**Voltage [V] (LV Side)**	**Current [A] (LV side)**	**Impedance (volts%) HV/LV-short-circuited**
1	151.8	913	20
2	149.82	924	19.84
3	147.84	936	19.74
4	145.86	948	19.61
5	143.88	960	19.46
6	141.9	973	19.36
7	139.92	986	19.25
8	137.94	1000	19.15
9	135.96	1014	19.07
10	133.98	1028	18.99
11(Nom.)	132	1043	18.93
12	130.35	1057	18.82
13	128.7	1072	18.75
14	127.05	1088	18.71
15	125.4	1105	18.68

Table 4.3: Transformer Technical Specifications [76], [97], [98].

Rated MVA ONAN/OFAF	120/240
HV/LV rated voltage(kV)	400/132
Vector group	YNa0d11
Tap range	+15% to -5% in 14 steps at LV
Tertiary voltage (kV)	13
Auxiliary losses (kW)	10
Max TOTR at rated load and 20℃ AT (K)	60
Max WTR at rated load and 20℃ AT (K)	65
Max HSTR at rated load and 20℃ AT (K)	78
Weight of core (kg)	102800
Weight of tank and fitting(kg)	37600
Weight of cooler(kg)	25550
Litre of oil (L) (no Conservator)	87749
Tank height (m)	4.45
Tank length (m)	8.3
Tank width (m)	4.57
Cooler height (m)	2.116
Cooler length (m)	6.8
Cooler width (m)	3
Thickness (m)(Assumed)	1.00E-02
Number of cooling plates	640 (in 20 blocks)
Area per cooling plate (m^2)	2.230264
Total air quantity from fans (m^3/s)	34.3 (from 10 cooling fans)
Characteristic length of oil convection (m)	29.56

Table 4.4: Parameters Outside of Specifications [1], [2], [23], [93], [99].

Specific heat of core and coil assembly ($W \cdot h/(K \cdot kg)$)	0.1323
Specific heat of tank and fitting ($W \cdot h/(K \cdot kg)$))	0.0882
Specific heat of litres of oil ($W \cdot h/(K \cdot L)$)	0.3513
Thermal capacitance of hot-spot ($W \cdot h/K$))	2.45E6
Thermal capacitance of the tank ($W \cdot h/(K \cdot kg)$))	2.53E6, 5.80E6(extra)
Thermal capacitance of the cooler ($W \cdot h/(K \cdot kg)$))	1.72E6, 3.94E6(extra)
Thermal capacitance of oil ($W \cdot h/(K \cdot kg)$))	2.35E7, 5.39E7(extra)
Hot spot factor	1.3
Thermal conductivity of the transformer wall material at 0/100℃ ($W/(m \cdot K)$)	12.1/14.1
Temperature coefficient of resistance for copper (-)	0.00398
Efficiency due to inhomogeneous temperature distribution (-)	0.212 (ONAN) 0.698 (OFAF)
Characteristic length over the effective cooling area of oil convection under ONAN mode (m^{-1})	0.050
Oil speed under OFAF mode (m/s)	0.23

The HST and TOT calculated using the thermal model (as solid black lines) under the conditions of recorded ambient temperatures, MVA loading (magenta dotted lines), tap position (grey dashed lines), and cooling situation over 23 hours, from 00:00 to 23:00, are shown in Figure 4.11 and Figure 4.12. The original measured values of WTI and TOT are represented by solid grey lines. The ambient temperature refers to the hall air temperature (i.e., the transformer enclosure air temperature, as blue dashed lines).

The supplied voltage can vary, but it is assumed that the output voltage in LV is always controlled at 1PU by OLTC. The initial temperature of HST and TOT is assigned to the first recorded value of HST and TOT. The solver used is [70].

The result is compared to the IEC standard models (red solid lines) [2] and the IEEE standard Annex G model (blue solid lines) [1]. The IEC standard model considers the tap position, cooling mode, and loading ratio at their respective tap positions and cooling modes. While the switch between cooling modes can only be represented as a change in the loading ratio with a different (higher) base power for the IEEE standard Annex G model, other parameters are assumed under the ONAN mode.

From these comparisons, it can be observed that the improved model reproduces the measured HST and TOT with good accuracy. Notably, the model captures the transient behaviour during changes in cooling mode, specifically the switching events from ONAN to OFAF and from OFAF back to ONAN. This indicates that the revised formulation not only enhances agreement with measured temperatures but also provides a more realistic representation of the thermal response during operational transitions.

The error analysis in Table 4.5 demonstrates that the improved thermal model provides a clear enhancement over both the IEC and IEEE Annex G formulations. For HST estimations, the improved model achieves a mean absolute error (MAE) of 1.23 °C and a root mean square error (RMSE) of 1.75 °C, which is substantially lower than the IEC model (MAE 2.45 °C, RMSE 2.99 °C) and the IEEE Annex G model (MAE 1.93 °C, RMSE 2.73 °C). A similar trend is observed for TOT, where the improved model again performs best, with an MAE of 1.07 °C and RMSE of 1.40 °C, compared to 2.32 °C and 3.24 °C for the IEC model and 4.13 °C and 5.10 °C for the IEEE model.

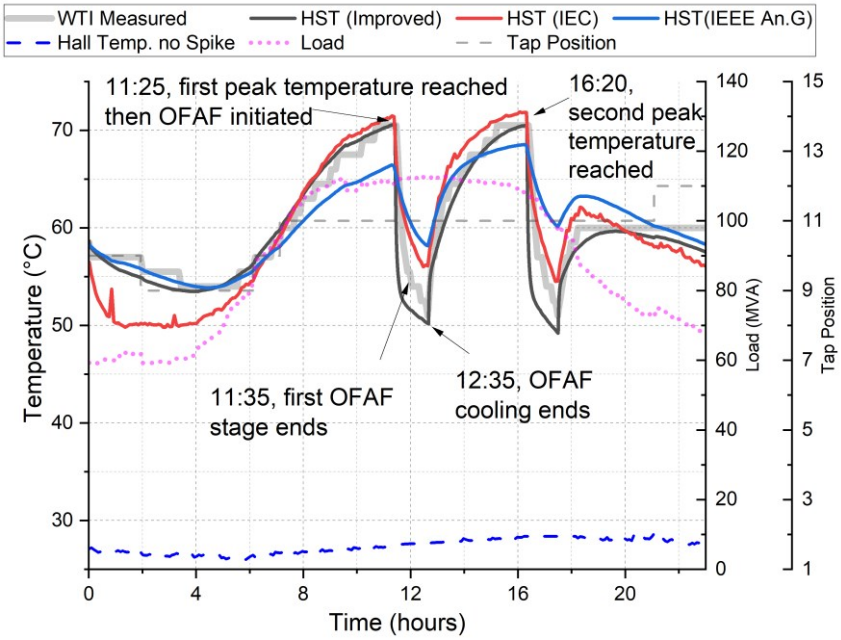

Figure 4.11: Comparison of the calculated value of HST using improved mode, IEC standard-based models [2] and IEEE Annex G model [1] to the recorded value.

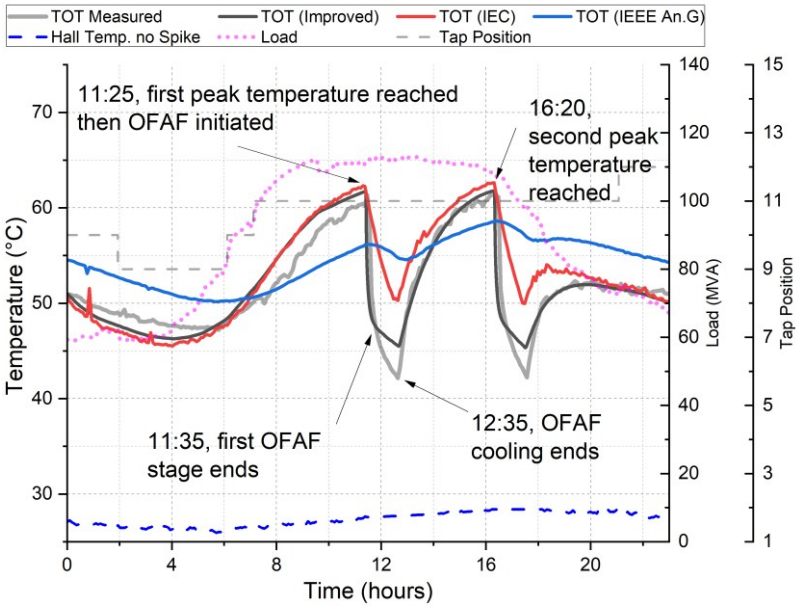

Figure 4.12: Comparison of the calculated value of TOT using the improved model, IEC standard-based model [2] and the IEEE Annex G model [1] to the recorded value.

The advantage of the improved model becomes more apparent when specific operating events are examined, as shown in Table 4.6. At critical points such as peak temperatures and transitions into and out of OFAF cooling, the improved model

generally tracks the measured behaviour more closely than the standards. For HST, the largest deviation occurs at the end of the first OFAF stage, where the improved model underestimates the measurement by approximately −6.3 °C. However, at other key points, the error is within ±1 °C. The IEC and IEEE models, however, display larger errors across these events, with deviations up to +7 °C during cooling transitions. For TOT, the improved model again shows closer agreement, with a maximum deviation of about +3.6 °C at the end of OFAF cooling, compared with errors exceeding +8 °C and +12 °C for the IEC and IEEE models, respectively.

Table 4.5: Temperature error metrics for different models (whole day).

Model	HST Error Metrics (°C)		TOT Error Metrics (°C)	
	MAE	RMSE	MAE	RMSE
Improved	1.23	1.75	1.07	1.4
IEC	2.45	2.99	2.32	3.24
IEEE (An.G)	1.93	2.73	4.13	5.1

Table 4.6: Temperature errors at key points.

HST Error at Key Points (°C)					
Model	Peak Temp. 1	OFAF initiated	First OFAF stage ends	First OFAF cooling ends	Peak Temp. 2
Improved	0.03	0.07	-6.28	-0.61	-0.04
IEC	0.9	-3.96	1.02	5.1	1.33
IEEE(An.G)	-4.21	-5.27	1.84	7.15	-2.06
TOT Error at Key Points (°C)					
Model	Peak Temp. 1	OFAF initiated	First OFAF stage ends	First OFAF cooling ends	Peak Temp. 2
Improved	1.34	0.38	-0.79	3.59	0.45
IEC	1.97	-0.37	7.71	8.13	1.38
IEEE(An.G)	-4.18	-5.17	5.17	12.62	-2.71

Taken together, these results show that the improved thermal model in this thesis provides the most reliable reproduction of both HST and TOT across a wide range of conditions. It maintains low overall errors, captures transient behaviour during ONAN–OFAF switching, and offers a conservative but accurate estimate of transformer temperatures during critical peak loading periods.

4.2 Thermal Ratings of Power Transformers

The assessment of SST, DTR, TTC, S/MTOR and CTR of the example power transformer is shown in the following evaluations. Two tap positions with significance are considered: tap position 11 (nominal) and 15 (maximum losses). The power transformer is assumed to operate continuously in OFAF cooling mode, which enables the maximum transformer NTR. It may also be operated in ONAN cooling mode at 50% of the NTR, so this is ignored at this stage and should be addressed in future work.

4.2.1 Steady-State Temperatures of Power Transformers

The SST of the power transformer is the steady-state HST calculated under the condition of -30℃ to 50℃ AAT, 0.5m/s or 1m/s WS, 0 to 1000W/m^2 SI, the transformer is assumed to be always operated in OFAF cooling mode, supplied at 1PU voltage and rated current at the HV side. Two tap positions, 11 (nominal) and 15 (-5%), are chosen for the assessment. The result for at position 11 is shown in Figure 4.13, and the result for tap position 15 is shown in Figure 4.14.

The transformer is assessed from 0.65 PU to 1PU of loading under different SI from 0 to 1000 W/m^2. It is to be noted that the transformer has two main limits, i.e., continuous HST limit at 98°C (double red lines) and emergency at 122°C (double black lines).

From the results in tap position 11, it can be seen that the change of WS from 0.5m/s to 1m/s makes little to no difference to the calculated HST. However, the high SI condition contributes a 3℃ increase in the HST, which is enough to overcome the temperature accuracy for WTI tripping.

From the results in tap position 15 in Figure 4.14, the continuous HST increased compared to the result on tap position 11 for the same loading current and supplied voltage on the HV (primary) side of the power transformer. This is as expected, as the tap 15 trade higher current with lowering the voltage and a higher impedance, which leads to a worse thermal performance, thus a lower rating when using the same continuous HST limit. The results on tap 15 also show that the effect of natural WS can be neglected, but the heating effect from the SI needs to be treated with caution.

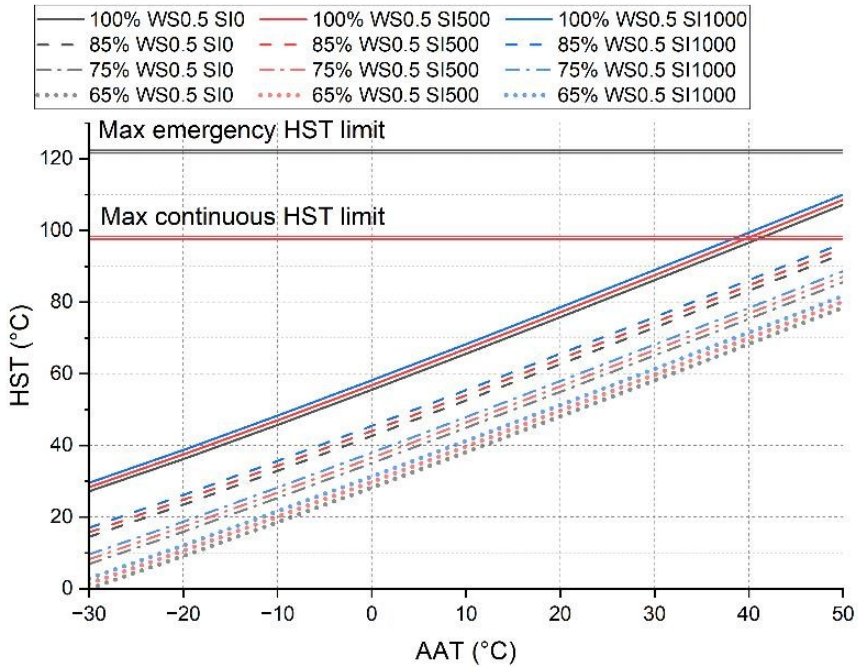

a) 0.5 m/s WS

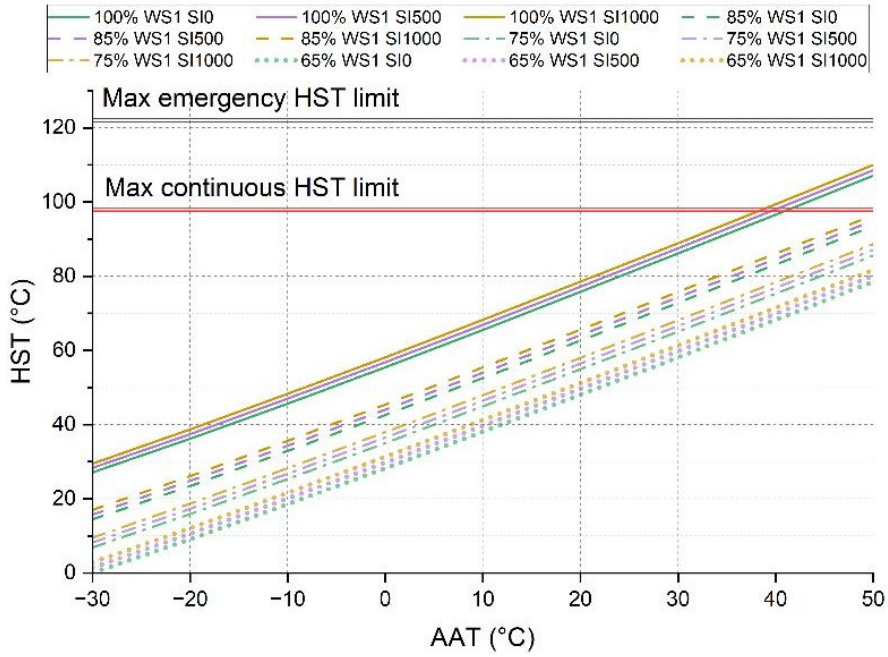

b) 1 m/s WS

Figure 4.13: Variation of steady-state HST at 0.5m/s WS (a) and 1m/s WS (b) of the power transformer in OFAF mode at tap position 11 with the variation of AAT and SI when loaded with respective 1PU, 0.85PU, 0.75PU, and 0.65PU constant NTR current.

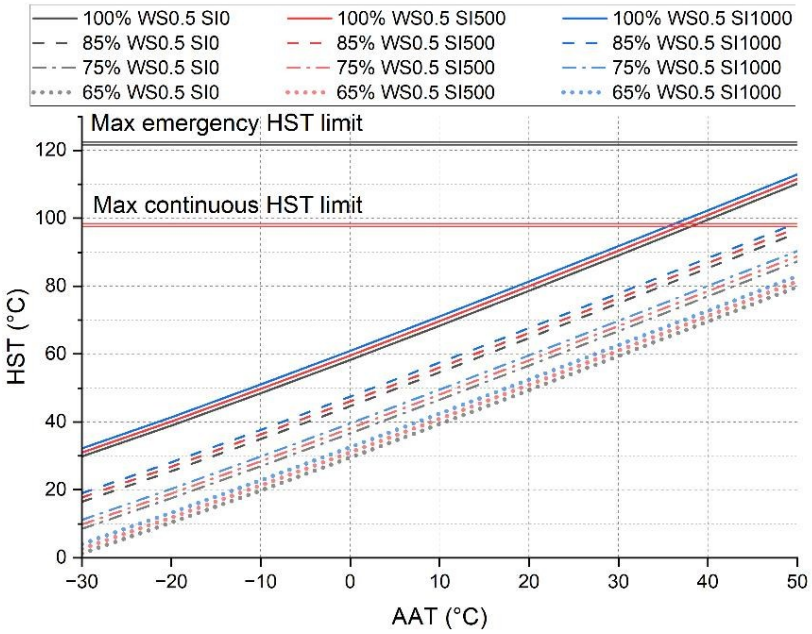

a) 0.5 m/s WS

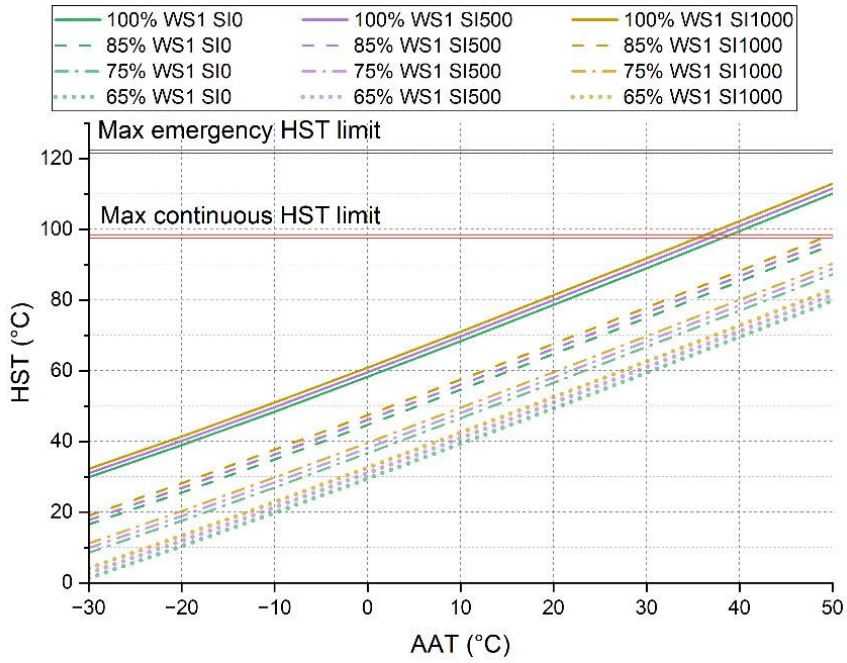

b) 1 m/s WS

Figure 4.14: Variation of steady-state HST at 0.5m/s WS (a) and 1m/s WS (b) of the power transformer in OFAF mode at tap position 15 with the variation of AAT and SI when loaded with respective 1PU, 0.85PU, 0.75PU and 0.65PU constant NTR current.

4.2.2 Dynamic and Nameplate Thermal Ratings of Power Transformers

After the calculation of the steady-state HST of the transformer, from the given temperature limit of the steady-state HST, the DTR of the power transformer can be calculated. According to [3], [14], [97], the HST limit of the continuous operation and emergency situation is 98℃ and 122℃, respectively.

4.2.2.1 Dynamic Thermal Ratings of Power Transformers in Power

The DTR of the power transformer is first expressed in per-unit (PU), where 1PU equal 240MVA loading on the transformer, which is also the nameplate rating of the example power transformer. The DTR is defined by assuming an indefinite operation, so, according to TGN 303 [14], the HST limit should be set on its maximum continues temperature when calculating the DTR of the power transformer. The result is shown in Figure 4.15.

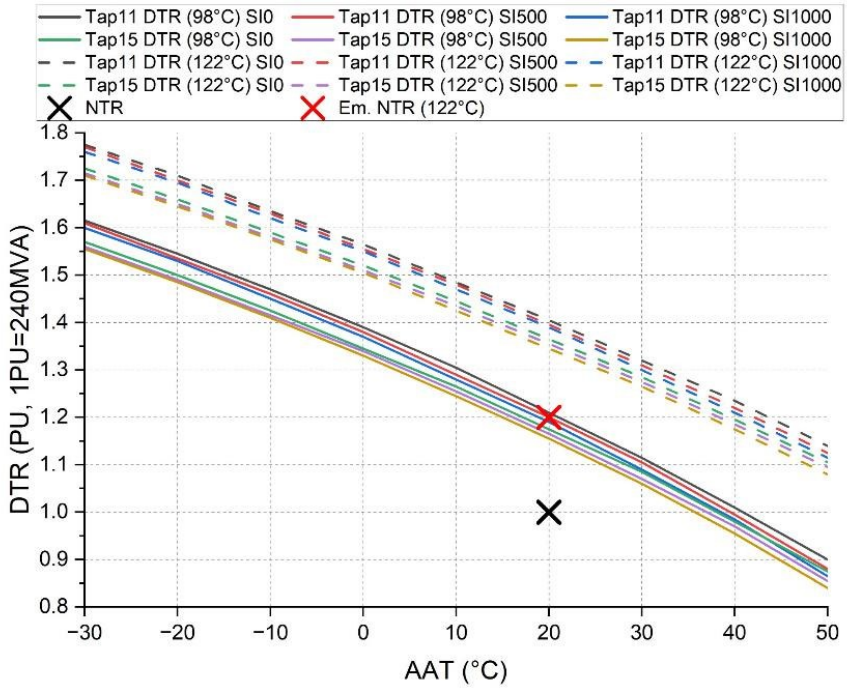

Figure 4.15: The calculated DTR in PU of base MVA of the power transformer under OFAF cooling mode for tap positions 11 and 15 with the variation of AAT and SI.

From the result, the DTR for tap position 11 is higher than tap position 15 due to the heat losses being higher in tap position 15 than in tap position 11. Thus, the thermal performance in tap position 11 is better, resulting in a higher DTR. It can also be seen that when calculating the DTR of the power transformer, the inclusion of SI will decrease the DTR of the power transformer. However, the reduction in DTR is minimal when compared to the case when calculating the DTR for OHL, FTC and ExpoC under high SI.

4.2.2.2 Dynamic Thermal Ratings of Power Transformers in Current

It becomes intricate when rating the power transformer for current, since it is equipped with OLTC, the turn ratio can change depending on the tapping operation. When the turn ratio of the power transformer changed, for the same supplied current and voltage in the primary side, in this case, the HV side, the output current and voltage on the LV side vary depending on the tap position. The result is shown in Figure 4.16.

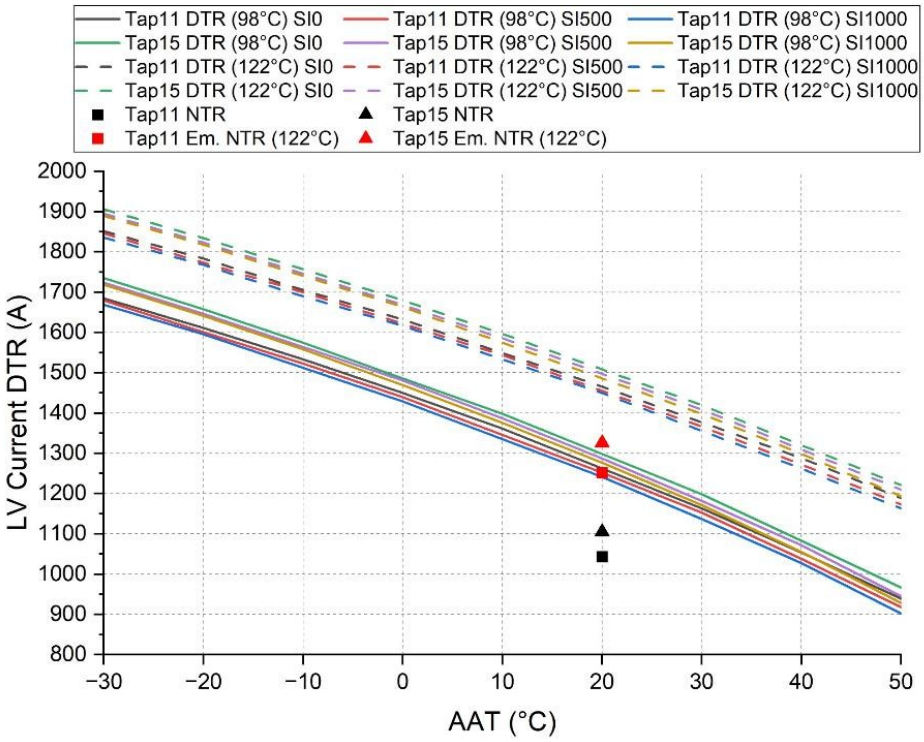

Figure 4.16: The calculated DTR in the current of the power transformer under OFAF cooling mode for tap positions 11 and 15 with the variation of AAT and SI.

From the result, it can be seen that when rating the power transformer on the LV side current, the rating of tap position 15 takes over that of tap position 11. This is in contrast to the result when rating the power transformer in MVA. This is because the OLTC at tap 15 increase the current output but with a decreased voltage as a trade-off. The current rating and power rating of the power transformer show an opposite result for different tap positions of the power transformer; such contradicting results suggest the rating unit of the transformer should be treated with caution.

As an initial conclusion, the maximum heat losses occur at tap position 15 (the lowest tap position at -5% voltage from nominal), which should be the worst amongst all other tap positions. The apparent increase in rating when the transformer is assessed based on LV current output is misleading, as it is simply a result of the reduced LV-side voltage. When rating the transformer by power in current, this decrease in output voltage is not properly reflected. The rating in power correctly reflects the worst thermal performance at tap position 15 compared to the nominal tap position. Thus, the rating of a power transformer is more accurately represented by the power (MVA) rating.

4.2.3 Thermal Time Constants of Power Transformers

When calculating the TTC of power transformers, in existing standard models [1], [2]. The transformer has multiple stages of heat transfer; the first important TTC is the TTC of TOT. The variation in TOT with time when loaded at 1PU, 0.85PU, 0.75PU and 0.65PU of NTR at tap positions 11 and 15 is shown in Figure 4.17, where the TTC does not differ much between the two tap positions.

The HST is calculated after the calculation of TOT, which differs from the winding TTC in [1], [2], where the time constant accounts only for heat transfer between the top-oil and the winding hot-spot. In those models, the thermal capacitance is represented solely by the winding's own thermal capacitance. The TTC of HST, for the example transformer represented in Figure 4.18. The TTC is calculated by considering all thermal capacitances in the transformer thermal model as part of a single-step response. The computation of the TOT serves only as an intermediate step. Figure 4.18

illustrates the time variation of HST under loading conditions from 1 to 0.65 PU of the NTR at tap positions 11 and 15.

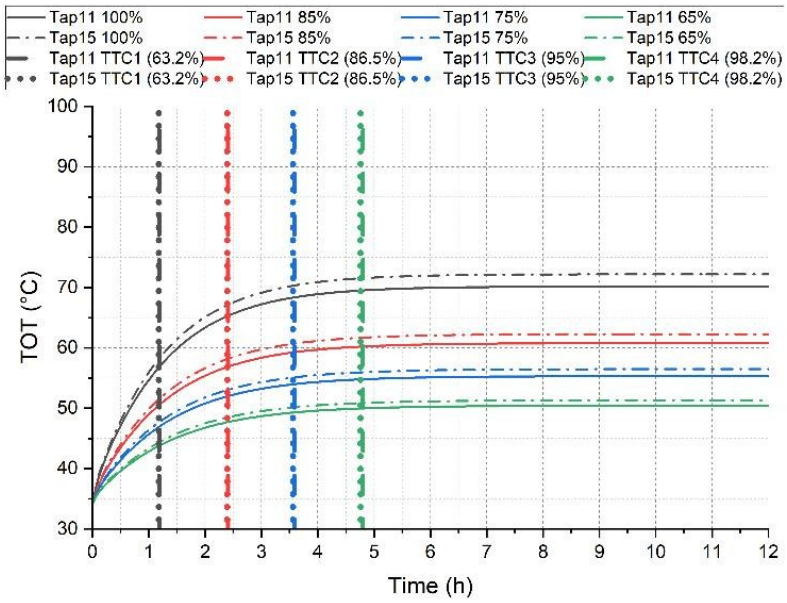

Figure 4.17: Variation of the TOT with time for the power transformer at tap positions 11 and 15 when supplied with 1PU voltage on the HV side, loaded with 1PU, 0.85PU, 0.75PU and 0.6PU of NTR current under summer ambient conditions.

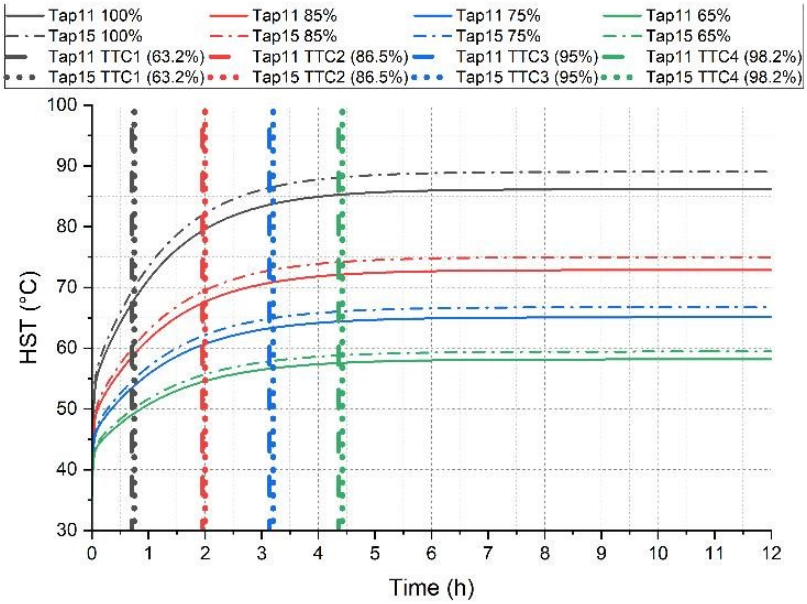

Figure 4.18: Variation of the HST with time for the power transformer at tap positions 11 and 15 when supplied with 1PU voltage on the HV side, loaded with 1PU, 0.85PU, 0.75PU and 0.6PU of NTR current under summer ambient conditions.

The HST time constants are consistently lower than those of the TOT due to the lower thermal capacitance represented in the hot-spot model. The first HST time constant is approximately half that of the TOT, indicating a much faster initial temperature rise. By the fourth TTC, the difference narrows to around 10%. This substantially shorter first TTC underscores the importance of caution when evaluating short-term overloading, as the HST responds significantly faster than the TOT for the immediately step change in loading.

4.2.4 Short-Term and Medium-Term Overloading Ratings of Power Transformers

In practice, as with other components, a power transformer typically operates below 100% of its continuous rating, whether based on NTR or DTR. This lower pre-fault loading means that, during a post-fault condition, the transformer can safely approach its maximum permissible emergency temperature. At the onset of the post-fault event (time 0), the transformer temperature must be below the specified emergency temperature limit. For a finite overloading period, the transformer can be loaded above its continuous rating to exploit its thermal inertia, allowing higher power transfer for a defined duration before reaching the temperature limit. Once this overloading period ends, the loading must be reduced to the emergency continuous rating, defined by either the emergency NTR or emergency DTR, to prevent overheating as measured by the winding temperature indicator (WTI) and to avoid triggering protective relays that would trip the transformer.

Figure 4.19 illustrates the HST variation of the example power transformer operating in OFAF cooling mode, loaded according to the S/MTOR profile with 0.85 PU pre-fault loading (based on the NTR) under different AAT. The short-term and medium-term overloading periods are followed by loading at the emergency NTR.

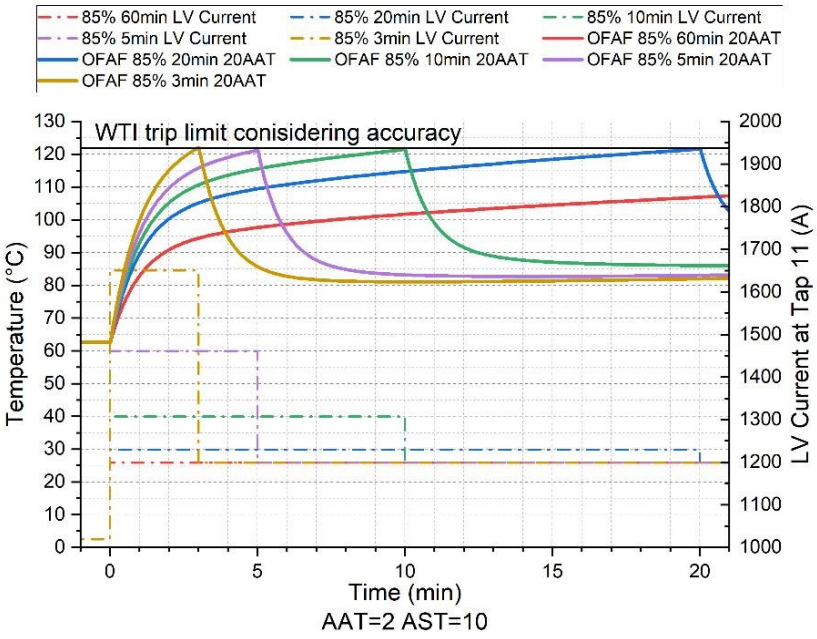

Figure 4.19: Example of the HST variation of the power transformer under OFAF cooling mode when loaded with S/MTOR using different overloading periods (up to 60min), pre-fault loading percentage in accordance with the NTR and different AAT.

4.2.4.1 Short-Term and Medium-Term Overloading Ratings of Power Transformers using Pre-Fault Loading in accordance with Nameplate Rating

This section presents the S/MTOR of the example power transformer, derived using pre-fault loading levels defined in accordance with the NTR, where 1 PU corresponds to 240 MVA at the rated HV-side voltage (346 A HV / 1043 A LV). Table 4.7 summarizes the calculated S/MTOR values at tap position 11 across a range of ambient air temperatures (AAT from −30 °C to 50 °C) and pre-fault loading percentages (85 %, 75 %, 65 %). The results demonstrate how both ambient conditions and pre-fault loading significantly influence the permissible short-term and medium-term loading capabilities before the transformer reaches its thermal limits.

Table 4.7 shows that the S/MTOR ratings decrease progressively as the AAT increases, reflecting the reduced thermal headroom available at higher ambient conditions. At very low AAT (−30 °C), the transformer can be loaded up to approximately 2.3 PU for short durations (3–5 minutes) when pre-fault loading is 65 %,

whereas at 50 °C ambient, this capability falls to around 1.65–1.72 PU for the same duration. The results also indicate that longer overloading periods significantly limit the available loading margin. For example, at 20 °C and 85 % pre-fault loading, the permissible loading is 1.91 PU for 5 minutes, but only 1.41 PU for a 360-minute (6-hour) period. Additionally, reducing pre-fault loading from 85 % to 65 % increases the available S/MTOR rating across all AATs, highlighting the role of thermal inertia in accommodating temporary overloads.

Table 4.7. Short-Term and Medium-Term Overloading Ratings of the Example Power Transformers at Tap Position 11 with variation of Ambient Air Temperatures, Pre-Fault loading Percentage in accordance with Nameplate Rating

AAT (°C)		-30	-20	-10	0	10	20	30	40	50
NTR (PU)		1								
Pre-fault loading%	**Duration (min)**	Pre-NTR S/MTOR at Tap 11 in PU (1PU=240MVA/346A/1043A, Power at 1PU primary voltage/HV Current/LV Current)								
100% corresponds to		1								
-	**inf**	1.775	1.71	1.635	1.565	1.485	1.41	1.32	1.24	1.14
85%	**360**	1.78	1.71	1.64	1.57	1.49	1.41	1.32	1.24	1.14
	60	1.98	1.92	1.85	1.77	1.68	1.59	1.49	1.38	1.26
	20	2.12	2.07	2.01	1.94	1.86	1.76	1.65	1.52	1.38
	10	2.14	2.12	2.08	2.02	1.94	1.84	1.73	1.6	1.45
	5	2.18	2.17	2.14	2.08	2.01	1.91	1.8	1.67	1.51
	3	2.29	2.27	2.23	2.17	2.09	1.99	1.87	1.72	1.56
75%	**360**	2.29	2.27	2.23	1.57	1.49	1.41	1.33	1.24	1.14
	60	2.29	2.27	2.23	1.79	1.7	1.61	1.52	1.41	1.29
	20	2.29	2.27	2.23	1.97	1.89	1.8	1.69	1.57	1.44
	10	2.29	2.27	2.23	2.04	1.97	1.89	1.78	1.66	1.52
	5	2.29	2.27	2.23	2.11	2.04	1.96	1.86	1.73	1.59
	3	2.3	2.28	2.25	2.2	2.13	2.04	1.93	1.8	1.65
65%	**360**	2.3	2.28	2.25	2.2	2.13	2.04	1.93	1.8	1.65
	60	2.3	2.28	2.25	2.2	2.13	2.04	1.93	1.8	1.65
	20	2.3	2.28	2.25	2.2	2.13	2.04	1.93	1.8	1.65
	10	2.3	2.28	2.25	2.2	2.13	2.04	1.93	1.8	1.65
	5	2.3	2.28	2.25	2.2	2.13	2.04	1.93	1.8	1.66
	3	2.3	2.29	2.27	2.22	2.16	2.08	1.98	1.86	1.72

Table 4.8 presents the S/MTOR results for the transformer at tap position 15 and shows broadly similar trends to Table 4.7, with ratings decreasing as ambient air

temperature rises and as overloading duration increases. However, compared with tap position 11, the absolute S/MTOR values are slightly lower across most conditions due to the higher LV current and resulting increased losses at this tap setting. This reduction is most noticeable at longer overload durations, where thermal steady-state conditions dominate. Nevertheless, the relative improvement from lower pre-fault loading (from 85 % to 65 %) remains consistent with the results at tap 11, confirming that thermal headroom and inertia remain the key factors enabling temporary overload capability.

Table 4.8. Short-Term and Medium-Term Overloading Ratings of the Example Power Transformer at Tap Position 15 with variation of Ambient Air Temperatures, Pre-Fault Loading Percentage in accordance with Nameplate Rating

AAT (°C)		-30	-20	-10	0	10	20	30	40	50
NTR (PU)		1								
Pre-fault loading%	**Duration (min)**	Pre-NTR S/MTOR at Tap 15 in PU (1PU=240MVA/346A/1105A, Power at 1PU primary voltage/HV Current/LV Current)								
100% corresponds to		1								
-	**inf**	1.72	1.66	1.59	1.52	1.44	1.36	1.28	1.19	1.11
85%	**360**	1.72	1.66	1.59	1.52	1.44	1.36	1.28	1.19	1.11
	60	1.92	1.86	1.79	1.71	1.63	1.54	1.44	1.33	1.21
	20	2.05	2.01	1.95	1.88	1.79	1.7	1.59	1.47	1.32
	10	2.08	2.06	2.01	1.95	1.87	1.78	1.66	1.53	1.38
	5	2.11	2.1	2.07	2.01	1.94	1.85	1.73	1.6	1.44
	3	2.22	2.2	2.15	2.1	2.01	1.91	1.79	1.65	1.48
75%	**360**	2.22	2.2	2.15	1.52	1.45	1.37	1.29	1.2	1.11
	60	2.22	2.2	2.15	1.73	1.65	1.56	1.47	1.36	1.25
	20	2.22	2.2	2.15	1.9	1.83	1.74	1.63	1.52	1.39
	10	2.22	2.2	2.15	1.98	1.91	1.82	1.72	1.6	1.46
	5	2.22	2.2	2.15	2.04	1.98	1.89	1.79	1.67	1.53
	3	2.23	2.22	2.18	2.13	2.06	1.97	1.86	1.73	1.58
65%	**360**	2.23	2.22	2.18	2.13	2.06	1.97	1.86	1.74	1.58
	60	2.23	2.22	2.18	2.13	2.06	1.97	1.86	1.74	1.58
	20	2.23	2.22	2.18	2.13	2.06	1.97	1.86	1.74	1.58
	10	2.23	2.22	2.18	2.13	2.06	1.97	1.86	1.74	1.58
	5	2.23	2.22	2.18	2.13	2.06	1.97	1.86	1.74	1.6
	3	2.24	2.23	2.2	2.15	2.09	2.01	1.92	1.8	1.66

4.2.4.2 Short-Term and Medium-Term Overloading Ratings of Power Transformers with Pre-Fault Loading in accordance with Dynamic Thermal Ratings

During pre-fault condition, the transformer can also be operated based on the DTR, which utilises the full thermal capacity up to the continuous temperature limit. In this case, the pre-fault loading percentage is referenced to the DTR (98°C) corresponding to the AAT under consideration, rather than the NTR. Consequently, the per-unit value of the pre-fault loading differs from that calculated using NTR as the 1 PU base. Prior to determining the S/MTOR in accordance with DTR (98°C), the adjusted pre-fault loading in PU must first be calculated. These recalculated pre-fault loading values are presented in Table 4.9, where 1 PU corresponds to 240 MVA at 1 PU voltage on both sides of the power transformer for the specified tap position.

Table 4.9: Values of Different Pre-Fault Loadings in accordance with the Dynamic Thermal Ratings of the Example Power Transformer

AAT (°C)	-30	-20	-10	0	10	20	30	40	50
Tap Position 11 (PU, 1PU=240MVA/346A/1043A, Power/HV Current/LV Current)									
100%	1.615	1.545	1.470	1.390	1.305	1.210	1.115	1.010	0.900
85%	1.373	1.313	1.250	1.182	1.109	1.029	0.948	0.859	0.765
75%	1.211	1.159	1.103	1.043	0.979	0.908	0.836	0.758	0.675
65%	1.050	1.004	0.956	0.904	0.848	0.787	0.725	0.657	0.585
Tap Position 15 (PU, 1PU=240MVA/346A/1105A, Power/HV Current/LV Current)									
100%	1.570	1.500	1.425	1.345	1.265	1.175	1.085	0.980	0.875
85%	1.335	1.275	1.211	1.143	1.075	0.999	0.922	0.833	0.744
75%	1.178	1.125	1.069	1.009	0.949	0.881	0.814	0.735	0.656
65%	1.021	0.975	0.926	0.874	0.822	0.764	0.705	0.637	0.569

The recalculated S/MTOR values, using DTR (98°C) as the 100 % pre-fault loading reference, are presented in Table 4.10 for the nominal tap position (tap 11) and in Table 4.11 for the maximum-loss tap position (tap 15).

Table 4.10 summarises the S/MTOR of the transformer at tap 11 when using DTR as the 100 % pre-fault reference. The results follow the same general trends as those obtained with NTR: ratings decrease with increasing AAT and with longer overloading duration. However, because DTR is typically higher than NTR, the resulting per-unit ratings are slightly lower for a given percentage pre-fault loading (since the base

loading is larger), leading to a more conservative utilisation margin. The table highlights that significant additional loading capacity is still available for short durations, with ratings exceeding 2.0 PU for 3-to-5-minute overloads at low and moderate AATs, even when using the DTR as the reference.

Table 4.10: Short-Term and Medium-Term Overloading Ratings of Power Transformer at Tap Position 11 with variation of Ambient Air Temperatures, Pre-Fault Loading Percentage in accordance with Dynamic Thermal Ratings

AAT (°C)		-30	-20	-10	0	10	20	30	40	50
Pre-Fault DTR (PU)		1.615	1.545	1.470	1.390	1.305	1.210	1.115	1.010	0.900
Post-Fault DTR (PU)		1.775	1.71	1.635	1.565	1.485	1.405	1.32	1.24	1.14
Pre-fault loading%	**Duration (min)**	Pre-DTR (98°C) S/MTOR at Tap 11 in PU (1PU=240MVA/346A/1043A, Power at 1PU primary voltage/HV Current/LV Current)								
100% corresponds to		1.615	1.545	1.470	1.390	1.305	1.210	1.115	1.010	0.900
-	**inf**	1.775	1.71	1.635	1.565	1.485	1.405	1.32	1.24	1.14
85%	**360**	1.775	1.71	1.64	1.56	1.485	1.41	1.33	1.24	1.14
	60	1.885	1.83	1.76	1.69	1.615	1.54	1.47	1.38	1.29
	20	1.995	1.95	1.88	1.82	1.745	1.68	1.6	1.52	1.43
	10	2.045	2	1.94	1.88	1.815	1.74	1.67	1.59	1.51
	5	2.085	2.05	1.99	1.94	1.875	1.81	1.74	1.66	1.58
	3	2.145	2.11	2.05	1.99	1.925	1.87	1.8	1.72	1.63
75%	**360**	1.775	1.71	1.64	1.57	1.485	1.41	1.33	1.24	1.14
	60	1.925	1.87	1.8	1.73	1.655	1.58	1.5	1.41	1.32
	20	2.045	2	1.94	1.88	1.805	1.73	1.66	1.57	1.48
	10	2.095	2.06	2	1.95	1.885	1.81	1.74	1.65	1.56
	5	2.145	2.11	2.06	2.01	1.945	1.89	1.81	1.73	1.64
	3	2.215	2.18	2.14	2.08	2.015	1.95	1.88	1.8	1.7
65%	**360**	1.775	1.71	1.64	1.57	1.485	1.41	1.33	1.24	1.14
	60	1.955	1.9	1.83	1.76	1.685	1.61	1.53	1.43	1.34
	20	2.085	2.05	1.99	1.93	1.855	1.78	1.71	1.62	1.52
	10	2.125	2.1	2.05	2	1.935	1.87	1.8	1.71	1.61
	5	2.175	2.15	2.11	2.07	2.005	1.94	1.87	1.79	1.7
	3	2.255	2.24	2.19	2.15	2.085	2.02	1.95	1.86	1.76

Table 4.11 presents the DTR-based S/MTOR results for tap position 15. As with Table 4.10, the ratings decrease with increasing AAT and with longer overloading durations, but the absolute values are slightly lower than those at tap 11 because of the

higher LV current (1105 A at 1 PU) and the resulting increase in winding losses at this tap. Compared with the NTR-based results, the DTR reference again yields slightly lower per-unit ratings for the same pre-fault percentage, since the base loading is higher. Nonetheless, Table 4.10 confirms that significant short-term loading capability remains available, with ratings exceeding 2.0 PU for 3 to 5-minute overloads at low to moderate AATs, even under this more conservative DTR reference.

Table 4.11: Short-Term and Medium-Term Overloading Ratings of Power Transformer at Tap Position 15 with variation of Ambient Air Temperatures, Pre-Fault Loading Percentage in accordance with Dynamic Thermal Ratings

AAT (°C)		-30	-20	-10	0	10	20	30	40	50
Pre-Fault DTR (PU)		1.570	1.500	1.425	1.345	1.265	1.175	1.085	0.980	0.875
Post-Fault DTR (PU)		1.725	1.66	1.59	1.52	1.445	1.365	1.29	1.2	1.11
Pre-fault loading%	**Duration (min)**	Pre-DTR (98°C) S/MTOR at Tap 15 in PU (1PU=240MVA/346A/1105A, Power at 1PU primary voltage/HV Current/LV Current)								
100% corresponds to		1.570	1.500	1.425	1.345	1.265	1.175	1.085	0.980	0.875
-	**inf**	1.725	1.66	1.59	1.52	1.445	1.365	1.29	1.2	1.11
85%	**360**	1.72	1.66	1.585	1.515	1.445	1.365	1.29	1.2	1.11
	60	1.83	1.77	1.715	1.645	1.575	1.495	1.42	1.34	1.26
	20	1.94	1.88	1.825	1.765	1.695	1.625	1.56	1.47	1.4
	10	1.98	1.93	1.885	1.825	1.755	1.695	1.62	1.55	1.47
	5	2.02	1.98	1.935	1.875	1.815	1.755	1.69	1.61	1.53
	3	2.08	2.04	1.985	1.935	1.875	1.805	1.74	1.67	1.59
75%	**360**	1.72	1.66	1.595	1.515	1.445	1.365	1.29	1.2	1.11
	60	1.87	1.81	1.745	1.675	1.605	1.535	1.45	1.37	1.28
	20	1.99	1.94	1.885	1.825	1.755	1.685	1.61	1.53	1.44
	10	2.03	1.99	1.945	1.895	1.825	1.755	1.69	1.61	1.52
	5	2.08	2.04	2.005	1.955	1.895	1.825	1.76	1.68	1.6
	3	2.16	2.11	2.075	2.015	1.955	1.895	1.82	1.74	1.66
65%	**360**	1.72	1.66	1.595	1.525	1.445	1.365	1.29	1.2	1.11
	60	1.89	1.84	1.775	1.705	1.635	1.555	1.48	1.39	1.3
	20	2.02	1.98	1.925	1.865	1.805	1.735	1.66	1.57	1.48
	10	2.07	2.03	1.995	1.945	1.885	1.815	1.74	1.66	1.57
	5	2.1	2.08	2.045	2.005	1.955	1.885	1.82	1.74	1.65
	3	2.2	2.17	2.125	2.085	2.025	1.955	1.89	1.81	1.72

The results show that when the 100 % pre-fault loading reference is changed from NTR to DTR for different AATs, the actual pre-fault loading in MVA becomes higher. This results in a higher initial temperature at the start of the post-fault period, effectively reducing the available overloading margin of the transformer. However, this reduction is relative, as the pre-fault loading reference under DTR generally represents a higher continuous rating, except under very high AAT conditions, meaning that the transformer is already operating closer to its thermal limit before the overload event.

4.2.5 Cyclic Thermal Ratings of Power Transformers

The CTR of the power transformer is calculated by applying the 24-hour cyclic loading and SI profiles. The calculation is initialised at the respective ambient temperature. Also, the temperature limit for the calculation of the CTR can be raised from the continuous temperature limit (98°C) to the emergency limit (122°C) [3], [14]. An example of the HST variation for the determination of the CTR for the example power transformer under nominal tap position (11) and 30°C AAT, no SI is shown in Figure 4.20. The 24-hour loading cycle is repeated 3 times for the CTR calculation of the example power transformer.

The results of the calculated CTR of the example power transformer are shown in Figure 4.21, its respective DTR under different AAT, SI and tap positions are also shown in the background for comparison reasons.

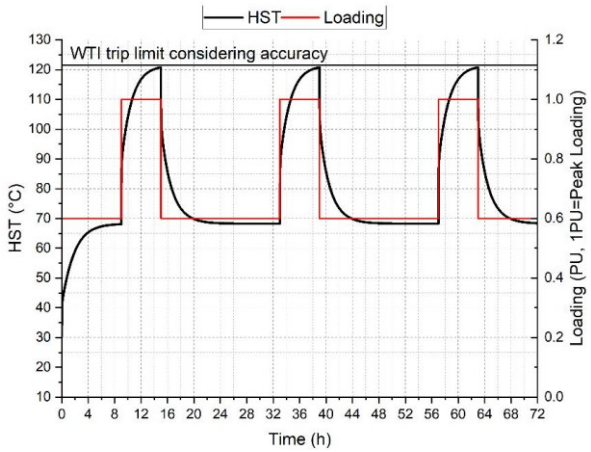

Figure 4.20: Example of the HST variation and the standard cyclic loading profile for the example power transformer under nominal tap position (11) at 30°C AAT.

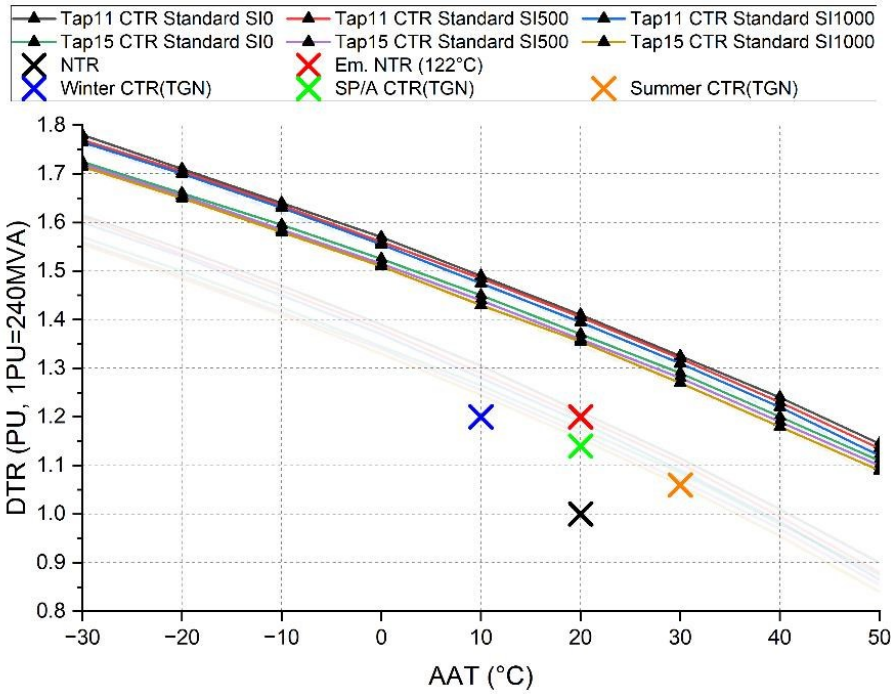

Figure 4.21: The calculated CTR in PU of base MVA of the power transformer under OFAF cooling mode for tap positions 11 and 15 with the variation of AAT and SI.

The results indicate that the CTR of the power transformer benefits from the combined effects of a higher HST limit, a non-constant peak loading profile, and a realistic SI profile. The influence of solar heating is less pronounced under CTR, as it does not assume constant, indefinite solar exposure as in DTR calculations. Overall, the use of CTR results in a significant increase in the permissible rating compared with DTR for the example power transformer.

4.3 Conclusions

This chapter presents an improved thermal model of the transformer using references from a transmission transformer. The new thermal model considered the significant ambient conditions and most of the transformer operation conditions and controlling mechanisms. The heat inputs are corrected in real-time based on temperature, tap position, and the supplied voltage. The additional ports for heat generated by the tertiary stabilisation winding and auxiliaries are also included.

The results of the calculated HST compared to the WTI and the calculated TOT compared to the measured TOT show that the model has good accuracy across different cooling modes and during the transient period between switching cooling modes, provided the values of HSTR and TOTR at the rated conditions of the transformer are available.

The results of the missing-parameter estimation algorithm and the thermal model demonstrated their capability to simulate variations in transformer temperatures, accounting for ambient conditions, tap-changing operations, and switching between cooling modes. The introduction of the separation of the temperature reference (ambient temperature) for the transformer tank and cooler enables the modelling of more complex transformers. The cooling model switch extends the operation condition modelling to account for different cooling modes.

From the evaluation results, the impact of natural wind speed under conservative assumptions is negligible, whereas the effect of high solar irradiance is alarming, potentially exceeding the WTI accuracy and causing the transformer to trip. Then, the DTR results using current and power as units at the two tap positions indicate that the rating unit should be in apparent power (MVA) rather than current when a voltage-manipulating device is present. However, the output voltage should also be reported alongside the apparent power rating. Lastly, the evaluation of DTR, S/MTOR, and CTR demonstrates the potential of power transformers across a wide range of ambient and operational conditions, using both effective and conservative approaches.

Chapter 5

AC Power Cables

AC power cables, or cables, are electrically insulated conductors used to transmit power in place when the installation of bare-conductor OHLs becomes an electrical hazard. Cables can be exposed to the air or buried underground. Buried cables are typically classified as directly buried cables (DBC), cables in ducts or conduits, cables in filled troughs (FTC), or cables installed in tunnels.

Deeply buried cables (1m depth) are largely unaffected by ambient conditions such as wind speed and solar irradiance. However, cables exposed to air can experience significant influence from both. In some installations, exposure to solar radiation may be minimal (e.g., shaded areas), or the surrounding structures may obstruct the wind flow, making the cooling effects of WS highly variable and site dependent. Offshore cables, which operate in entirely different thermal environments and are governed by distinct temperature and environmental constraints, are outside the scope of this thesis. Therefore, this chapter focuses exclusively on the thermal performance and rating methodologies of onshore AC power cables.

The temperature limit of the cable is determined by its maximum conductor temperature, violating or exceeding this temperature limit will cause irreversible damage to the cable insulation. This could lead to severe consequences, for instance, a significantly reduced lifetime, increased likelihood of faulting, and even becoming a source of electrical hazard. So, the cable rating needs to be evaluated using a careful, conservative thermal modelling. Any exceedance of the conductor temperature limit should not be allowed, in accordance with the cable thermal model.

This chapter presents the methodology for thermal modelling and rating assessment of AC power cables. Section 5.1 describes the modelling approaches for the three main cable types considered in this study: directly buried cables (Section 5.1.1),

filled trough cables (Section 5.1.2), and exposed cables (Section 5.1.3). Section 5.2 discusses the thermal rating evaluations, including steady-state, dynamic, and cyclic conditions, as well as short- and medium-term overloading scenarios. The chapter concludes in Section 5.3 with a summary of key findings and implications for cable rating assessment.

5.1 Methodology of Thermal Modelling for Cables

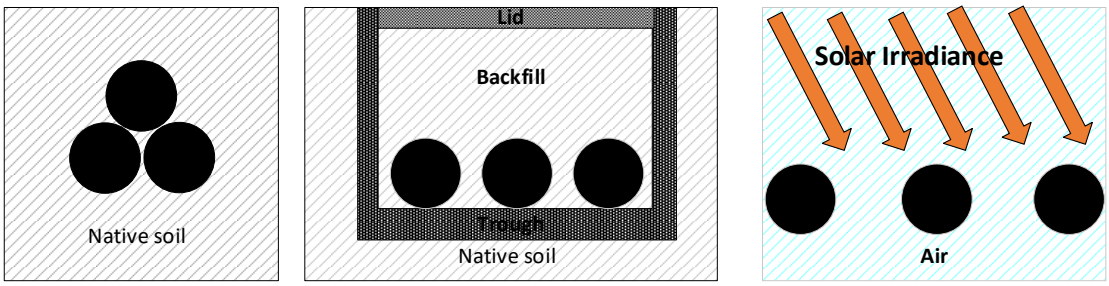

Figure 5.1: Cable examples and their ambient summary used in this thesis.

In this study, cables and their ratings are evaluated under three distinct ambient environments as defined and summarised in Figure 5.1 above, defined by their installation configuration:

- Directly Buried Cable (DBC) – Installed at approximately 1 m depth in trefoil formation, exchanging heat primarily with the surrounding soil. Thermal rating is governed by relatively stable soil temperature and soil thermal resistivity.
- Filled Trough Cable (FTC) – Installed at shallow depth (~0.3 m) in a spaced flat formation within a filled trough. The reduced cover depth and thermal properties of the backfill result in more pronounced diurnal temperature fluctuations compared to DBC.
- Exposed Cable (ExpoC) – Installed in spaced layout with sections exposed to ambient air. Cooling is directly influenced by air temperature, wind speed, and solar irradiance, making this the most weather-sensitive configuration.

Overall, the installation configuration sets the effective ambient boundary condition (soil, filled trough, or open air), which directly determines the thermal behaviour and rating of the cable system. It is to be noted that there are other configurations, such as a conduit or tunnel with forced ventilation capability, etc. However, these are not considered at this stage. In our analysis, it is assumed that the cables are first exposed, then filled in through, and lastly directly buried, meaning that the cables themselves form a circuit.

5.1.1 Thermal Model of Directly Buried Cables

The thermal model of DBC is adapted from the publication [57]. This publication presents a thermal model of the directly buried cable, which is divided into three parts and four heat-transfer phases, as shown in Figure 5.2. The three parts are the cable conductor, insulation, and sheath and jacket (considered as one part), and the surrounding environment. The four heat-transfer phases are labelled from A to D, and each has its own thermal resistance and thermal capacity.

The conductor part of the model consists of the total heat input to the model $q_{in,loss,t}$, the thermal capacity of the conductor and part of the thermal capacity of the insulation, sheath and jacket becomes the thermal capacity of phase A as $mCp_{A,db}$. The second part consists of the thermal resistance from the insulation, sheath and jacket of the cable $R_{th,A,db}$, and the remaining thermal capacity of the insulation, sheath and jacket of the cable and part of the thermal capacities of the environment $mCp_{B,db}$. The last part is the thermal resistance of the surrounding environment and its thermal capacities. The thermal resistances of the surrounding cylindrical environment are divided into three regions, containing the thermal resistances from $R_{th,B,db}$ to $R_{th,D,db}$. The thermal capacities of the surrounding environment, except for the part that is included in the B phase, the remaining are divided into two parts: $mCp_{C,db}$ and $mCp_{D,db}$. At the very end is the temperature reference of the model, which is the ambient temperature θ_a. For the DBC considered in this thesis, it is the AST1m.

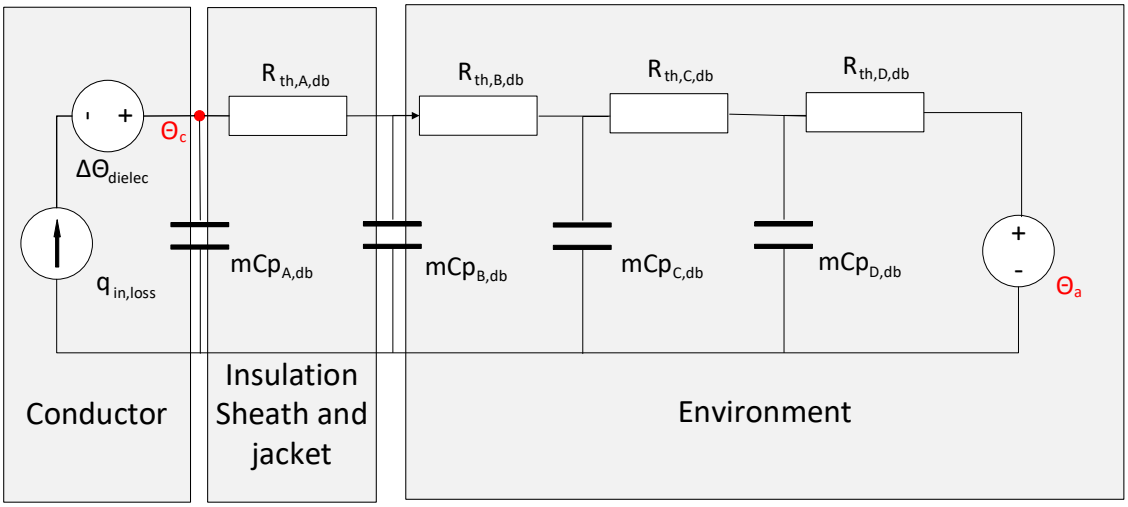

Figure 5.2: Thermal model for directly buried cables.

The thermal capacity of the conductor and part of the thermal capacity of the insulation, sheath, and jacket are the thermal capacity of phase A, which is denoted as $mCp_{A,db}$. This can be calculated by:

$$mCp_{A,db} = mCp_c + MEPC(r_i, r_c) \cdot mCp_i \tag{213}$$

where: mCp_c and mCp_i are the thermal capacities of the conductor and insulation in $J/(m \cdot K)$, respectively; r_i and r_c are the radius of the conductor and the main insulation in m, respectively. $MEPC$ is the function of the *modified equivalent π circuit*, expressed as:

$$MEPC(r_o, r_{inner}) = \frac{1}{2 \cdot \ln\left(\frac{r_o}{r_{inner}}\right)} - \frac{1}{\frac{{r_o}^2}{{r_{inner}}^2} - 1} \tag{214}$$

where: r_o and r_{inner} are the outer and the inner radius of the section, respectively.

The thermal resistance from the insulation, sheath and jacket of the cable $R_{th,A}$ is calculated by:

$$R_{th,A,db} = R_{th,1} + R_{th,3} \cdot (1 + \lambda_1) \tag{215}$$

where: $R_{th,1}$ and $R_{th,3}$ are the thermal resistances of the insulation and jacket in K/W, respectively; λ_1 is the ratio of the sheath to the conductor losses or the sheath loss factor. The remaining thermal capacity of the insulation, sheath and jacket of the cable and part of the thermal capacities of the environment mCp_B is expressed as:

$$mCp_{B,db} = (1 - MEPC(r_e, r_c)) \cdot (mCp_i + \frac{mCp_s + mCp_j}{1 + \lambda_1}) + MEPC(r_{B,db}, r_e) \cdot \frac{\pi({r_{B,db}}^2 - {r_e}^2)}{k_{tf}\rho_{th,s}\delta_s(1 + \lambda_1)} \quad (216)$$

where: mCp_s and mCp_j are the thermal capacities of the sheath and jacket in $J/(m \cdot K)$, respectively; r_e is the overall radius of the cable in m; $r_{B,db}$ is the depth of the B phase of the environment in m, set to the value of around $3 \cdot r_e$; $\rho_{th,s}$ is the thermal resistivity of the homogenous environment in $K \cdot m/W$; δ_s is the thermal diffusivity of the homogenous environment in m^2/s; k_{tf} is the scaling factor that adds the effect of the adjacent cables, which can be calculated as follows:

$$k_{tf} = 3 \cdot \frac{\ln\left(\frac{2L}{r_e}\right) - 0.63}{\ln\left(\frac{L}{r_e} + \sqrt{\left(\frac{L}{r_e}\right)^2 - 1}\right)} \quad (217)$$

where: L is the burial depth to the centre of the trefoil of the cables; r_e is the overall diameter of the cable or the cable-conduit complex. For a directly buried cable, $r_e = r_j$.

The thermal resistance of the surrounding environment at the B phase $R_{th,B,db}$ is expressed as:

$$R_{th,B,db} = \frac{k_{tf} \cdot \rho_{th,s} \cdot (1 + \lambda_1)}{2\pi} \cdot \ln\left(\frac{r_{B,db}}{r_e}\right) \quad (218)$$

The thermal capacity of the surrounding environment at the C phase mCp_C is calculated by:

$$mCp_{C,db} = (1 - MEPC(r_{B,db}, r_e)) \cdot \frac{\pi({r_{B,db}}^2 - {r_e}^2)}{k_{tf}\rho_{th,s}\delta_s(1+\lambda_1)} + MEPC(r_{C,db}, r_{B,db}) \cdot \frac{\pi({r_{C,db}}^2 - {r_{B,db}}^2)}{k_{tf}\rho_{th,s}\delta_s(1+\lambda_1)} \quad (219)$$

where: $r_{C,db}$ is the depth of the C phase of the environment in m.

The thermal resistance of the surrounding environment at the C phase $R_{th,C,db}$ is calculated by:

$$R_{th,C,db} = \frac{k_{tf} \cdot \rho_{th,s} \cdot (1+\lambda_1)}{2\pi} \cdot \ln\left(\frac{r_{C,db}}{r_{B,db}}\right) \quad (220)$$

The thermal resistance of the surrounding environment at the D phase $R_{th,D,db}$ is determined by:

$$R_{th,D,db} = R_{th,4} \cdot (1+\lambda_1) - (R_{th,B,db} + R_{th,c}) \quad (221)$$

where: $R_{Th,4}$ is the thermal resistance of the environment for the cable, and its value can be calculated by the standard [5].

The thermal capacity of the surrounding environment at D phase $mCp_{D,db}$ is expressed as:

$$mCp_{D,db} = (1 - MEPC(r_{C,db}, r_{B,db})) \cdot \frac{\pi({r_{C,db}}^2 - {r_{B,db}}^2)}{k_{tf}\rho_{th,s}\delta_s(1+\lambda_1)} + MEPC(r_{env}, r_{C,db}) \cdot \frac{\pi({r_{env}}^2 - {r_{C,db}}^2)}{k_{tf}\rho_{th,s}\delta_s(1+\lambda_1)} \quad (222)$$

where: r_{env} is the radius of the equivalent cylindrical environment, calculated by:

$$r_{env} = r_e \cdot \exp\left(\frac{2 \cdot \pi \cdot R_{th,4}}{k_{tf} \cdot \rho_s}\right) \quad (223)$$

5.1.2 Thermal Model of Filled Trough Cables

The thermal model of the FTC is shown in Figure 5.3 and was developed in accordance with [4], [5], [57], [59], [60]. The FTC can be modelled as a directly but shallowly buried cable with an extra layer of concrete trough and lid. The cable conductor, insulation, sheath and jacket are treated as the same as in [57]. The concrete trough and lid are modelled according to [59], [60]. The FTC is usually buried in a concrete trough, filled to a depth of 0.3m with selected fill, and covered by a concrete lid, which is exposed to SI. The effect of WS on the trough lid is unknown, so it is not included. Also, the WS could only help cool the thermal bodies considered in the model, thereby improving thermal performance. The current model is very conservative because it excludes the convective cooling effect from the WS.

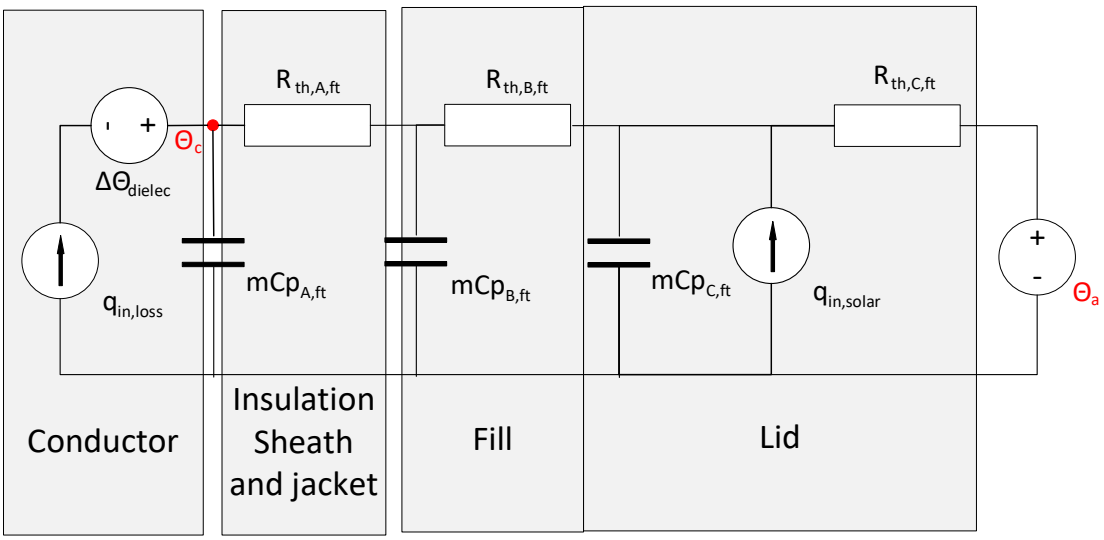

Figure 5.3: Thermal model for filled trough cables.

The FTC is usually buried in a filled concrete trough at a depth of 0.3m. The trough is filled with selected fill and covered by a concrete lid, which is exposed to SI [8].

The parameters at phase A, $mCp_{A,ft}$ and $R_{th,A,ft}$, parameters at phase B $mCp_{B,ft}$ and $R_{th,B,ft}$ are calculated using the same equations (213)-(216) and (218) as in DBC, but with different parameters due to changes in layout when installed in a filled trough and differences in burial depth. The FTC is buried much shallower than DBC, so the

radius of phase B is identical to the burial depth. The difference is the thermal resistance and thermal capacitance of the concrete trough with the lid in phase C, calculated by:

$$R_{th,C,ft} = \frac{k_{tf} \cdot \rho_{th,conc} \cdot (1 + \lambda_1) \cdot T_{\text{conc}}}{A_{conc}} \tag{224}$$

$$mCp_{th,C,ft} = \text{Cp}_{\text{conc}} \cdot \frac{\rho_{conc}}{A_{cross,conc}} \tag{225}$$

where: $\rho_{th,conc}$ is the thermal resistivity of the concrete material; T_{conc} is the thickness of the concrete trough wall; A_{conc} is the area of conduction per meter length of the trough; Cp_{conc} is the specific heat of the concrete material; ρ_{conc} is the density of the concrete material; and $A_{cross,conc}$ is the cross-sectional area of the trough.

5.1.3 Thermal Model of Exposed Cables

The thermal model of the exposed cables is in Figure 5.4, it is a hybrid model that combines the model from the cable conductor to the cable surface in [4], [5], [57] and the model from the cable surface to the ambient (air) in [9] by assuming the cable surface layer is similar to the OHL surface.

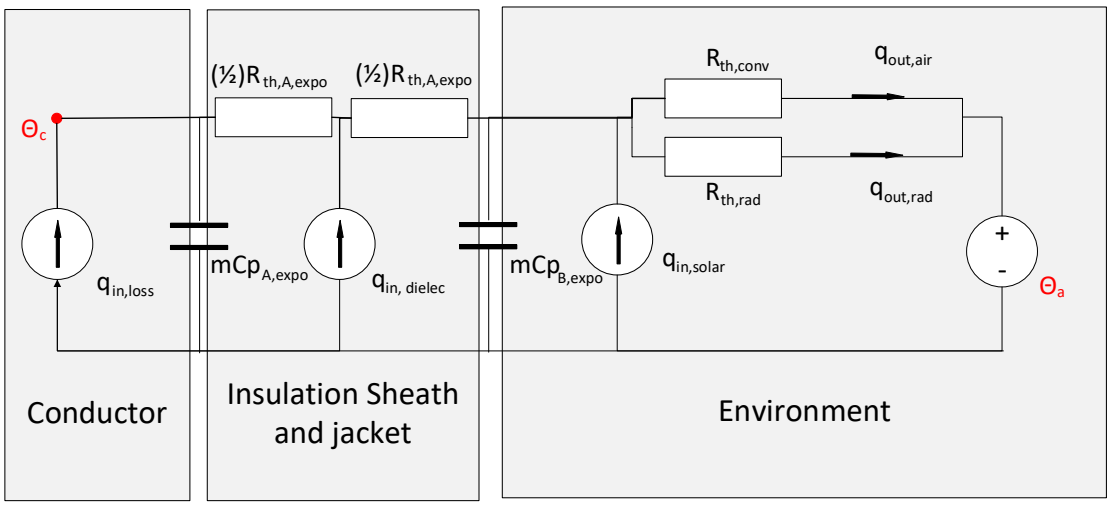

Figure 5.4: Thermal model for exposed cables.

The calculation of the parameters $R_{thA,expo}$, $mCp_{A,expo}$ and $mCp_{B,expo}$ in the cable conductor part and the cable insulation, sheath and jacket parts are also identical to those present in DBC (213)-(216) and (218). The third phase, from the cable surface to ambient air, is calculated assuming the cable surface is similar to the surface of OHLs. Thus, in the environment phase, the heat lost from the cable surface to the ambient and the heat input from solar irradiance are calculated using the same equation as present in (227)-(235).

5.2 Thermal Ratings of Cables

Information on cables for the Braintree-Pelham circuit is not available, and it is likely to be on the LV side. It is assumed that a cable is present on the LV side of the substation, based on the 400/132kV 240 MVA substation with a transformer on-load tap changer (OLTC) capable of changing the turn ratio over a range of +15/-5%. The maximum current on the LV side under the rated condition is 1105A. The cables are selected based on the respective voltages, insulation levels, and nameplate current ratings for the LV side of the substation.

For the example circuit of Pentir-Trawsfynydd, the rated voltage is 400kV, with a double-circuit cable and an OHL composite. The double-circuit cable is rated at 1638A (1135 MVA) for winter/normal cold rating season and 1432A (992 MVA) for summer/normal hot rating season. The information about the cable is unknown, but a cable with similar ratings is selected for the following assessment. Table 5.1 shows the cable specifications used in this thesis for both circuits.

5.2.1 Steady-State Conductor Temperatures for Cables

To evaluate cable DTR, it is vital to calculate the SST of the cable conductors. As there are three cable installation methods, the DBC results are shown first, followed by FTC, and lastly ExpoC. When calculating the SST, the thermal capacitances can be ignored because the SST is calculated in the steady-state.

Table 5.1: Specifications of cables used in the assessment [4], [5], [6], [59], [100], [101].

Cable Type	138kV single copper core cable XLPE-Cu-XLPE	400 kV single copper core cable XLPE-Cu-APL
Conductor area (mm^2)	2.000E+03	1.000E+03
Insulation thickness (m)	1.700E-02	2.900E-02
Outer radius of insulation (m)	4.830E-02	4.805E-02
Alloy sheath thickness (m)	4.150E-03	7.358E-03
Outer radius of sheath (m)	5.245E-02	5.541E-02
Non-metal sheath (Jacket) thickness (m)	6.500E-03	3.592E-03
Overall radius (m)	5.895E-02	5.900E-02
DC resistance at 20℃ (Ω/m)	1.490E-05	1.760E-05
AC resistance at 90℃ (Ω/m)	2.040E-05	2.760E-05
Thermal resistivity of insulation (K*m/W)	2.564	2.564
Thermal resistivity of jacket (K*m/W)	3.5	3.5
Specific heat capacity of conductor (J/(kg*K))	380	380
Specific heat capacity of insulation (J/(kg*K))	2200	2200
Specific heat capacity of sheath (J/(kg*K))	380	380
Specific heat capacity of jacket (J/(kg*K))	2200	2200
Maximum conductor temperature (℃)	90	90
Density of conductor material (kg/m^3)	8960	8960
Density of insulation material (kg/m^3)	944	944
Density of sheath material (kg/m^3)	8960	8960
Density of jacket material (kg/m^3)	1330	1330
Dielectric losses (W)	7.68	18.10
Buried depth, directly (m)	1	1
Buried depth, in filled trough (m)	0.25	0.25
Area of trough wall (m^2/m)	2.12	2.12
Cross-sectional area of trough wall (m^2)	0.3613	0.3613
Area of trough lid (m^2/m)	1.018	1.018
Absorptivity of trough lid	0.5	0.5
Absorptivity of cable surface	0.9	0.9
Heat capacitance of conductor (J/K) *	6.81E3	3.40E3
Heat capacitance of insulation(J/K) *	1.11E4	1.30E4
Heat capacitance of sheath (J/K) *	4.47E3	8.14E3
Heat capacitance of jacket (J/K) *	6.66E3	3.78E3

*Calculated using specific heat, density and radius assuming cylinder and tube objects.

5.2.1.1 Steady-State Conductor Temperatures of Directly Buried Cables

The DBC is usually buried at 1m depth, so it is unaffected by SI and WS. However, there is a hysteresis relation between the AAT and AST1m, as the focus point of this thesis is the effect and impact of the heat wave on the system/network/circuit components. Also, for conservative reasons, the S/NH (summer-to-winter) assumption is used for the relationship between AAT and AST1m. The AAT ranges from -30℃ to 50℃, and the results are shown in Figure 5.5. The relationship between AAT and AST under the S/NH assumption is also shown.

As AAT and loading increase (0.65PU-1PU), conductor and soil surface temperatures rise correspondingly. Under Summer STR reference AAT, loading at 1PU approaches the conductor temperature limit, whereas lower loading levels maintain additional thermal margin. Soil surface temperatures at high loads may approach the dry-out threshold, reducing thermal capacity. The effect of current loading is more pronounced for the 138 kV 2000 mm² DBC compared to the 400 kV 1000 mm² DBC. This difference arises because the 400 kV cable has significantly higher dielectric losses, which remain constant, thereby reducing the relative impact of load variation on its thermal response.

Figure 5.6 shows the variation of cable surface soil temperature with AAT at four loading levels (1.0–0.65 PU), plotted alongside the 1 m average soil temperature (AST1m). Results indicate that SST closely tracks AST1m but is elevated under higher current loading. Importantly, the SST crosses the critical dry-out temperature (~50 °C) even at relatively moderate AAT (near 0 °C) under 1.0 PU loading.

If soil dry-out occurs, thermal resistivity increases sharply, severely reducing the cable's ability to dissipate heat. This dry-out creates a positive feedback loop (hotter cable → drier soil → hotter cable) and may lead to thermal runaway if loading is not curtailed.

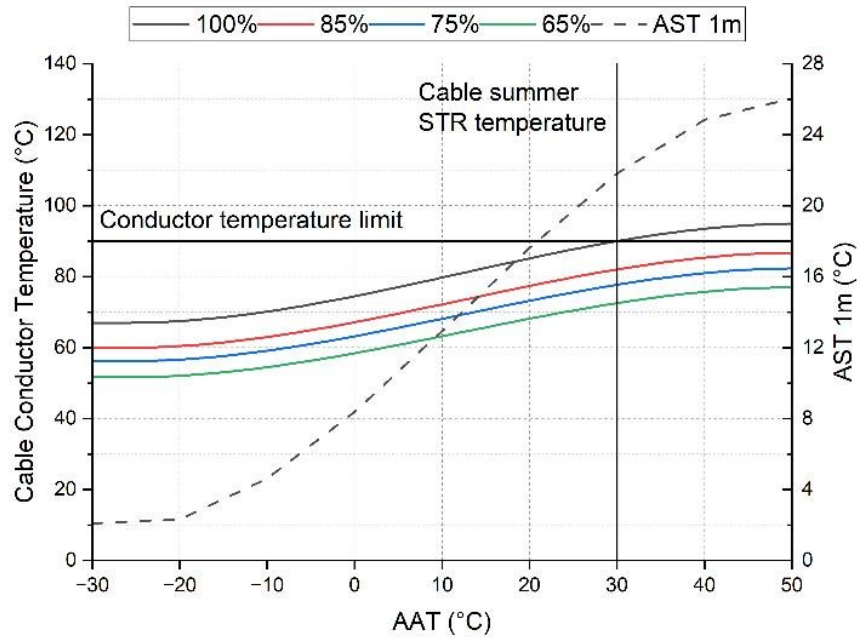

a) 138kV 2000mm^2, Braintree

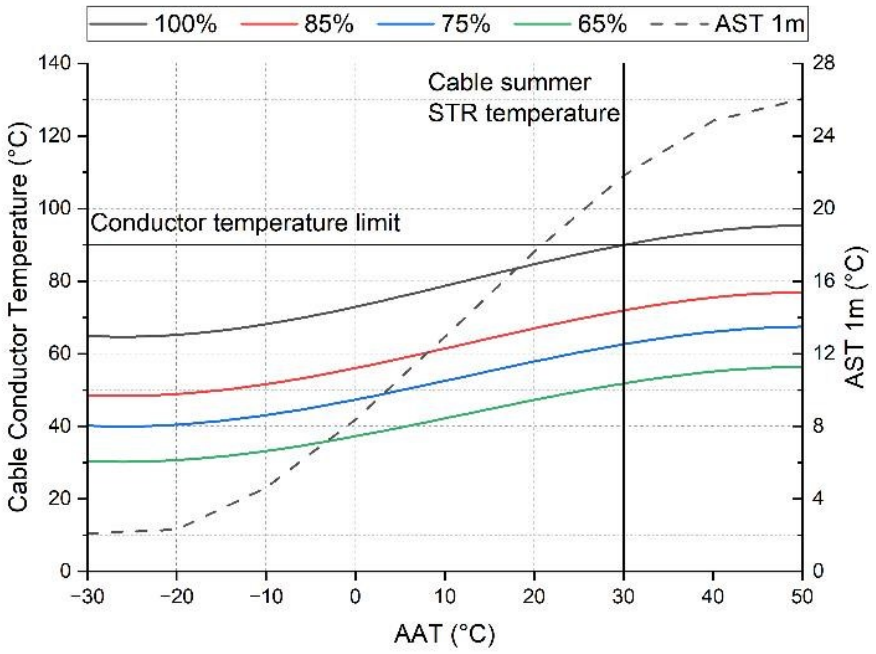

b) DBC and 400kV 1000mm^2, Pentir-Trawsfynydd

Figure 5.5: Variation of conductor temperature with the variation of AAT for a single 138kV 2000mm^2 (a) DBC and 400kV 1000mm^2 (b) DBC when loaded with respective 1PU, 0.85PU, 0.75PU and 0.65PU constant summer STR current.

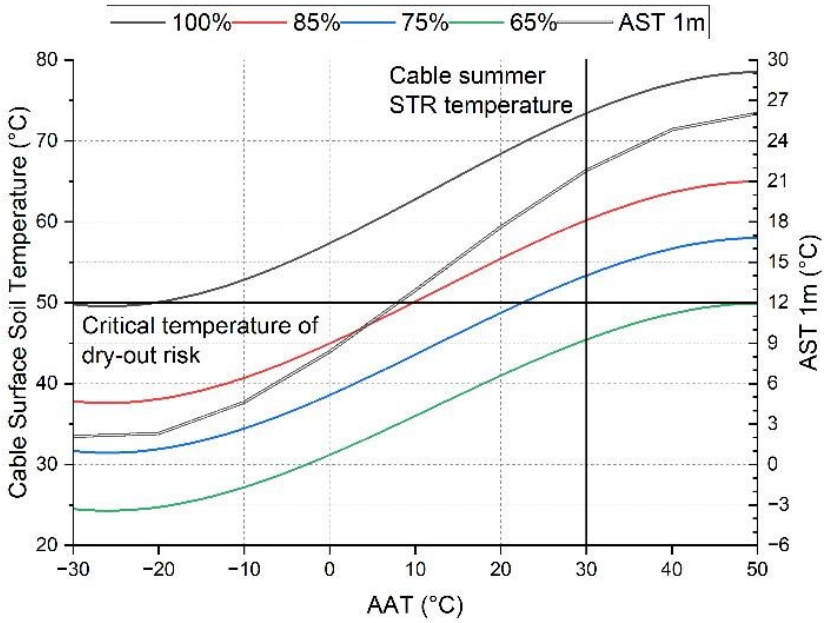

a) 138kV 2000mm^2, Braintree

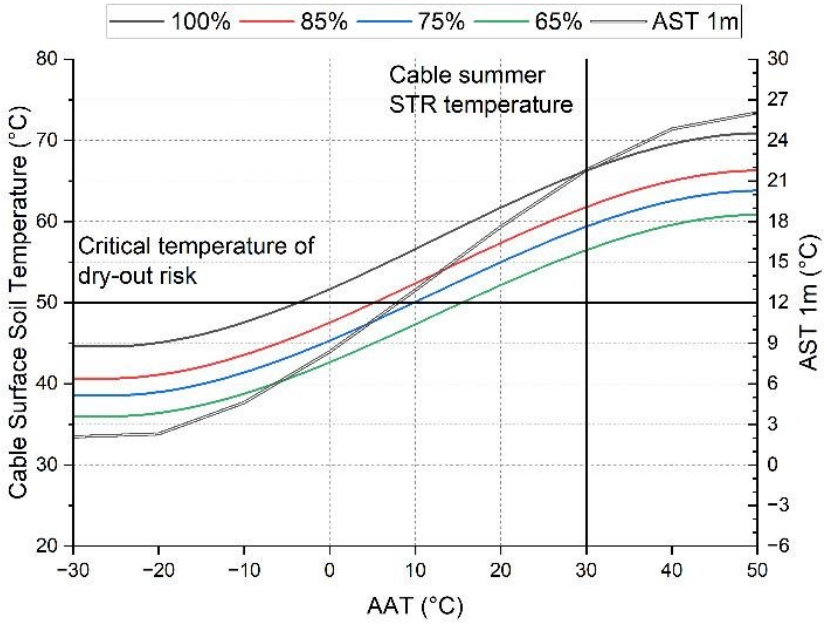

b) 400kV 1000mm^2, Pentir-Trawsfynydd

Figure 5.6: Variation of soil temperature near the cable surface with the variation of AAT for a single 138kV 2000mm^2 (a) DBC and 400kV 1000mm^2 (b) DBC when loaded with respective 1PU, 0.85PU, 0.75PU and 0.65PU constant summer STR current.

Overall, these results highlight that:

- Dry-out risk is not limited to extreme summer AAT – it can occur even in cold ambient conditions if loading is sustained.
- Proactive soil and thermal monitoring, along with potential derating, are required to avoid exceeding safe operating limits during prolonged high-load periods.
- This effect is more noticeable in 138 kV DBC, where current loading plays a larger role, whereas in 400 kV DBC constant dielectric losses dominate and reduce the relative sensitivity to load changes.

Figure 5.7 presents the conductor temperature profiles for the 138 kV 2000 mm² and 400 kV 1000 mm² DBCs, respectively, plotted against AAT for four loading levels (1.0–0.65 PU). When the soil transitions into a dry-out state, its thermal resistance rises significantly (from approximately 1.2 K·m/W to ~3 K·m/W). Under such conditions, conductor temperatures rise dramatically for the same summer STR current. If no corrective action is taken, this can lead to extreme overheating and potential thermal damage, as heat dissipation into the surrounding soil is severely restricted. The results demonstrate that:

- Thermal margins collapse rapidly under dry-out conditions, even at moderate AAT.
- Continuing to operate at STR loading levels in dry-out conditions would exceed conductor temperature limits.

This necessitates a substantial de-rating of the DBC during dry-out events to maintain safe operating temperatures and prevent insulation degradation.

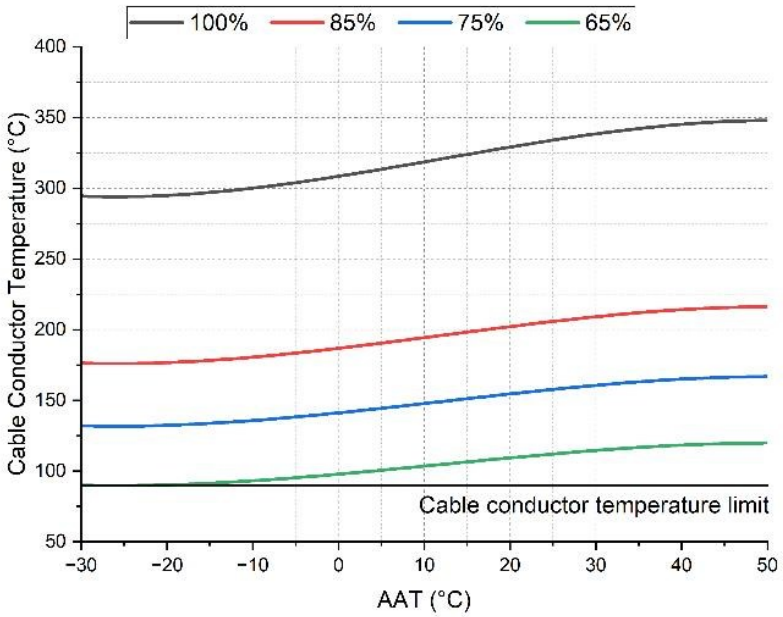

a) 138kV 2000mm^2, Braintree

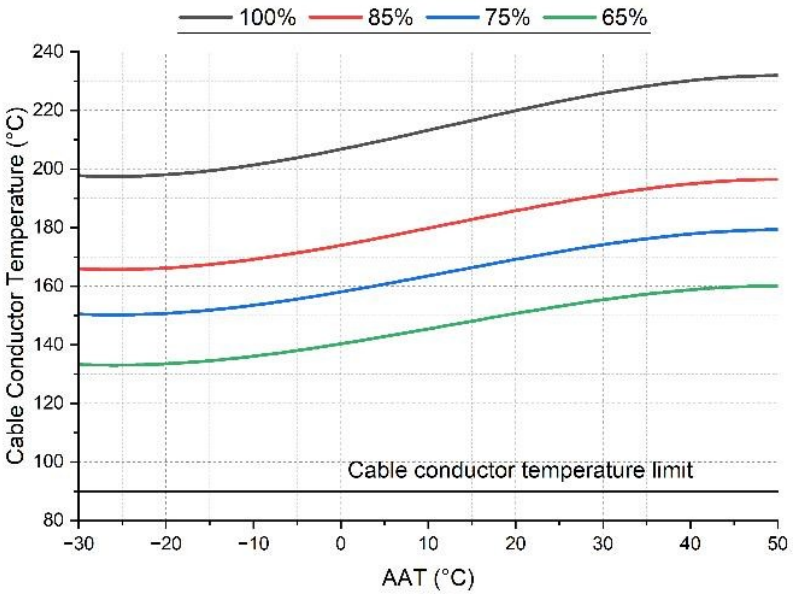

b) 400kV 1000mm^2, Pentir-Trawsfynydd

Figure 5.7: Variation of cable conductor temperature under dry-out conditions with variation of AAT for a single 138kV 2000mm^2 (a) DBC and 400kV 1000mm^2 (b) DBC when loaded with respective 1PU, 0.85PU, 0.75PU and 0.65PU constant summer STR current.

5.2.1.2 Steady-State Conductor Temperatures of Cables in Filled Trough

For conservative analysis, the variation in SST of FTCs with variations in AAT and SI when loaded with a current of 1PU to 0.65PU of summer STR and 1PU voltage, with the fill lid absorptivity set to 0.9, are shown in Figure 5.8 to Figure 5.9, with the cable conductor temperature limit marked. Their respective fill temperatures are also shown, with the dry-out critical temperature marked.

Figure 5.8 presents the steady-state conductor temperature variation with AAT for 138 kV 2000 mm² and 400 kV 1000 mm² FTC circuits, under multiple current loading levels (1.0–0.65 PU) and solar irradiance (SI) conditions (0, 500, 1000 W/m²).

Temperature Drivers: Solar irradiance is the dominant factor controlling conductor temperature in both FTC cables. Increasing SI from 0 → 500 → 1000 W/m² results in a much larger temperature rise than changing current loading from 0.65 → 1.0 PU. The shallower burial depth and partially enclosed trough design make FTC installations more sensitive to surface heat input than directly buried cables.

The results assume constant ambient conditions (indefinite SI), which is conservative because SI naturally varies diurnally. Concrete lid absorptivity was set at 0.9 to align with worst-case exposed cable assumptions. This significantly amplifies solar heat gain. Combining peak SI (1000 W/m²) with high absorptivity yields a highly conservative "upper-bound" temperature that may overestimate the risk of overheating in real operation. A more representative approach would apply an average SI (≈ 500 W/m²) with a realistic absorptivity (0.45–0.6) [102]. Since solar heating is proportional to SI and absorptivity, reducing absorptivity or scaling SI provides a more representative SI.

Both 138 kV and 400 kV FTCs are strongly solar driven, with the 138 kV case slightly more sensitive to current loading due to lower dielectric loss contribution. Thermal margin reduces substantially under high SI, particularly at 1PU loading, suggesting that summer peak conditions could bring conductor temperature close to its rating. Ignoring solar effects would be non-conservative, but continuously applying extreme SI would unnecessarily reduce available rating.

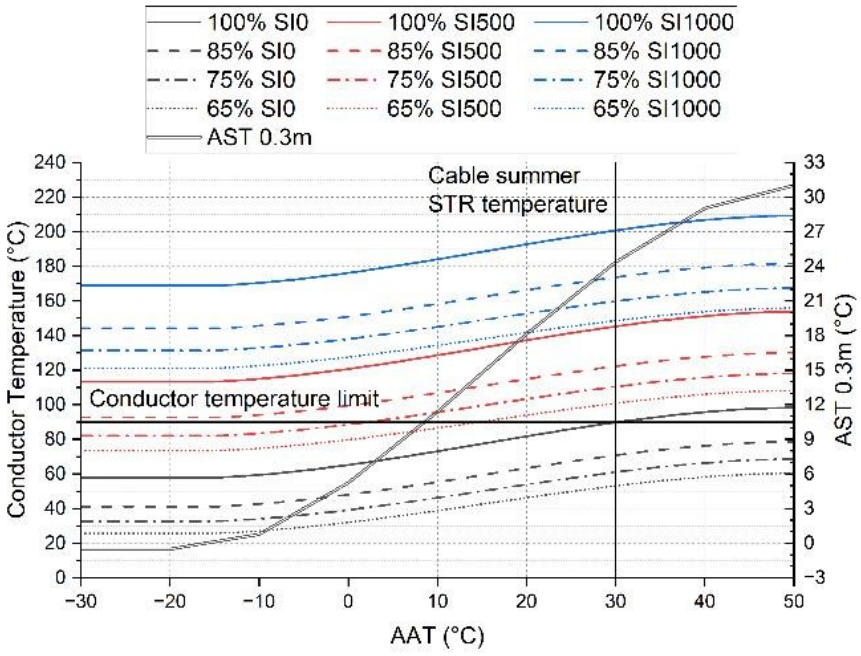

a) 138kV 2000mm^2, Braintree

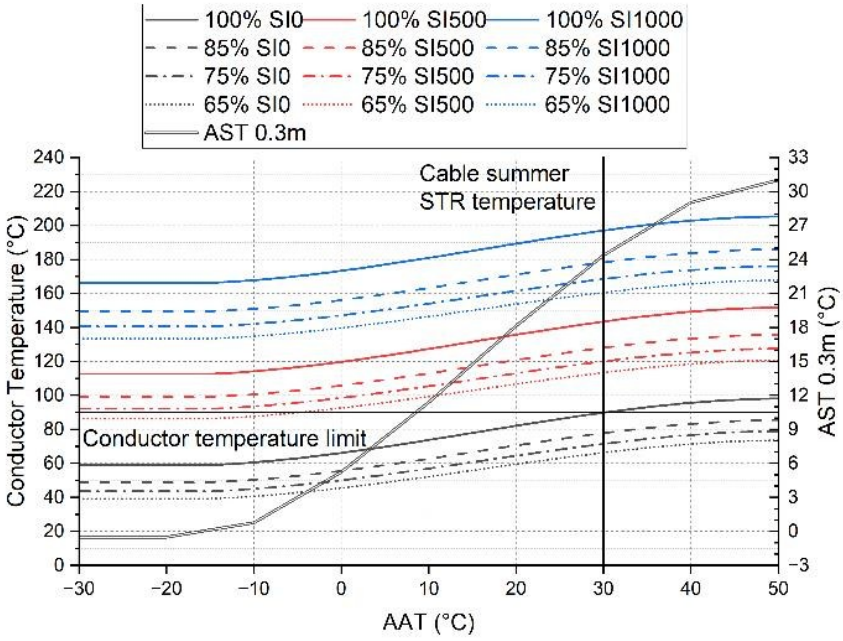

b) 400kV 1000mm^2, Pentir-Trawsfynydd

Figure 5.8: Variation of conductor temperature with the variation of AAT and SI for a single 138kV 2000mm^2 (a) FTC and 400kV 1000mm^2 (b) FTC when loaded with respective 1PU, 0.85PU, 0.75PU and 0.65PU summer STR current., using 0.9 absorptivity

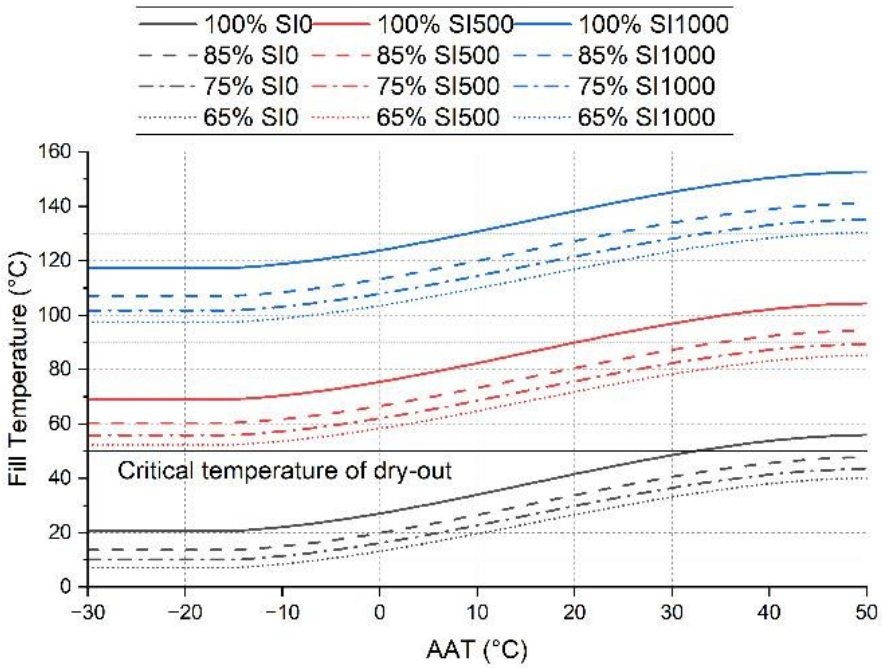

a) 138kV 2000mm^2, Braintree

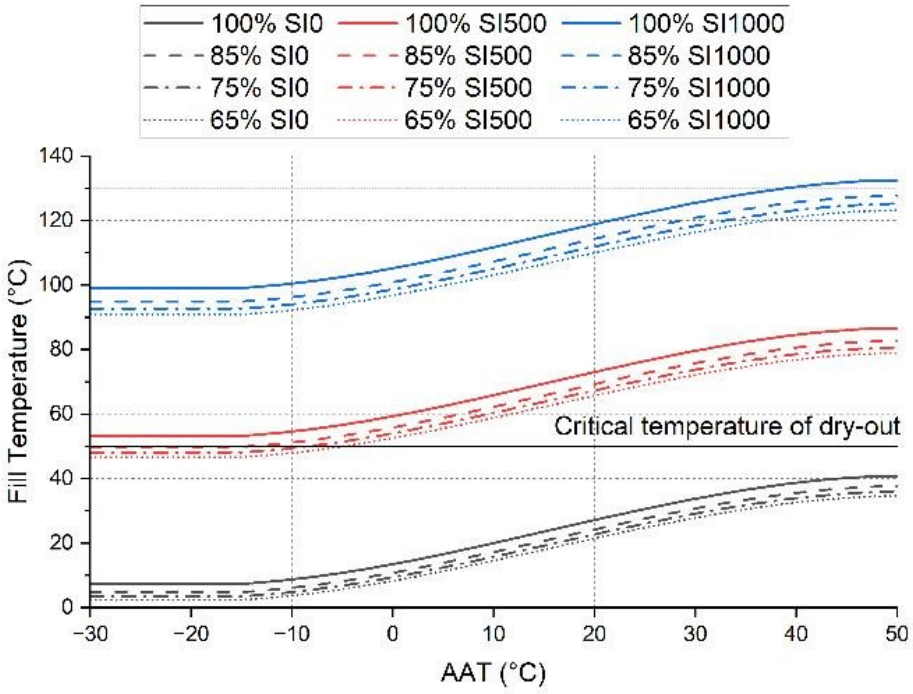

b) 400kV 1000mm^2, Pentir-Trawsfynydd

Figure 5.9: Variation of fill temperature with the variation of AAT and SI for a single 138kV 2000mm^2 (a) FTC and 400kV 1000mm^2 (b) FTC using 0.9 absorptivity when loaded with respective 1PU, 0.85PU, 0.75PU and 0.65PU summer STR current.

Figure 5.9 shows that across both cables, SI is the dominant driver of fill temperature. Moving from SI0 → SI500 → SI1000 increases fill temperature far more than changing load from 0.65 → 1.0 PU at 0.9 absorptivity. The critical dry-out temperature (~50 °C) is a practical threshold for trough backfill. Under SI1000, fill temperature exceeds 50 °C at all loads and across much of the AAT range. Under SI500, fill temperature often approaches or surpasses 50 °C at 0.85–1.0 PU, even when AAT is modest. Under SI0, fill temperature generally stays below 50 °C except at the highest AAT/load combinations.

Once the fill temperature pushes the backfill towards dry-out, its thermal resistivity rises sharply, reducing heat dissipation and causing additional increases in fill and conductor temperatures (positive feedback). In trough systems, this can develop quickly on sunny days because of the shallow depth and direct solar gain to the lid/backfill. Therefore, ignoring SI is non-conservative; conversely, assuming indefinite peak SI (1000 W/m²) with high absorptivity is over-conservative. A realistic approach is again to use time-averaged SI (~500 W/m²) with representative lid absorptivity (≈0.45–0.6). Both the 138 kV and 400 kV FTCs show the same ordering, where SI dominates, and load is secondary. The 138 kV case appears slightly more load-sensitive (lower dielectric loss fraction), but SI primarily governs the dry-out risk in both cases. Using an absorptivity of 0.9 is conservative, so another set of absorptivities is used in Figure 5.10 for sensitivity analysis. For a greyish concrete material, a value of 0.5 is chosen based on a previous study on concrete material [102]. The new results for conductor SSTs with 0.5 absorptivity are shown in Figure 5.10, with the conductor temperature limit marked. The calculated fill temperatures and the critical fill temperature for the risk of dry-out are shown in Figure 5.11.

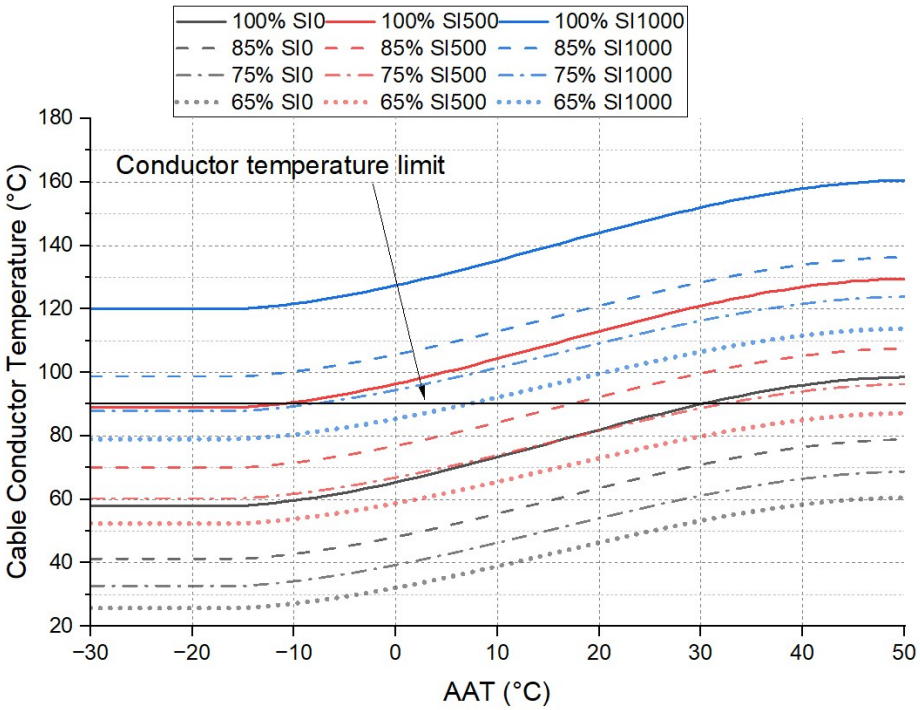

a) 138kV 2000mm^2, Braintree

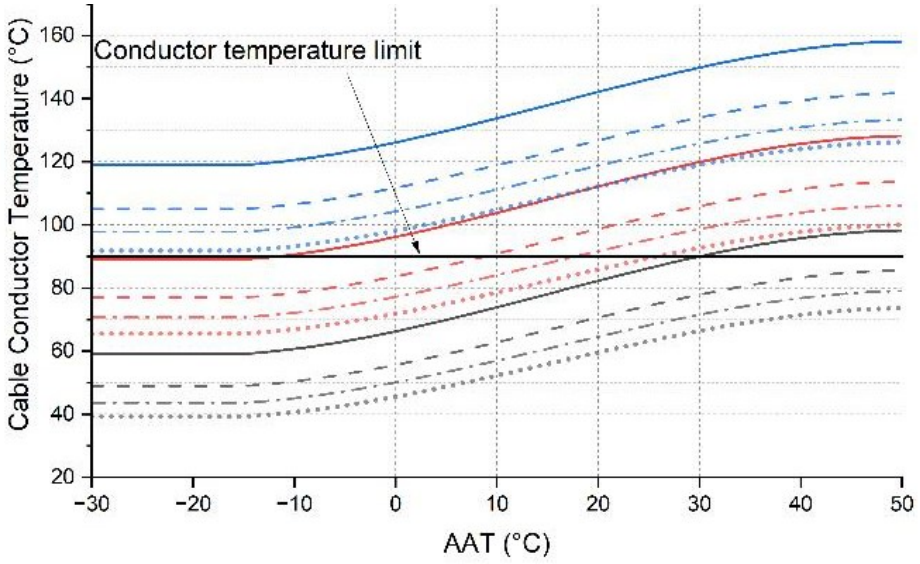

b) 400kV 1000mm^2, Pentir-Trawsfynydd

Figure 5.10: Variation of conductor temperature with the variation of AAT and SI for a single 138kV 2000mm^2 (a) FTC and 400kV 1000mm^2 (b) FTC using 0.5 absorptivity when loaded with respective 1PU, 0.85PU, 0.75PU and 0.65PU summer STR current.

In Figure 5.10, reducing the trough lid absorptivity from 0.9 to 0.5 significantly decreases the solar-driven component of conductor heating, cutting the temperature rise from solar input by roughly 44%. The SI = 0 curves remain unchanged, but the gap between the SI0, SI500, and SI1000 curves narrows considerably compared with the 0.9 case. As a result, peak conductor temperatures under SI1000 are materially lower, providing noticeably more margin to the conductor temperature limit, particularly at AAT values below 20–25 °C. At SI500, conductor temperatures now sit closer to the SI0 baseline and often remain below the thermal limit, where the 0.9 case was approaching or exceeding it. This makes the influence of current loading (0.65–1.0 PU) more visible, although solar irradiance still dominates the overall thermal behaviour for FTC installations.

Both the 138 kV and 400 kV FTC cables benefit from the reduced absorptivity, though the 138 kV cable remains slightly more sensitive to load because of its lower proportion of dielectric losses. The 400 kV FTC shows a clearer thermal margin across most load levels, although very high AAT combined with SI1000 can still reduce margin. Overall, using a realistic absorptivity in the range of 0.5–0.6 avoids the over-conservatism associated with $\alpha = 0.9$ while still accounting for solar effects.

In Figure 5.11, reducing the solar absorptivity from 0.9 to 0.5 noticeably lowers the fill temperature for both FTC cables, narrowing the gap between SI0, SI500, and SI1000 cases and keeping the fill temperature closer to the dry-out threshold. As a result, the risk of exceeding the critical dry-out temperature (~50 °C) is significantly reduced under typical conditions, especially at SI500 and moderate loading, meaning that dry-out events would be less frequent and less severe than in the more conservative absorptivity, $\alpha = 0.9$, case.

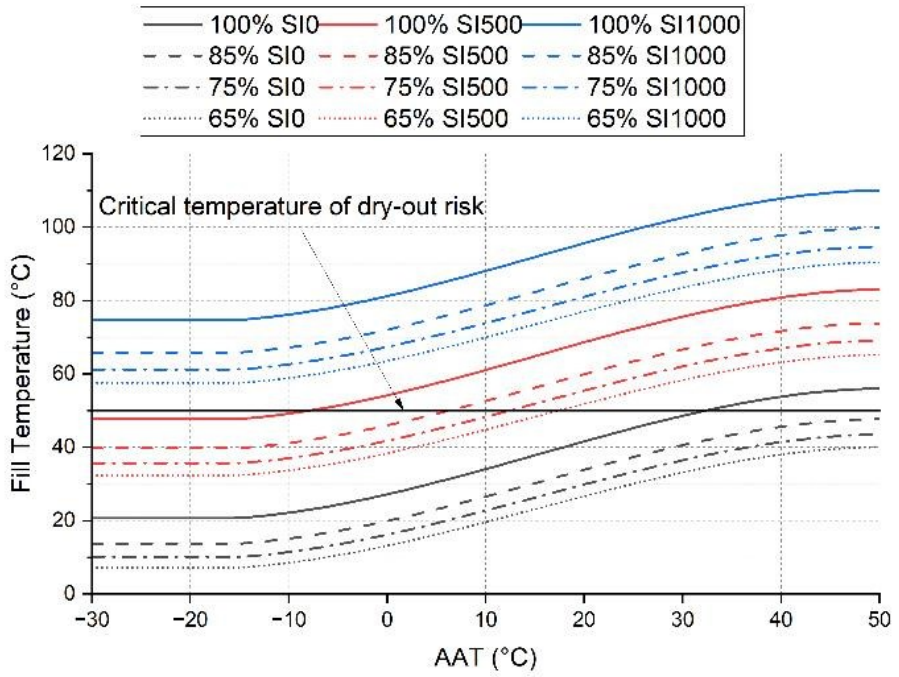

a) 138kV 2000mm^2, Braintree

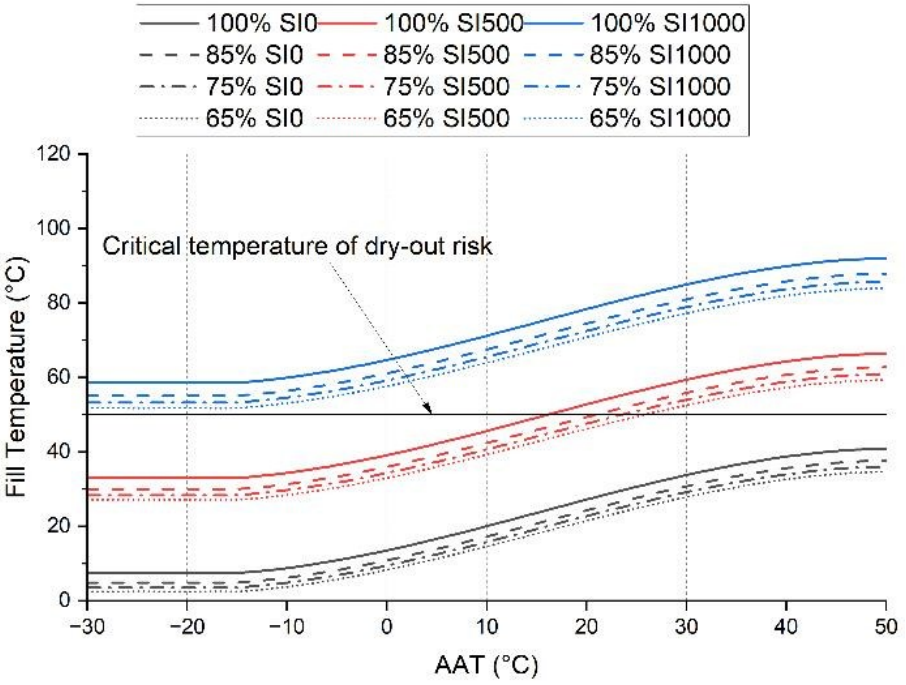

b) 400kV 1000mm^2, Pentir-Trawsfynydd

Figure 5.11: Variation of fill temperature with the variation of AAT and SI for a single 138kV 2000mm^2 (a) FTC and 400kV 1000mm^2 (b) FTC using 0.5 absorptivity when loaded with respective 1PU, 0.85PU, 0.75PU and 0.65PU summer STR current.

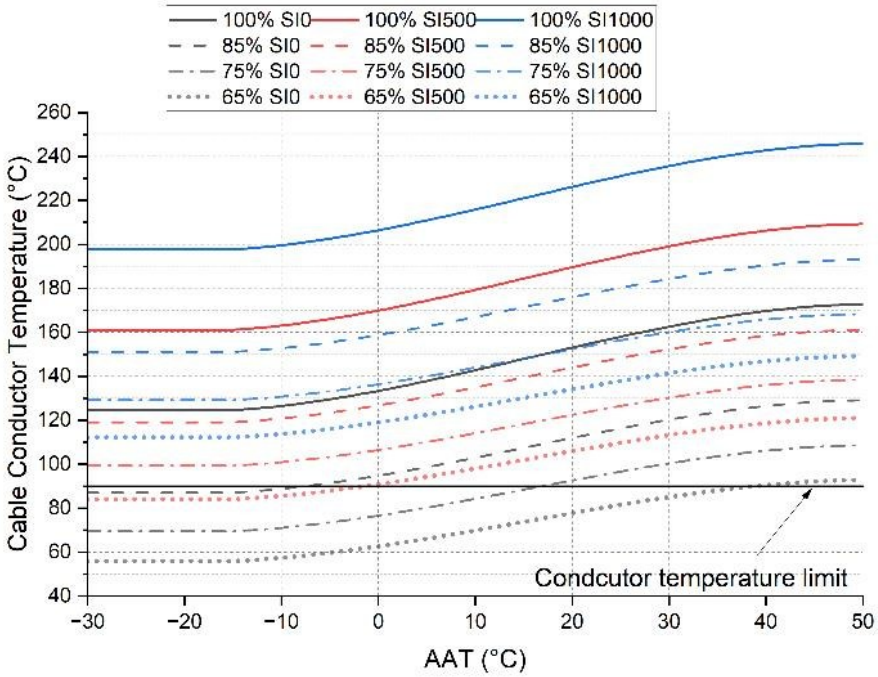

a) 138kV 2000mm^2, Braintree

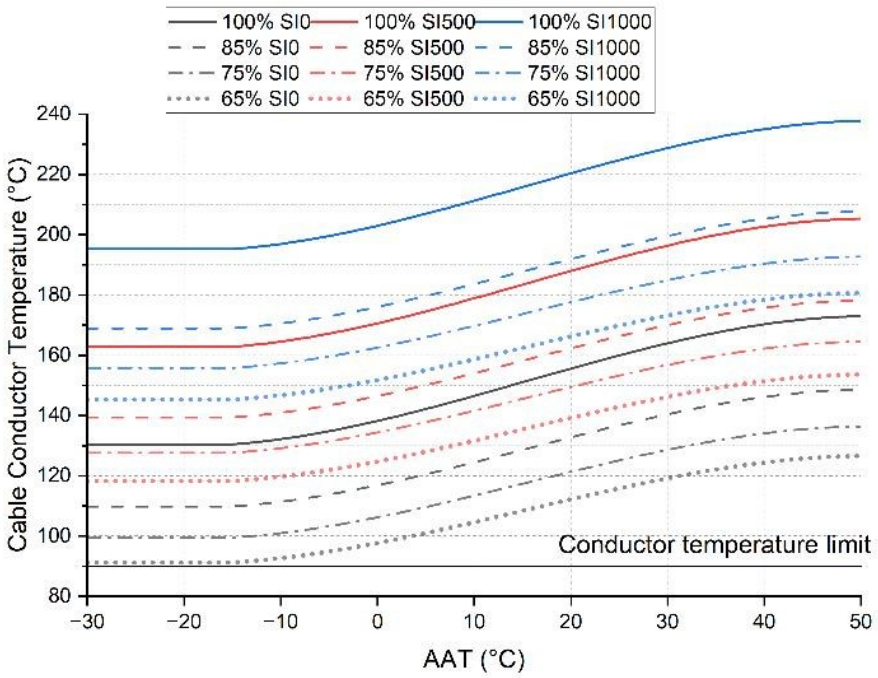

b) 400kV 1000mm^2, Pentir-Trawsfynydd

Figure 5.12: Variation of conductor temperature with the variation of AAT and SI for a single 138kV 2000mm^2 (a) FTC and 400kV 1000mm^2 (b) FTC using 0.5 absorptivity and considering dry-out of the fill when loaded with respective 1PU, 0.85PU, 0.75PU and 0.65PU summer STR current.

In Figure 5.12, for an absorptivity of 0.5, these results illustrate the effect of soil dry-out for both FTC cables. The figures show that dry-out dramatically raises the calculated surface soil temperature and, consequently, the conductor temperature, even under no solar irradiance (SI0) conditions. If the cables continue to be loaded at their summer STR current during dry-out, significant overheating occurs, requiring immediate de-rating to prevent thermal runaway. Medium- and high-SI conditions (SI500, SI1000) further worsen the situation, driving conductor temperatures to unrealistically high values that would likely cause insulation failure long before such temperatures could be reached in practice.

5.2.1.3 Steady-State Conductor Temperatures of Exposed Cables

The calculated SST of the ExpoC for WS of 0.5 m/s and 1 m/s with variation in AAT and SI are shown in Figure 5.13 and Figure 5.14. Where the exposed cables are perpendicular to the ground surface, the AA can be considered 90 degrees because the WS measured is parallel to the ground surface.

The ExpoC section is not directly affected by soil dry-out, as it is predominantly air-cooled, as described in Figure 5.13 and Figure 5.14. However, suppose sections of the same circuit are buried, either in a trough or directly buried near the ExpoC, and operate at a higher temperature. In that case, heat can conduct along the cable into the exposed section. This effectively becomes an additional heat source in the ExpoC thermal model, potentially raising its temperature above what would be predicted solely from ambient conditions. Furthermore, ExpoC sections are typically connected to terminations and other assets such as OHLs, and these terminations (with a temperature limit of 105 °C) often use the ExpoC as a heat sink. Under high solar irradiance, this additional heat input could bring the ExpoC closer to its temperature limit and should be considered in future studies.

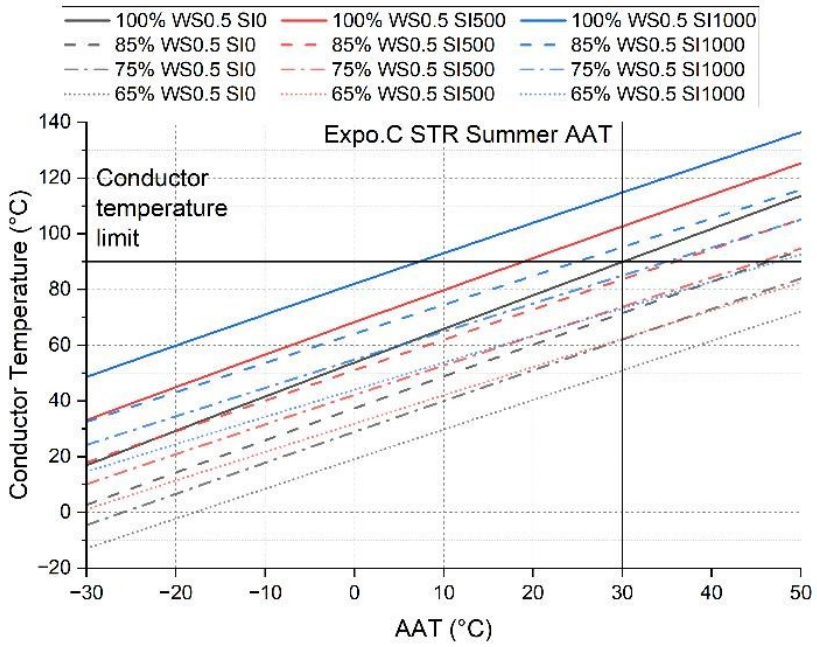

a) 138kV 2000mm^2, Braintree

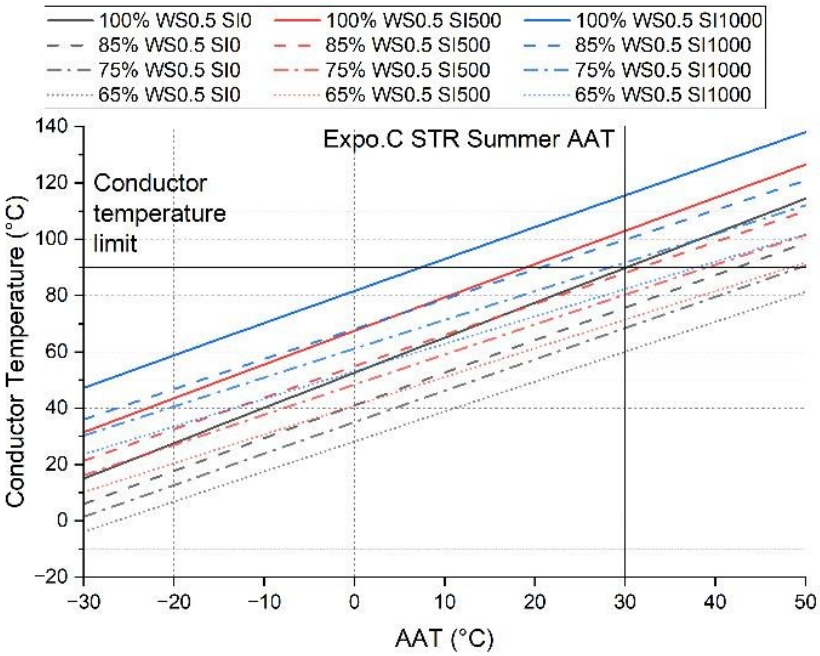

b) 400kV 1000mm^2, Pentir-Trawsfynydd

Figure 5.13: Variation of conductor temperature at 0.5m/s WS with the variation of AAT and SI for a single exposed 138kV 2000mm^2 cable (a) and exposed 400kV 1000mm^2 cable (b) when loaded with respective 1PU, 0.85PU 0.75PU and 0.65PU constant summer STR current.

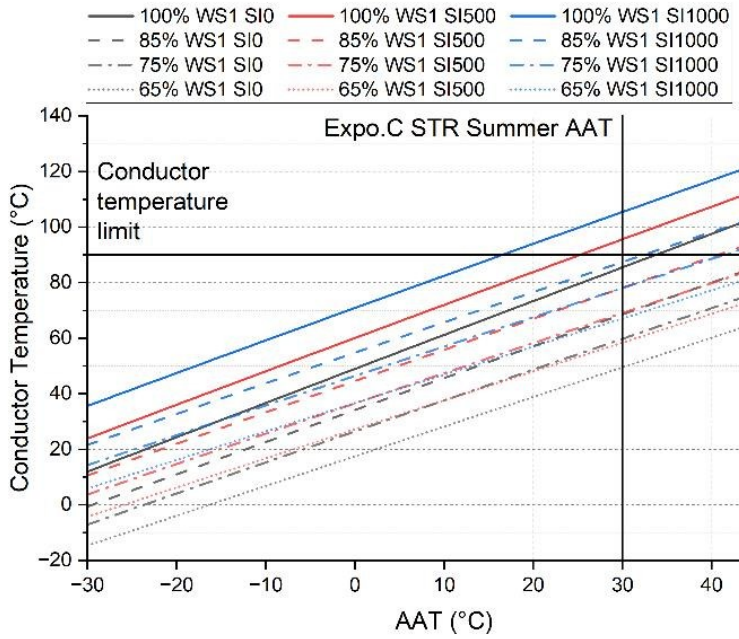

a) 138kV 2000mm^2, Braintree

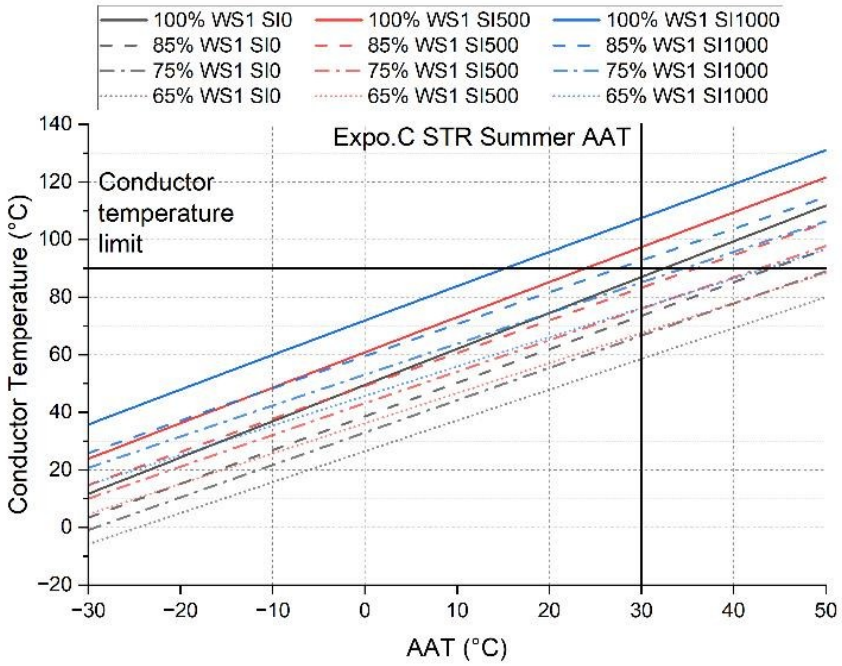

b) 400kV 1000mm^2, Pentir-Trawsfynydd

Figure 5.14: Variation of conductor temperature at 1m/s WS with the variation of AAT and SI for a single exposed 138kV 2000mm^2 cable (a) and exposed 400kV 1000mm^2 cable (b) when loaded with respective 1PU, 0.85PU 0.75PU and 0.65PU constant summer STR current.

Increasing the assumed wind speed from 0.5 m/s (Figure 5.13) to 1 m/s (Figure 5.14) provides significantly more cooling capacity for the ExpoC. The standard 0.5 m/s assumption is therefore slightly conservative, and adopting 1 m/s as a realistic worst-case would allow safe utilisation of additional thermal headroom and improve the available rating. This highlights the importance of including realistic meteorological conditions when setting ExpoC ratings.

5.2.2 Dynamic and Static Thermal Ratings of Cables

The DTR for the cables is defined as the maximum CCC or apparent power carrying capacity under a specific line voltage of the cable conductor under a given ambient condition that the cable is exposed to, that the conductor temperature of the cable will not violate its given temperature limit, assuming an indefinite long operation time without the consideration of ageing. When assessing cable individually, the cable cannot actively alter the voltage on its own, so, for simplicity, the cable ratings are given in current at 1PU voltage rather than power. The result of all the configurations of the 138kV 2000mm^2 cable is shown in Figure 5.15. The variation of the AST at 1m and 0.3m depth with the variation of AAT using the S/NH assumption is also shown.

From the results in Figure 5.15, when considering the 138 kV 2000 mm² cable as a single joint circuit across all configurations (DBC, FTC, and ExpoC), the DBC is almost always the limiting section in determining the joint circuit DTR. This is primarily due to the high thermal resistance imposed by its 1 m burial depth, which restricts heat dissipation and drives its temperature closer to the allowable limit. The only exception occurs under extreme AAT and SI conditions, where the DTR of the ExpoC section drops below that of the DBC, making ExpoC the new limiting section.

It is also important to note that each cable configuration can be limiting depending on the prevailing AAT and weather conditions. For instance, under moderate AAT and low SI, the DBC is the bottleneck, while at very high SI, the FTC or ExpoC sections may become more restrictive. This reinforces the need to treat the cable as a single integrated circuit, dynamically evaluating which section is limiting at any given time, rather than relying solely on a fixed static rating.

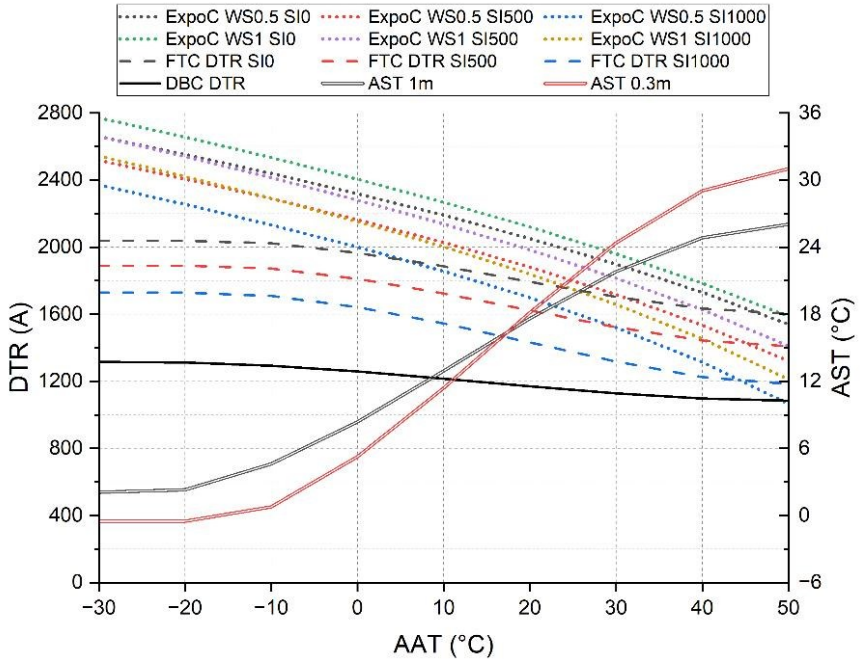

Figure 5.15: Comparison of the DTR for 138kV 2000mm^2 cable in different constructions and the respective AST with the variation of the AAT when considering both 0.5m/s and 1m/s WS.

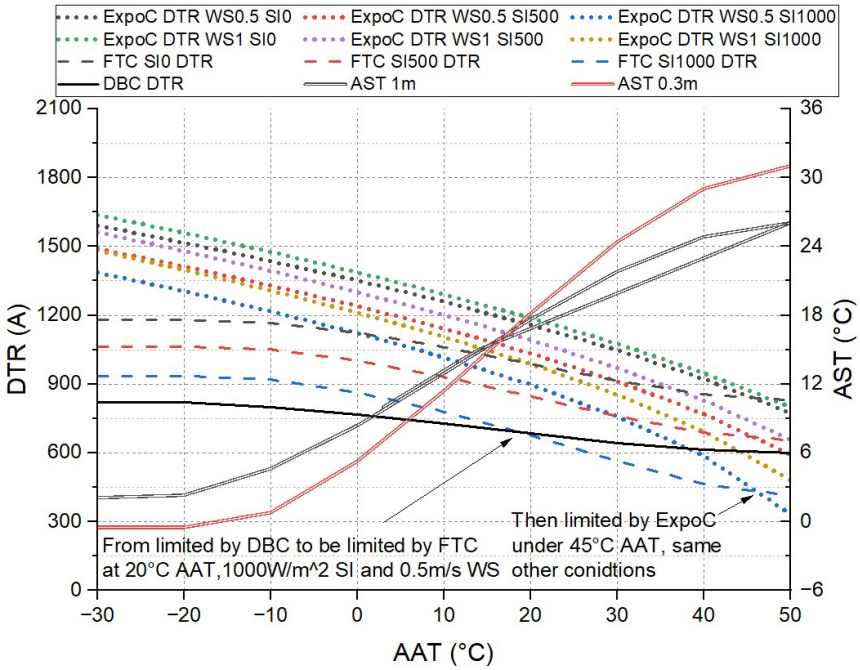

Figure 5.16: Comparison of the DTR for 400kV 1000mm^2 cable in different constructions and the respective AST with the variation of the AAT.

The result of all configurations of the 400kV 1000mm^2 cable is shown in Figure 5.16. The variation of the AST at 1m and 0.3m depth with the variation of AAT using the S/NH assumption is also shown.

For the 400 kV 1000 mm² cable in Figure 5.16, results show that different configurations become limiting under different weather conditions. At high SI, the FTC becomes the first limiting section once AAT rises above roughly 20 °C, driven by the shallow burial depth and strong solar coupling to the trough lid. At very high AAT approaching 50 °C, the ExpoC becomes the limiting section, though this represents an extreme condition. When a more realistic 1 m/s wind speed is assumed for heat-wave conditions, the FTC remains the limiting configuration even at high AAT, as additional wind cooling provides thermal headroom for the ExpoC. Under medium SI or no-SI conditions, the DBC again becomes the dominant limiting element due to its greater thermal resistance from 1 m burial depth.

As with the 138 kV circuit, the 400 kV cable should be treated as a single integrated thermal circuit, with whichever section (DBC, FTC, or ExpoC) is hottest defining the joint circuit DTR. This approach ensures that the overall circuit rating reflects the true thermal bottleneck for the prevailing ambient conditions.

5.2.3 Thermal Time Constants of Cables

Cables are known for their large thermal capacitance because of their generally greater conductor size and the layers of insulation, sheath, and jacket, which provide additional thermal capacitance. On top of that, the surroundings (ambient) of buried cables also cannot be ignored. The surroundings of the cable contribute significant thermal resistance when considering continuous operation, but also provide a large amount of thermal capacitance. In practice, cables rarely operate in a constant state indefinitely, so if the thermal capacitance in the cable model can be properly utilised, ratings can be improved by accounting for time and changes in loading state, compared to DTR, which considers changes in ambient conditions but assumes continuous, indefinite operation. To improve ratings that involve time and changes in loading state, the TTC of the cable must be investigated first.

5.2.3.1 Thermal Time Constants of Directly Buried Cables

The results of the temperature variation with time for both cables in DBC form are shown in Figure 5.17, with the calculated TTCs also marked. The cable is initialised in an unenergized state, so dielectric losses are not applied. At time 0, it is assumed that the cable is energised and loaded with its respective summer STR at 1PU voltage via a step change. The ambient conditions are considered to be the respective summer STR ambient conditions for DBC at 1m depth (AST1m = 21.8 ℃).

From the results, it can be seen that the 4th TTC of DBC is as long as 209 hours, almost 9 days. This suggests that, when assessing time-related ratings such as S/MTOR and CTR for the DBC, to reach steady-state and cyclic steady-state, the calculation period should not be less than 9 days. The lower TTC of the cables is 17 hours from the 400kV 1000mm^2 due to a smaller conductor size, thus less thermal capacitance for the cables.

5.2.3.2 Thermal Time Constants of Filled Trough Cables

The results of the temperature variation over time for both cables in the FTC construction are shown in Figure 5.18, with the calculated TTCs marked. The cable is initialised in an unenergized state, so dielectric losses are not applied. At time 0, it is assumed that the cable is loaded with its respective summer STR at 1PU voltage via a step change. The ambient conditions are considered to be the respective summer STR ambient conditions for the cable at 0.3m depth (AST0.3 m = 24.4 ℃).

From the results, the highest TTC of FTC is almost 60 hours, or 2.5 days. This suggests that, when assessing time-related ratings such as S/MTOR and CTR for the FTC, to reach steady-state and cyclic steady-state, the calculation period should not be less than 3 days. The lowest TTC of the cables is 5.8 hours from 400kV 1000mm^2 due to its smaller conductor size and thermal capacitance of cables.

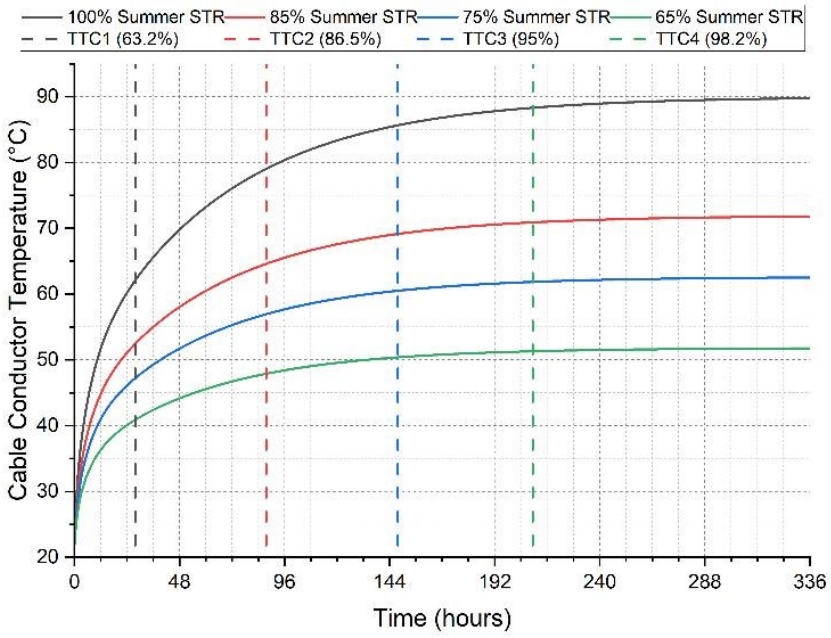

a) 138kV 2000mm^2, Braintree

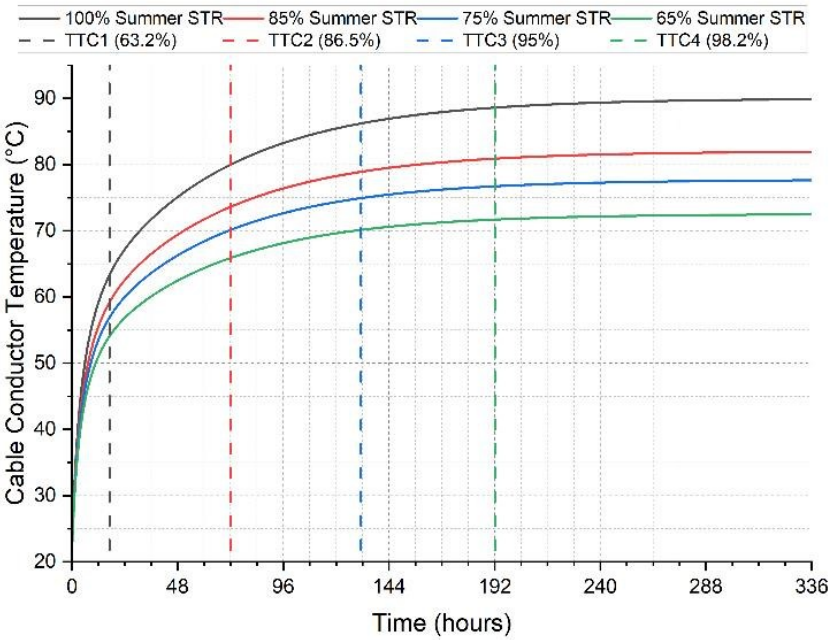

b) 400 kV 1000mm^2, Pentir-Trawsfynydd

Figure 5.17: Variation of the conductor temperature with time SI for a single 138kV 2000mm^2 DBC (a) and 400kV 1000mm^2 DBC (b) when loaded with 1PU, 0.85PU, 0.75PU and 0.6PU of respective constant summer STR current under summer STR ambient conditions.

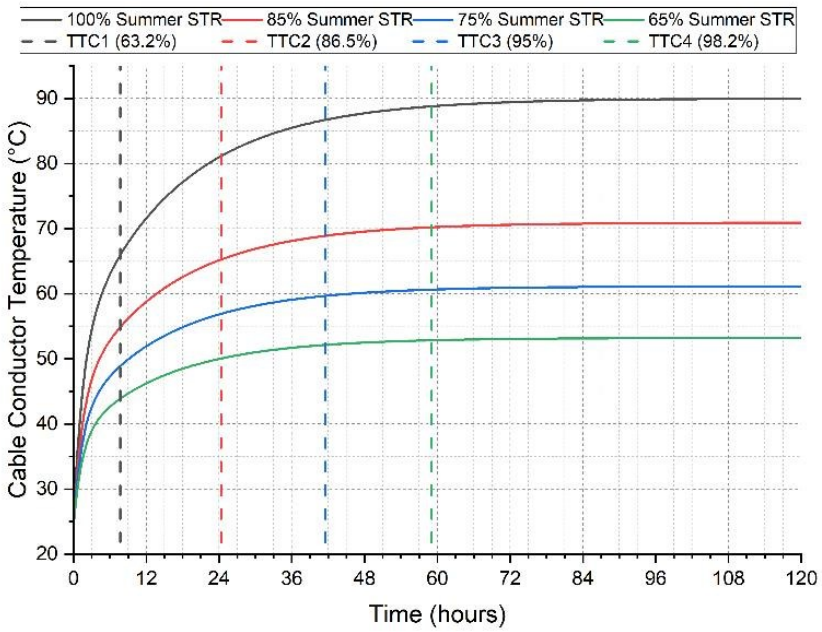

a) 138kV 2000mm^2, Braintree

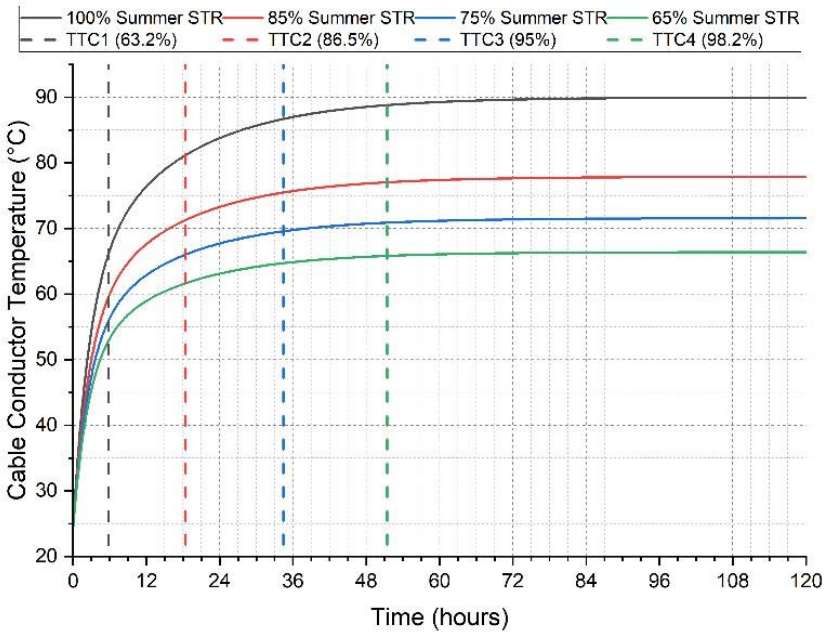

b) 400 kV 1000mm^2, Pentir-Trawsfynydd

Figure 5.18: Variation of the conductor temperature with time for a single 138kV 2000mm^2 FTC (a) and 400kV 1000mm^2 FTC (b) when loaded with 1PU, 0.85PU, 0.75PU and 0.6PU of respective constant summer STR current under summer STR ambient condition.

5.2.3.3 Thermal Time Constants of Exposed Cables

The results of the temperature variation over time for both cables in the ExpoC construction are shown in Figure 5.19, with the calculated TTCs marked. The cable is initialised in an unenergized state, so dielectric losses are not applied. At time 0, it is assumed that the cable is loaded with its respective summer STR at 1PU voltage via a step change.

From the results, the highest 4th TTC of ExpoC is 13.7 hours. This suggests that when assessing time-related ratings, such as S/MTOR and CTR for the ExpoC, to reach steady-state and cyclic steady-state, the calculation period should not be less than 1 day (24 hours). The lower 1st TTC of the cables is 2.4 hours from 138kV 2000mm^2.

Once the TTCs of the cable configurations are established, ratings that explicitly account for thermal inertia, such as S/MTOR and CTR, can be calculated with confidence. These TTC-derived ratings reflect the true heating and cooling behaviour of the cable and ensure that short-term loading opportunities and cyclic loading patterns are accurately captured.

5.2.4 Short-Term and Medium-Term Overloading Ratings of Cables

Short- and medium-term overloading ratings (S/MTOR) quantify the additional current a cable can safely carry for limited durations by utilising its thermal inertia before conductor temperatures reach their allowable limit. In this thesis, S/MTOR has been assessed for all three cable configurations, Exposed Cable (ExpoC), Filled Trough Cable (FTC), and Directly Buried Cable (DBC), under a range of ambient air temperatures (−30 °C to 50 °C), pre-fault loading levels (65–100 %), and overload durations (3–360 minutes). The three configurations differ significantly in thermal behaviour: DBC has the largest thermal mass and slowest response, making it more restrictive but also allowing longer thermal recovery times; FTC responds faster and is more sensitive to solar irradiance due to its shallow installation depth; and ExpoC, being directly air-cooled, has the fastest thermal response and benefits most from higher wind speeds. These differences are reflected in the S/MTOR results, where each configuration may become the limiting section depending on the prevailing conditions.

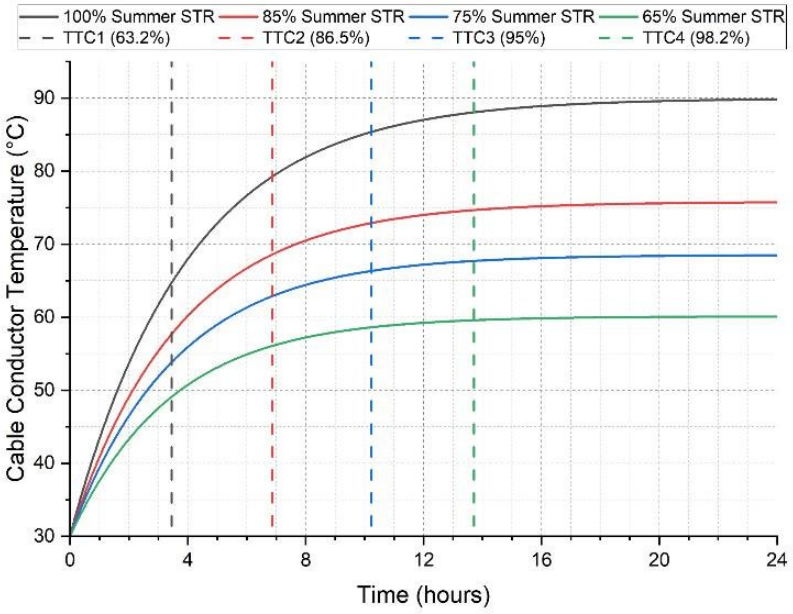

a) 138kV 2000mm^2, Braintree

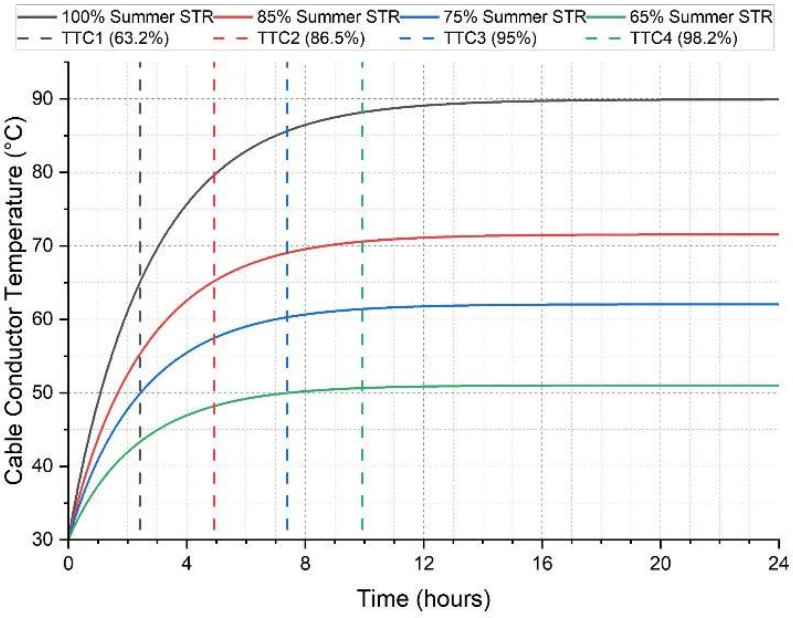

b) 400 kV 1000mm^2, Pentir-Trawsfynydd

Figure 5.19: Variation of the conductor temperature with time SI for a single exposed 138kV 2000mm^2 cable (a) and exposed 400kV 1000mm^2 cable (b) when loaded with 1PU, 0.85PU, 0.75PU and 0.6PU of respective constant summer STR current under summer STR ambient condition.

5.2.4.1 Short-Term and Medium-Term Overloading Ratings for Directly Buried Cables

The S/MTOR calculated for the DBC for the two example cables (138kV 2000mm^2 and 400kV 1000mm^2) across a wide AAT range from –30 °C to 50 °C are shown in Table 5.2 and Table 5.3.

Table 5.2: Short-Term and Medium-Term Overloading Ratings of Directly Buried 138kV 2000mm^2 Cable.

AAT (°C)		-30	-20	-10	0	10	20	30	40	50
AST1m (°C)		2.09	2.31	4.62	8.38	12.93	17.62	21.81	24.84	26.06
Pre-fault DTR (A)		1315	1313	1293	1259	1216	1171	1129	1097	1084
Post-fault DTR (A)		1315	1313	1293	1259	1216	1171	1129	1097	1084
Pre-fault loading%	**Duration (min)**	Pre-DTR S/MTOR in Amps at rated voltage								
100% corresponds to		1315	1313	1293	1259	1216	1171	1129	1097	1084
-	**inf**	1315	1313	1293	1259	1216	1171	1129	1097	1084
85%	**360**	1665	1663	1633	1589	1526	1461	1409	1367	1344
	60	2395	2393	2353	2279	2186	2081	1999	1937	1904
	20	3545	3543	3453	3354	3211	3056	2924	2837	2804
	10	4770	4768	4678	4504	4311	4131	3974	3837	3779
	5	6570	6568	6428	6204	5961	5681	5424	5237	5179
	3	8420	8418	8228	7954	7661	7281	6924	6687	6579
75%	**360**	1815	1813	1783	1729	1666	1601	1539	1487	1464
	60	2805	2803	2743	2659	2556	2441	2339	2267	2234
	20	4280	4278	4193	4034	3881	3691	3539	3417	3384
	10	5830	5828	5718	5509	5281	5041	4839	4667	4609
	5	8080	8078	7918	7759	7331	6991	6689	6467	6359
	3	10380	10328	10168	9809	9381	8941	8589	8317	8209
65%	**360**	1985	1983	1943	1889	1816	1741	1679	1627	1604
	60	3215	3213	3153	3059	2936	2811	2689	2607	2574
	20	5015	4988	4903	4734	4561	4361	4164	4032	3974
	10	6890	6863	6728	6509	6261	5986	5714	5532	5449
	5	9590	9563	9378	9059	8711	8286	7964	7732	7699
	3	12290	12263	12178	11659	11161	10686	10214	9882	9799

Table 5.3: Short-Term and Medium-Term Overloading Ratings of Directly Buried 400kV 1000mm^2 Cable

AAT (℃)		-30	-20	-10	0	10	20	30	40	50
AST1m (℃)		2.09	2.31	4.62	8.38	12.93	17.62	21.81	24.84	26.06
Pre-fault DTR (A)		820	819	800	769	729	685	644	613	600
Post-fault DTR (A)		820	819	800	769	729	685	644	613	600
Pre-fault loading%	**Duration (min)**	Pre-DTR S/MTOR in Amps at rated voltage								
100% corresponds to		820	819	800	769	729	685	644	613	600
-	**inf**	820	819	800	769	729	685	644	613	600
85%	**360**	980	979	960	919	859	805	754	713	700
	60	1450	1449	1410	1349	1259	1175	1094	1043	1010
	20	2200	2199	2135	2024	1909	1775	1644	1568	1510
	10	3025	3024	2910	2774	2584	2400	2244	2118	2060
	5	4175	4174	4010	3824	3584	3350	3094	2968	2910
	3	5325	5324	5160	4924	4584	4250	3994	3768	3660
75%	**360**	1060	1059	1030	979	929	865	814	773	750
	60	1700	1689	1650	1569	1479	1375	1284	1213	1180
	20	2675	2664	2575	2469	2304	2150	2009	1888	1855
	10	3675	3664	3550	3394	3179	2975	2759	2613	2530
	5	5125	5114	4950	4744	4429	4125	3809	3613	3530
	3	6575	6564	6400	6044	5679	5275	4909	4663	4530
65%	**360**	1110	1109	1080	1039	979	915	854	813	790
	60	1880	1869	1820	1739	1629	1525	1414	1343	1310
	20	3005	2994	2920	2764	2604	2425	2264	2118	2085
	10	4155	4144	4020	3839	3604	3350	3114	2968	2885
	5	5905	5894	5620	5339	5004	4700	4364	4118	4035
	3	7455	7494	7220	6889	6454	6000	5614	5318	5185

The 400 kV 1000 mm² DBC shows substantially lower absolute ratings than the 138 kV 2000 mm² DBC across all AATs and durations, reflecting its smaller cross-sectional area and higher dielectric losses. At 20 °C and 85 % pre-fault loading, the steady DTR is ~685 A for the 400 kV cable compared with ~1711 A for the 138 kV cable. Similarly, the 3-minute rating at 20 °C reaches only ~4250 A for the 400 kV cable, about half the ~7281 A available for the 138 kV DBC under the same conditions.

Despite the lower capacity, both cables follow the same general trend: shorter durations permit proportionally higher overloads, and lower AATs increase available

headroom. In practical terms, the 400 kV DBC is much more likely to be the limiting element under both normal and contingency conditions, and its lower thermal capacity means less short-term emergency loading can be safely applied compared to the 138 kV equivalent.

5.2.4.2 Short-Term and Medium-Term Overloading Ratings of Filled Trough Cable

Compared with the DBC (138 kV), the FTC in Table 5.4 shows generally higher S/MTOR values across all AATs and durations, reflecting the lower external thermal resistance. At 20 °C AAT, the DTR is about 1794 A for FTC versus ~1171 A for DBC, with a similar gap visible at other durations. For instance, the 3-minute rating at 20 °C reaches ~7733 A for FTC, roughly 6 % higher than the 7281 A available on DBC under the same conditions.

The overall trend remains consistent with the DBC: shorter duration allows substantially higher overloads, and lower pre-fault loading yields additional margin. However, the shallower slope of the FTC ratings means its available headroom is slightly more constrained, particularly at high AAT, where soil thermal resistance increases and dry-out is more likely to occur.

Compared with the 138 kV 2000 mm² FTC, the 400 kV 1000 mm² FTC in Table 5.5 exhibits lower S/MTOR values across all AATs and durations, reflecting its higher operating voltage, smaller cross-sectional area, and greater dielectric loss contribution, which keeps its steady-state conductor temperature closer to the thermal limit.

Despite lower absolute values, both cables follow the same general trends: higher AAT compresses the thermal margin, and shorter-duration overloads allow significantly higher currents. The reduced thermal capacity of the 400 kV FTC means that it is more likely to be the limiting section under high-load, high-temperature conditions in a mixed circuit, whereas the 138 kV FTC can absorb more short-term loading before approaching its temperature limit.

Table 5.4: Short-Term and Medium-Term Overloading Ratings of Filled Trough 138kV 2000mm^2 Cable

AAT (℃)		-30	-20	-10	0	10	20	30	40	50
AST0.3m (℃)		-0.5	-0.5	0.8	5.3	11.4	18.2	24.4	29	31
Pre-fault DTR (A)		2039	2039	2023	1966	1886	1794	1704	1634	1603
Post-fault DTR (A)		2039	2039	2023	1966	1886	1794	1704	1634	1603
Pre-fault loading%	**Duration (min)**	S/MTOR in Amps at rated voltage								
100% corresponds to		2039	2039	2023	1966	1886	1794	1704	1634	1603
-	**inf**	2039	2039	2023	1966	1886	1794	1704	1634	1603
85%	**360**	2241	2241	2224	2151	2063	1952	1855	1770	1736
	60	2862	2862	2825	2733	2608	2456	2321	2215	2162
	20	3997	3997	3966	3817	3624	3413	3210	3063	2990
	10	5285	5285	5243	5046	4768	4490	4202	4009	3914
	5	7236	7236	7179	6875	6496	6087	5725	5435	5306
	3	9192	9192	9121	8734	8294	7733	7273	6939	6775
75%	**360**	2333	2333	2314	2238	2147	2032	1921	1842	1807
	60	3194	3194	3153	3050	2910	2741	2591	2472	2413
	20	4712	4712	4652	4477	4252	4004	3766	3593	3507
	10	6324	6324	6275	6039	5735	5400	5054	4822	4707
	5	8745	8745	8634	8309	7891	7431	6989	6635	6477
	3	11166	11166	11079	10610	10075	9488	8879	8514	8270
65%	**360**	2403	2403	2385	2306	2201	2094	1979	1898	1862
	60	3442	3442	3415	3286	3136	2954	2792	2664	2600
	20	5206	5206	5140	4972	4721	4446	4182	3990	3895
	10	7057	7057	7002	6773	6400	6027	5668	5408	5280
	5	9808	9808	9683	9366	8939	8376	7878	7479	7338
	3	12586	12586	12488	12019	11413	10694	10058	9596	9369

Table 5.5: Short-Term and Medium-Term Overloading Ratings of Filled Trough 400kV 1000mm^2 Cable

AAT (°C)		-30	-20	-10	0	10	20	30	40	50
AST0.3m (°C)		-0.5	-0.5	0.8	5.3	11.4	18.2	24.4	29	31
Pre-fault DTR (A)		1179	1179	1167	1123	1061	987	914	856	829
Post-fault DTR (A)		1179	1179	1167	1123	1061	987	914	856	829
Pre-fault loading%	**Duration (min)**	S/MTOR in Amps at rated voltage								
100% corresponds to		1179	1179	1167	1123	1061	987	914	856	829
-	**inf**	1179	1179	1167	1123	1061	987	914	856	829
85%	**360**	1277	1277	1264	1211	1143	1059	976	913	885
	60	1757	1757	1739	1658	1550	1428	1309	1219	1176
	20	2593	2593	2553	2434	2264	2076	1894	1755	1692
	10	3480	3480	3427	3266	3038	2772	2529	2343	2260
	5	4813	4813	4739	4494	4180	3814	3480	3208	3110
	3	6145	6145	6051	5767	5337	4895	4421	4096	3990
75%	**360**	1323	1323	1309	1254	1184	1096	1010	941	912
	60	1991	1991	1970	1878	1755	1610	1476	1374	1325
	20	3072	3072	3040	2883	2682	2459	2255	2089	2015
	10	4206	4206	4142	3948	3672	3367	3072	2846	2745
	5	5875	5875	5757	5487	5103	4680	4269	3956	3815
	3	7539	7539	7387	7040	6548	5975	5451	5051	4872
65%	**360**	1363	1363	1349	1292	1214	1124	1036	964	935
	60	2167	2167	2134	2044	1901	1752	1606	1488	1443
	20	3411	3411	3376	3218	2993	2758	2516	2332	2249
	10	4718	4718	4646	4428	4139	3777	3462	3208	3110
	5	6589	6589	6521	6184	5752	5275	4836	4459	4322
	3	8498	8498	8368	7936	7418	6769	6205	5750	5602

5.2.4.3 Short-Term and Medium-Term Overloading Ratings of Exposed Cable

The S/MTOR were calculated for the ExpoC under 0.5 m/s WS and no solar irradiance (SI = 0) across a wide AAT range from –30 °C to 50 °C in Table 5.6. Results under 1 m/s WS are shown in Table 5.7. Results are given for multiple pre-fault loading levels (85 %, 75 %, and 65 %) and overload durations ranging from 3 minutes to 360 minutes.

Table 5.6: Short-Term and Medium-Term Overloading Ratings of Exposed 138kV 2000mm^2 Cable considering both 0.5m/s Wind Speed and no Solar Irradiance

AAT (℃)		-30	-20	-10	0	10	20	30	40	50
Pre-fault DTR (A)		2660	2553	2440	2319	2191	2051	1899	1731	1541
Post-fault DTR (A)		2660	2553	2440	2319	2191	2051	1899	1731	1541
Pre-fault loading%	**Duration (min)**	S/MTOR in Amps at rated voltage, 0.5m/s WS, 0 SI								
100% corresponds to		2660	2553	2440	2319	2191	2051	1899	1731	1541
-	**inf**	2660	2553	2440	2319	2191	2051	1899	1731	1541
85%	**360**	2750	2633	2500	2369	2231	2091	1929	1751	1561
	60	3620	3413	3220	3019	2811	2601	2379	2151	1891
	20	5145	4838	4520	4194	3886	3576	3254	2926	2541
	10	6920	6488	6045	5619	5186	4691	4244	3811	3316
	5	9820	9188	8545	7919	7286	6391	5794	5161	4466
	3	12970	12388	11495	10669	9836	9001	7444	6611	5766
75%	**360**	2800	2673	2540	2399	2261	2111	1949	1771	1571
	60	4010	3773	3550	3319	3091	2851	2609	2341	2061
	20	6010	5648	5275	4919	4541	4116	3781	3390	2966
	10	8285	7748	7225	6719	6216	5541	5081	4550	3966
	5	11635	11098	10375	9619	8866	8101	7031	6300	5466
	3	15635	14498	13325	12469	11466	10501	9451	8150	7113
65%	**360**	2850	2713	2580	2439	2291	2131	1959	1781	1581
	60	4410	4153	3900	3649	3391	3131	2859	2571	2251
	20	6885	6453	6050	5649	5216	4806	4359	3921	3426
	10	9585	9003	8425	7849	7266	6656	6059	5421	4726
	5	13385	12503	11675	10849	10166	9406	8509	7571	6526
	3	17035	16503	15975	14899	13716	12546	11309	10071	8726

As expected, available overload capacity decreases with increasing AAT, reflecting reduced thermal headroom at higher ambient temperatures. At full pre-fault loading (100 %), the post-fault DTR under steady-state conditions falls from ~2660 A at –30 °C to ~1540 A at 50 °C, showing the strong influence of ambient temperature on cable current-carrying capacity. Reducing pre-fault loading significantly improves available short-term capacity. For example, at 85 % loading and 20 °C AAT, the 20-minute S/MTOR is 3576 A – almost 74 % above the steady-state 100 % loading current

rating – while a 3-minute rating allows up to 9001 A, more than 3.5 times the steady-state current.

Table 5.7: Short-Term and Medium-Term Overloading Ratings of Exposed 138kV $2000mm^2$ cable considering 1m/s Wind Speed and no Solar Irradiance

AAT (°C)		-30	-20	-10	0	10	20	30	40	50
Pre-fault DTR (A)		2771	2656	2534	2405	2268	2121	1961	1785	1588
Post-fault DTR (A)		2771	2656	2534	2405	2268	2121	1961	1785	1588
Pre-fault loading%	**Duration (min)**	S/MTOR in Amps at rated voltage, 1m/s WS, 90AA, 0 SI								
100% corresponds to		2771	2656	2534	2405	2268	2121	1961	1785	1588
-	**inf**	2771	2656	2534	2405	2268	2121	1961	1785	1588
85%	**360**	2851	2716	2584	2445	2308	2151	1981	1805	1598
	60	3691	3486	3274	3075	2868	2641	2421	2185	1918
	20	5216	4886	4574	4250	3943	3591	3271	2935	2568
	10	7016	6536	6099	5675	5218	4751	4306	3850	3363
	5	9916	9236	8599	7975	7318	6651	6056	5400	4663
	3	13416	12486	11599	10725	9868	9191	8106	7250	6313
75%	**360**	2881	2756	2614	2475	2328	2171	2001	1815	1608
	60	4061	3826	3604	3365	3138	2891	2631	2375	2088
	20	6086	5701	5329	4965	4588	4176	3806	3390	2983
	10	8361	7801	7279	6765	6263	5701	5156	4615	4033
	5	11961	11201	10429	9665	8913	8151	7056	6565	5733
	3	15961	14851	13529	12515	11513	10511	9456	8265	7283
65%	**360**	2921	2786	2644	2495	2348	2181	2011	1825	1618
	60	4451	4196	3934	3685	3428	3161	2881	2585	2278
	20	6926	6496	6084	5685	5253	4836	4406	3935	3453
	10	9651	9046	8459	7885	7303	6686	6081	5435	4753
	5	13401	12546	11709	10985	10253	9436	8531	7635	6553
	3	17551	16996	16109	14935	13753	12556	11331	10085	8733

Compared with the 0.5 m/s case, increasing wind speed to 1 m/s provides notable additional thermal headroom across all AATs and durations as described in Table 5.7. At 20 °C AAT, the post-fault steady DTR at 100 % loading rises from ~2051 A (0.5 m/s) to 2121 A, and the 3-minute overload rating increases from ~9001 A to 9191 A.

At 85 % pre-fault loading and 20 °C AAT, admissible currents are approximately 2151 A (360 min), 2641 A (60 min), 3591 A (20 min), 4691 A (10 min), 6391 A (5 min)

and 9191 A (3 min) — all slightly higher than the corresponding values at 0.5 m/s. The benefit becomes more pronounced at lower pre-fault loading levels, where 65% loading for 3 minutes reaches ~12,536 A, representing a very significant short-term capacity gain.

The overall pattern remains the same: higher AAT compresses the overload margin, but higher wind speed provides a consistent uplift in rating. This confirms that using 1 m/s as a realistic worst-case wind speed can unlock more usable short-term capacity without compromising thermal security. These results support adopting 1 m/s as the default assumption for exposed cable S/MTOR assessments, in line with similar arguments for overhead lines, thereby avoiding overly conservative ratings and enabling the safe exploitation of additional network capacity.

Compared with the 138 kV 2000 mm² exposed cable, the 400 kV 1000 mm² cable shows consistently lower absolute S/MTOR values across all AATs and durations, reflecting its higher thermal resistance and lower base current rating in Table 5.8. At 20 °C AAT, the post-fault steady-state DTR is about 1158 A, nearly 45 % lower than the 138 kV case. However, the relative gains from short-term overload are comparable. For example, the 3-minute rating at 20 °C reaches ~6278 A, representing a 5.4× multiple of the steady current, similar to the overload factor seen in the 138 kV cable.

The overall behaviour remains consistent: shorter-duration events unlock substantially higher overload capacity, and colder AAT significantly increases the permissible current. While absolute ratings are lower, the thermal utilisation potential remains high, confirming that even the 400 kV exposed cable can safely withstand significant short-term overloads when pre-fault loading is managed and recovery time is observed. This also means the 400 kV ExpoC section is less likely to be the rating bottleneck except under extreme AAT/SI conditions, as seen in the DTR analysis.

Increasing the wind speed from 0.5 m/s to 1 m/s results in a consistent increase in the dynamic ratings of the 400 kV 1000 mm² exposed cable across all ambient air temperatures and overload durations, as shown in Table 5.9. At 20 °C, the post-fault steady-state rating rises from 1158 A to 1189 A, giving roughly a 3% gain. Similar

improvements are seen in the short-term ratings, with the 3-minute S/MTOR increasing from 6278 A to 6324 A and the 5-minute rating rising from 4628 A to 4674 A.

Table 5.8: Short-Term and Medium-Term Overloading Ratings of Exposed 400kV $1000mm^2$ Cable considering both 0.5m/s Wind Speed and no Solar Irradiance

AAT (°C)		-30	-20	-10	0	10	20	30	40	50
Pre-fault DTR (A)		1592	1516	1436	1351	1259	1158	1048	922	775
Post-fault DTR (A)		1592	1516	1436	1351	1259	1158	1048	922	775
Pre-fault loading%	**Duration (min)**	S/MTOR in Amps at rated voltage, 0.5m/s WS, 0 SI								
100% corresponds to		1592	1516	1436	1351	1259	1158	1048	922	775
-	**inf**	1592	1516	1436	1351	1259	1158	1048	922	775
85%	**360**	1712	1616	1516	1421	1309	1198	1078	952	795
	60	2502	2326	2146	1971	1799	1628	1448	1252	1035
	20	3802	3501	3196	2921	2649	2378	2098	1802	1485
	10	5277	4826	4421	3996	3624	3228	2848	2452	2010
	5	7577	6926	6321	5746	5174	4628	4048	3452	2860
	3	10327	9476	8621	7796	7024	6278	5498	4702	3860
75%	**360**	1762	1656	1556	1451	1339	1228	1098	962	805
	60	2822	2616	2416	2221	2019	1828	1618	1402	1155
	20	4472	4116	3791	3446	3144	2803	2468	2127	1755
	10	6272	5766	5291	4821	4369	3903	3443	2952	2430
	5	9122	8366	7641	6971	6319	5653	4943	4252	3480
	3	11472	10966	10441	9521	8619	7703	6793	5802	4780
65%	**360**	1822	1706	1596	1491	1369	1248	1128	982	815
	60	3142	2916	2696	2471	2259	2038	1808	1562	1295
	20	5117	4716	4346	3996	3634	3263	2883	2487	2045
	10	7242	6691	6146	5621	5109	4588	4058	3487	2870
	5	10542	9741	8946	8171	7459	6688	5908	5087	4170
	3	13792	12641	11646	10621	9409	8588	8058	6937	5720

Although the absolute improvement is modest, the additional margin becomes more valuable at higher ambient temperatures, where thermal headroom is naturally more limited. These results confirm that using 1 m/s as the default wind speed assumption for exposed cables provides a slightly less conservative but still secure rating, enabling more network capacity to be utilised safely under both normal and contingency conditions.

Table 5.9: Short-Term and Medium-Term Overloading Ratings of Exposed 400kV $1000mm^2$ cable considering 1m/s Wind Speed and no Solar Irradiance

AAT (°C)		-30	-20	-10	0	10	20	30	40	50
Pre-fault DTR (A)		1638	1559	1476	1387	1292	1189	1076	948	800
Post-fault DTR (A)		1638	1559	1476	1387	1292	1189	1076	948	800
Pre-fault loading%	**Duration (min)**	S/MTOR in Amps at rated voltage, 1m/s WS, 0 SI								
100% corresponds to		1638	1559	1476	1387	1292	1189	1076	948	800
-	**inf**	1638	1559	1476	1387	1292	1189	1076	948	800
85%	**360**	1758	1649	1556	1447	1342	1229	1106	968	820
	60	2548	2359	2176	2007	1832	1649	1466	1278	1060
	20	3873	3559	3251	2957	2682	2399	2116	1828	1510
	10	5348	4884	4451	4057	3657	3274	2891	2478	2035
	5	7698	7034	6401	5807	5257	4674	4091	3528	2885
	3	10498	9584	8701	7907	7107	6324	5591	4778	3935
75%	**360**	1798	1699	1586	1477	1372	1249	1126	988	830
	60	2868	2649	2446	2247	2052	1849	1646	1428	1180
	20	4543	4174	3821	3497	3177	2849	2521	2178	1780
	10	6343	5849	5346	4872	4427	3974	3496	3003	2480
	5	9243	8449	7746	7072	6377	5724	5046	4353	3580
	3	11843	11149	10596	9622	8727	7824	6846	5903	4830
65%	**360**	1848	1739	1626	1517	1402	1279	1146	1008	840
	60	3178	2949	2726	2507	2282	2059	1836	1588	1320
	20	5178	4774	4401	4032	3682	3309	2911	2513	2095
	10	7328	6749	6226	5682	5182	4659	4111	3538	2920
	5	10678	9849	9076	8282	7532	6759	5961	5138	4270
	3	13928	12799	11776	10732	9532	8659	8161	7038	5820

5.2.4.4 Summary

Among the three configurations, the DBC shows the lowest S/MTOR values, as shown from Table 5.2 to Table 5.9, confirming that it is generally the most limiting section for short- and medium-term rating. Using results from 138kV $2000mm^2$ cable as an example, the 3-minute rating at 20 °C reaches ~7281 A for DBC, compared with ~7733 A for FTC and ~9001 A for ExpoC, highlighting its reduced short-term headroom.

All three cable types follow the same trend: shorter durations allow higher overloads, and colder conditions unlock additional capacity. DBC remains the thermal

bottleneck under most conditions due to its greater depth of burial and higher external thermal resistance. FTC typically provides intermediate capacity, while ExpoC offers the highest short-term ratings thanks to direct air cooling and faster heat dissipation.

5.2.5 Cyclic Thermal Ratings of Cables

The CTR of cable is calculated by applying the 24-hour cyclic loading profile. The calculation is initialised at the respective ambient temperature. The temperatures are calculated according to the cyclic loading profile. The 24-hour loading cycle is repeated 2 times for the CTR calculation of ExpoC and 14 times for the FTC and DBC to ensure the loading cycle reaches cyclic steady-state. An example of the temperature variation and cyclic current loading using the calculated CTR for the 400kV 1000mm^2 DBC at 30°C AAT, which is equivalent to 21.8°C AST1m, is shown in Figure 5.20.

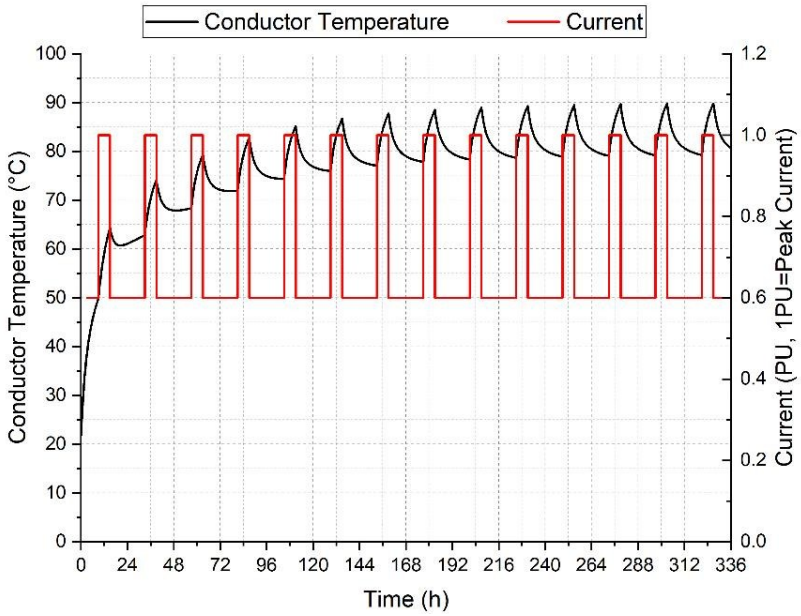

Figure 5.20: Example of the temperature variation and cyclic current for the 400kV 1000mm^2 DBC at 30°C AAT, which is equivalent to 21.8°C AST1m.

The result of the calculated CTR for the different constructions of 138kV 2000mm^2 and 400kV 1000mm^2 cables are shown in Figure 5.21 and Figure 5.22, respectively. The CTR results for the 138 kV 2000 mm^2 cable show a clear improvement in available capacity compared with static DTR. The most significant uplift is observed

for the ExpoC, where the CTR leverages its fast thermal response and effective cooling to support noticeably higher continuous loading.

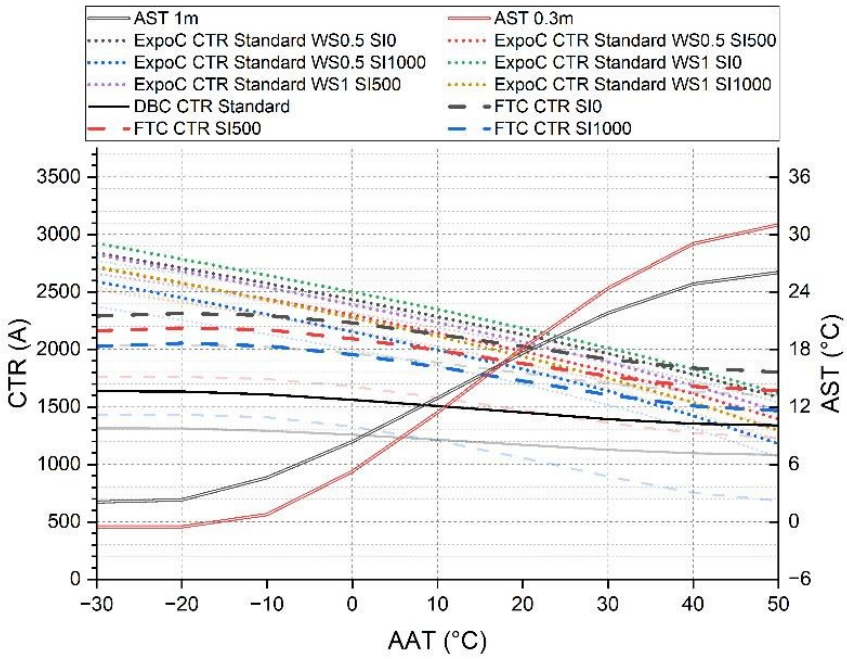

Figure 5.21: Comparison of the CTR for 138kV 2000mm^2 cable in different constructions and the respective AST with the variation of the AAT.

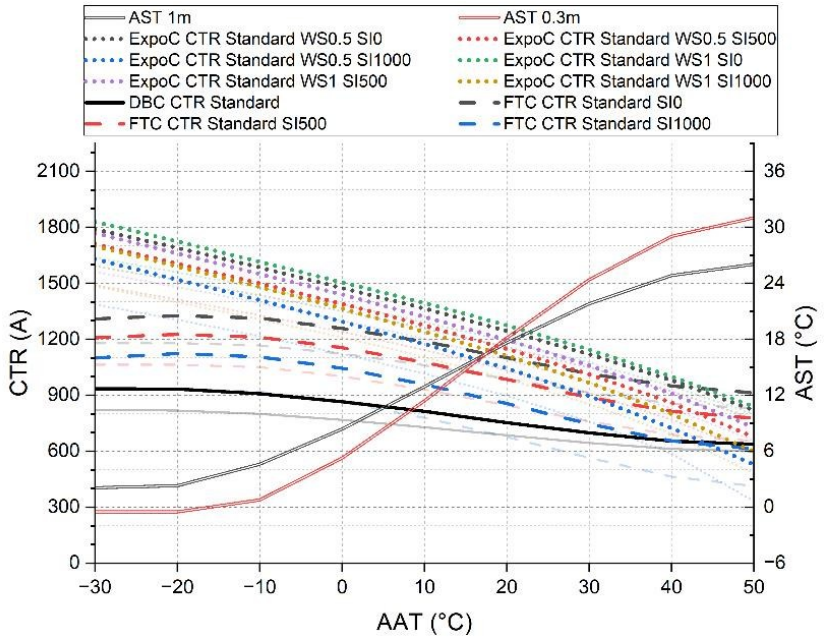

Figure 5.22: Comparison of the CTR for 400kV 1000mm^2 cable in different constructions and the respective AST with the variation of the AAT.

The FTC and DBC also show appreciable CTR gains over DTR, with the FTC benefiting from its intermediate thermal inertia and the effect of SI being much less pronounced under cyclic conditions. This means FTC ratings under realistic solar cycles are less restrictive than those predicted by constant worst-case SI assumptions. By contrast, for the 400 kV 1000 mm² DBC, the improvement offered by CTR becomes marginal, especially under high annual AST, since the deep burial depth and high thermal resistance result in a very slow thermal response that limits the benefit of load cycling.

5.3 Conclusions

The analysis showed that identical cables exhibit different thermal behaviours depending on their installation configuration and exposure to ambient conditions. DBC demonstrated the lowest thermal performance due to limited heat dissipation at the burial depth of 1 m. However, this depth also provides insulation from direct SI. In contrast, the FTC experiences a significant impact from SI because they are buried much shallower, while ExpoC is directly subjected to both solar heating and variable wind cooling.

The cyclic loading profile, which allows the cable to cool, enables it to achieve a much higher rating during the peak loading period. Nevertheless, as 3.3.3 suggests, the cyclic loading profile in future loading patterns may feature longer and flatter peaks, resembling continuous operation. Under such conditions, the advantage of cable CTRs may lose its advantages over DTRs, or the difference may become negligible.

Lastly, cable has a hard temperature limit that can not be violated. Exceeding it will cause the cable's insulation to suffer irreversible damage, leading to a significantly reduced lifetime or an increased risk of insulation failure. The results concerning soil dry-out effects are particularly concerning, though limited by the scarcity of available measurement data. Further experimental and modelling studies are recommended to better understand and quantify this phenomenon in future work.

Chapter 6

Bare Overhead Line Conductors

Bare overhead line conductors, or OHLs, are one of the most essential elements of the electric power network. OHLs are a group of simple, bare conductors that use the surrounding air as insulation, offering low cost and long transmission distances. As a trade-off for air exposure, the bare conductor OHL is a source of electrical hazard, and its operating temperature is easily affected by ambient conditions, i.e., AAT, WS, AA, and SI.

The thermal rating of an OHL is primarily governed by its safety clearance, which is affected by conductor sag resulting from temperature rise and loss of tensile strength. The maximum allowable conductor temperature, and thus the thermal rating, is determined by the need to maintain adequate clearance between the conductor and the ground or nearby objects. Some OHL conductor however, due to been greased, are limited by the grease preserving temperature. Other factors, such as tower geometry and the topography beneath the line, can also influence the effective rating, though these are outside the scope of this study.

The thermal behaviour and rating of OHLs are most commonly evaluated using a set of heat balance equations, as established in international standards [9], [10], [61]. This thesis follows the methodology outlined in IEEE Standard 738 [9], applying it to the analysis and modelling of OHL thermal performance.

Section 6.1 describes the methodology used for thermal modelling of overhead lines. This includes the derivation of the heat balance equation (6.1.1) and the calculation of heat losses by convection (6.1.2) and radiation (6.1.3), as well as the determination of heat input from solar irradiance (6.1.4). The section also covers the calculation of conductor resistance (6.1.5), maximum current-carrying capacity (6.1.6), and thermal capacitance (6.1.7), followed by a case study (6.1.8).

Section 6.2 presents the thermal ratings of OHLs, including steady-state conductor temperatures (6.2.1), dynamic and static ratings (6.2.2), thermal time constants (6.2.3), short- and medium-term overloading ratings (6.2.4), and exceedance ratings (6.2.5).

Section 6.3 concludes the chapter with a summary of the main findings and observations regarding the thermal behaviour and rating characteristics of bare overhead line conductors.

6.1 Methodology of Thermal Modelling for Overhead Lines

The thermal model of the OHL conductor is shown in Figure 6.1. The thermal model of OHL includes two heat sources: heat input from Joule losses and solar irradiance; two heat losses: heat lost from convection and heat lost from radiation; and one heat capacitance: total heat capacitance of the OHL conductor. As the heat lost from convection and the heat lost from radiation can be directly calculated by [9]. Their respective thermal resistances are presented only for demonstration purposes.

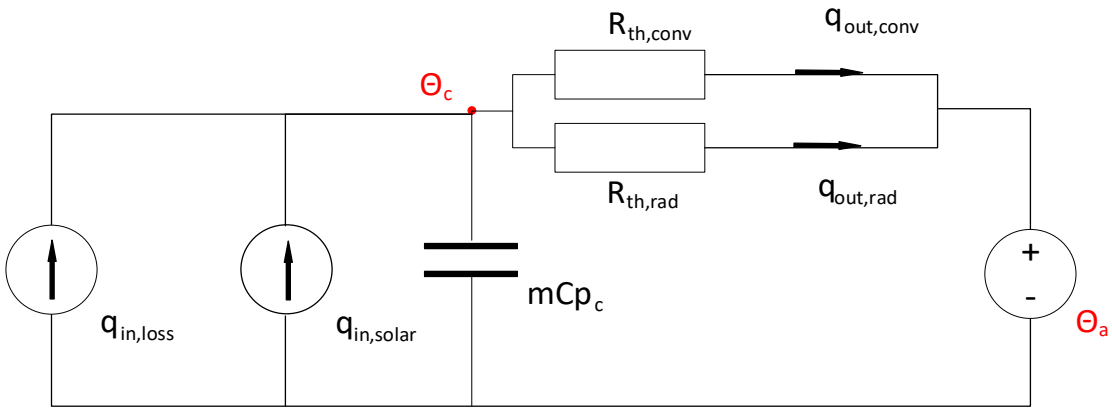

Figure 6.1: Thermal model for the overhead lines.

6.1.1 Heat Balance Equation of Overhead Lines

The IEEE thermal model of the OHL conductor at a steady-state operating point in [9] is given by the same thermal balance equation as in [10]:

$$q_c + q_r = q_s + I^2 R_{AC}(\theta_c) \tag{226}$$

where: q_c is the rate of the convection heat loss; q_r is the rate of the radiated heat loss; q_s is the rate of the solar heat gain; I is the line current; $R_{AC}(\theta_c)$ is the AC resistance of the conductor in Ω/m at the conductor temperature θ_c.

6.1.2 Calculation of the Heat Loss from Convection

The convection heat loss rate q_c is determined by the maximum of the following three quantities calculated by (227)-(229), which represent: a) natural convection heat loss rate q_{cn}, b) forced convection heat loss rate at low wind speeds q_{c1}, and c) forced convection heat loss rate at high wind speeds q_{c2}:

$$q_{cn} = 3.645\rho_f{}^{0.5} D^{0.75}(\theta_c - \theta_a)^{1.25} \tag{227}$$

$$q_{c1} = [1.01 + 1.35(\frac{D\rho_f V_w}{\mu_f})^{0.52}]k_f K_{angle}(\theta_c - \theta_a) \tag{228}$$

$$q_{c2} = 0.754(\frac{D\rho_f V_w}{\mu_f})^{0.6} k_f K_{angle}(\theta_c - \theta_a) \tag{229}$$

where: ρ_f is the density of air at the film (or boundary layer) of the conductor and the ambient in $^{kg}/_{m^3}$; D is the diameter of the conductor in m; θ_a is the ambient temperature in ℃; V_w is the wind speed in m/s; μ_f is the dynamic viscosity of air at the film in kg/(m·s); k_f is the thermal conductivity of the air at the film in $W/(m \cdot \mathrm{K})$; K_{angle} is the factor of the direction of the wind;

The density of air in the film ρ_f, the thermal conductivity of the air in the film k_f and a factor of the direction of the wind K_{angle} can be calculated by:

$$\rho_f = \frac{1.293 - (1.525E-4)\cdot H_e + (6.379E-9)\cdot H_e{}^2)}{1 + 0.00367\theta_{flim}} \tag{230}$$

$$k_f = 0.02424 + \theta_{flim}(7.477E-05) - (4.407E-09)\theta_{flim}{}^2 \tag{231}$$

$$K_{angle} = 1.194 - \cos(\phi) + 0.194\cos(2\phi) + 0.368\sin(2\phi) \tag{232}$$

where: H_e is the altitude of the conductor relative to the sea level; ϕ is the wind AA between wind direction and the conductor axis (the effects of WS with different AA values are considered in [9]); θ_{flim} is the temperature at the boundary layer of the conductor and the air, calculated by:

$$\theta_{flim} = \frac{\theta_c + \theta_a}{2} \tag{233}$$

6.1.3 Calculation of the Heat Loss from Radiation

The radiated heat loss rate can be calculated as:

$$q_r = 17.8 \cdot D \cdot \varepsilon[(\frac{\theta_c + 273.15}{100})^4 - (\frac{\theta_a + 273.15}{100})^4] \tag{234}$$

where: ε is the emissivity, no fundamental difference between the calculation of heat losses from radiation in [9] and [10].

6.1.4 Calculation of the Heat Input from Solar Irradiance

The input heat from solar irradiance is obtained as:

$$q_s = \alpha \cdot Q_{se} \sin(\theta)\, A' \tag{235}$$

where: α is the solar absorptivity; Q_{se} is the total solar and sky radiated heat flux rate, elevation corrected, in W/m^2; θ is the effective sun's ray incidence angle in degrees; A' is the projected area of the conductor per unit length in m^2/m. The projected area per unit length A' is given by:

$$A' = D \tag{236}$$

There is no fundamental difference between the calculation of the heat input from solar irradiance in [9] and [10].

6.1.5 Calculation of the Resistance of the Conductor

The AC resistance of the conductor at a given temperature θ_c can be calculated by:

$$R_{AC}(\theta_c) = (R_{\theta_{high}} - R_{\theta_{low}})/\,(\theta_{high} - \theta_{low}) \cdot (\theta_c - \theta_{low}) + R_{\theta_{low}} \quad (237)$$

where: $R_{\theta_{high}}$ is the AC resistance of the conductor at a higher temperature θ_{high}; $R_{\theta_{low}}$ is the AC resistance of the conductor at the lower temperature θ_{low}.

6.1.6 Calculation of the Maximum Current Carrying Capacity

The steady-state heat balance equation, as previously given in (111), can again be written for the calculation of the maximum CCC of the OHL by:

$$I_{max} = \sqrt{\frac{q_c + q_r - q_s}{R_{AC}(\theta_c)}} \quad (238)$$

6.1.7 Calculation of Thermal Capacitance of Overhead Lines

The heat capacity of the conductor per unit length mCp_c is calculated by [61]:

$$mCp_c = \sum_{i=1}^{Num_{mate}} m_i \cdot Cp_i \quad (239)$$

where: Num_{mate} is the total number of materials used for the OHL; m_i is the mass of the number i material of the conductor per unit length in kg, respectively; Cp_i is the specific heat capacity of number i material in $J/(kg \cdot K)$, respectively.

6.1.8 Case Study

In Chapter 3, it is stated that the WS assumption is 0.5 m/s or 1 m/s, and the AA is 12 degrees. It is worth studying the effects of different WS and AA on the OHL. The following case study presents the impact of WS and AA on the DTR result under 20℃ AAT and no SI. Then, the study of heating from SI to eliminate cooling from WS, with a velocity greater than 0.5 m/s, under a 12-degree AA and a variation in AAT from -30 to 50℃, is presented. Followed by the cooling effect of WS to eliminate the heating effect of SI with the initial condition of 0.5 m/s WS, 12-degree AA and a variation of

AAT from -30 to 50°C. Finally, a study on the equivalent WS under no SI condition that yields the same DTR result across a range of WS with constant 1k SI is shown.

6.1.8.1 Impact of Wind Speed and Attacking Angle

The comparison of the DTR variation with WS under 20°C AAT and no SI using high-speed, low-speed and natural convection equations in [9] calculated for an example OHL conductor under 0 (minimal), 12 (standard assumption) and 90 (maximum) degree AA and WS is shown in Figure 6.2. The final result is also marked in the figure. The OHL used in this ambient sensitivity test is type AAAC Sorbus.

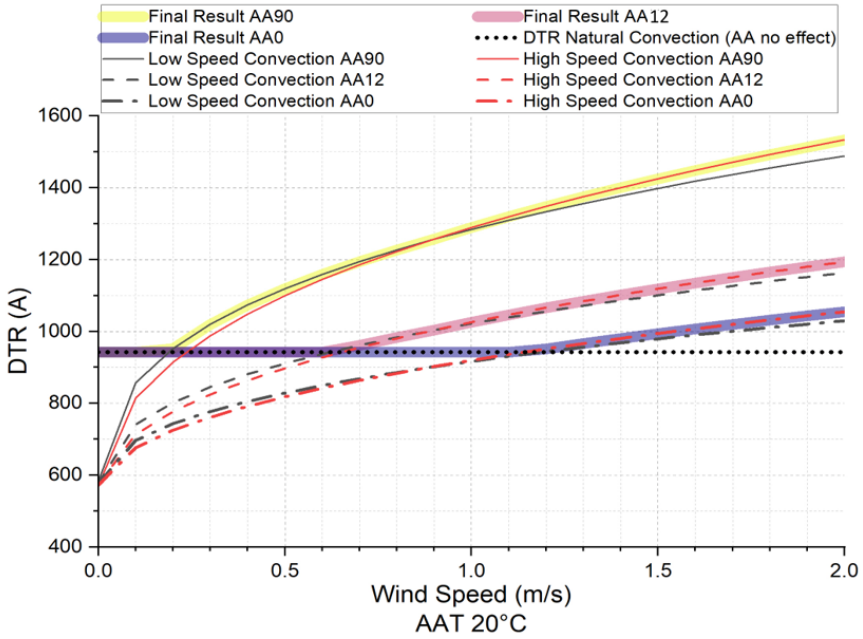

Figure 6.2: Comparison of the DTR variation using three convection equations in [9] of an example OHL conductor under different attacking angles and wind speeds, with the final result marked.

From the results, it can be seen that the 0-degree AA yields the lowest DTR, and the 90-degree AA yields the highest DTR, as expected. Then, under 12-degree AA, the resulting DTR is calculated by the natural convection equation, as suggested by [9] that the higher result from the three convection equations should be taken, so it does not matter whether the WS considered is 0.5 m/s or 0, as the natural convection driven by the temperature difference between the film air and the ambient air determines the DTR

result. However, from the DTR result using 90-degree AA, the 0.5 m/s WS using the low-speed convection equation yields a DTR that is 20% higher than that using 12-degree AA. The DTR result, assuming 1 m/s WS and a 12-degree AA, increased by 9% compared to that calculated with 0.5 m/s WS. Next, under 1 m/s WS, with different AA, both DTR results are determined by the high-speed convection equation. The result under 90-degree AA was 25% higher than under 12-degree AA.

6.1.8.2 Equivalent Solar Irradiance for the Neglect of High Wind Speed

The study of equivalent heating from SI to eliminate cooling from WS, with a velocity greater than 0.5 m/s, under a 12-degree AA and a variation in AAT from -30 to 50°C, is shown in Table 6.1.

Table 6.1: Equivalent heating from solar irradiance to eliminate the cooling from wind speed.

AAT (°C)	Equivalent SI (W/m^2) for				
	WS 1m/s	WS 2m/s	WS 3m/s	WS 4m/s	WS 5m/s
-30	435	1720	2760	3670	4490
-25	445	1740	2785	3700	4525
-20	450	1755	2810	3730	4560
-15	460	1770	2830	3760	4595
-10	470	1785	2850	3780	4625
-5	475	1800	2870	3805	4650
0	485	1815	2885	3825	4670
5	495	1825	2905	3845	4695
10	500	1835	2915	3860	4710
15	515	1845	2930	3870	4725
20	530	1855	2940	3885	4735
25	540	1865	2950	3890	4745
30	555	1875	2955	3900	4755
32	560	1875	2960	3900	4755
34	565	1880	2960	3905	4755
36	570	1880	2960	3905	4755
38	580	1885	2965	3905	4760
40	585	1885	2965	3905	4760
42	590	1890	2965	3910	4760
44	595	1890	2970	3910	4760
46	600	1890	2970	3910	4760
48	605	1895	2970	3910	4760
50	610	1895	2970	3910	4760

From the results, it can be seen that for WS greater than or equal to 2 m/s, for the possible SI level in the UK (up to $1000 W/m^2$) cannot eliminate or overcome the cooling effect of WS. The cooling effect increase of 1 m/s from 0.5 m/s WS might be overwhelmed by the heating effect from SI.

6.1.8.3 Equivalent Wind Speed for the Neglection of Solar Irradiance in Practice

The cooling effect of WS to eliminate the heating effect of SI with the initial condition of 0.5 m/s WS, 12-degree AA and a variation of AAT from -30 to 50℃ is shown in Table 6.2.

Table 6.2: Equivalent cooling from wind speed to eliminate the heating from solar irradiance.

AAT (℃)	Equivalent WS (m/s) for SI (W/m^2)									
	SI100	SI200	SI300	SI400	SI500	SI600	SI700	SI800	SI900	SI1000
-30	0.78	0.84	0.9	0.97	1.04	1.11	1.18	1.25	1.32	1.4
-25	0.77	0.84	0.9	0.96	1.03	1.1	1.17	1.24	1.31	1.39
-20	0.76	0.83	0.9	0.96	1.03	1.09	1.16	1.23	1.31	1.38
-15	0.76	0.82	0.89	0.95	1.02	1.09	1.16	1.23	1.3	1.37
-10	0.75	0.82	0.89	0.95	1.01	1.08	1.15	1.22	1.29	1.36
-5	0.74	0.81	0.88	0.94	1.01	1.07	1.14	1.21	1.28	1.36
0	0.73	0.8	0.87	0.94	1	1.07	1.14	1.21	1.28	1.35
5	0.72	0.79	0.86	0.93	1	1.06	1.13	1.2	1.27	1.34
10	0.72	0.78	0.85	0.92	0.99	1.06	1.12	1.19	1.26	1.33
15	0.71	0.77	0.84	0.91	0.98	1.05	1.12	1.19	1.26	1.33
20	0.7	0.76	0.83	0.9	0.97	1.05	1.11	1.18	1.25	1.32
25	0.69	0.75	0.82	0.89	0.96	1.04	1.11	1.17	1.24	1.31
30	0.68	0.75	0.81	0.88	0.95	1.03	1.1	1.17	1.24	1.31
32	0.68	0.74	0.81	0.88	0.95	1.03	1.1	1.17	1.24	1.31
34	0.68	0.74	0.8	0.87	0.94	1.03	1.1	1.16	1.23	1.3
36	0.67	0.74	0.8	0.87	0.94	1.03	1.09	1.16	1.23	1.3
38	0.67	0.73	0.8	0.87	0.94	1.03	1.09	1.16	1.23	1.3
40	0.67	0.73	0.79	0.86	0.93	1.02	1.09	1.16	1.23	1.3
42	0.66	0.73	0.79	0.86	0.93	1.02	1.09	1.16	1.23	1.3
44	0.66	0.72	0.79	0.85	0.93	1.02	1.09	1.15	1.22	1.29
46	0.66	0.72	0.78	0.85	0.92	1.02	1.08	1.15	1.22	1.29
48	0.65	0.72	0.78	0.85	0.92	1.02	1.08	1.15	1.22	1.29
50	0.65	0.71	0.78	0.84	0.91	1.01	1.08	1.15	1.22	1.29

From the result, it can be seen that as the AAT increases, the equivalent WS needed to eliminate the heating from SI decreases. Then, up to 1.4 m/s of WS is needed to eliminate the highest possible heating from SI ($1000W/m^2$), which is calculated under the AAT of -30°C. At the maximum AAT considered in this thesis, 50°C, the WS needed to eliminate heating from $1000W/m^2$ SI is 1.29m/s.

6.1.8.4 Equivalent Wind Speed for the Neglection of High Solar Irradiance in Practice

A study on the equivalent WS under no SI condition that yields the same DTR result across a range of WS with constant 1k SI is shown in Table 6.3.

Table 6.3: Equivalent WS under no SI condition for the variation of WS with 1k SI.

AAT	Equ. WS when no SI for the initial condition of 1k SI and				
	Initial WS2	Initial WS1.75	Initial WS1.5	Initial WS1.25	Initial WS1
-30	1.03	0.89	0.76	-	-
-25	1.03	0.9	0.76	-	-
-20	1.04	0.9	0.76	-	-
-15	1.04	0.91	0.76	-	-
-10	1.05	0.91	0.76	-	-
-5	1.05	0.91	0.75	-	-
0	1.05	0.91	0.75	-	-
5	1.06	0.91	0.75	-	-
10	1.06	0.91	0.74	-	-
15	1.06	0.9	0.74	-	-
20	1.06	0.9	0.74	-	-
25	1.06	0.9	0.73	-	-
30	1.06	0.89	0.73	-	-
32	1.06	0.89	0.73	-	-
34	1.06	0.89	0.73	-	-
36	1.06	0.89	0.73	-	-
38	1.06	0.89	0.72	-	-
40	1.06	0.89	0.72	-	-
42	1.06	0.88	0.72	-	-
44	1.06	0.88	0.72	-	-
46	1.06	0.88	0.72	-	-
48	1.06	0.88	0.71	-	-
50	1.06	0.88	0.71	-	-

From the result, it can be seen that the equivalent WS under no SI can not be calculated when the initial condition is 1000 W/m^2 SI and WS lower than 1.25m/s, which means that at a WS equal to or lower than 1.25m/s, the neglect of the heating effect from 1000 W/m^2 SI cannot be compensated for the neglect of the cooling effect of WS anymore.

6.2 Thermal Ratings of Overhead Lines

According to the information available, the OHL conductor used in the example circuit, Braintree-Pelham, is ACSR Quad-Zebra with a temperature limit of 50°C. The OHL used in the example circuit of Pentir-Trawsfynydd is AAAC Twin-Sorbus with a temperature limit of 75°C. The specifications of a single ACSR Zebra and a single AAAC Sorbus are shown in Table 6.4. Some parameters are calculated from the specifications according to [9], [10], [93].

Table 6.4: Specification of the example OHL conductors [71], [103].

Line type	ACSR Zebra	AAAC Sorbus
Diameter (mm)	28.62	33.4
Absorptivity (-)	0.9	0.9
Emissivity (-)	0.6	0.6
DC resistance 20°C (Ω/km)	0.06868	-
AC resistance 25°C (Ω/km)	0.06463 (Calculated)	0.066897
AC resistance 75°C (Ω/km)	0.0771 (Calculated)	0.079371
Aluminium mass (kg/km)	1434.984	1822.5
Steel mass (kg/km)	186.0164	-
Thermal capacitance (J/(K*km))	1458.953	1634.783
Conductor temperature limit (°C)	50	75
Heat lost from convection under summer STR condition at maxi conductor temperature (W)	20	44
Heat lost from convection under summer STR condition, but 10m/s WS at max conductor temperature (W)	115	229

6.2.1 Steady-State Conductor Temperatures of Overhead Lines

The results were evaluated against the summer STR reference conditions of 20 °C ambient, 0.5 m/s wind speed, and zero solar irradiance for the two OHL types.

Assessment Conditions:

- Air Temperature (AAT): –30 °C to 50 °C.
- Solar Irradiance (SI): 0, 500, and 1000 W/m² (representing no solar (night), typical UK summer, and heatwave/2022 summer conditions).
- Wind Speed: 0.5 m/s (conservative, per TGN or standard) and 1 m/s (less conservative, but closer to realistic worst-case), at 12° attacking angle.
- Load Levels: 1.0, 0.85, 0.75, and 0.65 PU, representing varying pre-fault reserve margins.

Figure 6.3 below shows the Zebra OHL conductor temperature at 65 % loading under 0.5 and 1 m/s wind speed for three solar irradiance cases:

- 1000 W/m² (Blue – Heatwave/2022 Conditions): The conductor reaches its thermal limit at approximately 12 °C AAT. Even at mild ambient temperatures, the line is already thermally constrained.
- 500 W/m² (Red – Typical Summer): The thermal limit is reached at around 25 °C AAT, providing more headroom compared to the heatwave case.
- 0 W/m² (Black – No Solar): The conductor can sustain 65 % loading even at 38 °C AAT without breaching the temperature limit.

Figure 6.3b below illustrates the same scenario at 1 m/s wind speed, which shifts all curves to the right, indicating increased thermal capacity due to enhanced convective cooling. For example, under 1000 W/m² irradiance, the effective allowable AAT before reaching the 50 °C limit is shifted by roughly +8 °C, enabling higher loading under the same temperature limit.

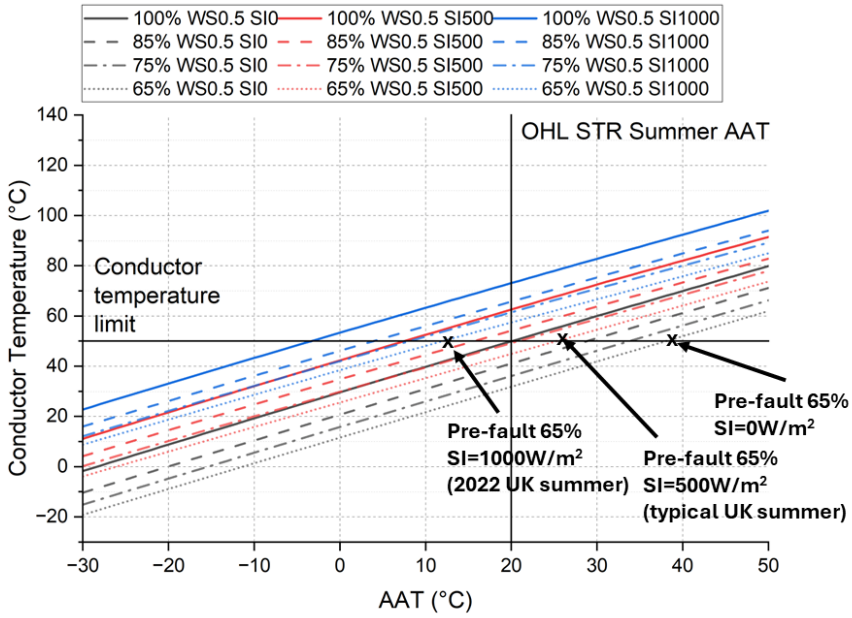

a) ACSR Zebra 0.5 m/s WS

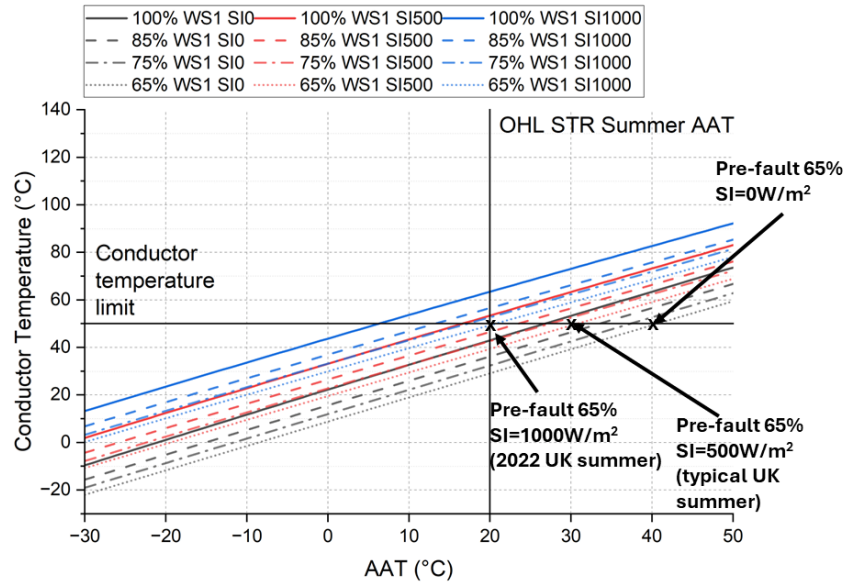

b) ACSR Zebra 1 m/s WS

Figure 6.3: Variation of a single ACSR Zebra OHL conductor temperature with the variation of AAT and SI for 0.5m/s and 1 m/s WS values when loaded with the respective 1PU, 0.85PU, 0.75PU and 0.65PU summer STR current.

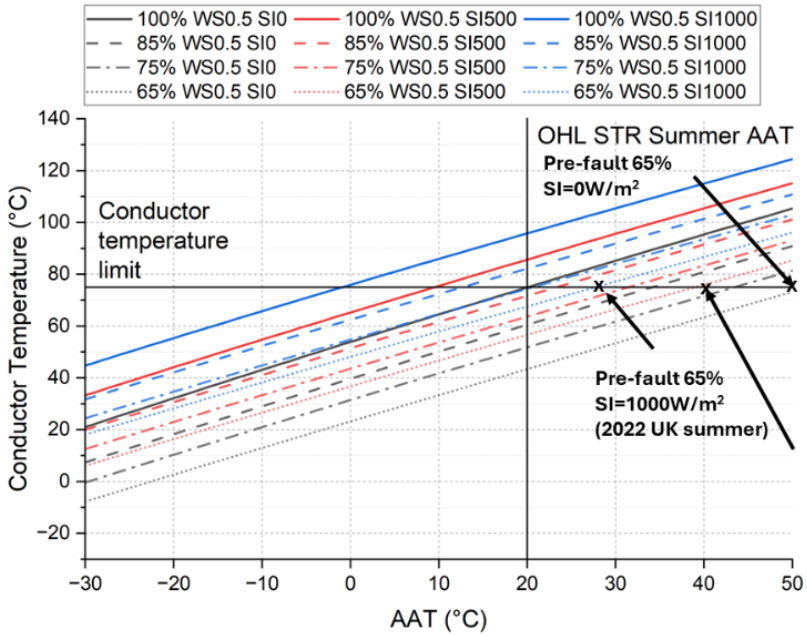

a) AAAC Sorbus 0.5m/s

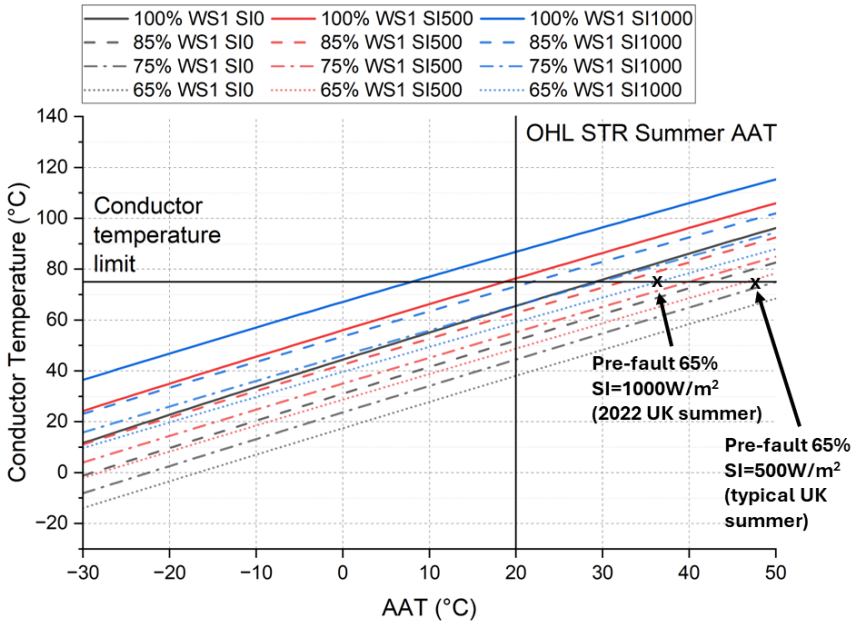

b) AAAC Sorbus 1 m/s

Figure 6.4: Variation of a single AAAC Sorbus OHL conductor temperature with the variation of AAT and SI for 0.5m/s and 1 m/s WS values when loaded with the respective 1PU, 0.85PU, 0.75PU and 0.65PU summer STR current.

A similar assessment was carried out for the AAAC Sorbus OHL in Figure 6.4, which operates at a higher thermal design limit of 75 °C. As expected, this results in

greater available thermal capacity compared to the Zebra conductor. In the plots, the temperature-limit curves for Sorbus are shifted upwards and to the right, meaning that for the same ambient temperature, wind, and solar conditions, the line can carry more current before reaching its limit. The overall behaviour, however, remains consistent with that observed for Zebra:

- High solar irradiance still brings forward the point where the thermal limit is reached.
- Lower wind speeds remain the most restrictive case, while a 1 m/s wind speed provides additional margin.
- Cooler ambient temperatures continue to offer significant headroom.

The comparison between the (a) (0.5 m/s) and (b) (1 m/s) plots illustrates the sensitivity to wind cooling. The shift to the right under 1 m/s conditions demonstrates that a less conservative wind assumption allows operation at higher ambient temperatures for the same current.

From the result, it can be seen that the SST variation of OHL conductor generally follows the variation of AAT given a constant WS and SI. For the same AAT, the SST increases when the SI increases, and the SST decreases when the WS decreases. The result follows the expectation of the thermal balance equation [9]. For the calculated SST lower than the respective OHL conductor temperature limit, it means the CCC of the OHL can be increased greater than the summer STR and for a calculated SST greater than the temperature limit, the CCC of the OHL needs to be decreased from the summer STR to avoid violation of the temperature limit.

6.2.2 Dynamic and Static Thermal Ratings of Overhead Line Conductors

The DTR can be calculated as a map of CCC or MVA carrying capacity for a given line voltage using a range of ambient conditions: AAT, WS, AA and SI. The temperature limit of ACSR Zebra is very close to the maximum AAT considered in this thesis, so the SI variation for the calculation of DTR used a step of 100 W/m^2 instead of 500 W/m^2 used by other components.

The static thermal ratings (STR) are parts of DTR with specific ambient conditions for the respective rating seasons, which are marked in the DTR results. The DTR calculated is the post-fault DTR, where the pre-fault DTR is 0.85PU of the post-fault DTR as required in TGNs [14] and [11]. The DTR results of ASCR Zebra and AAAC Sorbus are shown in Figure 6.5 and Figure 6.6, respectively.

The ACSR Zebra conductor reaches its thermal limit of 50 °C at approximately 25 °C AAT under low wind conditions (WS = 0.5 m/s) and high solar irradiance (SI = 1 kW/m²). Under these conditions, further loading is not permissible without breaching the design limit. This suggests that the existing 50 °C temperature limit for ACSR Zebra may be overly conservative, particularly in summer conditions. STR, calculated at 20 °C with no solar gain, already embed some exceedance risk. The Zebra conductor is highly sensitive to hot, sunny, low-wind conditions, making it the most constrained element during extreme summer events. Increasing the assumed wind speed from 0.5 m/s to 1.0 m/s results in considerably higher thermal ratings, particularly at higher AATs. These finding highlights that the 0.5 m/s wind speed assumption is overly conservative, potentially under-utilising available conductor capacity during real-world operating conditions.

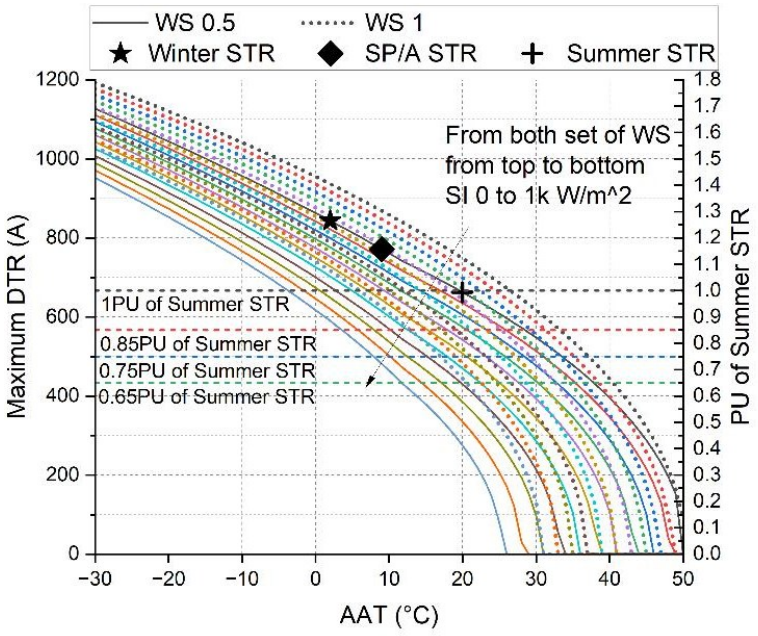

Figure 6.5: Variation of the maximum DTR with different AAT, WS and SI for a single ACSR Zebra 50°C limit OHL conductor.

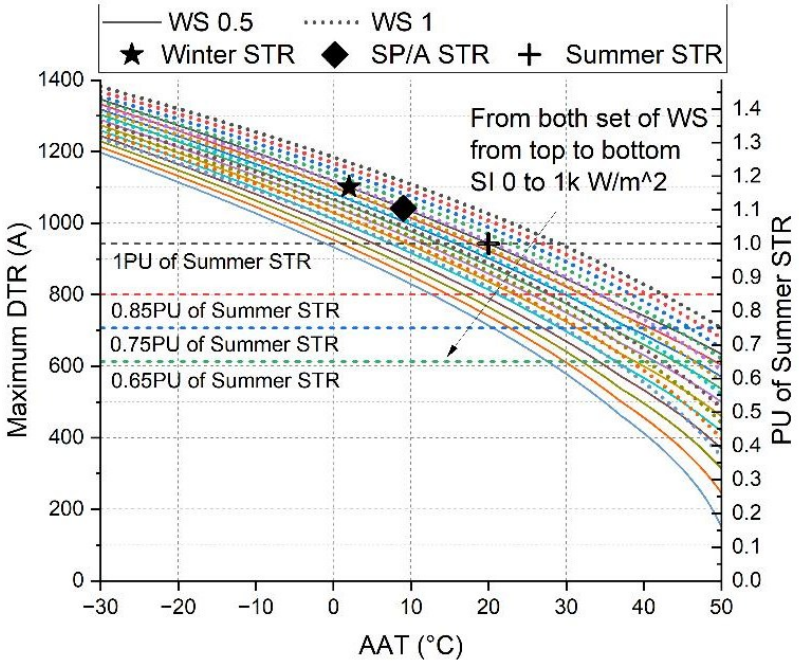

Figure 6.6: Variation of the maximum DTR with the variation of AAT, WS and SI for a single AAAC Sorbus 75°C limit OHL conductor.

The AAAC Sorbus conductor, with its higher thermal limit (75 °C), avoids the early violations observed for ACSR Zebra and provides greater thermal headroom under identical operating conditions. Its DTR profile shows a smooth decline with increasing AAT, with a noticeable gradient change around 40 °C, consistent with the convective heat-loss regime switch defined in IEEE 738 [9]. This conductor demonstrates greater resilience under extreme hot, low-wind scenarios, due to a higher thermal limit, enabling higher load transfer before reaching its limit.

It must be noted that DTR exceedances are treated probabilistically and are not strictly avoided. Hence, exceedance ratings (on which STR is based) remain a valid planning approach. All results presented are for steady-state, indefinite loading conditions and do not consider cyclic loading or transient thermal behaviour.

6.2.3 Thermal Time Constants of Overhead Lines

OHLs do not behave as if they are in indefinite steady-state conditions. Each conductor possesses a thermal time constant, typically on the order of minutes, which

governs the rate at which conductor temperature responds to changes in current and ambient conditions.

Variation of the conductor temperature with time for ACSR Zebra and AAAC Sorbus when loaded with 1, 0.85, 0.75 and 0.6PU of constant summer STR current under constant summer STR ambient conditions is shown in Figure 6.7. The conductor temperatures of OHLs are initialised at the AAT of the summer STR, which is 20°C. Then the OHLs are loaded with constant current via a step change to the respective PU of summer STR for 360 minutes. The TTCs are marked according to the 1PU current temperature variation. The TTCs are calculated using the mathematical definition, which is the time required to reach 63.2%, 86.5%, 95%, and 98.2% of the change from the initial state temperature to the final steady-state temperature.

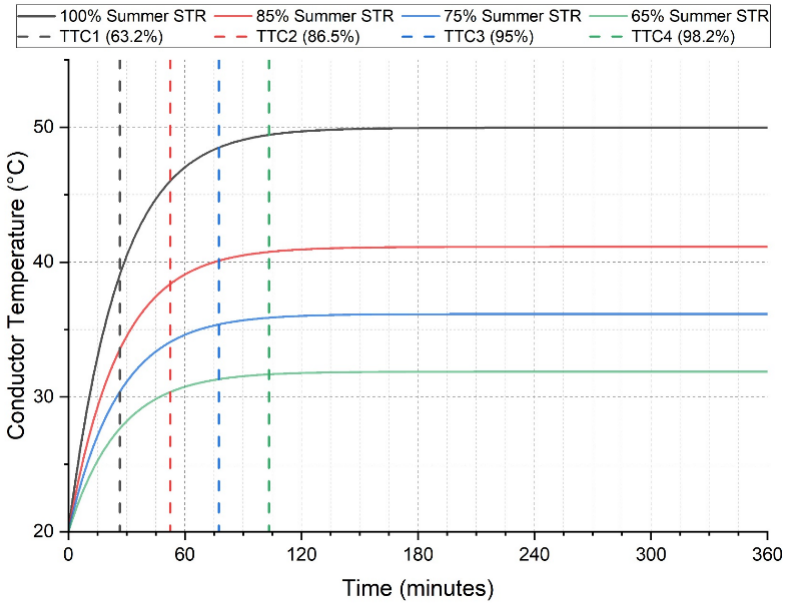

Figure 6.7: Variation of the conductor temperature with time for ACSR Zebra at OHL Summer STR condition when loaded with 1, 0.85, 0.75 and 0.6 PU of constant summer STR current.

From the result of the TTC of OHLs, it can be seen that the first TTC is around 30 minutes for both OHL conductors, and the fourth TTC is no more than 2 hours. Such results indicate that the maximum resolution of the ambient data is 1 hour. Any longer

period between measurements will cause the calculated DTR of overhead to be notably over-rated or under-rated.

However, the largest temperature change occurs within the first few minutes, making sub-hourly dynamics critical for accurate modelling. Conductor temperature exhibits an exponential rise toward a new steady-state value after a step change in load. Higher loading results in a higher final steady-state temperature, whereas lower loading leads to a lower final temperature.

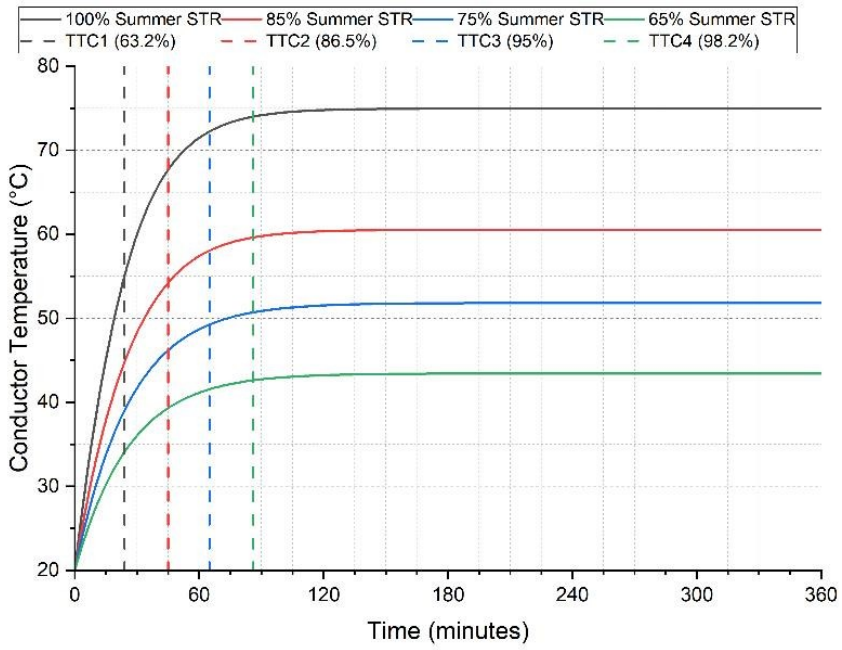

Figure 6.8: Variation of the conductor temperature with time for AAAC Sorbus at OHL Summer STR condition when loaded with 1, 0.85, 0.75 and 0.6 PU of constant summer STR current.

For the AAAC Sorbus conductor, the thermal time constant is shorter compared to the ACSR Zebra. This is primarily due to Sorbus having a lower thermal mass, resulting in a faster temperature rise and cooling response under the same loading and ambient conditions.

6.2.3.1 Thermal Time Constants under High Solar Irradiance

The 2022 UK summer recorded heat wave of high AAT and high SI, it would be worth investigating how the TTC changes under high solar irradiance conditions, the new temperature variation and its TTC is calculated under 40℃ AAT, 0.5m/s WS, 12 degrees AA and $1000 W/m^2$ SI. The results are shown in Figure 6.9 for ACSR Zebra and Figure 6.10 for AAAC Sorbus.

It can be seen that the TTC under high AAT and high SI conditions generally shortened the STR summer condition by 10%-15%, indicating that the final steady-state temperature will be reached faster than in the usual summer condition. Additionally, the conductor temperature limits are violated in both OHLs.

This dynamic behaviour can now govern how long and how often thermal limits are exceeded, thereby directly affecting the calculated exceedance levels on which STR is based. These results confirm that hourly-resolution modelling may underestimate short-term limit violations during the transient phase when hourly or higher resolution is chosen. To accurately capture exceedances and inform operational decisions, dynamic rating studies should be performed at sub-hourly resolution. This will be discussed further in section 6.2.5.

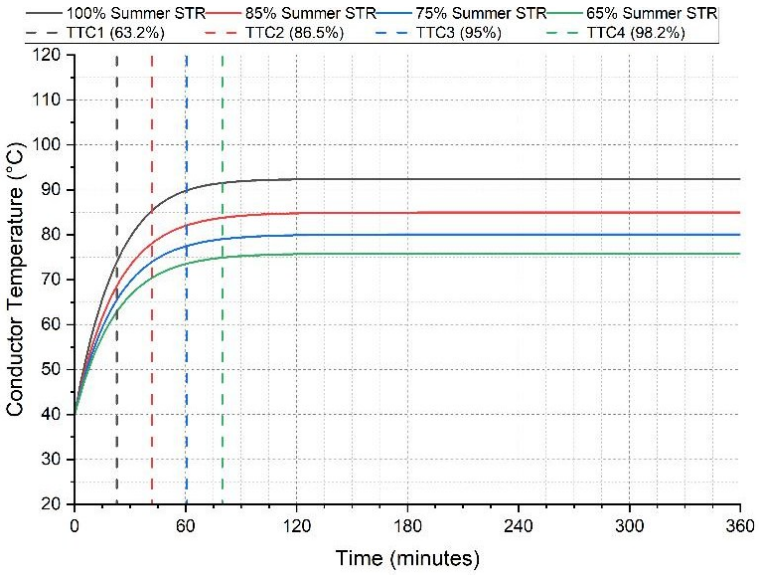

Figure 6.9: Variation of the conductor temperature with time for ACSR Zebra at OHL during Heatwave UK summer when loaded with 1, 0.85, 0.75 and 0.6 PU of constant summer STR current.

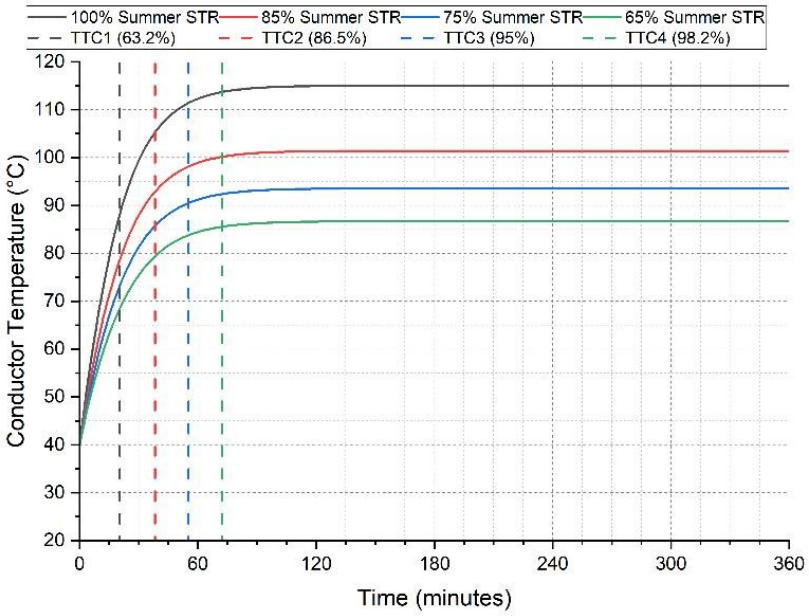

Figure 6.10: Variation of the conductor temperature with time for AAAC Sorbus at OHL during Heatwave UK summer when loaded with 1, 0.85, 0.75 and 0.6 PU of constant summer STR current.

6.2.4 Short-Term and Medium-Term Overloading Ratings of Overhead Lines

The 3rd and 4th TTCs of example OHL conductors exceed 60 minutes, as shown in previous results. The pre-fault ratings of OHLs leave extra CCC and thermal capacities as reserve. This reserve means the OHL under pre-fault condition should not reach its temperature limit.

From the results shown in the previous section, under high SI conditions, the OHL may reach, and even exceed, its temperature limit. However, if a non-zero exceedance level sets the pre-fault temperature limit of OHL, the ratings are calculated without considering SI. So, CCC and thermal capacities reserve under pre-fault conditions give extra CCC during post-fault conditions greater than the post-fault DTR for a set of durations, given the condition that SI is ignored, as the STR also ignores the SI. This extra CCC is denoted as an overload rating. Depending on the actual overloading duration, it is split into short-term (less than 20 minutes) and medium-term

(less than 6 hours) overloading ratings, with the 6-hour overloading equivalent to the post-fault DTR of OHL [11], [14].

An example of the temperature variation of the calculation of the S/MTOR is shown in Figure 6.11. In this example, the ambient condition is set to winter STR with 2°C AAT, 0.5 m/s WS, 12 degrees AA, and no SI. The OHL is loaded with the pre-fault current of 0.85PU winter STR before time 0, where time 0 represents the initial of the fault. And the 0.85PU is the maximum pre-fault loading of the OHL as required by TGN [14]. After time 0, the OHL entered the post-fault condition and was loaded with the respective current of S/MTOR for 3 to 60 minutes, then returned to post-fault continuous loading at 1PU of the winter STR.

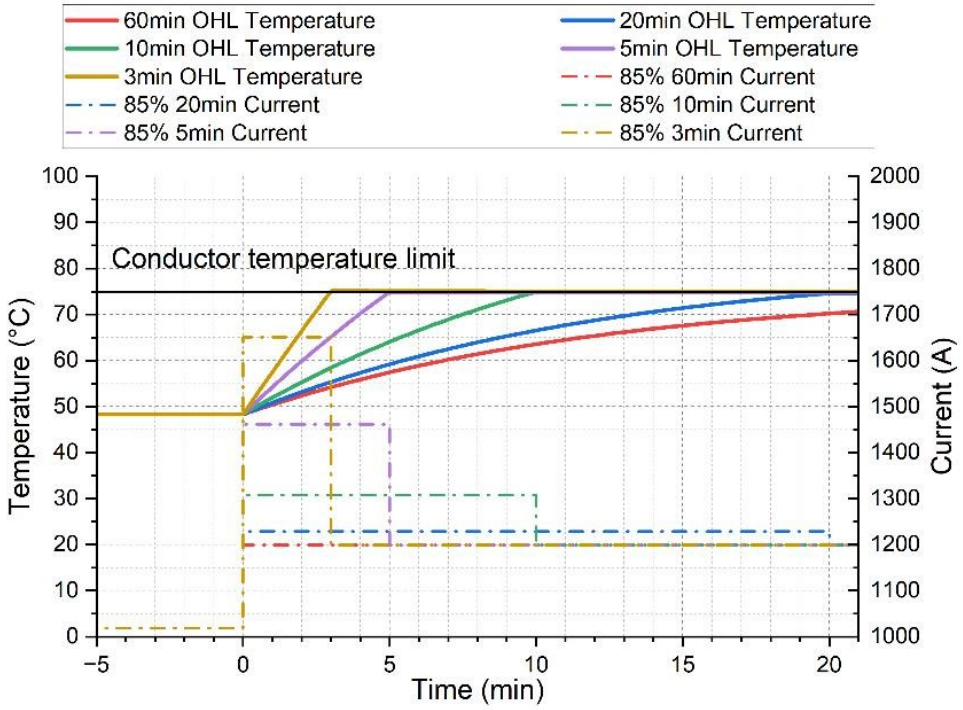

Figure 6.11: An example of the OHL conductor temperature variation when loaded with the respective S/MTOR current.

It can be seen when using S/MTOR that, for a given period, the OHL with a certain pre-fault loading can be loaded higher than the maximum continuous post-fault loading for that duration to reach exactly its pre-set temperature limit. In this example, the maximum post-fault continuous rating is the winter STR of this OHL conductor, and

the CCC during the given overloading duration to reach the temperature limit of the OHL conductor at the end of the overloading duration is the S/MTOR of that duration for the OHL. After the overload using the S/MTOR for a given duration, it must return to its maximum continuous post-fault loading to prevent a violation of the preset temperature limit.

Based on the example S/MTOR calculation process shown, the results of the S/MTOR for the two OHLs in this thesis, with variation in AAT, are shown in Table 6.5 to Table 6.8. The pre-fault loadings used are the DTR under the ambient condition used in the assessment.

Table 6.5: Short-Term and Medium-Term Overloading Ratings of ACSR Zebra 50°C Limit Considering 0.5m/s Wind Speed and 0 Solar Irradiance

AAT (°C)		-30	-20	-10	0	10	20	30	40	50
Pre-fault DTR (A)		939	870	798	719	634	553	457	329	-
Post-fault DTR (A)		1127	1044	957	863	761	663	548	395	-
Pre-fault loading%	**Duration (min)**	S/MTOR in Amps at rated voltage, 0.5m/s WS, 12 AA, 0 SI								
100% corresponds to		1127	1044	957	863	761	663	548	395	-
-	**inf**	1127	1044	957	863	761	663	548	395	
85%	**360**	1127	1044	957	863	761	663	548	395	-
	60	1139	1054	966	871	771	672	555	399	-
	20	1229	1139	1041	941	841	732	605	434	-
	10	1384	1279	1171	1056	956	832	680	489	-
	5	1644	1509	1381	1256	1146	992	810	579	-
	3	1954	1819	1621	1496	1386	1202	980	699	-
75%	**360**	1127	1044	957	863	761	663	548	395	-
	60	1146	1061	972	878	777	678	559	402	-
	20	1291	1191	1092	993	887	773	634	452	-
	10	1511	1396	1277	1168	1052	913	744	532	-
	5	1891	1736	1587	1458	1322	1143	934	662	-
	3	2291	2106	1927	1778	1612	1393	1134	802	-
65%	**360**	1127	1044	957	863	761	663	548	395	-
	60	1152	1067	978	883	783	682	562	404	-
	20	1342	1242	1143	1038	928	802	657	469	-
	10	1627	1502	1393	1263	1133	982	802	569	-
	5	2077	1922	1773	1643	1473	1272	1032	739	-
	3	2587	2392	2223	2033	1833	1582	1282	909	-

Table 6.6: Short-Term and Medium-Term Overloading Ratings of ACSR Zebra 50°C Limit Considering 1m/s Wind Speed 0 Solar Irradiance

AAT (°C)		-30	-20	-10	0	10	20	30	40	50
Pre-fault DTR (A)		994	933	868	796	715	624	514	369	-
Post-fault DTR (A)		1193	1120	1041	955	858	749	617	443	-
Pre-fault loading%	**Duration (min)**	S/MTOR in Amps at rated voltage, 1m/s WS, 12 AA, 0 SI								
100% corresponds to		1193	1120	1041	955	858	749	617	443	-
	inf	1193	1120	1041	955	858	749	617	443	-
85%	**360**	1193	1120	1041	955	858	749	617	443	-
	60	1208	1132	1051	963	865	754	621	445	-
	20	1313	1227	1136	1033	925	804	661	470	-
	10	1478	1377	1271	1153	1030	894	731	520	-
	5	1778	1647	1511	1363	1210	1044	851	610	-
	3	2108	1947	1771	1603	1450	1254	1021	720	-
75%	**360**	1193	1120	1041	955	858	749	617	443	-
	60	1216	1139	1057	968	868	757	623	447	-
	20	1376	1279	1182	1078	963	837	683	487	-
	10	1621	1504	1382	1253	1118	967	788	562	-
	5	2031	1874	1722	1553	1378	1187	968	682	-
	3	2441	2274	2082	1873	1668	1437	1158	822	-
65%	**360**	1193	1120	1041	955	858	749	617	443	-
	60	1223	1145	1062	972	872	760	625	448	-
	20	1428	1330	1227	1117	997	865	705	503	-
	10	1728	1600	1472	1337	1187	1025	835	593	-
	5	2218	2040	1872	1697	1517	1305	1065	753	-
	3	2738	2520	2332	2107	1867	1605	1305	923	-

Each table lists the allowable post-fault current (A) for a given AAT, pre-fault loading level (85/75/65% of the DTR of the respective ambient condition), and overload duration (3–360 min), assuming WS = 0.5 and 1 m/s and SI = 0. The “inf” rows point to the post-fault maximum DTR (i.e., the maximum continuous capability under these ambient conditions).

Entries are valid only when the pre-fault conductor temperature (at time 0) is below its temperature limit. That pre-fault temperature is calculated from the ambient and loading in the previous period (e.g., the previous hour). If the conductor is already

at or above its limit, no overloading value from the table applies unless a higher limit is explicitly authorised, which is outside the scope of this thesis at this stage.

Table 6.7: Short-Term and Medium-Term Overloading Ratings of AAAC Sorbus 75°C Limit Considering 0.5m/s Wind Speed 0 Solar Irradiance

AAT (°C)		-30	-20	-10	0	10	20	30	40	50
Pre-fault DTR (A)		1122	1061	998	931	861	786	703	618	528
Post-fault DTR (A)		1346	1273	1197	1117	1033	943	844	741	633
Pre-fault loading%	**Duration (min)**	S/MTOR in Amps at rated voltage, 0.5m/s WS, 12 AA, 0 SI								
100% corresponds to		1346	1273	1197	1117	1033	943	844	741	633
-	**inf**	1346	1273	1197	1117	1033	943	844	741	633
85%	**360**	1346	1273	1197	1117	1033	943	844	741	633
	60	1358	1284	1207	1126	1041	950	851	749	639
	20	1463	1379	1297	1206	1116	1015	916	814	689
	10	1633	1539	1442	1346	1241	1130	1021	914	774
	5	1933	1819	1702	1586	1461	1340	1211	1084	914
	3	2273	2139	2032	1896	1751	1590	1441	1304	1094
75%	**360**	1346	1273	1197	1117	1033	943	844	741	633
	60	1365	1290	1213	1131	1046	955	856	754	643
	20	1525	1440	1353	1261	1161	1065	961	849	723
	10	1780	1675	1568	1461	1351	1235	1121	999	843
	5	2210	2085	1948	1811	1671	1525	1401	1239	1053
	3	2680	2515	2358	2191	2011	1845	1691	1509	1273
65%	**360**	1346	1273	1197	1117	1033	943	844	741	633
	60	1372	1296	1218	1136	1051	960	860	758	646
	20	1582	1496	1403	1306	1206	1105	1000	883	746
	10	1902	1791	1688	1571	1456	1340	1205	1068	901
	5	2432	2291	2138	1991	1866	1720	1555	1378	1161
	3	3032	2841	2658	2471	2296	2120	1925	1708	1431

Where the pre-fault temperature is below the limit, the tables give the allowable post-fault current for the chosen duration and AAT. Solar irradiance is ignored in the tabulated values for consistency with the pre-fault limit definition. However, overloads could also be derived for cases with solar included, provided the pre-fault temperature at time 0 still sits below the limit.

Table 6.8: Short-Term and Medium-Term Overloading Ratings of AAAC Sorbus 75°C Limit Considering 1m/s Wind Speed 0 Solar Irradiance

AAT (°C)		-30	-20	-10	0	10	20	30	40	50
Pre-fault DTR (A)		1151	1100	1046	988	924	855	778	690	588
Post-fault DTR (A)		1381	1320	1255	1185	1109	1026	933	828	706
Pre-fault loading%	**Duration (min)**	S/MTOR in Amps at rated voltage, 1m/s WS, 12 AA, 0 SI								
100% corresponds to		1381	1320	1255	1185	1109	1026	933	828	706
-	**inf**	1381	1320	1255	1185	1109	1026	933	828	706
85%	**360**	1381	1320	1255	1185	1109	1026	933	828	706
	60	1398	1334	1267	1195	1118	1033	939	833	710
	20	1518	1444	1367	1285	1198	1103	999	883	750
	10	1708	1624	1532	1435	1333	1223	1109	978	830
	5	2058	1934	1822	1705	1573	1433	1299	1138	960
	3	2438	2294	2152	1995	1843	1693	1539	1358	1140
75%	**360**	1381	1320	1255	1185	1109	1026	933	828	706
	60	1407	1343	1274	1201	1123	1037	942	835	712
	20	1592	1513	1429	1341	1248	1147	1037	915	777
	10	1877	1773	1669	1561	1448	1327	1192	1055	892
	5	2357	2213	2079	1941	1788	1637	1472	1285	1082
	3	2867	2693	2519	2341	2158	1967	1762	1545	1302
65%	**360**	1381	1320	1255	1185	1109	1026	933	828	706
	60	1415	1350	1280	1207	1127	1041	945	838	714
	20	1650	1570	1480	1387	1287	1181	1070	943	799
	10	2005	1895	1780	1662	1537	1406	1270	1118	944
	5	2575	2425	2260	2112	1947	1786	1610	1418	1194
	3	3175	2985	2790	2612	2417	2206	1980	1738	1464

In shorter durations (3–20 min), it shows the short-term emergency headroom created by thermal inertia; while moving right to higher AAT reduces headroom. Lower pre-fault loading (65–75 %) yields larger dynamic thermal margins at time 0, so higher short-term currents are permissible. Comparing conductors, AAAC Sorbus (75 °C limit) supports higher overloads than ACSR Zebra (50 °C limit) at the same AAT/duration because of its higher thermal ceiling.

From the tables, the short-duration rows are often 60–110% above the 6-hour (≈ continuous) values at the same ambient, because the conductor has thermal headroom at time zero. For example, at 20 °C AAT, 1m/s WS:

- ACSR Zebra, 85% pre-load: 3 min ≈ 1,254 A vs 360 min ≈ 749 A → ~1.7 times.
- AAAC Sorbus, 85% pre-load: 3 min ≈ 1,693 A vs 360 min ≈ 1,026 A → ~1.65 times.

At lighter pre-load, the margin is even larger (e.g., Zebra 65% at 20 °C, 1m/s WS: 3 min 1,605 A vs 360 min 749 A → ~2.1×). Colder ambient conditions push these multipliers up; hotter ambient conditions push them down.

This behaviour is a direct consequence of thermal time response. Assets with significantly greater thermal mass, notably power transformers (oil and winding) and cables (larger conductor, insulation, and soil/backfill), generally permit even higher short-term overloads relative to their continuous rating because their temperatures rise more slowly. The trade-offs differ by asset (transformer hot-spot ageing, cable joint temperatures and soil dry-out), but the principle holds: the shorter the event and the greater the pre-fault headroom, the more overload it can carry without exceeding temperature limits.

6.2.5 Exceedance Level-Based Ratings of OHLs

Exceedance level-based ratings form the foundation of STRs of OHL. They recognise that conductor cooling depends on variable weather conditions, and that extreme combinations of wind, temperature, and solar radiation rarely occur simultaneously. By defining ratings on a statistical basis, where the conductor is allowed to exceed its design temperature for only a small, quantified proportion of time, previous work by Gibbon and Price [62] established a practical method for setting continuous ratings. This exceedance approach became the basis for the STR methodology still used for overhead lines, which is implemented in TGN26 [11].

The original experiment was designed in 1977, where the OHL type Zebra was exposed to ambient conditions for 1 year with a resolution of 6 minutes. The OHL is loaded with a constant current, $I_{applied}$ of 1020 A. Every 6 minutes, if the OHL exceeds certain bin temperatures (45°C to 90°C, in 5°C increments), the exceedance for that bin is recorded, along with its frequency of exceedance. To capture the thermal dynamics (and inertia) of OHLs, 6-minute intervals were used in the original experiment. Below

are the input parameters of ambient conditions and loading chosen during the experiment.

- $I_{applied}$ = 1020 Amps (constant); "Load currents were chosen so that statistically significant excursions were obtained over the range of design temperatures applied to overhead lines". This is close to Ambient temperature of 20°C, Wind Speed of 0.5 m/s, Attacking Angle of 0°, and Solar Irradiance of 1000 W/m^2, which is typically used by manufacturers for stating the thermal rating of a given OHLs.
- θ_{design} = Design or Operational temperature is based on 45°C to 90°C conductor temperature with 5°C intervals. At θ_{design}, ambient temperatures of 20°C (summer, which are defined as May to August), 9°C (Normal Hot/Cold), and 2°C (Winter) are fixed according to seasons, at WS of 0.5 m/s (12° AA), and at zero SI. Its corresponding currents for these sets of temperature intervals with the fixed ambient conditions are called I_{design}.

6.2.5.1 Problem Statements and Objectives

The sub-hourly ambient data resolution (5 minutes) is important as OHLs thermal gradient is highest in the sub-hourly mark, as shown by its TTCs. Preferably, data with a resolution of 5 minutes (or finer) is desired to capture the correct dynamic thermal response of OHLs. Therefore, in evaluating the impact of changes in weather conditions, especially during summer and heatwaves, it is crucial that the ambient data with the correct resolution for OHLs is available. However, most of the available open-source data is recorded in hourly intervals.

According to Figure 6.12 at St. Johns Wood, with 5 minutes and hourly averaged data, most of the winter and spring data are missing. Nonetheless, most of the data in the summer and autumn months is available. In the context of OHLs as well as their circuits, the seasonal analysis can still be done in these 2 seasons to evaluate their exceedance levels, but cannot be further extended to other seasons. While 5-minute measurement data are not available as open source and have to be directly obtained or measured, hourly measurements of ambient weather data can be sourced easily (assuming that the nearest weather station to the substation exhibits the same ambient conditions).

Based on the ambient conditions in Figure 6.12, dynamic ratings of OHL Type Zebra are calculated using IEEE std. 738 [9] using both 5-minute and hourly resolution (averaged from 12 instances of 5 minutes) ambient data in Figure 6.13. The 5-minute data show a higher range of DTR variations, with 10% of the data below the applied current of 1020A, with 6 % for the hourly data.

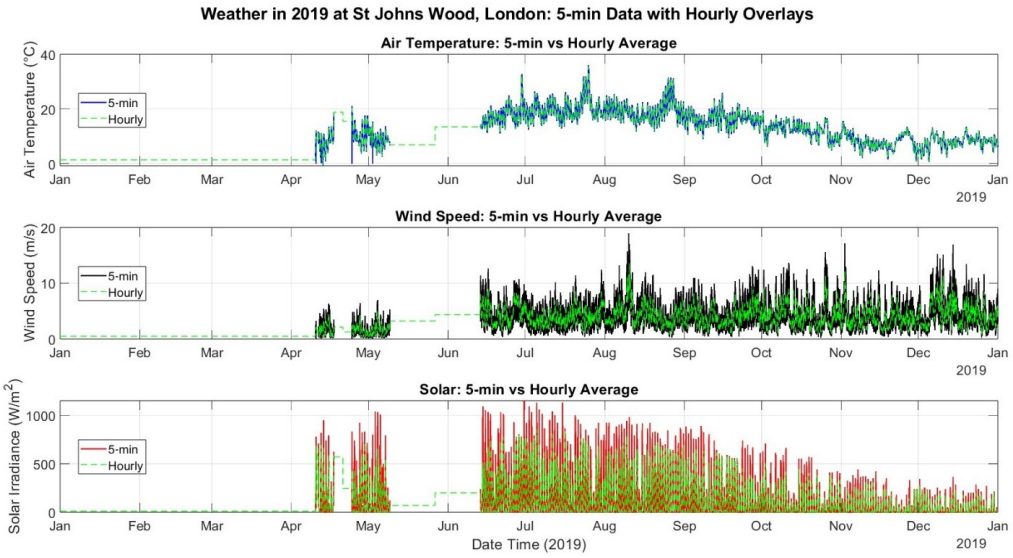

Figure 6.12: Recorded ambient weather data at St. Johns Wood substation.

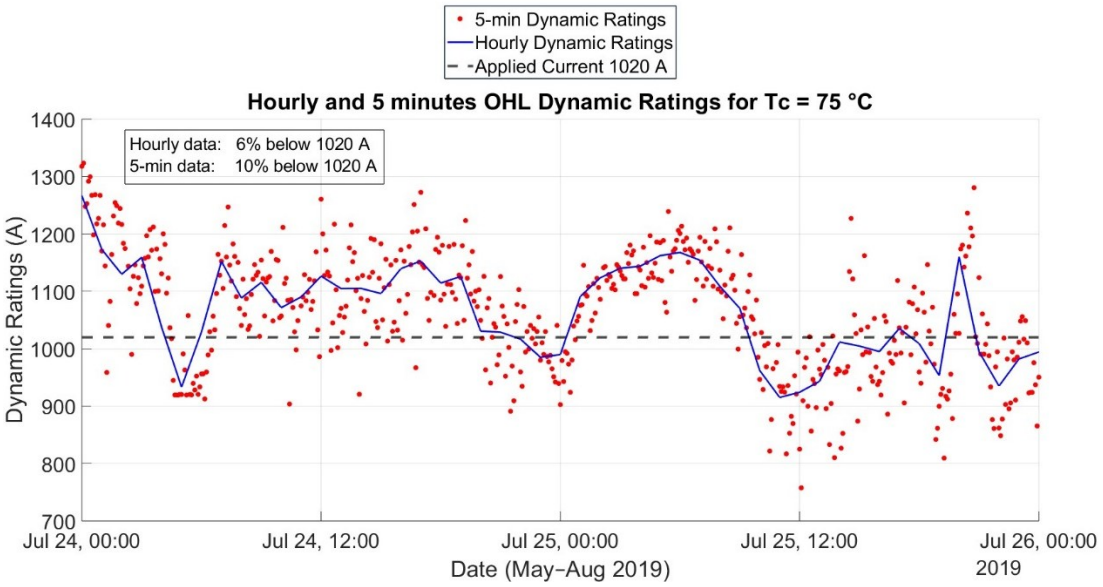

Figure 6.13: Example of 5 minutes and hourly DTR against a constant applied current.

To emulate the original 1977 Leatherhead experiment on the exceedance of OHL temperatures, we face a limitation: five-minute resolution weather data from that period are unavailable. The only dataset available for 1977 is hourly data from Heathrow (MET-Office)[79]. However, we have five-minute data from St. John's Wood in 2019 available, which, while not from the same year, is geographically close to the original Leatherhead site and suitable for a proof of concept. The approach is therefore to first compute exceedance statistics directly from the St. John's Wood five-minute data.

Next, this dataset is averaged to an hourly resolution and repeated in the exceedance analysis. The hourly values are then processed by binning (12×5) and applying linear interpolation back to five-minute resolution. By comparing these interpolated exceedance results with the original five-minute exceedance data, we can test whether interpolation from hourly records is a valid method. If the agreement is close, this approach can then be applied to the 1977 Heathrow hourly dataset to emulate the original experiment. Figure 6.14 shows the locations of the three sites, and Table 6.9 summarises the weather data overview of the sites.

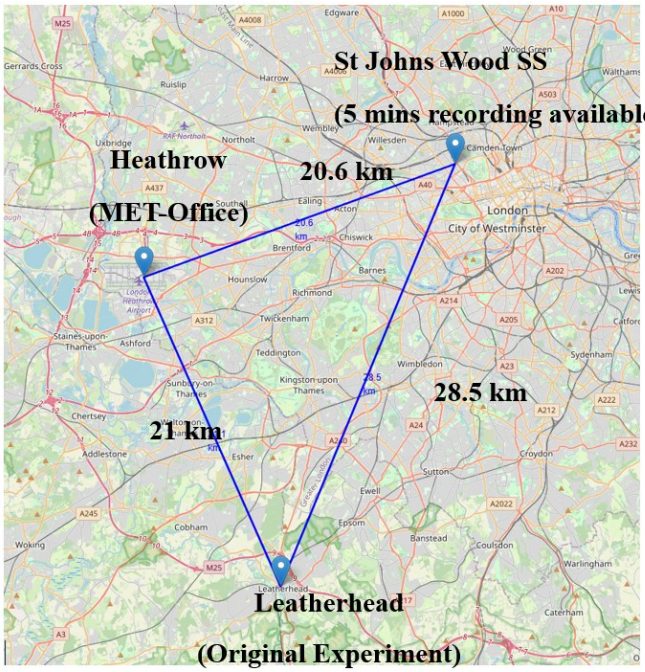

Figure 6.14: Location of available weather data for the exceedance analysis.

Table 6.9: Weather data overview (nearby original experiment location) [79], [83]

Location	Available	Year	Resolution
St Johns Wood	Yes	2019	5 mins
Heathrow	Yes	1956-2023	1 Hour
Leatherhead	No	1977	6 minutes

In our analysis, the temperature of the conductor is recorded for thermal responses every 5 minutes and every hour, where OHL is exposed to the 5-minute and hourly weather data, using IEEE standard 738 [9]. The probabilistic rating for a given exceedance is determined by counting the number of excursions occurring when the applied current $I_{applied}$ produces the temperature of the conductor above θ_{design} for the experiment for a given time (every 5 minutes or an hour, depending on the chosen resolution).

Then, the correlation term C_T is used to determine the exceedance level, where:

$$C_T = (\frac{I_{applied}}{I_{design}})^2 \tag{240}$$

A C_T curve in the context of exceedance ratings is a statistical tool that links conductor temperature exceedance with time of occurrence. In the original methodology, conductor temperatures are monitored, and the proportion of time a given design temperature is exceeded and counted. By plotting the ratio of applied to design current against the percentage of total time that temperature is exceeded, a C_T curve is obtained.

This curve provides a direct way to see, for any chosen design temperature, how often it will be exceeded under real weather conditions. It is the foundation of the STR method, since it allows static thermal ratings to be set not as an absolute maximum, but on a statistical basis (e.g. allowing exceedance only for 12% of the year). The knowledge of the relationship C_T (as a function of a known exceedance) therefore enables one to deduce a probabilistic rating, I_{prob} for the required exceedance by using:

$$I_{prob} = \sqrt{C_T}.I_{design} \tag{241}$$

In the statistical approach by Gibbon and Price [62], the correlation term in (240) was derived by varying the design temperature over a range of 45 °C to 90 °C while maintaining a fixed applied current under ambient exposure. This approach is experimentally pragmatic, since it requires energising only one test conductor and interpreting each temperature band as representing an equivalent "design condition." It avoids the cost of changing current loadings with multiple conductors while maintaining identical weather conditions.

However, this introduces a conceptual asymmetry in the physical interpretation of C_T. The equation implies that C_T represents the ratio of applied Joule heating to the design-condition heat loss, yet in the experiment, the Joule heating ($I^2_{applied}R$) was essentially held constant, while the denominator in (240), which is the $I^2_{design}R$ is varied from 45 °C to 90 °C. Strictly speaking, what is required is the reverse: C_T should be determined by varying the applied current (and thus the Joule losses) while holding the design temperature constant, to represent how additional heating affects exceedances of conductor temperature at a fixed conductor temperature limit under ambient conditions.

The adopted method, therefore, infers the same relationship by inversion, assuming that varying design temperature with constant heat input is thermally equivalent to varying heat input at constant design temperature. This assumption is reasonable as a first-order approximation, but it is not strictly valid because conductor resistance, emissivity, and convective coefficients are nonlinear functions of temperature. Consequently, the resulting C_T curve is an empirical correlation rather than a true representation of the physical dependence between current and temperature rise.

In summary, the experimental design used by Gibbon and Price [62] was cost-efficient and practically justified, but conceptually, the causality of the heat-balance relationship is reversed. The intended quantity is the ratio of heating inputs at constant design temperature, not the ratio of design temperatures at constant heating input. It should be noted that expressing the applied current as a function of exceedance probability in (241), at a fixed design temperature (for example, 50 °C), is not strictly

equivalent to maintaining the conductor at 50 °C and directly varying the applied current. The two approaches can yield similar trends but are not physically identical. The former provides an approximation to the latter by inferring the heating effect indirectly from temperature-dependent cooling behaviour, rather than by explicit variation of Joule input under fixed design conditions. In practical terms, this inversion is much easier to implement experimentally, as was done in the original experiment, requiring only one energised conductor exposed to natural ambient conditions, but it sacrifices some accuracy in how the heat balance responds to changes in applied current.

In the presented work in this section, our initial C_T curve analysis is intended primarily to demonstrate that the original Gibbon and Price [62]correlation can be re-emulated using available weather and conductor parameters. However, the assessment of exceedance risk for OHL operation is carried out using a single applied constant current corresponding to the STR in accordance with TGN 26 [11], with a fixed conductor temperature limit as used by NGET in their circuits, especially under the pre-fault conditions, in which the lines are expected to operate indefinitely. This ensures that exceedance statistics are based on the operational design current rather than on the derived correlation between C_T and design temperature.

Table 6.10: Summary of TGN26 guidelines for OHLs' exceedances.

Operating condition	**Requirement (relative to design current)**	**Exceedance level**	**Notes**
Post-fault (1 PU applied current)	$I_{applied}$ must not exceed design current by more than the allowed margin	≤ 12%	Based on TGN26 standard for STR
Pre-fault (normal operation at 0.85 PU applied current)	$0.85*I_{applied} > I_{design}$	≤ 0.1%	Ensures normal loading remains secure
Temperature rise	Conductor temperature ≤ (design temperature + 5 °C), when $0.85*I_{applied} > I_{design}$	≤ 0.01%	Sag becomes critical beyond this point

According to TGN26 [11] the exceedance level for $I_{applied}$ during post-fault (at 1 PU loading current) must be within 12% where $I_{applied} > I_{design}$. At the pre-fault level of 84% (or 85%) of $I_{applied}$, this should correspond to 0.1% of exceedance, where, $0.85 * I_{applied} > I_{design}$. Correspondingly, the temperature rise of 5°C above design temperature should occur only below 0.01% of the time, as sag becomes critical. This is summarised in Table 6.10.

The main objectives of the exceedance ratings analysis are:

- To emulate the original methodology as proposed by Gibbon & Price, and to see how C_T curves has changed from past to present.
- To utilise linearly interpolated hourly ambient conditions into 12 by 5-minute datasets, enabling the use of open-source hourly Met Office data for generating high-resolution inputs that capture the thermal response of OHL.
- To quantify, by how much have the weather ambient conditions changed hitherto (from the 1980s to present) and their exceedance ratings, especially during the heatwaves in summer months.
- To propose a new ambient design condition based on C_T curves, to a desired exceedance rating.
- To quantify the risk under the present post-fault STR design ambient conditions, based on TGN26 guidelines.

By using the metrics of exceedance levels and C_T curves, the original 1977 experimental values to the present conditions can be compared. Before evaluating the exceedance levels at chosen circuits (Pentir-Trawsfynydd and Braintree), evaluation of the metrics must first be validated at the nearest site to the original experiment in Leatherhead, while using the correct resolution at 5 minutes from readily available measurements at St Johns Wood in 2019. Only then, the evaluation of exceedance levels at the chosen NG circuits can be carried out.

6.2.5.2 Correlation Terms Curves and Exceedances (St Johns Wood vs Heathrow vs Leatherhead)

The aim is first to compare the original C_T curves, but under the conditions of current (2019) ambient conditions at St. Johns Wood, where 5-minute resolution of recorded ambient conditions is available.

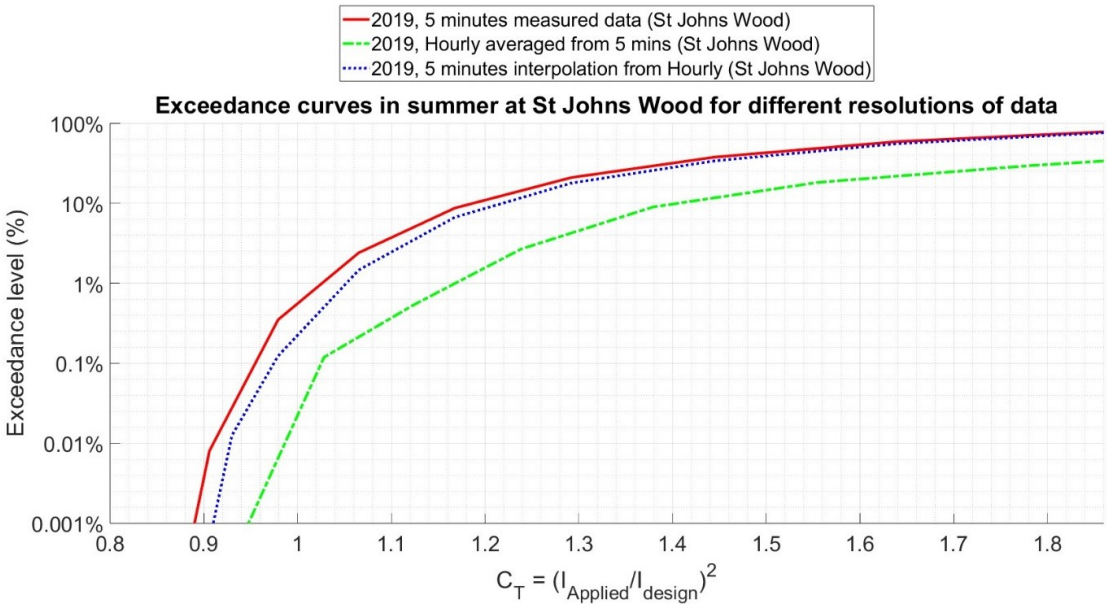

Figure 6.15: 2019 C_T curve at St. Johns Wood

This is shown in Figure 6.15, where the C_T curves are shown for 3 cases. The red solid line is the C_T curve generated using the 5 minutes recorded ambient conditions, while the green dash-dotted line is the curve from averaging the 5-minute recorded values into hourly values, and the blue dotted line is the 5-minute interpolated values from the hourly values (green dashed-dotted line).

It can be seen that the hourly curve produced the lowest exceedance level given a C_T value. This is expected as the hourly values could not capture the "hidden" exceedances happening in the sub-hourly region. The blue-dotted 5-minute interpolated curve approximates the 5-minute recorded curve. This implies that, should only hourly ambient weather data be available (usually from MET-Office), using the linearly interpolated method, by interpolating the hourly ambient data into 12 by 5-minute intervals, a close approximation to the 5-minute sub-hourly conditions can be emulated.

This is essential to capture the OHL's thermal response, as it is the fastest during these sub-hourly conditions. Therefore, we can use this method to reproduce the original experiment in 1977, where hourly ambient data is available at Heathrow, which is the closest weather station to Leatherhead. However, it is to be noted that the solar irradiance data is not available for 1977. For the sake of initial comparison between 1977 and 2022, the solar irradiance between these two years is assumed to be identical, where the focus is on global warming due to the ambient temperature rise. Nonetheless, the wind speed in 1977 is available from the MET Office.

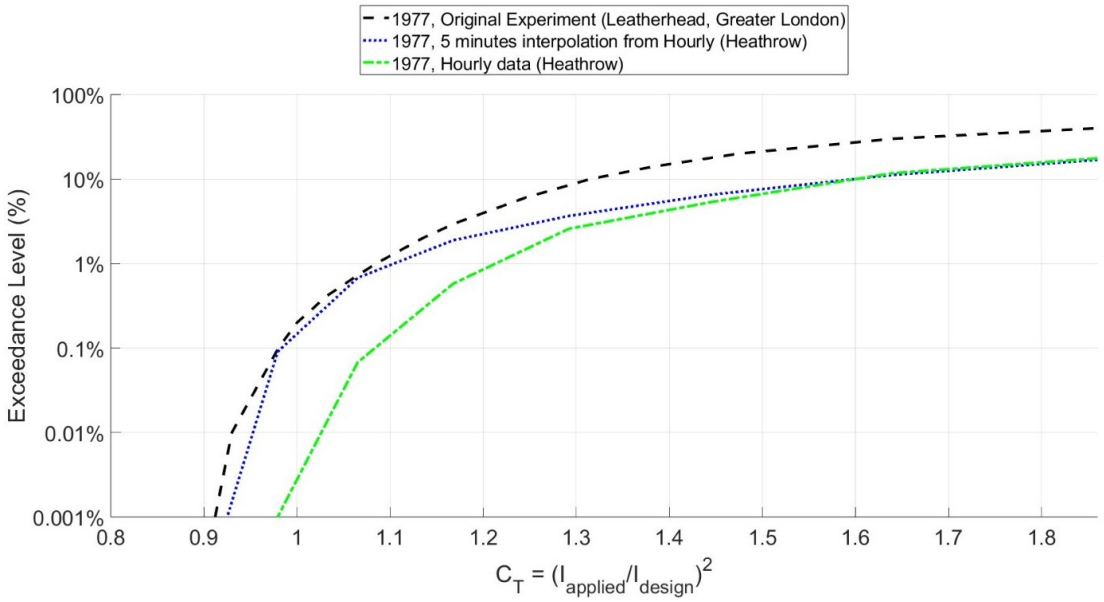

Figure 6.16: 1977 C_T curve at Heathrow vs original experiment (Leatherhead)

In Figure 6.16, the 5-minute interpolation from hourly data (blue dotted line) in Heathrow 1977, especially at values of $C_T \leq 1.1$, are approximate to the original experiment in 1977 (black dashed line). The 1977 Original C_T and exceedance values are directly extracted from their tabulated results in [62]. The hourly ambient conditions (green dashed-dotted line) did not produce any close approximation to the original values, and using hourly inputs underestimates the frequency of exceedance, relative to the 5-minute data. For values of $C_T \geq 1.1$, the approximation started to differ from the original experiment when comparing the 5-minute interpolation values to the original experiment.

It is generally windier at Heathrow than any other parts of London due to its "open terrain" nature, with average wind speed during the year at 4.3 m/s compared to 2.6 m/s at Kew Gardens (which is located in the middle of the city) [79]. Additionally, Heathrow is located further west of central London, where the westerly winds that are common in the area are more pronounced. Therefore, the exceedance level at higher C_T values which correspond to non-extreme cases (combination of moderate wind and temperature) are rarely exceeded at Heathrow. Nonetheless, exceedances at lower C_T values which typically correspond to exceedances of extreme events (heatwaves) are close to each other for Heathrow and Leatherhead. Therefore, in the absence of a 5-minute recording of ambient weather data, we can approximate the exceedance level at 5-minute resolution by linearly interpolating the hourly ambient recorded data.

To see how exceedance levels have changed from 1977 to the hottest summer in 2022, a new current-exceedance curve derived from C_T curve is produced in Figure 6.17. Given C_T and its percentage of exceedance, the exceedance current was rearranged from (240) to (241) with an example of conductor temperature limit of 75°C adopted for the design current. The curves are used as follows: the blue dotted curve represents the current or loading as a function of exceedance derived from 1977 ambient conditions, and the red curve represents the same relationship under 2022 ambient conditions. At a fixed current of 1020 A, the exceedance increased from approximately 2% in 1977 to approximately 6% in 2022.

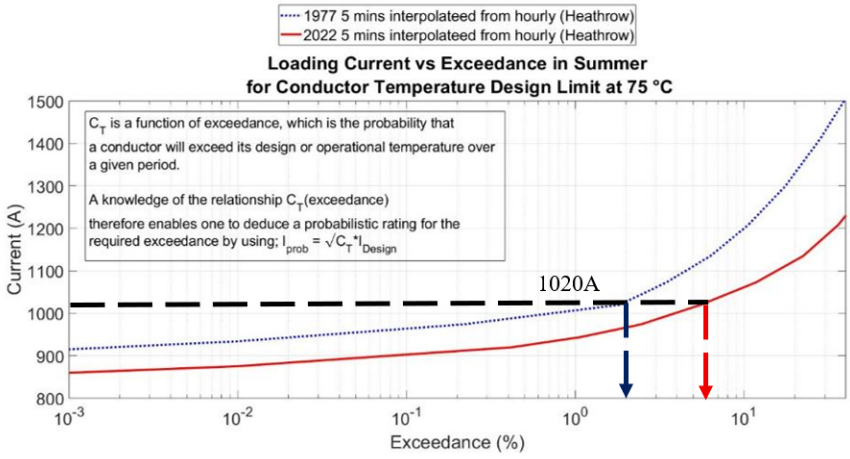

Figure 6.17: Probabilistic loading current for exceedance level at Heathrow (1977 vs 2019)

If the exceedance level is to be held constant when moving from 1977 to 2022 conditions, the allowable current must be reduced according to the 2022 curve, which is equivalent to adopting a higher ambient design temperature. For example, an STR based on ambient temperature of 20 °C yields about 1000 A at 1% exceedance in 1977. Increasing the design ambient temperature to 24 °C in 2022 reduces the allowable current to approximately 950 A while maintaining the same exceedance level at 1% for 2022.

In summary, this subsection confirms that by using the 12-by-5-minute interpolation of hourly data, a reasonable approximation of OHL thermal response can be captured to emulate the original experiment, when only hourly measurements from open-sourced data are available. Additionally, the C_T curves provided a quick estimation of how exceedances have changed from the 1980s to present conditions. Moreover, an insight into how to derate the OHL ratings based on their exceedances was also provided, as provided in Figure 6.17.

6.2.5.3 Use Cases: Pentir-Trawsfynydd and Braintree

In this section, the focus is placed on the exceedance level and the corresponding temperature rise observed in circuits Braintree (Zebra OHL at 50°C conductor temperature limit) and Pentir-Trawsfynydd (Sorbus OHL at 75°C conductor temperature limit. The evolution of these parameters over the years is examined rather than focusing on two particular years, with particular attention given to whether the limits specified in TGN26 are violated. The ambient data were extracted as far back as what is available at the corresponding circuits.

The Zebra and Sorbus OHL were assessed under loading at both 1.0 PU (post-fault) and 0.85 PU (pre-fault) STR current levels (20℃ AAT, 0.5 m/s WS,12 ° AA, and no SI). The 1 PU loading of a single circuit Zebra is 663 A and 943 A for Sorbus, respectively. Similarly, exceedances were identified at each 5-minute interval in which conductor temperature exceeded the conductor's design limit exposed to 5-minute ambient conditions at Pentir-Trawsfynydd and Braintree circuits. For every exceedance event, the corresponding temperature rise above the design limit was also recorded.

- Compliance was evaluated against the criteria specified in TGN-26:
- At 1.0 PU post-fault loading, exceedances must not exceed 12 %.
- At 0.85 PU pre-fault loading, exceedances must remain below 0.1 %.
- Temperature rises exceeding 55°C for Zebra and 80°C for Sorbus (5 °C above design limit) must occur in no more than 0.01 % of instances, as sag becomes critical at this level.
- These exceedance levels were analysed across multiple years (2008-2024 at Braintree and 2011-2024 at Pentir-Trawsfynydd) to assess their long-term evolution and determine potential trends relative to TGN26 compliance.

6.2.5.4 Circuit Braintree: Zebra OHL at 50°C conductor limit

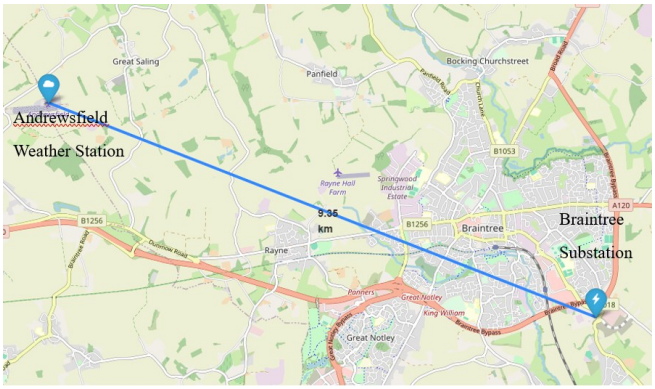

Figure 6.18: Braintree Substation and Andrewsfield Weather Station (9.35 km).

As only minimal data is recorded from the Braintree, Braintree substation (only in 2019 with 50% data availability), the MET-Office weather station in Andrewsfield is used as the representative historical ambient conditions at Braintree substation. The Braintree substation is located 9.35 km away from the Andrewsfield weather station, as shown in Figure 6.18. The data availability for the needed (joint) ambient conditions (AAT, WS, and SI) spans from 2008 to 2024, in hourly resolution, which is then linearly interpolated to 12 by 5-minute resolution, which is shown in Figure 6.19 below for summer 2022.

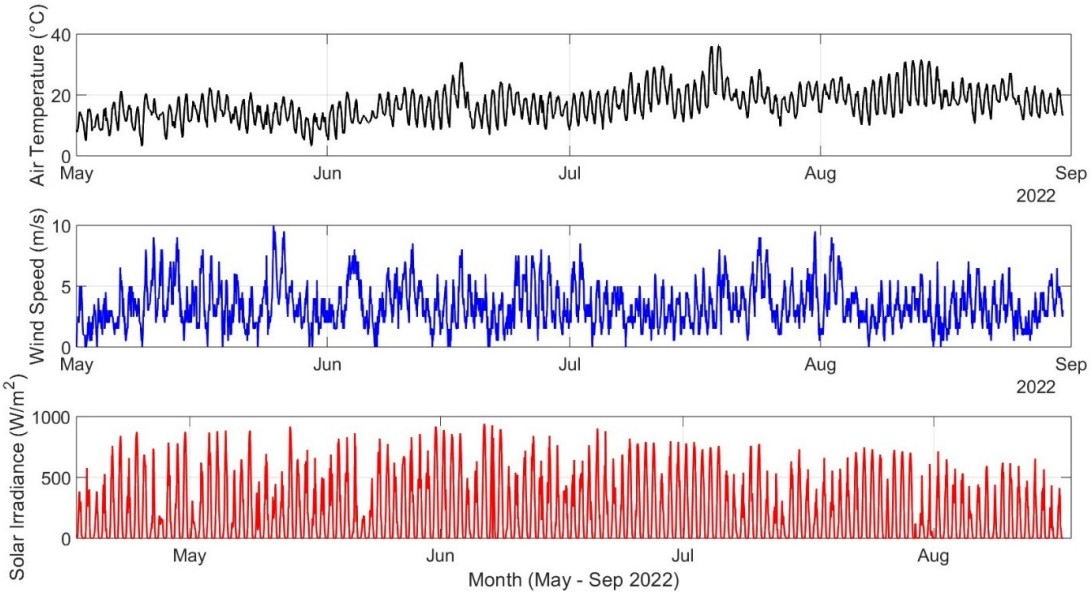

Figure 6.19: Representative ambient weather conditions at Braintree.

Using an example from the ambient conditions in Figure 6.19, the conductor temperature is evaluated for summer 2022 as shown in Figure 6.20 under 1 PU post-fault (blue line) and 0.85 PU pre-fault (red-dashed line) loading conditions, with a zoomed view in Figure 6.21. Occurrences of exceedances above the conductor design temperature, i.e., Zebra at 50°C, are counted, and the temperature rise when exceedances occur is recorded. This is done for the years 2008 to 2024 and will be used in the next sections to generate yearly C_t curves and temperature rise against exceedance curves.

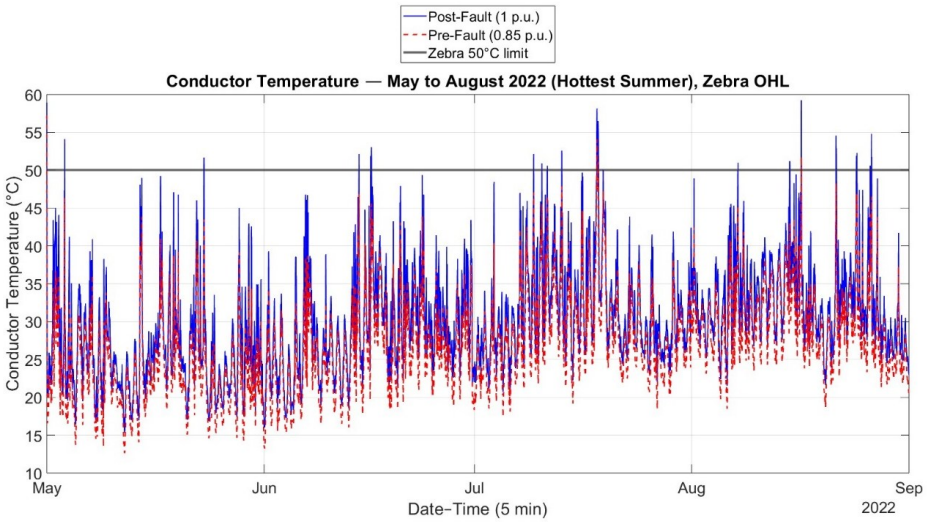

Figure 6.20: Braintree Zebra OHL Exceedance Ratings at 1 PU and 0.85 PU STR Summer Current in 2022.

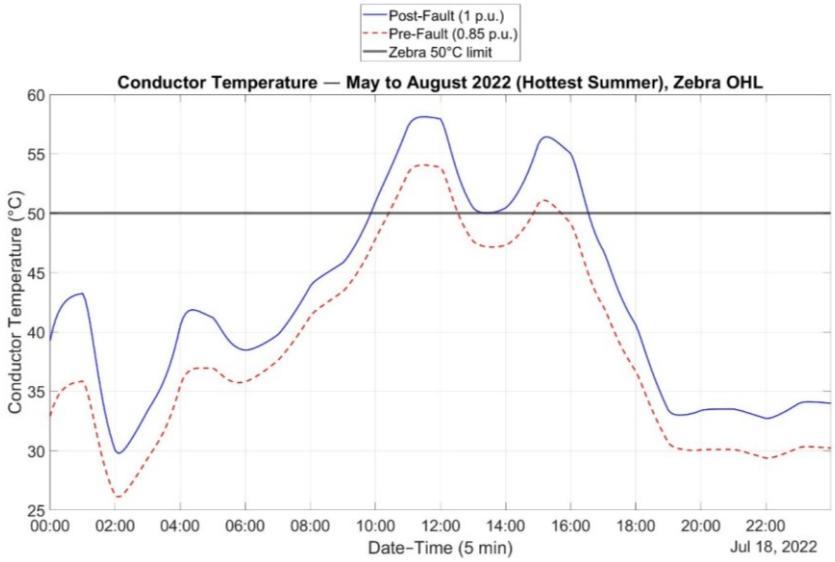

Figure 6.21: Zoomed in Figure 6.20 during a heatwave.

6.2.5.5 Circuit Pentir-Trawsfynydd: Sorbus OHL at 75°C conductor limit

Figure 6.22: Pentir-Trawsfynydd, Garth OHL-Cable Compound and Porthmadog Weather Station.

The map in Figure 6.22 is shown to illustrate the straight-line distance between the Porthmadog MET-Office weather station, which is used as the representative ambient conditions for the Garth OHL-Cable compound. The available weather station recording is in hourly resolution, which is then linearly interpolated into 12 by 5-minute resolution. The data availability for the required (joint) ambient conditions (AAT, WS, and SI) spans from 2011 to 2024. The Pentir-Trawsfynydd study location is the Garth Sealing End Compound near Minffordd (which is part of the Pentir-Trawsfynydd circuit), located at coordinates 52.92819° N, −4.09042° E. The calculated straight-line

distance between the two sites is approximately 4.73 km. The ambient weather conditions at the site are shown in Figure 6.23 below.

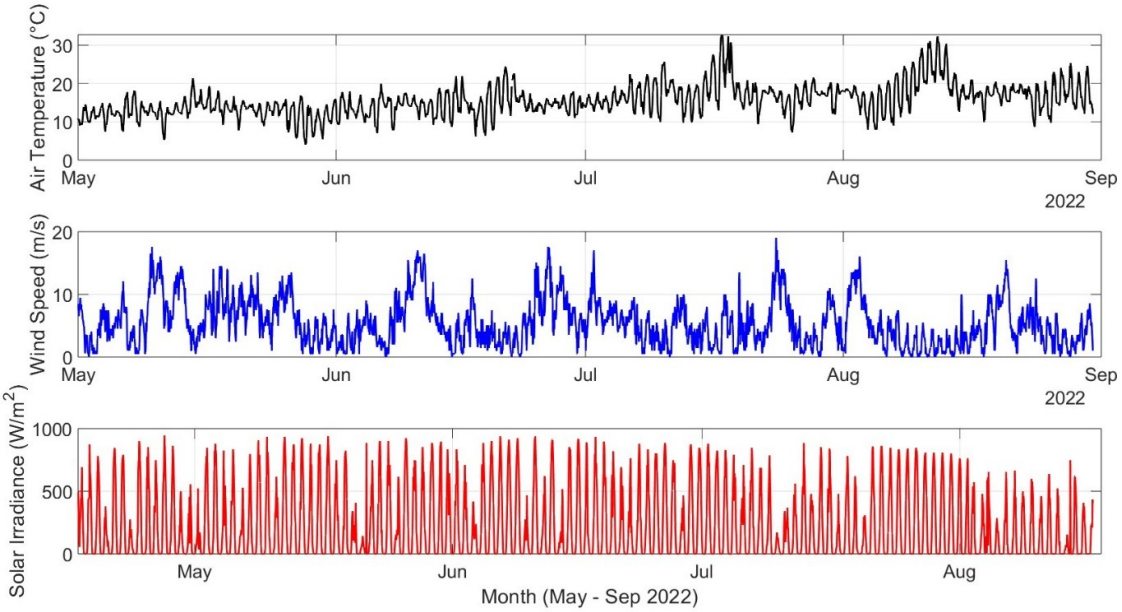

Figure 6.23: Representative ambient weather conditions at Pentir-Trawsfynydd in 2022.

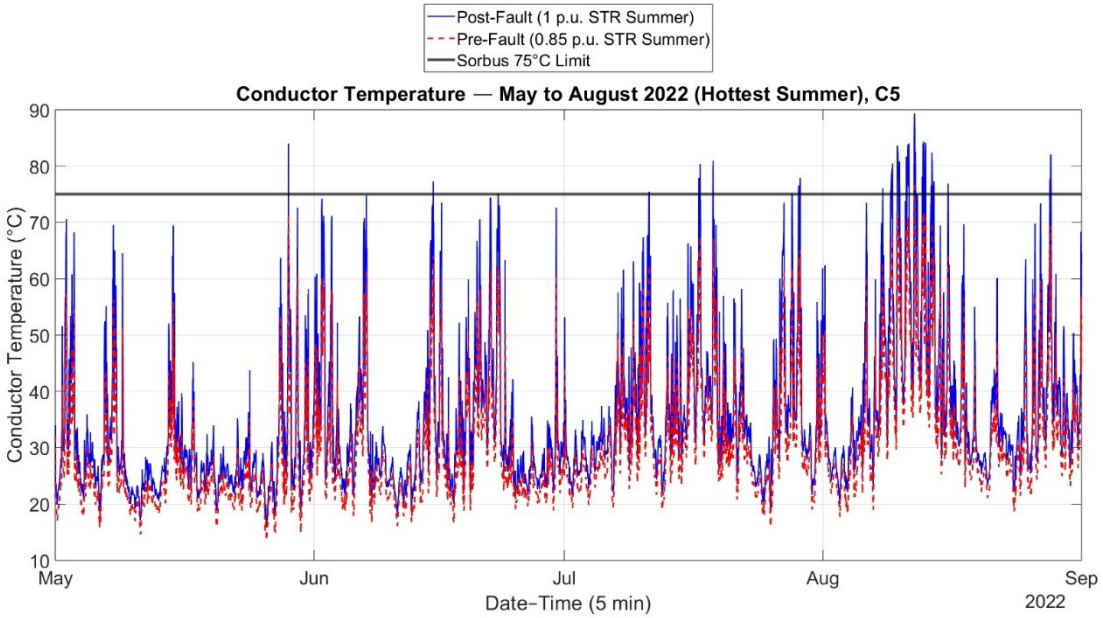

Figure 6.24: Pentir-Trawsfynydd, Sorbus OHL Exceedance Ratings at 1 PU and 0.85 PU STR Summer Current in 2022.

Using an example from the ambient conditions in Figure 6.23, the conductor temperature is evaluated for summer 2022 as shown in Figure 6.24 under 1 PU post-fault (blue line) and 0.85 PU pre-fault (red-dashed line) loading conditions. Occurrences of exceedances above conductor design temperature, i.e., Sorbus at 75°C in this case, are counted, and its temperature rise when exceedances occurred is recorded. Similarly, this is done for the years 2011 to 2024 and will be used in the next sections to generate yearly C_T curves and temperature rise against exceedance curves.

6.2.5.6 Correlation Term Curves over the years for Braintree OHLs

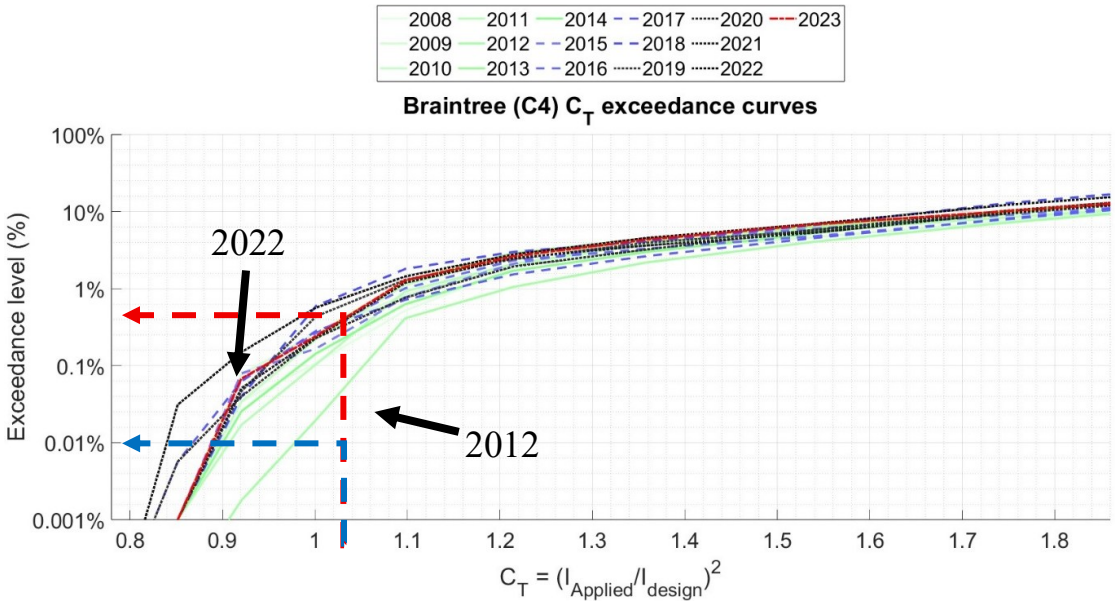

Figure 6.25: Braintree exceedances throughout the years.

Figure 6.25 shows the C_T curve variations from 2008 to 2023 at Braintree. It can be seen that the exceedance level in 2022 is the highest, especially when $C_T < 1$, where this region indicates headroom relative to design, or when the applied current is lower, so exceedances should be rarer. With the highest exceedances occurring in 2022 in this region, this would only mean that the headroom is less now due to occurrences of heatwave events, and even with a lower current applied, the highest exceedance was observed in this year. This is in agreement with the heatwave events that occurred recently in 2022, where 2022 recorded the highest temperature events in summer.

It can also be seen that the earlier years (green lines to blue lines) produced lower exceedances collectively at the location, confirming that the global warming effects indeed reduce the headroom of the OHLs, resulting in increased exceedances throughout the years. For example, using C_T = 1 value in 2012 against 2022 would yield exceedances of 0.02% vs around 0.8% respectively, increasing the value of exceedances by 40 times, albeit by comparing the two highest and lowest exceedance years.

Heatwaves and hot years effectively weaken cooling (higher air temperature and often low wind with high solar irradiance), so the operating point is pushed to the left and exceedance increases even if the current is only moderate. To keep the exceedance level unchanged in a hot year, C_T must be pulled back to the right by reducing the design STR current for a given temperature limit or operating at a lower applied current. Assuming that the applied current cannot be reduced, reducing the design STR current would be the logical approach. This can be achieved by either increasing the assumed ambient temperature, e.g., from 20°C in Summer to 24°C, or by assuming a certain solar irradiance to take into account the heat gain effects.

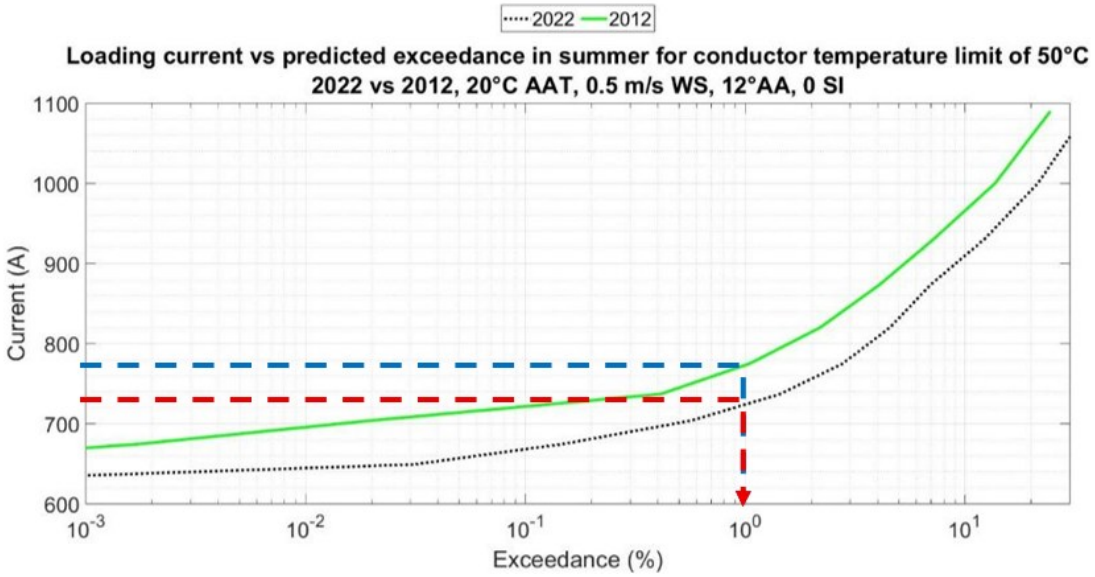

Figure 6.26: Loading current vs exceedance for highest and lowest exceedance years at Braintree 2022 and 2012.

To figure out how the loading in ampacity of the conductor varies with exceedances, Figure 6.26 shows the loading current derived from equation (241) at the

50°C conductor temperature limit for the two highest and lowest years of exceedances. For the same exceedance level of 1% in 2022, the 2012 current must now be reduced from around 780A to 720A. Alternatively, if a target exceedance is known for pre- and post-fault conditions, the selected line ampacity can be chosen based on the figure for the intended year. For the sake of conservative assumptions, it is better to take the hottest year (in this case, 2022), in order to select the loading current, or use the envelope of C_T curve for every exceedance value to derive the loading current.

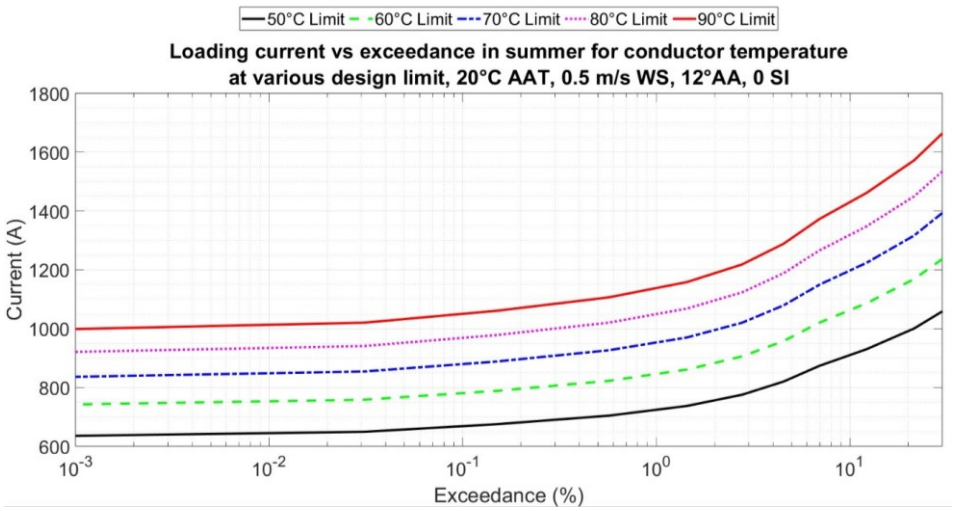

Figure 6.27: Braintree, different operating design limits and their corresponding exceedances for the year 2022.

Figure 6.27 shows the different operating currents at various operating STR temperature limits, derived from the C_T curve of Figure 6.25 for the year 2022 and equation (241). This figure shows that, should the OHL be permitted to operate at a higher design temperature limit, its exceedances can be greatly reduced, especially for the first few per cent of exceedances. However, this is strictly under the notion that the OHL would not violate any height clearance or grease temperature limit regulations. For grease-filled ACSR such as Zebra, National Grid guidance caps the continuous temperature at 50°C to protect the grease from softening and draining. Short-term exceedances are permissible, typically allowing temperatures up to 75°C for a maximum of 15 minutes under contingency conditions. Sustained operation above the grease drop

point can lead to grease migration, loss of corrosion protection, and accelerated conductor ageing.

6.2.5.7 Correlation Term Curves over the years for Pentir-Trawsfynydd OHLs

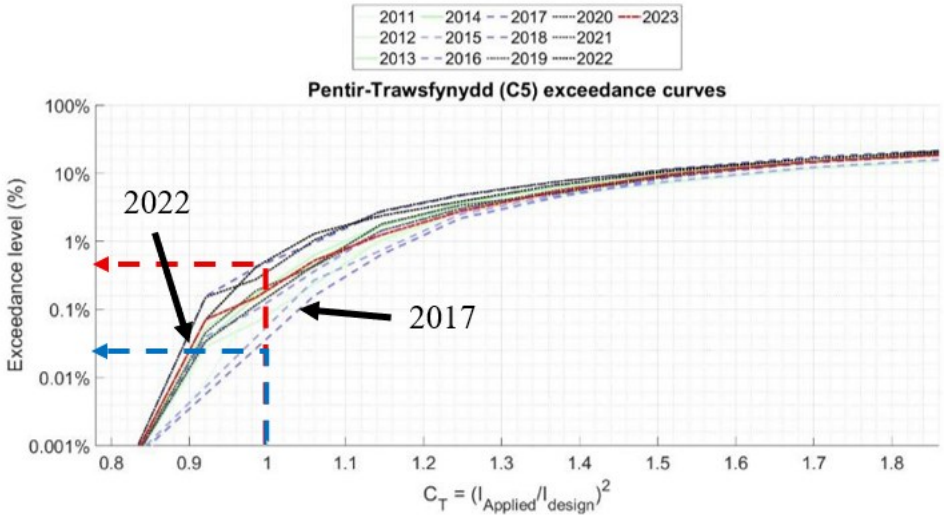

Figure 6.28: Pentir-Trawsfynydd exceedances throughout the years.

Figure 6.28 shows the C_T curve for Pentir-Trawsfynydd OHL with AAAC Sorbus. The C_T curve is shifted slightly to the right. The exceedance value from 2022 at $C_T = 1$, is around 0.06% compared to the Braintree in Figure 6.25 at 0.8%. The lowest exceedance occurred in 2017 at $C_T = 1$, with 0.02% exceedances. This is roughly 30 times increment of exceedance from the lowest exceedance in 2017 to the highest exceedance in 2022 at Pentir-Trawsfynydd. The aggregate trend at Pentir-Trawsfynydd for exceedances throughout the year is not heavily pronounced compared to Braintree, where there is a clear change in exceedances moving from earlier years to the present. This could be due to the coastal location of Pentir-Trawsfynydd, as shown in Figure 6.22. The influence of global warming on local temperatures is generally moderated in coastal areas, as the nearby ocean acts as a thermal buffer, reducing temperature extremes compared to inland cities.

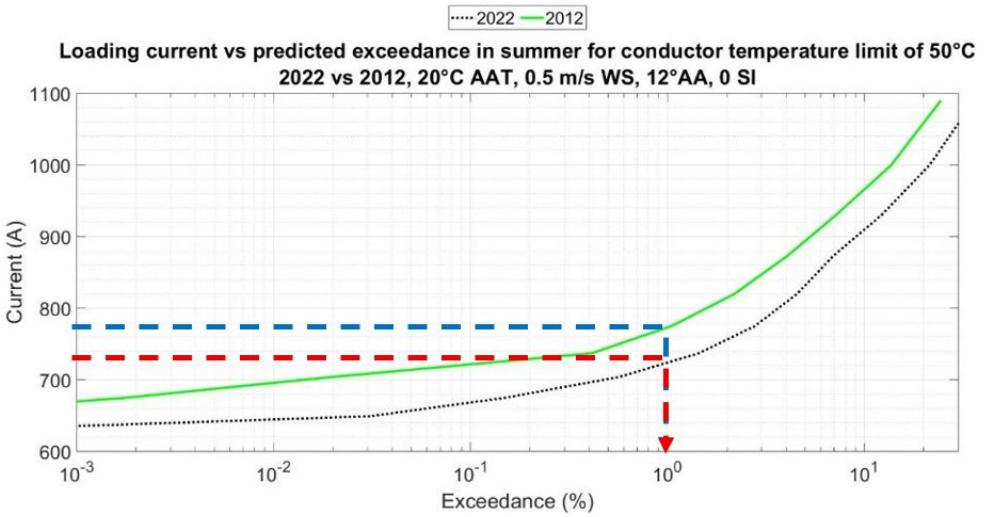

Figure 6.29: Loading current vs exceedance for highest and lowest exceedance years at Pentir-Trawsfynydd 2022 and 2017.

Figure 6.29 shows the AAAC Sorbus at 75°C conductor temperature limit for the two highest and lowest years of exceedances. Assuming an exceedance of 1%, the current must be reduced by roughly 7%.

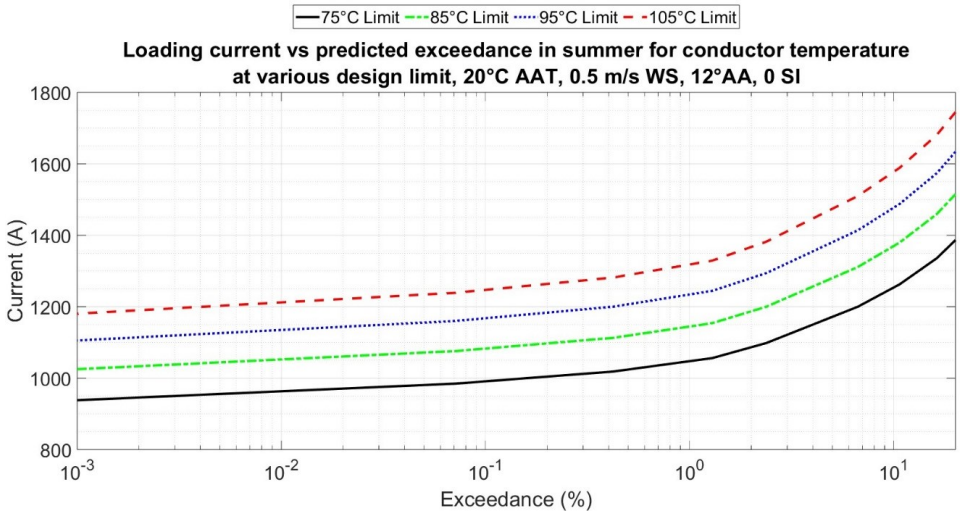

Figure 6.30: Pentir-Trawsfynydd, different operating design limits and their corresponding exceedances for the year 2022.

Similar to Figure 6.27, the Figure above shows how the increment of operating at a higher conductor temperature limit can significantly decrease the risk of the exceedance of that operating temperature. The exceedance (1%) of the operating limit

of roughly 1000 A at 75°C conductor temperature is equivalent to 0.001% exceedance of the 85°C operating limit, which is 1000 times smaller. However, it is to be noted that other constraints, such as clearance limits, are not violated.

6.2.5.8 Risks of Operating Using the Present OHL STR Design Conditions.

Previous analyses focused on deriving conservative or suitable operating currents from the hottest years or years with the highest exceedance levels by building C_T curves and determining the expected exceedance for each year. This is suitable for planning cases to determine the limit based on exceedances. This approach primarily assessed the current levels required to maintain acceptable risk under those extreme conditions.

In this section, the emphasis shifts to quantifying the risk of operating under the present STR operation in Summer for pre- and post-fault scenarios. Specifically, we evaluate operation at 663 A for ACSR Zebra (50 °C conductor temperature limit) and 943 A for AAAC Sorbus (75 °C conductor temperature limit) under the design ambient condition of 20 °C, with 0.5 m/s wind speed, 12° wind attack angle, and zero solar irradiance. In line with the guidance provided in TGN 26 in Table 6.10, this assessment not only considers the frequency of exceedances but also the magnitude of temperature rise above the defined limits. This additional quantification of thermal risk allows us to demonstrate whether operation at current STR loading levels remains within the acceptable risk envelope defined by TGN 26.

6.2.5.8.1 Pre-Fault and Post-Fault Risks at Braintree

Similar to the previous analysis, the dynamic transient thermal response of the Zebra OHL in Figure 6.31 at the Braintree circuit was evaluated using 5-minute real-time ambient air data under pre-fault loading at 85% of nominal rating (typical operational limit). Exceedance levels were computed for each year and grouped into four colour-coded blocks for clarity.

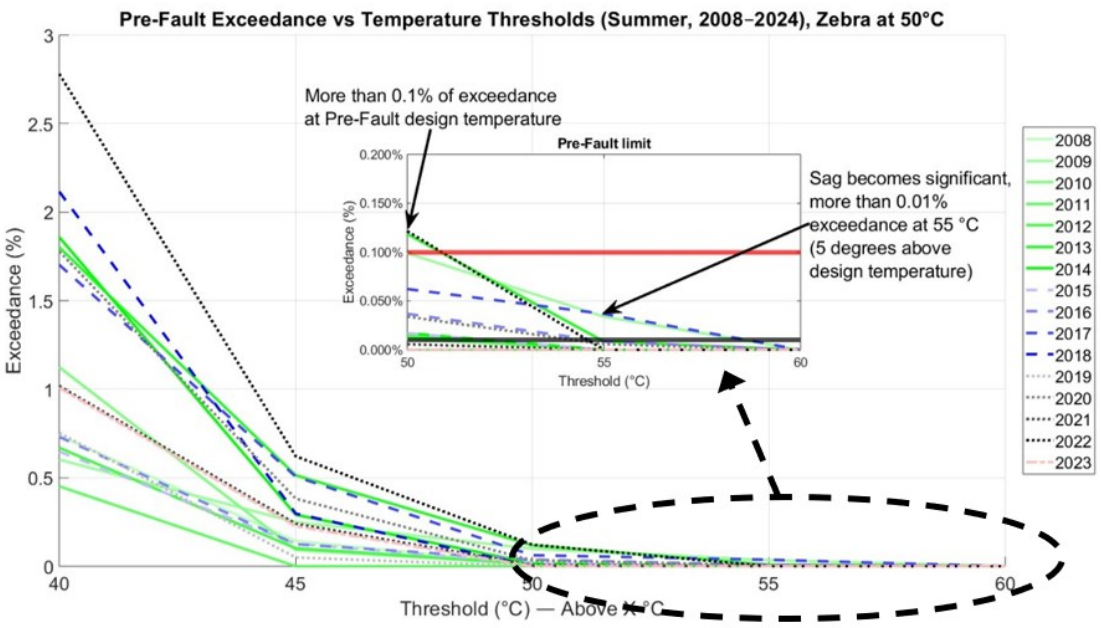

Figure 6.31: Pre-fault exceedance level under summer STR design conditions for Braintree, 85% of 663 A(20°C AAT, 12° AA, 0.5 m/s WS, and 0 W/m^2 SI), Zebra at 50 °C limit, from 2008 to 2023.

Results indicate a general increase in exceedances of temperature rise above conductor temperature limit over the years, with the highest values observed in 2022, corresponding to extreme heatwave conditions found in 2022. Two exceedance thresholds were applied as per TGN26. The pre-fault design temperature limit (red solid line), which must not be exceeded more than 0.1% of the time in the inset and the critical sagging threshold (black solid line) corresponding to a 5 °C rise above the design temperature, which must remain below 0.01% occurrence. Analysis shows that in 2022 and 2013, the 50 °C design temperature was exceeded more than 0.1% of the time, while in 2018 and 2009, the 5 °C margin was also exceeded beyond the 0.01% criterion. Mitigation options were evaluated with a 10% reduction in loading at 1 PU STR or specifying a higher ambient design temperature (e.g., increasing from 20°C to 27°C design AAT for STR or from 663 A to 597 A at 1 PU STR) will restore exceedance levels within the acceptable limits defined in TGN 26 [11].

When considering post-fault loading at 100% (1 PU) for the Zebra conductor with a 50 °C temperature limit in Figure *6.32*, the exceedance remains well within

acceptable limits. According to TGN26, post-fault operation permits up to 12% exceedance, whereas the calculated exceedance is no more than 1% under the evaluated conditions. This confirms that post-fault loading at 1 PU is acceptable and compliant with the 12% exceedance criterion defined in TGN 26 [11] specified in Table 6.10.

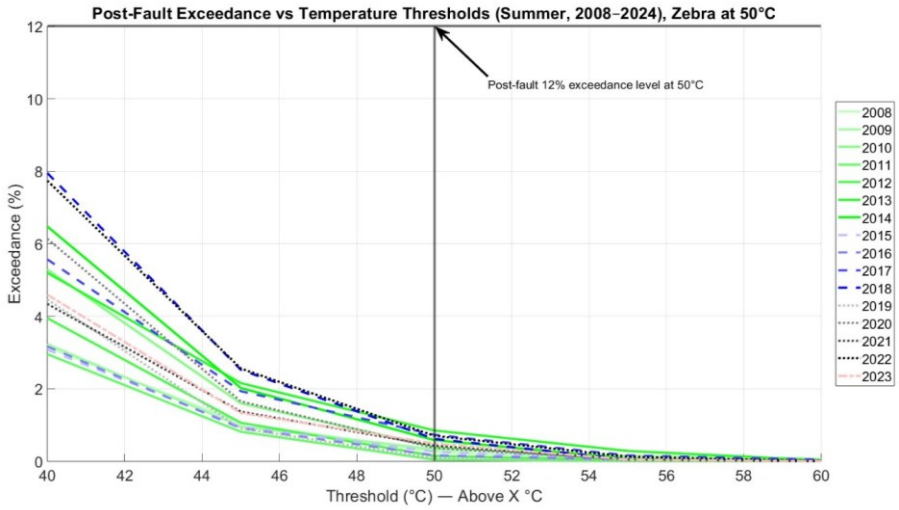

Figure 6.32: Post-fault exceedance level under summer STR design conditions for Braintree, 100% of 663A (20℃ AAT, 0.5 m/s WS, and 0 W/m^2 SI), Zebra at 50 ℃ limit, from 2008 to 2023.

6.2.5.8.2 Pre-Fault and Post-Fault Risks at Pentir-Trawsfynydd

According to Figure 6.33 at the pre-fault loading of 0.85 PU, the 75 °C conductor temperature limit is exceeded in 2022, with a recorded exceedance of 0.14%. However, the additional 5°C temperature rise criterion (80°C threshold) remains within the 0.01% limit, indicating that critical sagging conditions were not violated. Mitigation analysis of 5% reduction in post-fault loading at 1 PU from 943 A to approximately 887 A, or 801 A to 754 A at 0.85 PU, respectively, or an equivalent adjustment of the summer design ambient temperature from 20 °C to 23 °C would ensure that no violations occur.

It is also noted that the higher conductor temperature limit of 75 °C provides more thermal headroom compared to the 50 °C limit of the ACSR Zebra, which is more susceptible to violations during heatwave conditions due to its closer proximity to higher ambient temperatures.

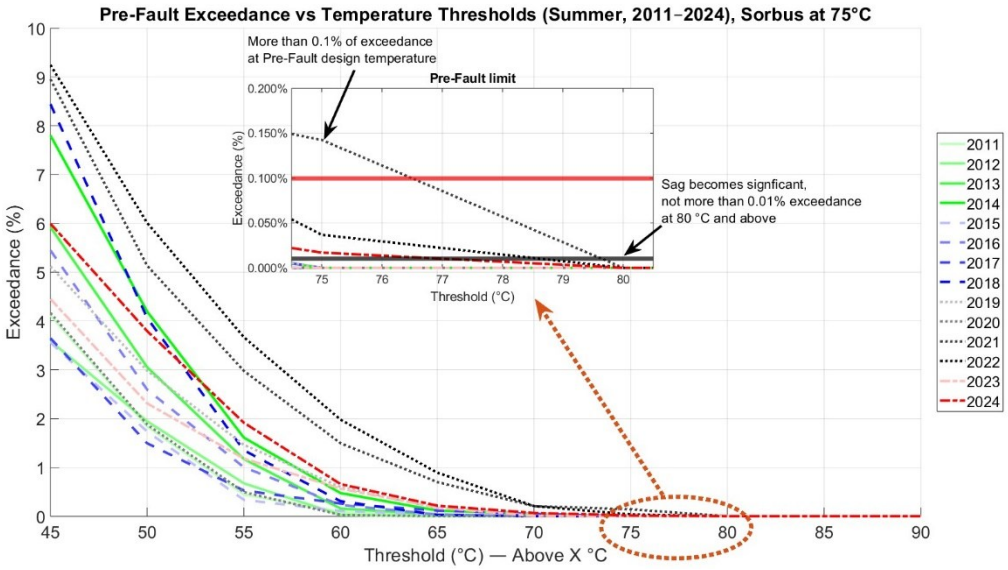

Figure 6.33: Pre-fault exceedance level under summer STR design conditions for Pentir-Trawsfynydd, 85% of 943A (20℃ AAT, 0.5 m/s WS, and 0 W/m^2 SI), Sorbus at 75 ℃ limit, from 2011 to 2024.

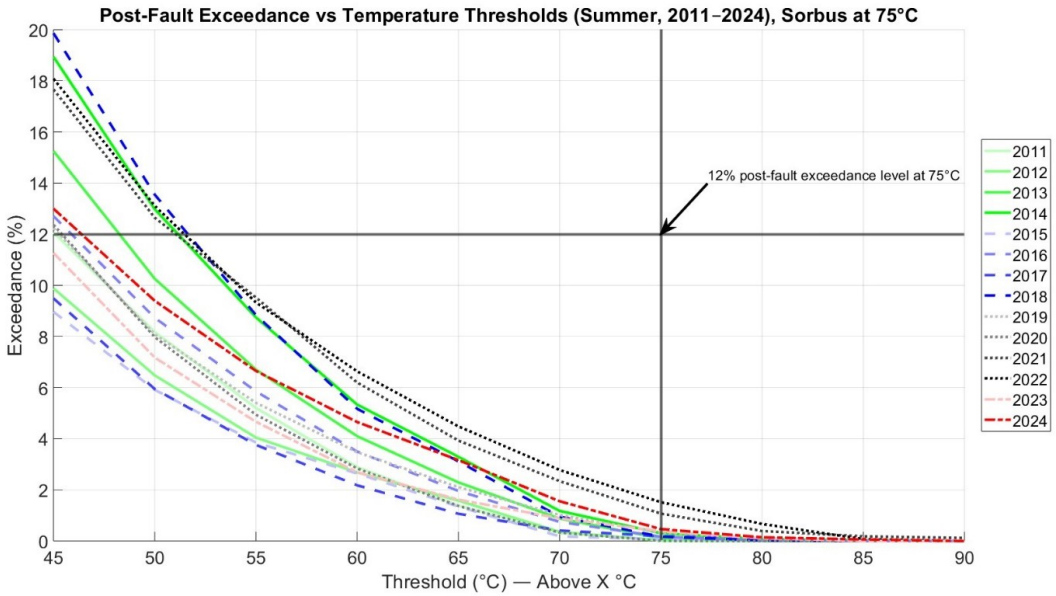

Figure 6.34: Post-fault exceedance level under summer STR design conditions 100% of 943A for Pentir-Trawsfynydd (20℃ AAT, 0.5 m/s WS, and 0 W/m^2 SI), Sorbus at 75 ℃ limit, from 2011 to 2024.

For post-fault loading at 100% (1 PU) in Figure 6.34, the AAAC Sorbus conductor with a 75°C temperature limit remains within the allowable exceedance defined in TGN 26. The calculated exceedance remains well below the 12% threshold, confirming compliance with the post-fault loading criterion.

It is important to note that the exceedance rating analysis presented here applies solely to the OHL. While OHLs may be operated beyond their nominal rating for short durations without significant risk, other components within the same circuit, such as underground cables or transformers, are subject to absolute thermal limits that cannot be exceeded under any circumstances. Therefore, any decision to permit OHL exceedance must consider the most restrictive element in the circuit to ensure overall system integrity and compliance with design limits.

The exceedance ratings provide valuable insight into the frequency and severity of thermal limit breaches under both historical and projected ambient conditions. However, as OHLs are increasingly operated in conjunction with other network components such as cables and transformers within integrated circuits, it becomes essential to extend this exceedance-based assessment across all asset types. Understanding how OHL exceedances translate to thermal stress, loading constraints, and ageing impacts on associated components will allow a more realistic evaluation of circuit-level performance and security. Moving forward, the exceedance rating evaluation should therefore be expanded to consider composite circuit behaviour, ensuring that coordinated design and operation strategies are developed for OHL–transformer-cable systems under unified ambient design conditions and pre-fault continuous and post-fault operation scenarios.

6.3 Conclusions

Among the components analysed in this thesis, OHLs are the most sensitive to variations in ambient weather conditions. Their relatively small TTC and direct exposure to SI make them highly responsive to rapid temperature fluctuations. Unlike transformers and cables, OHLs cannot benefit from CTR because their limited thermal inertia prevents sufficient cooling during low-load periods. As a result, defining a

continuous rating for OHLs is particularly challenging: it can either be overly conservative under mild conditions or risky under heatwave conditions.

The concept of the exceedance level-based rating is used in practice to define the STR of OHLs. This rating acknowledges a quantified and acceptable level of risk that the conductor temperature may exceed its design limit for a specified duration. Exceedance levels are defined as probabilistic thresholds (e.g., ≤ 12 % for post-fault, ≤ 0.1 % for pre-fault, and ≤ 0.01 % for 5 °C over-temperature), consistent with Technical Guidance Note (TGN) 26 [11]. The analysis using sub-hourly (5-minute) interpolated data from 1981 and 2022 showed that exceedance events are becoming more frequent and of longer duration in recent years, primarily due to higher air temperatures and reduced wind cooling. This finding highlights the growing importance of exceedance-based approaches to complement traditional static and dynamic ratings.

If the calculated exceedance levels at present conditions violate TGN 26 limits under expected operating conditions, a new STR ambient design criterion must be proposed to ensure compliance and safety. This adaptive approach enables the OHL rating methodology to reflect both operational reliability and evolving climate trends.

The exceedance level-based ratings cannot be calculated for cables and transformers. Because the cable's conductor temperature limit is a hard limit, exceeding it will result in irreversible damage to the insulation of the cable. While for transformers, their emergency temperature limit set by WTI cannot be violated, as it will cause the transformer to trip. And the violation of the continuous temperature limit will accelerate the transformer's winding insulation, which is a subject of ageing-based rating instead of exceedance level-based rating, that is, risk-based.

The S/MTOR confirm that OHLs can be temporarily overloaded beyond their continuous post-fault CCC, provided that 20 % of the pre-fault CCC is maintained for post-fault conditions. However, the smaller TTC of OHLs limits the duration and magnitude of such overloads compared to other components, such as transformers and cables. Following any overload event, the OHL must return to its post-fault rating promptly to prevent exceeding the temperature limit.

In this study, the S/MTOR calculations were performed under a defined set of ambient conditions, excluding solar irradiance and using conservative assumptions for wind speed. While this approach provides a safe estimate, it may underestimate the realistic performance of the OHL since the cooling effect of wind often offsets the heating from solar gain. Future work should therefore incorporate dynamic and measured wind speed and solar irradiance data to produce more representative and climate-responsive ratings.

Chapter 7

Thermal Ratings and Loading Limits of Joint Circuits

In previous chapters, the evaluation of the individual components that might be present in a joint circuit was present. A joint circuit is a circuit composed of two or more types of components. Due to the different thermal behaviour of components, the variation of thermal rating with changes in ambient, operating, and rating conditions will exhibit different characteristics. Because each component exhibits different thermal characteristics and responds differently to ambient and operating conditions, their combined behaviour determines the overall thermal performance of the circuit. The limiting component, that which reaches its thermal limit first, dictates the joint-circuit thermal rating.

Understanding how thermal interactions between components influence circuit-level performance is therefore essential for ensuring safe, reliable, and efficient operation, particularly under varying environmental and loading conditions. This chapter focuses on developing and applying a unified methodology to evaluate the thermal ratings and loading limits of joint circuits, addressing the challenges identified in Section 2.2.

Two representative circuit configurations, typical of transmission network arrangements, are selected and analysed to illustrate these interactions and assess the resulting joint-circuit capacities. Due to missing or unavailable information in this study, some type of components in the joint circuit has to be assumed. The actual types of components need to be selected from publicly available sources. In practice, the selection of components for the joint circuit should be based on location, geological conditions, policy, and economic conditions; e.g., OHL should not pass through densely populated areas, and buried cables are better suited for such areas if needed. However,

this topic is outside the scope of this thesis, which focuses on the thermal rating of components and circuits. It is worth noting that, before the assessment of thermal rating, the joint circuit should first fulfil the requirements and regulations with greater importance and significance.

Section 7.1 describes the selection of components used to construct the representative joint circuits analysed in this study.

Section 7.2 examines the choice of rating units and explores how voltage variations and load types influence thermal ratings and circuit performance. This includes detailed investigations into the impact of voltage fluctuations (7.2.1), the combined effect of load type and voltage variation (7.2.2), and the variation of load units under a fixed branch current (7.2.3). A summary of key findings is provided in Section 7.2.4.

Section 7.3 presents the evaluation of thermal ratings and loading limits for joint circuits. It includes two main case studies: the OHL–cable composite circuit (7.3.1) and the OHL–transformer–cable substation circuit (7.3.2), representing typical transmission and grid-entry configurations, respectively.

7.1 Selection of Components in Joint Circuits

After the basic component types are selected for the joint circuit, the first rating to be considered is the STR for OHLs and cables. As for power transformers, it is NTR. The current worst-case assumption is the summer STR, as reviewed in Chapter 2. As a summary, the ambient conditions under the current summer STR assumption are shown in Table 7.1.

Table 7.1: Ambient conditions under the summer STR assumption in practice [3], [8], [11], [14], [56], [77].

Component	OHL	ExpoC	FTC	DBC	Transformer
Source(s)	[11], [14], [77]	[8], [14], [56]			[3], [14]
Ambient Temperature (°C) (AAT or AST)	20 AAT	30 AAT	35 AST	15 AST	Nameplate rating
Wind speed (m/s)	0.5	-	-	-	
Attacking angle (degree)	12	-	-	-	
Solar irradiance (W/m^2)	0	-	-	-	
Soil resistivity ($K \cdot m/W$)	-	-	1.2	1.2	

From the table above, it can be seen that there is a clear distinction in the AT for the components of OHL, ExpoC and transformer, even though they are exposed in the same AT, which is AAT in this case. However, as previously reviewed and discussed, the AAT assumption in STR for the OHL is based on its exceedance level [11], [62]. As the proposed thermal model of the components differs, and the ambient assumption is updated to account for global warming and heat waves. As a result, a new set of assumptions for summer STR ambient conditions is proposed, as shown in Table 7.2.

Table 7.2: New ambient conditions for summer STR considered global warming and heat waves.

Component	OHL	ExpoC	FTC	DBC	Transformer
Ambient Temperature (°C) (AAT or AST)	20 AAT	30 AAT	24.4 AST	21.8 AST	Nameplate rating and the tap position with the highest rated current
Wind speed (m/s)	0.5	0.5	-	-	
Attacking angle (degree)	12	90	-	-	
Solar irradiance (W/m^2)	0	-	-	-	
Soil resistivity ($K \cdot m/W$)	-	-	1.2	1.2	

For an existing circuit with an unknown type and size of some of the components. Based on the calculated summer STR or known NTR in that joint circuit. The assumed type and size of the component are calculated and selected based on the new summer STR assumption above.

7.2 Rating Unit Selection and the Impact of Voltage Variations and Load Types

From the result shown in 4.2.2, it can be seen that when the component with active voltage control capability is present (e.g., a power transformer with OLTC) in the joint circuit, the rating unit of the joint circuit has to be in apparent power (MVA), but the output voltage also needs to be noted. However, when the circuit is without a component with voltage-control capability, i.e., no transformer is involved, the rating can be safely expressed in ampacity (A) based on the circuit voltage. Such circuit voltage depends only on the supplied voltage at the point considered, it cannot alter the voltage by itself.

When converting the current limit to the power limit, the first obvious choice is to use the maximum voltage limit of the individual component. As each component also has a maximum voltage limit. For cable, it is determined by its electric insulation, for example, a 400kV cable should be able to withstand at least 400kV voltage with some buffer, e.g., 10% more voltage. Then, as discussed in Chapter 4, the thermal rating of the OHL is limited by its safely clearances, this safely clearances are determined by its breakdown voltage to the surroundings that may cause a fault. However, due to limited information on the construction of the OHL, e.g., geometry of the pylon, this should be a work for the future.

As the components work within the circuit in the power system, for a properly designed power system, it should have a rated voltage where it is designed to be operated at, and then it has a certain range of voltage variation that can be accepted. The voltage applied to the components also depends on the power system voltage limit. The variation of the voltage inside the system impacts the voltage applied to the component.

7.2.1 Impact of Voltage Variations

As shown in Figure 2.22, when the component is rated in current, its apparent power rating is only dependent on the voltage applied to the component at the given point in question. The relationship between the current rating and the power rating is only affected by the voltage.

7.2.2 Impact of Load Types and Voltage Variations

To assess the impact of load types, a case study is performed. Assuming a 2-bus single-phase system, an infinitely strong variable voltage source with voltage control (i.e., a transformer with OLTC, the HV side is connected to the grid) is connected to bus 0, and a load with the demand S_{base} connected to bus 1. Buses 0 and 1 are connected by branch 0, which represents the circuit between them. In this case, branch 0 is assumed to have no impedance, shown in Figure 7.1.

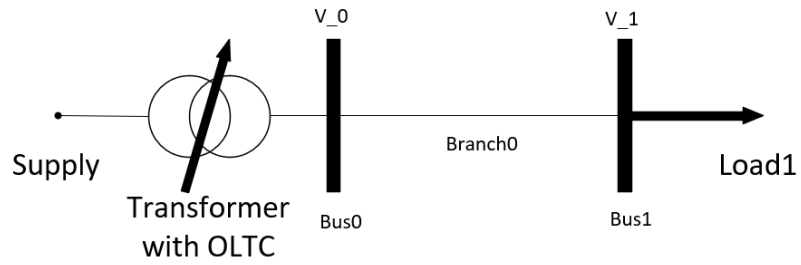

Figure 7.1: Diagram of the 2-bus test system without impedance in branch 0.

The base voltage V_{base} with a zero degree voltage angle is outputted on the LV side of the transformer at nominal tapping, which is the voltage on bus 0 and bus 1. The current flow through branch 0 is the base current I_{base}. The demand at the load at 1PU voltage is the base power S_{base} where:

$$S_{base} = V_{base} \cdot I_{base} \tag{242}$$

The base impedance of the load is:

$$Z_{base} = \frac{{V_{base}}^2}{S_{base}} \tag{243}$$

There are three basic types of load: constant impedance (ConstZ) load, constant power (ConstPQ) load and constant current (ConstI) load. When the voltage at bus 1 varies, for a constant impedance load, the power demand of the new voltage is calculated by:

$$S_{1,ConstZ} = \frac{{V_1}^2}{Z_{base}} \tag{244}$$

The current flow from bus 0 to bus 1 is then calculated by:

$$I_{0,ConstZ} = \frac{S_{1,ConstZ}}{V_1} = \frac{V_1}{Z_{base}} \tag{245}$$

For a constant power load, the power demand is constant, and the current flow from bus 0 to bus 1 is calculated by:

$$S_{1,ConstPQ} = S_{base} \tag{246}$$

$$I_{0,ConstPQ} = \frac{S_{base}}{V_1} \tag{247}$$

For a constant current load, the power demand varies with the voltage, the current demand is the base current, and it does not change with the voltage:

$$S_{1,ConstI} = V_1 \cdot I_{base} \tag{248}$$

$$I_{0,ConstI} = I_{base} \tag{249}$$

Therefore, the supplied voltage at bus 0 varies from 0.9PU to 1.1PU with a 0.01PU step (e.g., transformer OLTC +-1% in 21 steps). The variation of power demand at load 1 and the current flow from bus 0 to bus 1 are shown in Figure 7.2 and Figure 7.3, respectively.

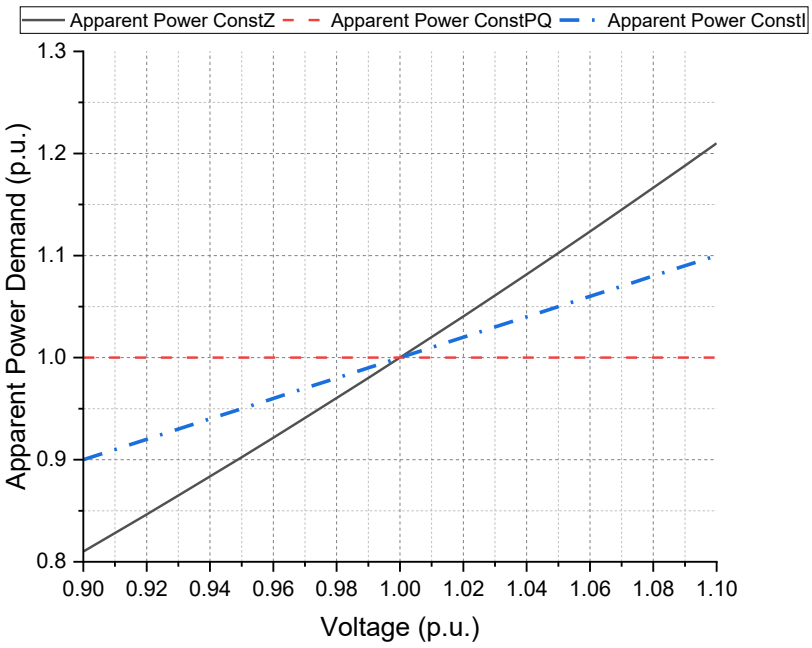

Figure 7.2: Comparison of the apparent power demand to the load with the voltage variation for different load types.

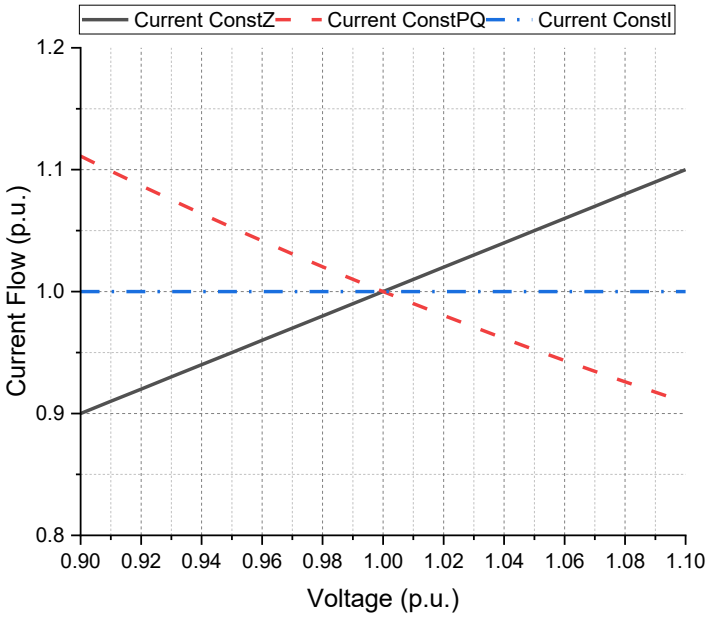

Figure 7.3: Comparison of the current flow to the load with the voltage variation for different load types.

7.2.3 Load Unit Variation with Fixed Current in Branch

Assuming the branch in the system is OHL, the current limit I_{limit} of the branch is determined by the specification of the OHL conductor and the ambient, independent from the network. Assuming the base current of the network is equal to the current limit, and it is a constant value. For a given value of the current equal to the current limit in the branch, the power flow to the load is calculated by:

$$S_1 = V_1 \cdot I_{limit} \tag{250}$$

For different types of loads to keep the current flow in the branch at the maximum allowed limit, the ratio of the load unit at bus 1 K_1 with the variation of voltage at bus 1 V_1 is calculated by:

$$K_{1,ConstZ} = \frac{Z_{L1,base} \cdot S_1}{{V_1}^2} = \frac{Z_{L1,base} \cdot I_{limit}}{V_1} \tag{251}$$

$$K_{1,ConstPQ} = \frac{S_1}{S_{L1,base}} = V_1 \cdot \frac{I_{limit}}{S_{L1,base}} \tag{252}$$

$$K_{1,ConstI} = \frac{S_1}{V_1 \cdot I_{L1,base}} = \frac{I_{limit}}{I_{L1,base}} \tag{253}$$

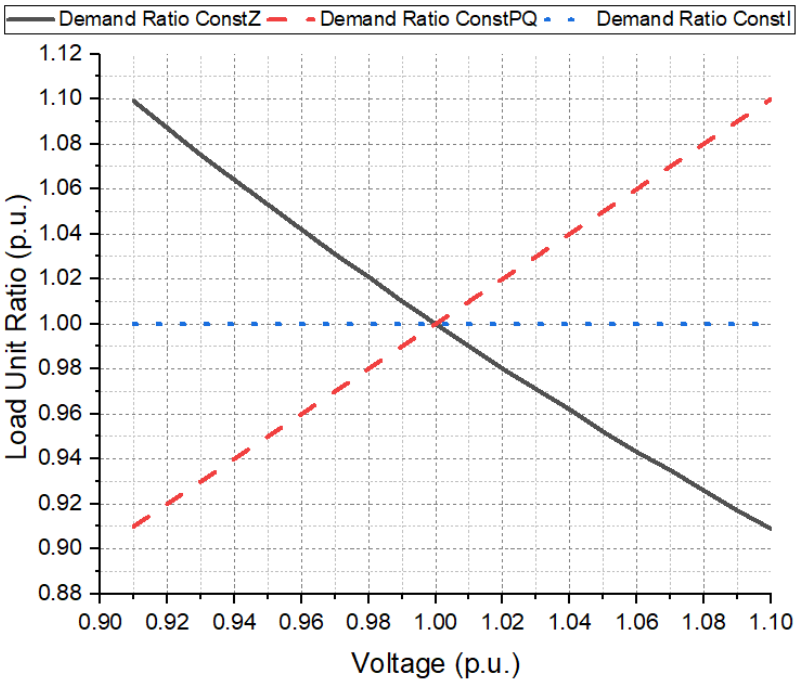

Figure 7.4: Variation of the ratio of the load unit with voltage to keep the current in the branch constant.

The results are shown in Figure 7.4. From the results, it can be seen that to keep the current in the branch at the maximum allowed limit, the ConstZ load is correlated with the reciprocal of the voltage, the ConstPQ load is correlated with the voltage, and the ConstI load is not affected by the voltage. The apparent power flow of all load types is shown in Figure 7.5. It can be seen that, for a constant current in the branch with no impedance considered, the limit of the apparent power flow depends only on the voltage.

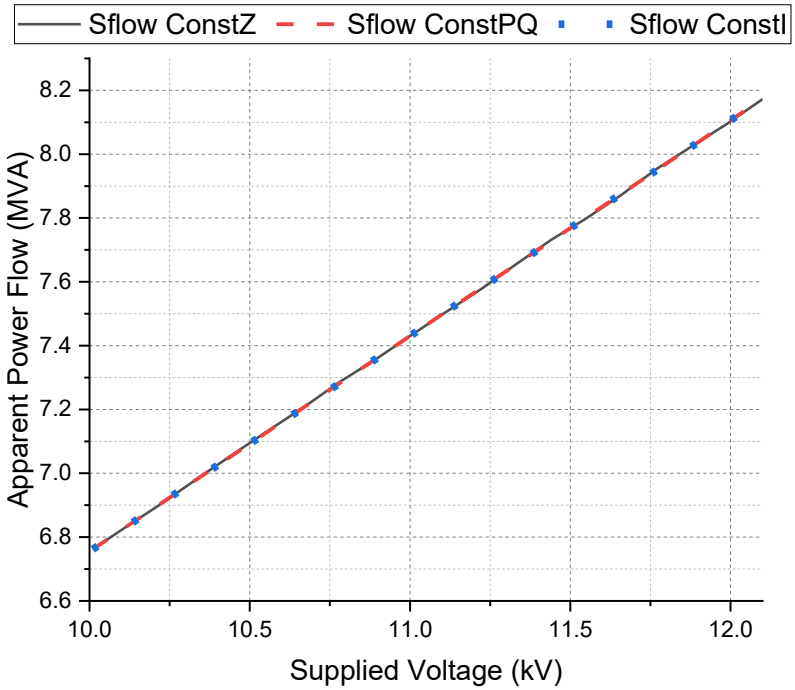

Figure 7.5: Variation of apparent power flow with voltage variation from a constant current.

From (226)-(238), it is found that the CCC of the OHLs is only dependent on the construction parameters of the conductor and the ambient conditions. This finding implies that the limiting factor is only current for OHLs and cables. The DTR of the OHL for different load types is shown in Figure 7.5, indicating that the DTR of the OHL is not affected by the load type.

The diagram of the new 2-bus test system is shown in Figure 7.6. Bus 0 is still considered the reference bus, with the constant voltage determined by the LV side of the transformer. Because it is assumed that the grid supplying the transformer is infinitely strong, bus 1 is always at a zero-degree voltage angle. An impedance has been added to branch 0, connecting buses 0 and 1.

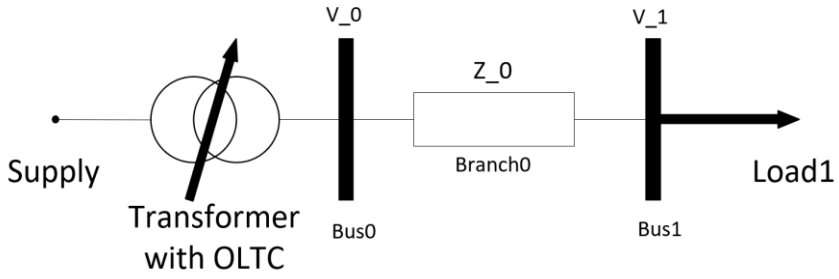

Figure 7.6: Diagram of the 2-bus test system with impedance added between bus0 and bus1.

The impedance at branch 0 Z_0 consists of both resistance at branch 0 R_0 and reactance at branch 0 X_0, defined by:

$$Z_0 = R_0 + jX_0 \tag{254}$$

The complex power received by bus 1 $\overline{S_1}$ is defined by:

$$\overline{S_1} = P_1 + jQ_1 = \overline{V_1} \cdot \overline{I_0^*} \tag{255}$$

For current at branch 0, it can be rewritten to:

$$\overline{I_0} = \frac{P_1 - jQ_1}{\overline{V_1^*}} \tag{256}$$

The limit of the magnitude of the current/ absolute value of the current is determined by the conductor specification. The angle is not the limiting factor, so it can be ignored. For a given current limit in the branch, the maximum apparent power received by bus 1 can be calculated by:

$$S_1 = V_1 \cdot I_{0,limit} \tag{257}$$

The voltage of bus 1 can be calculated by:

$$\overline{V_1} = \overline{V_0} - (R_0 + jX_0) \cdot I_0 = \overline{V_0} - (R_0 + jX_0) \cdot \frac{P_1 - jQ_1}{\overline{V_1^*}} \tag{258}$$

For a given voltage drop from bus 0 to bus 1 $\overline{\Delta V_{01}}$, it can be rewritten to

$$\overline{\Delta V_{01}} = (R_0 + jX_0) \cdot I_0 = (R_0 + jX_0) \cdot \frac{P_1 - jQ_1}{\overline{V_1^*}} = Z_0 \cdot I_0 = Z_0 \cdot \frac{P_1 - jQ_1}{\overline{V_1^*}} \quad (259)$$

$$\overline{\Delta V_{01}} = Z_0 \cdot \frac{\overline{S_1^*}}{\overline{V_1^*}} \quad (260)$$

The voltage limit is the magnitude, or absolute value, of the voltage. The voltage angle is not a limiting factor, so it can be ignored in the calculation. It can be further rewritten to:

$$\Delta V_{01} = Z_0 \cdot \frac{S_1}{V_1} = V_0 - V_1 \quad (261)$$

The apparent power received by bus 1 for a given voltage lower limit $V_{1,min}$ is calculated by:

$$S_1 = \frac{(V_0 - V_{1,min}) \cdot V_{1,min}}{Z_0} \quad (262)$$

For a given current limit in the branch and a voltage lower limit of the bus, the lower limit of the apparent power that can flow into bus 1 $S_{1,min}$ can be calculated by:

$$S_{1,min} = \min\left(\frac{(V_0 - V_{1,min}) \cdot V_{1,min}}{Z_0}, V_1 \cdot I_{0,limit}\right) \quad (263)$$

For a given current limit in the branch and the voltage upper limit of the bus, the upper limit of the apparent power that can flow into bus1 $S_{1,max}$ can be calculated by:

$$S_{1,max} = \min\left(\frac{(V_0 - V_{1,min}) \cdot V_{1,min}}{Z_0}, V_{1,max} \cdot I_{0,limit}\right) \quad (264)$$

7.2.3.1 Case Study

For the base case, when supplied with 1 PU voltage at bus 0, to supply the demand at 100% load unit in bus 1, the voltage drop effect due to 1 PU current flow

from bus 0 to bus 1 and the impedance in the branch is 0.05 PU, resulting in a 0.95 PU voltage at bus 1.

The current limit is 1 PU in the branch, and the voltage limit is from 0.9 to 1.1 PU. The demand on bus 1 at the base case is calculated by:

$$S_{1,base} = V_{1,base} \cdot I_{0,limit} = (V_{base} - \Delta V_{drop,base}) \cdot I_{0,limit} = 0.95 S_{base} \quad (265)$$

The impedance of ConstZ load, the apparent power of ConstPQ load and the current of ConstI load are calculated by:

$$Z_{L1,base} = \frac{{V_{1,base}}^2}{S_{1,base}} = 0.95 \quad (266)$$

$$S_{L1,base} = S_{1,base} = 0.95 \quad (267)$$

$$I_{L1,base} = I_{0,base} = 1 \quad (268)$$

When considering the current limit only (or significantly relaxed limit of upper and lower voltage, e.g. from 1.5 to 0.5PU), the maximum load unit ratio for ConstZ, ConstPQ and ConstI types of load when the voltage supplied in bus 0 varies from 0.9 to 1.1 PU is calculated by:

$$K_{ConstZ,LimitI} = \frac{Z_{L1,base} \cdot I_{limit}}{V_1} = \frac{Z_{L1,base} \cdot I_{limit}}{V_0 - I_{limit} Z_0} \quad (269)$$

$$K_{ConstPQ,LimitI} = \frac{V_1 \cdot I_{0,limit}}{S_{L1,base}} = \frac{(V_0 - I_{0,limit} \cdot Z_0) \cdot I_{0,limit}}{S_{L1,base}} \quad (270)$$

$$K_{ConstI,LimitI} = \frac{I_{0,limit}}{I_{L1,base}} = 1 \quad (271)$$

The term maximum load unit ratio represents the maximum load in PU that can be connected to bus1. When considering the voltage limit only from 0.9 PU to 1.1 PU, the maximum load unit ratio for ConstZ, ConstPQ and ConstI types of load when the voltage supplied in bus 0 varies from 0.9 to 1.1 PU is calculated by:

$$K_{ConstZ,LimitV} = \frac{Z_{L1,base} \cdot I_0}{V_{min}} = \frac{Z_{L1,base} \cdot \frac{V_0 - V_{min}}{Z_0}}{V_{min}} \tag{272}$$

$$K_{ConstPQ,LimitV} = \frac{V_{min} \cdot I_0}{S_{L1,base}} = \frac{V_0 - V_{min}}{S_{L1,base} \cdot Z_0} \tag{273}$$

$$K_{ConstI,LimitV} = \frac{I_{0,limit}}{I_{L1,base}} = \frac{V_0 - V_{min}}{I_{L1,base} \cdot Z_0} \tag{274}$$

The load unit ratio can be determined by the lower of the two:

$$K_{ConstZ} = \min\left(K_{ConstZ,LimitI}, K_{ConstZ,LimitV}\right) \tag{275}$$

$$K_{ConstPQ} = \min\left(K_{ConstPQ,LimitI}, K_{ConstPQ,LimitV}\right) \tag{276}$$

$$K_{ConstI} = \min\left(K_{ConstI,LimitI}, K_{ConstI,LimitV}\right) \tag{277}$$

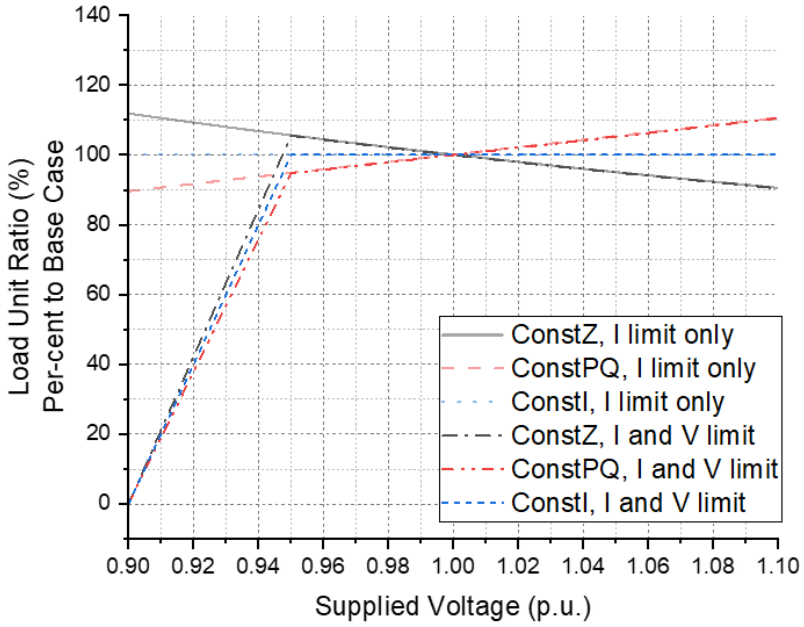

Figure 7.7: Variation of the load unit ratio with voltage to keep the current in the branch constant when considering only the current limit and considering both voltage and current limit.

From the results, when the branch is limited only by current, and the demand is a pure ConstPQ load, increasing the supplied voltage can effectively increase the load

unit ratio, allowing more loads to be connected. However, when the demand is the pure ConstZ load, increasing the supplied voltage will decrease the load unit ratio; i.e., some load needs to be curtailed to avoid violating the current limit in the branch. The pure ConstI load is unaffected. Then, if the voltage limits of the buses are considered, the difference compared to the no-voltage-limit case is observed only under low-supplied-voltage conditions, i.e., less than 0.95PU of supplied voltage. Due to the voltage drop across the branch impedance and current flow, when the supplied voltage is low, the system's ability to connect the load is limited by the voltage. To preserve the voltage on bus 2, fewer loads can be connected to the system to minimise voltage drop and prevent the lower voltage limit from being violated.

7.2.4 Summary

From the analysis, it can be seen that when the component has no active voltage regulation capability, e.g., OHL and cables, the rating unit can be chosen in current, as the voltage limit requirement exceeds the capability of such components. When the current limit of a component is given, the power limit is calculated by the multiplication of the voltage applied to that component. To meet the voltage limit requirement, it is the responsibility of the voltage supply control and the voltage drop along the component in the branch. The power rating of a component rated by current can be calculated based on the voltage at the point chosen. These voltages cannot be determined or controlled by OHL or cable. To simplify the evaluation, when the rated voltage is known but the actual voltage applied to the component is not given, it is better to rate the OHL and cables at the current. If needed, the power rating can be calculated based on the circuit's rated voltage.

However, when using the power as the rating of the component, it is worth noting that due to the voltage variations and load types, non-pure ConstPQ loads at non-rated voltage will change their power demand. For example, at 1.1PU output voltage, the pure ConstZ load can increase its power demand to 1.21PU. This indicates that when connecting loads to the transformer, the impact of the voltage variations and the load types has to be taken into account, e.g., a 240MVA load may demand 290MVA for a

+10% LV side voltage compared to the rated voltage. In that case, the transformer will be overloaded, so less load should be connected.

7.3 Evaluation of Thermal Ratings and Loading Limits of Joint Circuits

In this thesis, two groups of joint thermal ratings for two representative circuits, Braintree and Pentir–Trawsfynydd, are determined by combining the ratings of their series components (OHL, transformer, and cables: ExpoC, FTC, and DBC) under a single, consistent ambient assumption set. Individual components and their ratings from previous chapters (STR, DTR, S/MTOR, CTR) are evaluated under common conditions and then combined by the minimum-of-limits to produce joint circuit pre-fault, post-fault, emergency, and cyclic ratings.

Ratings are reported in MVA whenever the transformer is present, and in Ampacity when no active voltage change is present. The work determines which component limits at each point in the ambient space (AAT, AST, WS, and SI) using joint circuit DTR, quantifies time-limited loading limit using joint circuit S/MTOR with explicit pre-fault loading and duration, and establishes joint circuit CTR envelopes that respect daily recovery.

In this first example of the joint circuit, no transformer with tap-changing ability is involved. Thus, it is less complex. The second example introduced a transformer with tap-changing capability. The tap-changing of the transformer not only affects its own thermal performance but also changes the voltage and current output on the secondary side. Where the change in thermal performance, thus the variation in the maximum loading capability of the transformer, affects the components connected to the transformer on both sides, the change in the voltage and current on the secondary side does not affect the components on the primary side. The second example should present a more comprehensive joint rating that considers the control mechanism in the system, which, for now, only consists of tap-changing of the transformer, but could be expanded in the future.

Last but not least, the components in the circuit are not limited to OHL, cable and transformers. Various other components might be installed in the circuit along with the three main components. For instance, the termination between OHL and cable, and the bushing. These should be considered in future work after the three main components.

7.3.1 Joint Circuit Ratings of Overhead Line and Cable Composite Circuit

Figure 7.8 shows the circuit at Pentir–Trawsfynydd in North Wales. The incoming OHL terminates at the substation and is connected to a bushing and outdoor termination with a short section of exposed cable. From this point, the circuit transitions underground, where it is assumed to be an FTC before continuing as a DBC cable section.

Figure 7.8: Pentir-Trawsfynydd, Garth cable compound, OHL – Cables

7.3.1.1 Joint Circuit Dynamic Thermal Ratings of Overhead Line and Cable Composite

The example case for the joint DTR of OHL and cable composite is based on the Pentir-Trawsfynydd circuit. Where the DTR is a result of the joint individual rating of the AAAC Twin-Sorbus 75°C limit and Twin 400kV 1000mm^2 cable, the following result will only consider a single AAAC Sorbus 75°C limit and 400kV 1000mm^2 cable instead of twin-OHL and twin-cables (as it is assumed that the twin is just twice the amount of a single circuit, since enough space out is applied to minimise the mutual

heating effect). The result of the joint circuit post-fault DTR of the example composite circuit is shown in Figure 7.9.

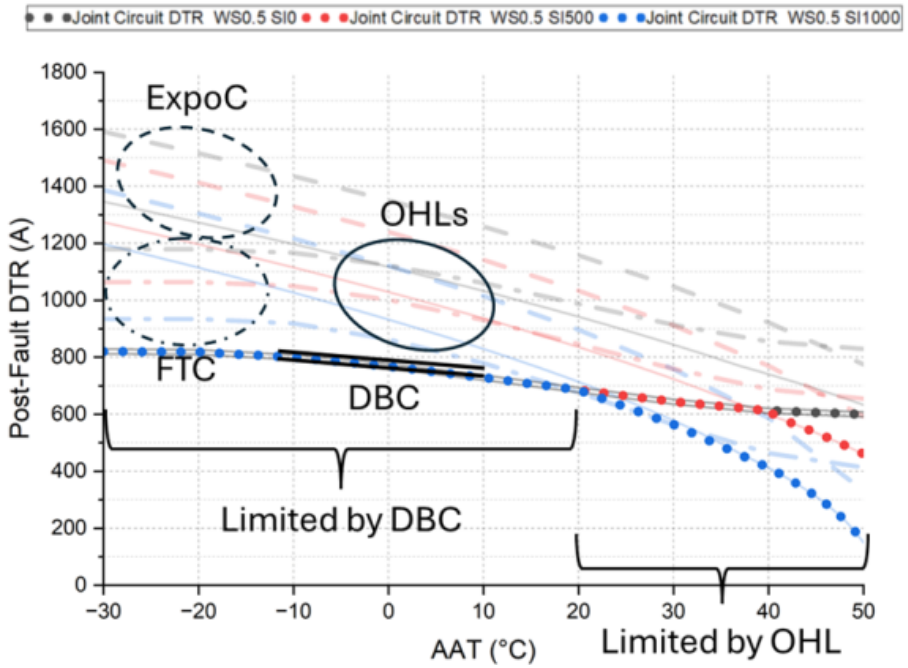

a) Post-fault 1 PU DTR, 0.5 m/s WS, limit at example of 1000 W/m^2

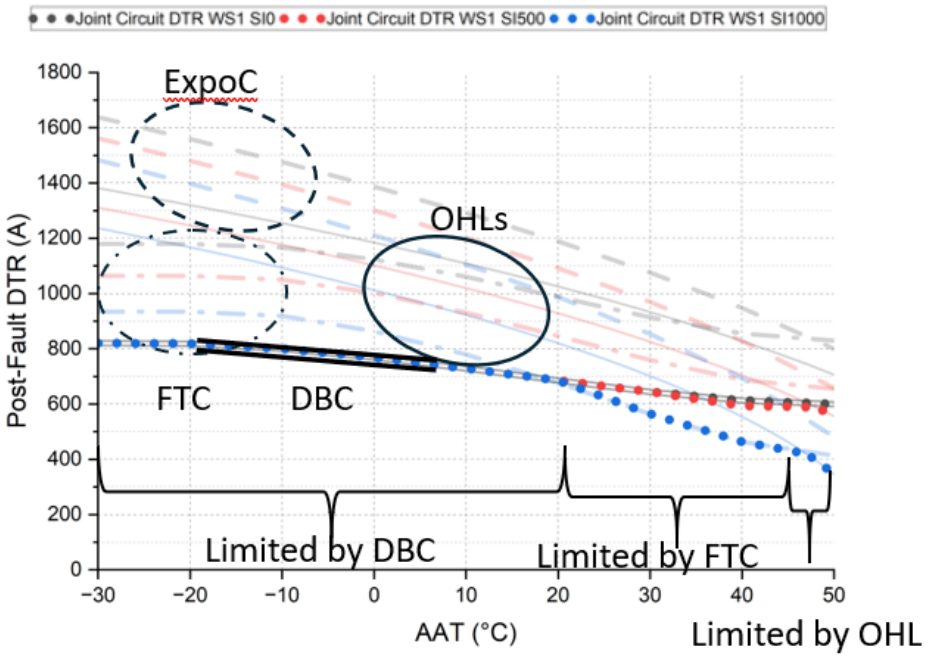

b) post-fault 1 PU DTR, 1 m/s WS, limit at example of 1000 W/m^2

Figure 7.9: Variation of the joint circuit post-fault DTR with the variation of AAT, SI under 0.5m/s WS (a) and 1m/s WS (b) for the example OHL and cable composite circuit.

The circuit comprises four thermal components:

- OHL (solid line, grouped with solid black circle)
- Exposed cable (ExpoC) section (dashed line)
- Filled trough cable (FTC) (dash-dotted line)
- Direct-buried cable (DBC) (double line)

Under 1000 W/m² solar irradiance (worst-case condition) in Figure 7.9a, the DBC limits the circuit rating from –30 °C to approximately 20°C ambient AAT. Beyond this point, the OHL becomes the limiting element, controlling the circuit rating up to 50 °C. Under 500 W/m² solar irradiance in the same figure (following the thick red dotted line), the limiting component transitions at a higher temperature. The DBC constrains the rating from –30 °C to approximately 40 °C AAT, after which the OHL dictates the rating up to 50 °C.

Figure 7.9b shows the joint circuit post-fault DTR of the OHL and cable sections under 1 m/s wind speed and 1000 W/m² solar irradiance, complementing the results previously presented for 0.5 m/s wind speed. The figure reveals that from –30 °C to approximately 20 °C AAT, the circuit rating remains limited by the DBC, as indicated by the lowest blue curves. Between 20 °C and 45 °C AAT, the FTC becomes the limiting component, shifting the rating control away from the OHL. Above 45 °C AAT, the OHL governs the rating, as shown by the blue dotted line becoming the lowest envelope curve up to 50 °C.

This contrasts with the 0.5 m/s wind speed case, where the OHL became the limiting component much earlier (from roughly 20 °C upwards). The higher wind speed increases the OHL's cooling capacity, delaying the point at which it becomes thermally limiting and allowing the FTC to govern the rating over a wider temperature range. As before, the circuit rating must be set based on the minimum-capacity component over each temperature range to ensure safe and reliable operation under indefinite post-fault loading conditions.

This analysis highlights that circuit rating is governed by the lowest-capacity component within the series arrangement. Therefore, for indefinite loading conditions, the applicable circuit rating must be set based on the component that governs within each temperature range:

- DBC sets the rating for lower AAT ranges (cold conditions).
- FTC and OHL set the rating for higher AAT ranges (warm to hot conditions).
- ExpoC is not the limiting factor for the circuit post-fault DTR. However, it is to be noted that the AA of 90° is used as it is assumed that ExpoC is perpendicular to the WS. Different resulting AA could decrease this further and needs to be treated with caution.
- Finally, note that the pre-fault DTR is applied only to the OHL, as it must provide an additional ~20 % headroom to accommodate post-fault loading capability.

As required in TGNs [14] and [11], OHLs are required to preserve 20% of the capacity from the pre-fault as a reserve for the post-fault situations. Which means when considering the post-fault DTR as 1 PU, the pre-fault DTR is 0.84 PU of the post-fault DTR. The pre-fault DTR of the circuit is defined in Figure 7.10. From the results, under pre-fault conditions and when assessing the joint circuit DTR, the OHL becomes the limiting component under 0.5 m/s wind speed in Figure 7.10a, non-zero solar SI, and higher AAT. Under high SI, this transition occurs at a lower AAT (at around 5°C) compared with the medium SI case (at around 20°C), as the additional solar heating reduces the thermal margin of the OHL more rapidly.

When considering 1 m/s wind speed in Figure 7.10b, the behaviour shifts: under high SI conditions, the FTC becomes the limiting component first, governing the circuit rating up to approximately 20 °C AAT. As the AAT increases further, the OHL DTR falls below the FTC DTR around 40 °C AAT, making the OHL the new limiting element.

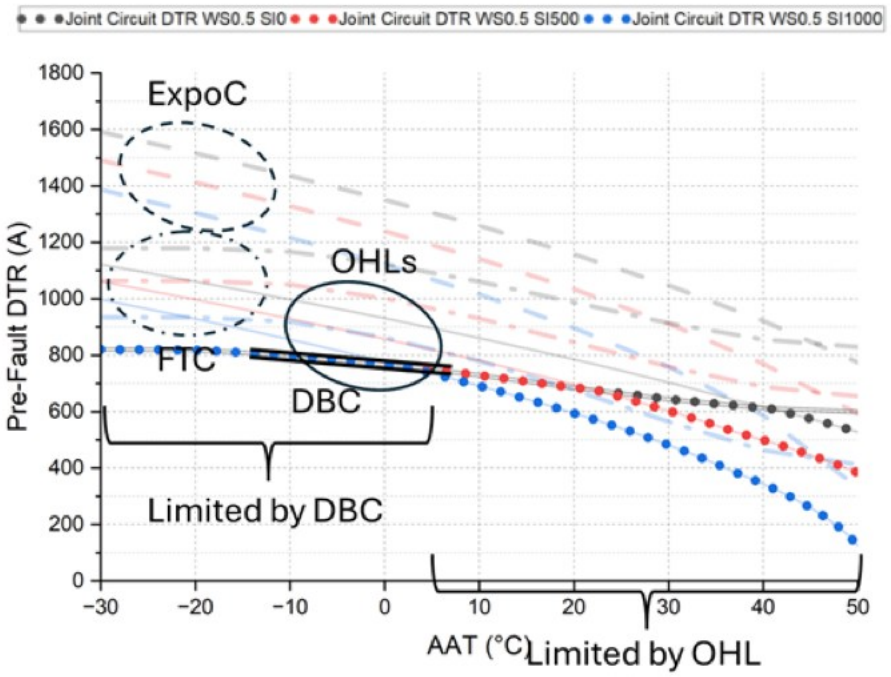

a) pre-fault 1 PU DTR, 0.5 m/s WS, limit at example of 1000 W/m^2.

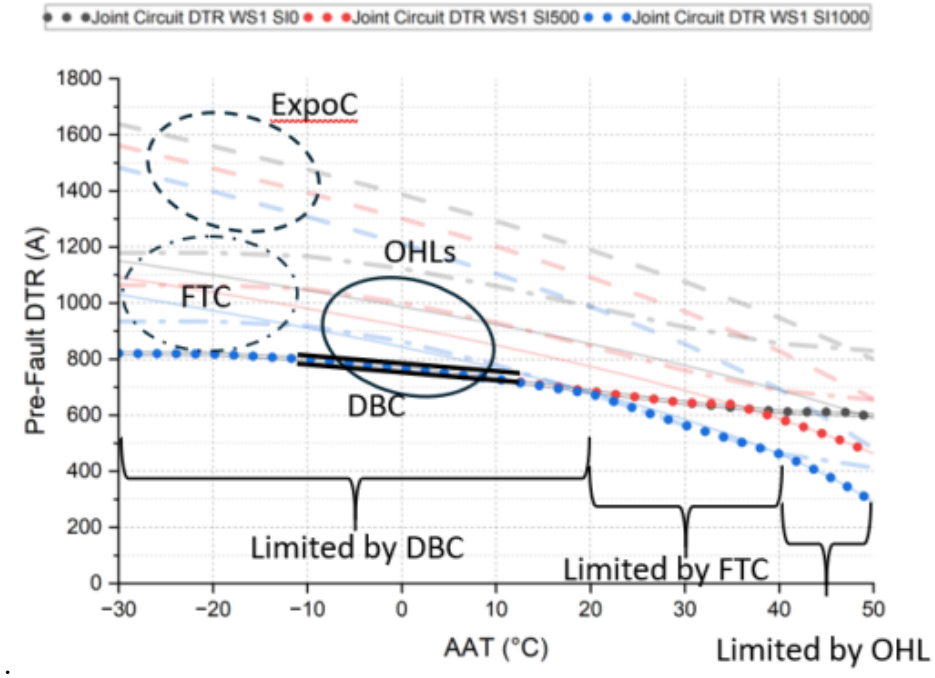

.

b) pre-fault 1 PU DTR, 1 m/s WS, limit at example of 1000 W/m^2.

Figure 7.10: Variation of the joint circuit pre-fault DTR with the variation of AAT, SI under 0.5m/s WS (a) and 1m/s WS (b) for the example OHL and cable composite circuit.

It is important to note, however, that previous studies have shown that the solar heating impact on cables (particularly FTC) is often overestimated when calculating DTR. The OHL solar heating estimation, by contrast, is generally accurate. Consequently, when assessing the joint circuit CTR of the OHL–cable composite circuit, the limiting influence of the FTC under high SI conditions may be less severe than suggested by these DTR results.

7.3.1.2 Joint Circuit Short-Term and Medium-Term Overloading Ratings for Overhead Line and Cable Composite

Unlike the S/MTOR of an individual component, the joint circuit DTR is defined as the lowest DTR among all components within that circuit. This means that the joint circuit 100 % DTR does not necessarily correspond to the DTR of any single component. For example, an 85 % pre-fault loading level for the joint circuit will be lower than the 85 % pre-fault loading of the OHL alone, because it is governed by another component, which is the weakest in the series. In this case, the 100% pre-fault loading is the post-fault DTR for both OHL and cables, as the pre-fault and post-fault DTR of cables are the same [8], [11], [14].

Therefore, the S/MTOR must be calculated using the joint circuit DTR rather than the DTR of individual elements. This is done by first calculating the S/MTOR for each component based on the joint circuit DTR, then selecting the lowest S/MTOR among all components as the governing S/MTOR for the entire OHL–cable composite circuit. The resulting joint circuit S/MTOR values for the OHL–cable composite, as a function of AAT under 0.5 m/s wind speed and zero SI, are summarised in Table 7.3.

A key observation from this table is that the joint circuit S/MTOR is not simply the S/MTOR of the OHL or cable taken individually. Instead, it reflects the lowest available capacity among all series components for each temperature and duration. For example:

- Pre-fault DTR is governed entirely by the DBC up to 40 °C AAT, after which the OHL becomes the limiting element. This shifts the joint circuit rating below what would be expected if only the OHL were considered.

- At 85 % pre-fault loading, the medium-term ratings of 360 min remain DBC-limited across nearly the full temperature range, meaning that the available emergency headroom is strongly constrained by the cable thermal capacity rather than the OHL.
- At higher overload magnitudes (e.g. 20 min, 10 min, 5 min, 3 min ratings), the OHL becomes the governing component over most of the temperature range. This reflects the fact that the OHL is heated faster (shorter TTC) and therefore is not able to accommodate higher transient currents than the DBC for very short durations.

This comparison highlights a fundamental difference between the S/MTOR of individual components and the joint circuit:

- For an OHL assessed in isolation, the S/MTOR values would be significantly higher in cold conditions.
- When joint with a thermally critical DBC section, the overall circuit rating is capped by the DBC capacity until ambient temperature rises sufficiently for the OHL to become the weaker component.

This behaviour underscores the importance of calculating S/MTOR based on joint circuit DTR, rather than applying OHL S/MTOR curves directly, as doing so would overestimate the circuit's permissible emergency loading in most low- to moderate-temperature scenarios.

The resulting joint circuit S/MTOR values for the OHL–cable composite, as a function of AAT under 0.5 m/s wind speed and 1000 W/m^2 SI, all assuming constant, are present in Table 7.4.

Table 7.3: Short-Term and Medium-Term Overloading Ratings of Overhead Line Sorbus and 400kV $1000mm^2$ Cable Composite 0.5m/s WS and 0 SI

AAT (°C)		-30	-20	-10	0	10	20	30	40	50
AST 0.3m (°C)		-0.5	-0.5	0.8	5.3	11.4	18.2	24.4	29.0	31.0
AST 1m (°C)		2.09	2.31	4.62	8.38	12.93	17.62	21.81	24.84	26.06
Pre-fault DTR (A) /Limited by		820 /DBC	819 /DBC	800 /DBC	769 /DBC	729 /DBC	685 /DBC	644 /DBC	613 /DBC	528 /OHL
Post-fault DTR (A)		820 /DBC	819 /DBC	800 /DBC	769 /DBC	729 /DBC	685 /DBC	644 /DBC	613 /DBC	600 /DBC
Pre-load%	**Duration (min)**	Pre-Joint DTR S/MTOR in Amps at rated voltage, 0.5m/s WS and 0 SI								
100% corresponds to		820 /DBC	819 /DBC	800 /DBC	769 /DBC	729 /DBC	685 /DBC	644 /DBC	613 /DBC	600 /DBC
-	**inf**	820 /DBC	819 /DBC	800 /DBC	769 /DBC	729 /DBC	685 /DBC	644 /DBC	613 /DBC	600 /DBC
85%	**360**	980 /DBC	979 /DBC	960 /DBC	919 /DBC	859 /DBC	805 /DBC	754 /DBC	713 /DBC	628 /OHL
	60	1370 /OHL	1299 /OHL	1220 /OHL	1139 /OHL	1049 /OHL	955 /OHL	854 /OHL	753 /OHL	638 /OHL
	20	1650 /OHL	1539 /OHL	1440 /OHL	1329 /OHL	1229 /OHL	1115 /OHL	994 /OHL	863 /OHL	728 /OHL
	10	2040 /OHL	1899 /OHL	1760 /OHL	1629 /OHL	1499 /OHL	1355 /OHL	1204 /OHL	1033 /OHL	868 /OHL
	5	2680 /OHL	2479 /OHL	2280 /OHL	2109 /OHL	1929 /OHL	1745 /OHL	1544 /OHL	1313 /OHL	1098 /OHL
	3	3330 /OHL	3099 /OHL	2830 /OHL	2619 /OHL	2399 /OHL	2195 /OHL	1934 /OHL	1603 /OHL	1348 /OHL
75%	**360**	1060 /DBC	1059 /DBC	1030 /DBC	979 /DBC	929 /DBC	865 /DBC	814 /DBC	733 /OHL	628 /OHL
	60	1380 /OHL	1299 /OHL	1220 /OHL	1139 /OHL	1049 /OHL	955 /OHL	854 /OHL	753 /OHL	648 /OHL
	20	1670 /OHL	1569 /OHL	1470 /OHL	1359 /OHL	1259 /OHL	1145 /OHL	1024 /OHL	893 /OHL	758 /OHL
	10	2100 /OHL	1959 /OHL	1830 /OHL	1689 /OHL	1559 /OHL	1415 /OHL	1264 /OHL	1083 /OHL	918 /OHL
	5	2770 /OHL	2569 /OHL	2390 /OHL	2219 /OHL	2039 /OHL	1855 /OHL	1644 /OHL	1403 /OHL	1178 /OHL
	3	3460 /OHL	3249 /OHL	3010 /OHL	2769 /OHL	2549 /OHL	2315 /OHL	2044 /OHL	1733 /OHL	1468 /OHL
65%	**360**	1110 /DBC	1109 /DBC	1080 /DBC	1039 /DBC	979 /DBC	915 /DBC	844 /OHL	733 /OHL	628 /OHL
	60	1380 /OHL	1309 /OHL	1220 /OHL	1139 /OHL	1059 /OHL	965 /OHL	864 /OHL	763 /OHL	648 /OHL
	20	1700 /OHL	1599 /OHL	1490 /OHL	1389 /OHL	1279 /OHL	1165 /OHL	1044 /OHL	913 /OHL	768 /OHL
	10	2150 /OHL	2009 /OHL	1880 /OHL	1749 /OHL	1609 /OHL	1465 /OHL	1304 /OHL	1133 /OHL	958 /OHL
	5	2870 /OHL	2659 /OHL	2480 /OHL	2309 /OHL	2129 /OHL	1925 /OHL	1714 /OHL	1483 /OHL	1248 /OHL
	3	3610 /OHL	3349 /OHL	3110 /OHL	2889 /OHL	2689 /OHL	2435 /OHL	2164 /OHL	1843 /OHL	1558 /OHL

Table 7.4: Short-Term and Medium-Term Overloading Ratings of Overhead Line Sorbus and 400kV 1000mm^2 Cable Composite 0.5m/s WS and 1000 SI

AAT (°C)		-30	-20	-10	0	10	20	30	40	50
AST 0.3m (°C)		-0.5	-0.5	0.8	5.3	11.4	18.2	24.4	29.0	31.0
AST 1m (°C)		2.09	2.31	4.62	8.38	12.93	17.62	21.81	24.84	26.06
Pre-fault DTR (A) /Limited by		820 /DBC	819 /DBC	800 /DBC	769 /DBC	691 /OHL	595 /OHL	482 /OHL	344 /OHL	125 /OHL
Post-fault DTR		820 /DBC	819 /DBC	800 /DBC	769 /DBC	729 /DBC	685 /DBC	565 /OHL	413 /OHL	150 /OHL
Pre-load%	**Duration (min)**	S/MTOR using pre-fault joint circuit DTR in Amps at rated voltage, 0.5m/s WS and 1000 SI								
100% corresponds to		820 /DBC	819 /DBC	800 /DBC	769 /DBC	729 /DBC	685 /DBC	565 /OHL	413 /OHL	150 /OHL
-	**inf**	820 /DBC	819 /DBC	800 /DBC	769 /DBC	729 /DBC	685 /DBC	565 /OHL	413 /OHL	150 /OHL
85%	**360**	980 /DBC	979 /DBC	960 /DBC	919 /DBC	830 /OHL	714 /OHL	578 /OHL	413 /OHL	151 /OHL
	60	1217 /OHL	1132 /OHL	1041 /OHL	944 /OHL	838 /OHL	719 /OHL	582 /OHL	417 /OHL	152 /OHL
	20	1412 /OHL	1292 /OHL	1176 /OHL	1054 /OHL	923 /OHL	774 /OHL	622 /OHL	447 /OHL	162 /OHL
	10	1702 /OHL	1547 /OHL	1396 /OHL	1234 /OHL	1063 /OHL	869 /OHL	697 /OHL	502 /OHL	182 /OHL
	5	2202 /OHL	1977 /OHL	1776 /OHL	1544 /OHL	1313 /OHL	1039 /OHL	827 /OHL	592 /OHL	212 /OHL
	3	2722 /OHL	2427 /OHL	2176 /OHL	1884 /OHL	1603 /OHL	1239 /OHL	977 /OHL	702 /OHL	252 /OHL
75%	**360**	1060 /DBC	1059 /DBC	1027 /OHL	933 /OHL	830 /OHL	714 /OHL	578 /OHL	413 /OHL	151 /OHL
	60	1220 /OHL	1134 /OHL	1043 /OHL	946 /OHL	840 /OHL	722 /OHL	584 /OHL	419 /OHL	153 /OHL
	20	1430 /OHL	1319 /OHL	1203 /OHL	1081 /OHL	950 /OHL	802 /OHL	644 /OHL	469 /OHL	168 /OHL
	10	1765 /OHL	1604 /OHL	1448 /OHL	1291 /OHL	1125 /OHL	932 /OHL	749 /OHL	544 /OHL	198 /OHL
	5	2275 /OHL	2074 /OHL	1858 /OHL	1661 /OHL	1415 /OHL	1152 /OHL	929 /OHL	674 /OHL	238 /OHL
	3	2855 /OHL	2544 /OHL	2298 /OHL	2041 /OHL	1745 /OHL	1382 /OHL	1109 /OHL	824 /OHL	298 /OHL
65%	**360**	1110 /DBC	1109 /DBC	1027 /OHL	933 /OHL	830 /OHL	714 /OHL	578 /OHL	413 /OHL	151 /OHL
	60	1222 /OHL	1136 /OHL	1045 /OHL	948 /OHL	843 /OHL	724 /OHL	586 /OHL	421 /OHL	153 /OHL
	20	1452 /OHL	1341 /OHL	1225 /OHL	1103 /OHL	968 /OHL	824 /OHL	666 /OHL	481 /OHL	173 /OHL
	10	1797 /OHL	1656 /OHL	1500 /OHL	1338 /OHL	1168 /OHL	984 /OHL	796 /OHL	581 /OHL	208 /OHL
	5	2357 /OHL	2146 /OHL	1950 /OHL	1738 /OHL	1518 /OHL	1254 /OHL	1016 /OHL	741 /OHL	268 /OHL
	3	2977 /OHL	2706 /OHL	2400 /OHL	2148 /OHL	1878 /OHL	1534 /OHL	1256 /OHL	921 /OHL	328 /OHL

From the result, it can be seen that due to the presence of a constant 1000 W/m^2 SI, compared to the result with zero SI. The OHL becomes the limiting component at 10°C AAT for both pre-fault joint circuit DTR, as shown in Figure 7.9 and Figure 7.10. However, the 100% pre-fault limit becomes OHL at 30°C due to the 100% pre-fault limit of OHL is the post-fault DTR of the OHL. The limiting component of the joint circuit S/MTOR also shifts. The OHL becomes the limiting component start at 0°C for 85% pre-fault loading and -10°C for 75% and 65% pre-fault loading, because the DBC is unaffected by the SI, whereas a high SI significantly impacts the thermal performance of OHL. The presence of a constant peak SI over 6 hours is very unlikely in practice, but it is worth noting that a peak SI within and including 1 hour is possible in practice. The OHL could in need to be overloaded when the SI is at its peak. Such a situation should be taken into consideration when following the S/MTOR under zero SI during the peak SI. As shown, the S/MTOR results are significantly lower under high SI than under no SI. Continuing to follow the S/MTOR calculated under no SI conditions could lead to exceeding or violating the temperature limit.

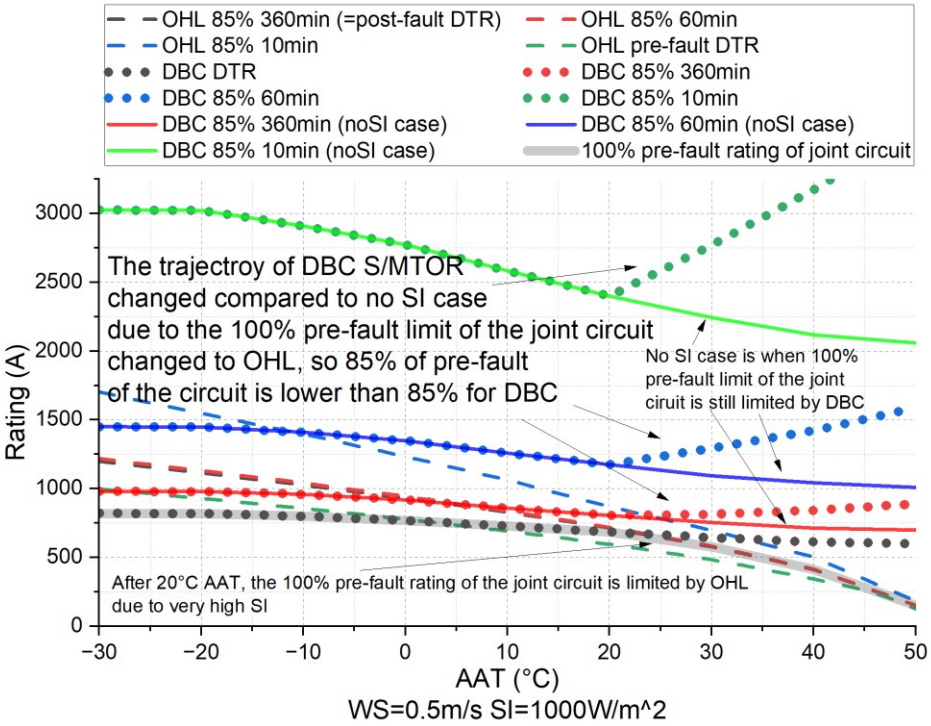

Figure 7.11: Variation of the S/MTOR of individual components in a joint circuit with the variation of AAT under high SI and 0.5m/s WS assumption.

The variation of the S/MTOR at 85% pre-fault loading for 360-, 60- and 10-minute overloading duration of the individual OHL and DBC in the joint circuit, is shown in Figure 7.11, together with the pre- and post-fault DTRs and the correspond 100% pre-fault rating of the joint circuit. The result from the no SI case for DBC is also present. From Figure 7.11, a clear change in the trajectory of the S/MTOR of DBC under the high SI case compared to the no SI case is shown after 20°C AAT. This is due to the 100% pre-fault limit of the joint circuit becoming OHL, which means the 85% pre-fault load level of the joint circuit is not 85% pre-fault loading of DBC under this high SI case. The actual pre-fault loading applied to DBC is lower than 85% of the pre-fault loading of DBC. Thus, the S/MTOR result is higher than the no SI case, where DBC entirely governs the 100% pre-fault rating of the joint circuit.

7.3.1.3 Cyclic Thermal Ratings for Overhead Line and Cable Composite

The CTR of the OHL–cable composite circuit, calculated using the standard cyclic loading profile, is presented in Figure 7.12 as a function of AAT, SI, and WS. For reference, the background curves show the DTR values previously obtained when assessing the CTR of the individual components. For the OHL, the DTR values are used directly to represent the CTR, since the TTC of the OHL is less than six hours, shorter than the six-hour duration of the peak load period in the standard cyclic profile. This means that the OHL effectively reaches steady-state temperature during the peak load window, making the DTR a valid approximation for its CTR.

When focusing on the 0.5 m/s WS, 1000 W/m² case (blue curve) in Figure 7.12a, the worst-case solar heating scenario, the following behaviour is observed:

- From –30 °C to approximately 10 °C AAT, the circuit rating is governed by the direct-buried cable (DBC). Compared with the joint circuit DTR under the same conditions, the DBC remains the limiting component over a wider temperature range (up to 20 °C rather than 10 °C).
- This shift is expected, as CTR generally provides higher available capacity than DTR for all cable sections due to the thermal inertia effect under cyclic loading. As a result, the cable ratings in this figure are extended upward relative to their DTR counterparts.

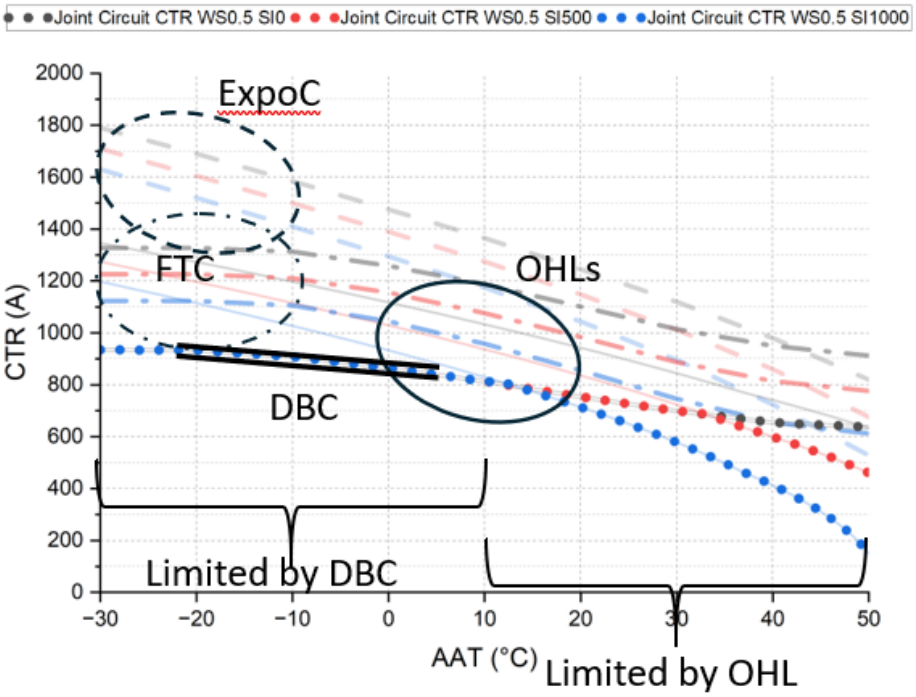

a) CTR, 0.5 m/s WS, limit at example of 1000 W/m^2.

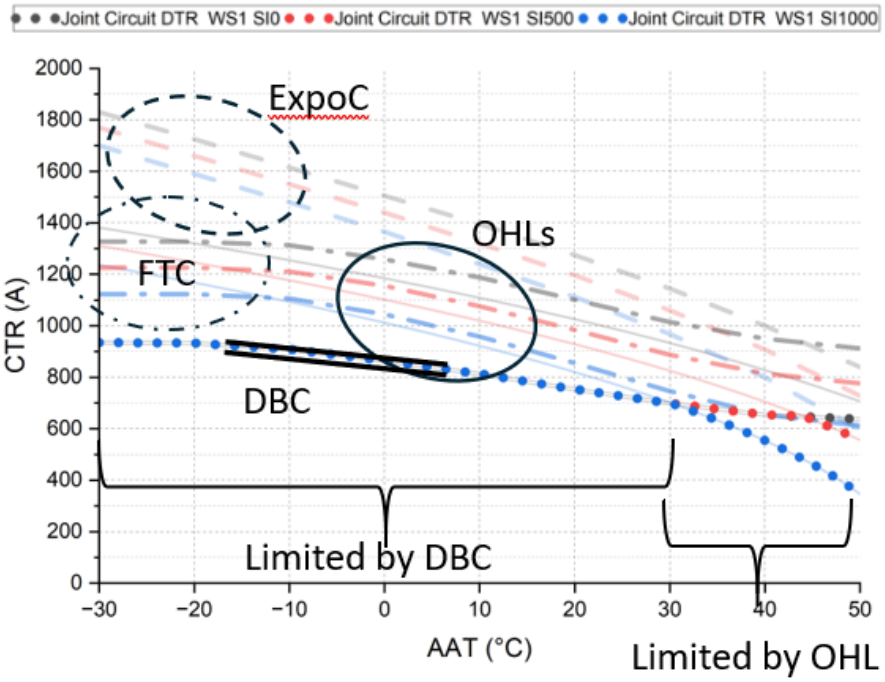

b) CTR, 1 m/s WS, limit at example of 1000 W/m^2.

Figure 7.12: Variation of the joint circuit CTR using standard cyclic loading profile with the variation of AAT, SI under 0.5m/s WS (a) and 1m/s WS (b) for the example OHL and cable composite circuit.

- From 10 °C to 50 °C AAT, the OHL becomes the limiting component, as indicated by the CTR envelope following the OHL curve. Notably, the OHL CTR remains identical to its DTR, since the OHL thermal time constant is shorter than the six-hour peak load duration used in the cyclic profile.

Figure 7.12b shows the joint circuit CTR of the OHL–cable composite circuit under 1 m/s wind speed and varying SI levels. The blue curve represents the envelope for 1000 W/m² SI, corresponding to the most severe thermal loading condition considered. Compared with the DTR results under the same conditions, a clear shift in the governing components is observed:

- Under DTR, the limiting components followed a three-stage progression: DBC at low AAT, FTC in the mid-range, and OHL at high AAT.
- Under CTR, however, the FTC no longer governs the circuit rating. Its thermal capacity increases significantly under cyclic loading, removing it as the limiting element.

As a result, only two governing regions remain in the joint circuit CTR curve:

- DBC-limited region: from –30 °C to approximately 30 °C AAT.
- OHL-limited region: from ~30 °C to 50 °C AAT, where the OHL becomes the dominant constraint on circuit capacity.

This highlights the benefit of CTR application for cable sections, their cyclic capacity is enhanced enough that they no longer control the overall circuit rating except at very low AAT, leaving the OHL as the principal thermal bottleneck over most practical operating temperatures during heatwaves.

However, according to TGN [14], when applying the CTR at the circuit level, the pre-fault rating of the OHL must be aligned with the CTR of the other components. The results presented earlier were based on the 1 PU DTR of the OHL, which represents the post-fault rating. To ensure consistency, the joint circuit CTR must therefore be recalculated using the pre-fault DTR of the OHL. The updated joint circuit CTR results are presented in Figure 7.13.

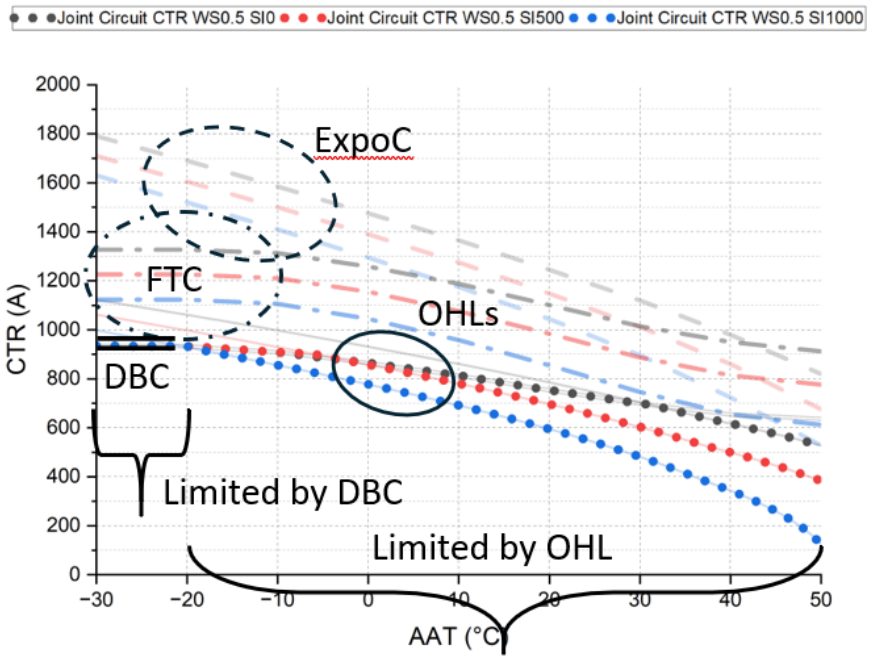

a) CTR, 0.5 m/s WS, limit at example of 1000 W/m^2.

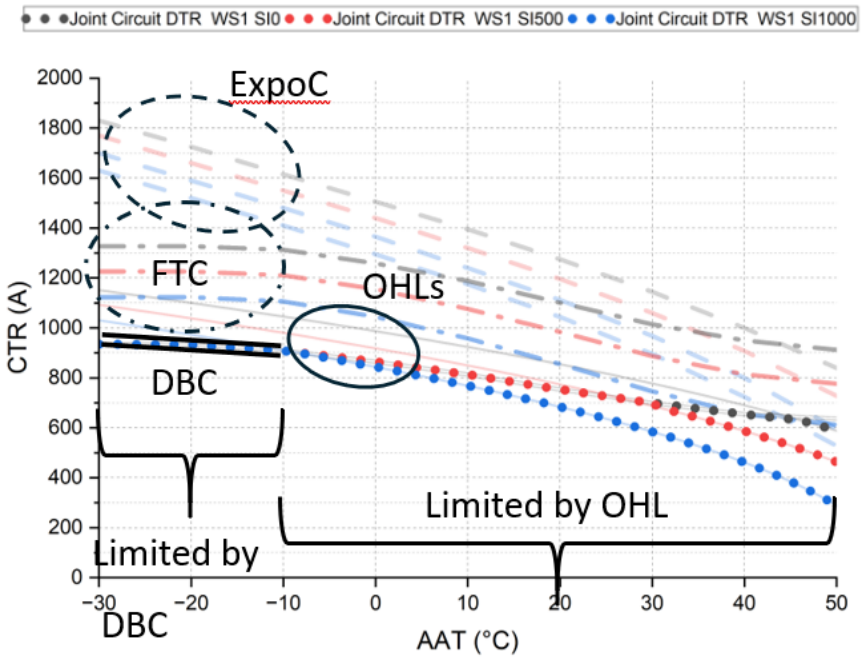

b) CTR, 1 m/s WS, limit at example of 1000 W/m^2

Figure 7.13 Variation of the joint circuit CTR using standard cyclic loading profile with the variation of AAT, SI under 0.5m/s WS (a) and 1m/s WS (b) for the example OHL and cable composite circuit when considering the 20% spare capacity of OHL during pre-fault condition.

Figure 7.13a and Figure 7.13b suggest that when considering a 20% margin that must be reserved for OHL, it is now becoming the limiting factor in most of the AAT operating region, especially under high SI, where the former ranges from –20 °C to 50 °C and the latter from –10 °C to 50 °C. This case further exacerbates the OHL as the main limiting factor for the circuit. Therefore, careful emphasis should be given to OHL when operating together with cables, not only due to its exposure to more extreme ambient conditions, but also the margin that has to be kept, and its fast thermal responses, which leave a lower CCC overall in terms of operating a cyclic load.

7.3.1.4 Summary

From the results presented, when cables of various constructions are joined with the OHL to form a single circuit, the DBC consistently emerges as the limiting component at lower AAT. This is primarily due to the higher thermal resistance associated with the 1 m burial depth, which restricts heat dissipation.

As AAT increases, the rate of increase in average soil temperature at 1 m depth (AST1m) becomes less pronounced. Under very high AAT conditions, approaching 50 °C, the OHL becomes the governing element of the circuit rating. The available OHL rating is further reduced by two key factors:

- The presence of SI, which accelerates conductor heating and causes the OHL to become limiting at lower AAT.
- The requirement to maintain a 20 % mandatory spare CCC under pre-fault conditions effectively reduces the pre-fault OHL loading capability.

When the cyclic loading profile is applied, the cable CCC increases due to thermal inertia, making the OHL the limiting factor at even lower AATs than under steady-state (DTR) conditions.

Introducing a higher, but realistic, wind speed (1 m/s) instead of the standard 0.5 m/s slightly increases the OHL CCC, shifting the point at which the OHL becomes limiting to a somewhat higher AAT. However, it should be noted that a 1 m/s wind speed is only representative of high-AAT, high-SI heatwave conditions (typically > 30 °C and peak 1000 W/m² SI). Results using 1 m/s wind speed at lower AAT or lower SI are

included here only for comparative and illustrative purposes and should not be applied as operational ratings outside of extreme weather scenarios.

7.3.2 Joint Circuit Thermal Ratings with Transformers (Substations)

The example joint circuit representing a typical substation layout is based on the Braintree substation, comprising an OHL–transformer–cable configuration. The OHL is identified as ACSR Quad-Zebra, operating with a 50°C temperature limit, and the transformer is a 400/132 kV, 240 MVA transformer.

The low-voltage (LV) side of the transformer at Braintree is not publicly specified. For the purpose of this assessment, it is assumed to be a single 138 kV, 2000 mm² cable. This cable is modelled as an ExpoC section connecting the transformer LV bushing and connector (Figure 6.1), transitioning into an FTC as suggested in [35], and finally terminating at the 132 kV busbar via a DBC. The installation configurations are assumed as follows: trefoil formation for DBC, flat spaced (non-touching) formation for FTC, and flat spaced formation for ExpoC.

Considering the 132 kV voltage level and the worst-case rated current of 1105 A on the transformer LV side, the selected cable must be capable of withstanding this load. Accordingly, a 138 kV, 2000 mm² cable with a continuous CCC of 1195 A in trefoil DBC (worst) configuration under S/NH STR ambient conditions has been selected for the LV side representation in this study.

Figure 7.14: Example of a transmission power transformer, with its LV side connected by cable, indicating parts of the cable are exposed to ambient air and solar irradiance [104].

Figure 7.14 shows a representation of the Braintree substation transformer with its LV side connected by power cables. The image illustrates the physical arrangement where the cable leaves the transformer bushing, with a portion of the cable exposed to air before transitioning into the ground. This exposed section is subject to direct SI and ambient air temperature effects, which must be considered when determining the cable's thermal rating and current-carrying capacity. It is assumed that the ExpoC is then connected to the FTC and then the DBC towards the LV side.

7.3.2.1 Joint Circuit Dynamic Thermal Ratings for Substation

Due to the presence of the power transformer, as present in section 4.2.2, the joint circuit DTR for the substation is calculated in power instead of current due to the OLTC as discussed in section 4.2.2. The joint circuit rating will be shown in two different scenarios: post-fault and pre-fault, due to both OHL and transformer having distinctive differences in rating between post-fault and pre-fault situations. While the cable pre-fault and post-fault ratings are considered the same [3], [8], [11], [14].

7.3.2.1.1 Joint Circuit Pre-Fault Dynamic Thermal Rating of Substation

Figure 7.15a&b presents the joint circuit DTR of the OHL–transformer–cable circuit at Braintree substation under pre-fault loading conditions, using Tap 11 of the 400/132 kV, 240 MVA transformer. Figure 7.15a shows the full AAT range (-30 °C to 50 °C), while Figure 7.15b provides a detailed view highlighting the limiting components.

In this joint circuit representation, the OHL ratings are shown as dashed lines, with colour indicating SI exposure: black for SI = 0 W/m², red for SI = 500 W/m², and blue for SI = 1000 W/m². The exposed cable (ExpoC) sections on the transformer LV side are shown as dotted lines, again with colour representing SI exposure. The FTC sections are shown as dash-dotted lines, and the DBC rating, unaffected by solar irradiance, is shown as a thick double black line.

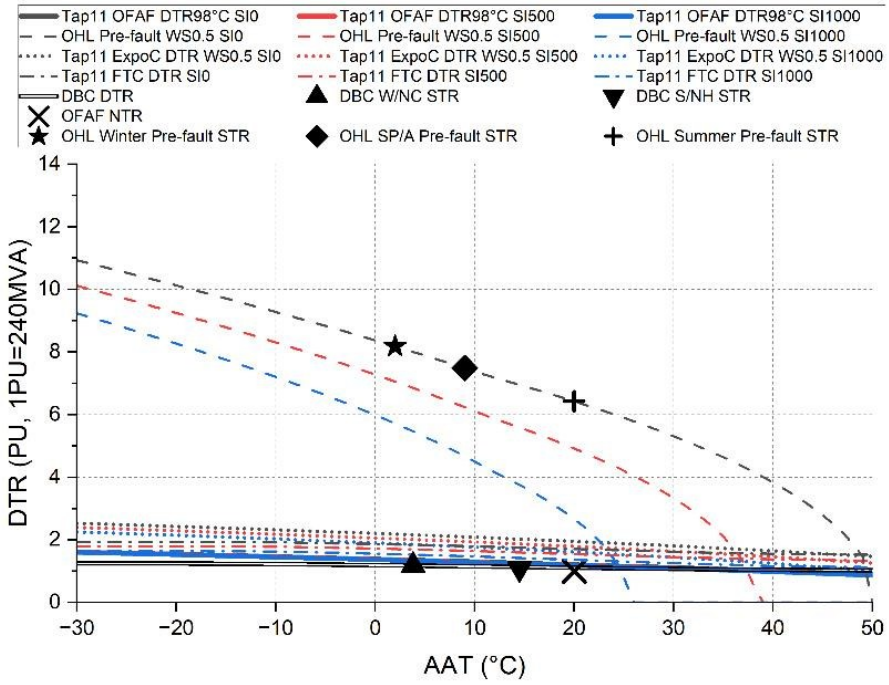

a) Joint circuit ratings full view

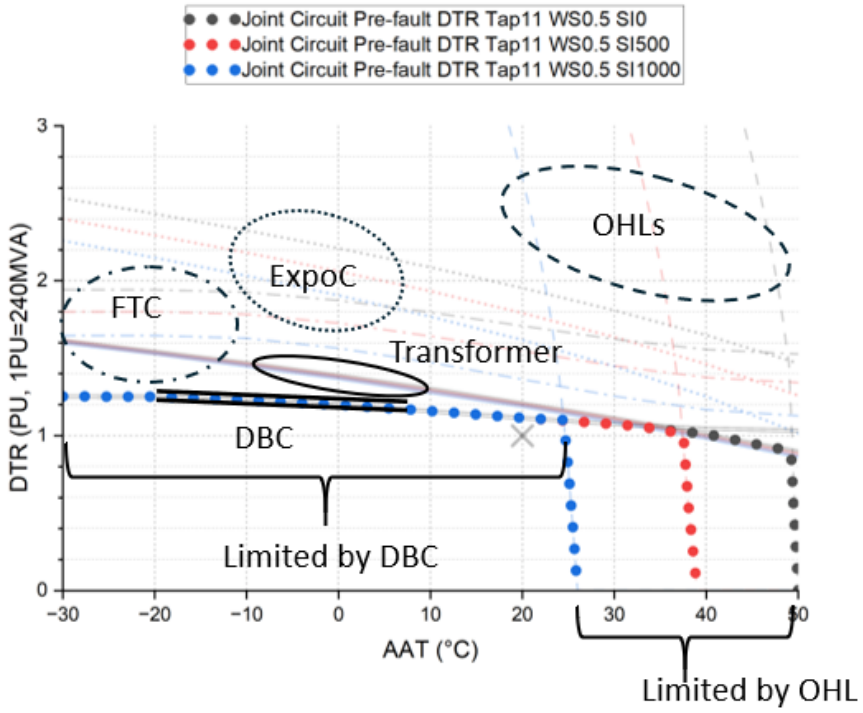

b) Joint circuit ratings detailed view, using 1000 W/m^2 as an example

Figure 7.15: Joint Circuit DTR of substation under pre-fault condition, tap position 11, 0.5m/s WS, full view (a) and detailed (b).

The detailed view (Figure 7.15b) clearly illustrates which component constrains the overall circuit rating at various AAT. Under the worst condition (SI = 1000 W/m², blue line), the joint circuit is initially limited by the DBC rating for AAT between -30 °C and approximately 25 °C. Above this temperature, the circuit becomes OHL-limited, as the Quad-Zebra conductor reaches its 50 °C operating limit. This leaves no additional headroom for circuit loadability, effectively capping the pre-fault loading capability at higher AATs.

A similar trend is observed for the normal UK SI case (500 W/m², red dotted line), with the OHL becoming the limiting component at AAT just below 40 °C. This observation raises a practical concern: at extreme weather events such as the 2022 UK heatwave, where AAT exceeded 40 °C for several hours in London, the OHL would theoretically be fully loaded with no margin available for pre-fault loading. Under such circumstances, network operators would need to consider emergency loading allowances or alternative operational strategies, since completely unloading the circuit for 3–4 hours would not be realistic.

It is also worth noting that despite being a Quad-Zebra line with significant thermal capacity (approximately ten times the capacity of the transformer and LV cable combined), the OHL still becomes the constraining element under extreme ambient and solar conditions, primarily due to the imposed 50 °C temperature limit. The transformer starts to become a limiting factor from 30°C onwards for all SI conditions, but is limited to a sudden drop of OHL as seen in Figure 7.15a.

Comparison of joint circuit DTR for WS = 0.5 m/s and WS = 1 m/s can be highlighted using Figure 7.16. The focus here is on the dotted blue and red lines, which represent the limiting exposed cable (ExpoC) sections under SI = 1000 W/m² and SI = 500 W/m², respectively.

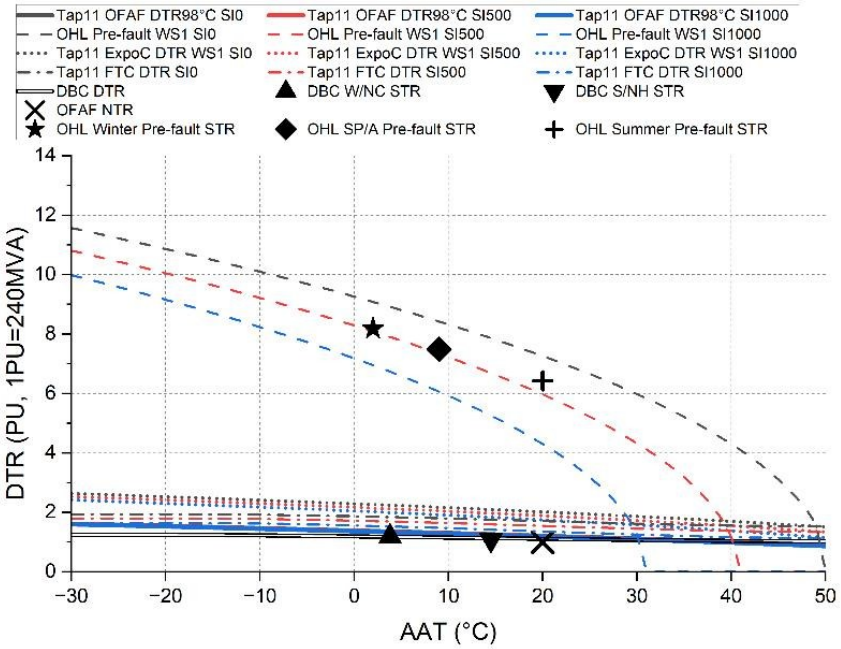

a) Joint circuit ratings full view

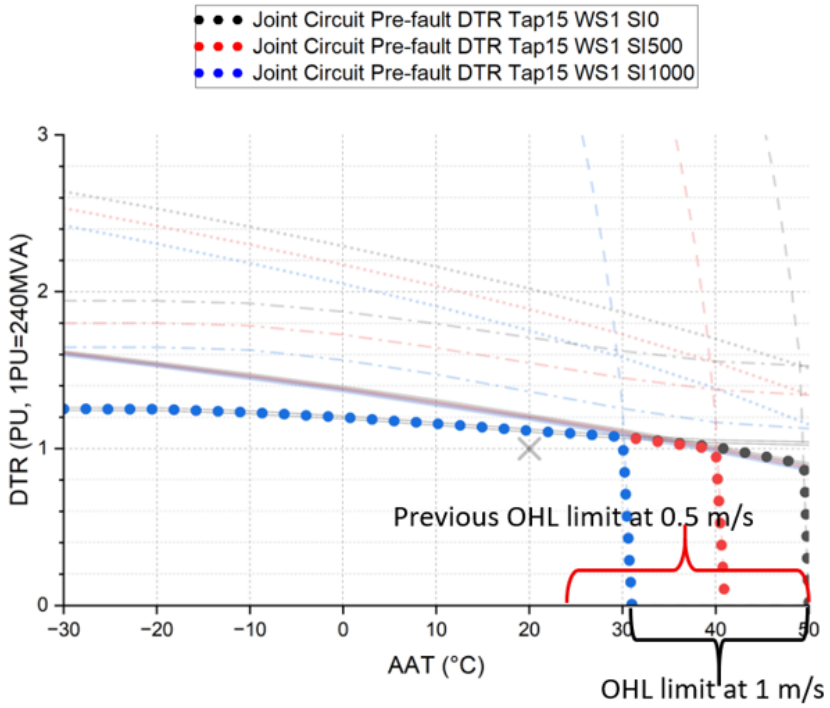

b) Joint circuit ratings detailed view, using $1000 W/m^2$ as an example

Figure 7.16: Joint DTR of substation under pre-fault condition, tap position 11, 1m/s WS, full view and detailed.

At WS = 0.5 m/s from Figure 7.15, the blue dotted curve (SI = 1000 W/m²) shows that the circuit becomes OHL-limited at around 25 °C AAT, leaving no further margin for circuit loadability. This is because the Quad-Zebra OHL reaches its 50 °C temperature limit under these low wind and high solar conditions. When the wind speed increases to WS = 1 m/s, as seen in Figure 7.16, the OHL temperature rise is reduced, effectively shifting the OHL-limited point to the right. For SI = 1000 W/m², the limiting AAT increases to around 30 °C before the OHL reaches its thermal limit. Similarly, for SI = 500 W/m² (red dotted line), the limiting point moves from just below 40 °C to around 42 °C. This improvement indicates that a moderate increase in wind speed enhances circuit loadability, allowing the OHL to carry higher current before reaching its thermal limit.

Overall, the comparison highlights that assuming WS = 0.5 m/s is conservative, and using WS = 1 m/s better reflects realistic operating conditions, particularly during high ambient and high solar loading scenarios. This adjustment could reduce unnecessary curtailment of circuit capacity during hot weather. Additionally, operating the conductor at the 50 °C limit would be problematic in the future, especially during heatwaves.

Figure 7.17 shows the joint circuit pre-fault DTR of the OHL–transformer–cable circuit at Tap 15. Compared to Tap 11 (nominal tap), the overall circuit rating is slightly reduced across the entire AAT range due to higher joule losses from the tap, caused by increased current on the LV side for the same MVA transfer.

At Tap 15, the circuit remains cable-limited (primarily DBC and OHL under high SI) up to roughly 25 °C AAT for the SI = 1000 W/m² case (blue dotted line), similar to Tap 11. However, the crossover points where the OHL becomes limiting now occur slightly earlier, which marginally lowers the maximum available pre-fault loading at higher AATs. The difference is subtle but visible in the detailed plot: the blue and red dotted curves (SI = 1000 W/m² and SI = 500 W/m²) intersect the OHL limit at a slightly lower DTR compared with Tap 11.

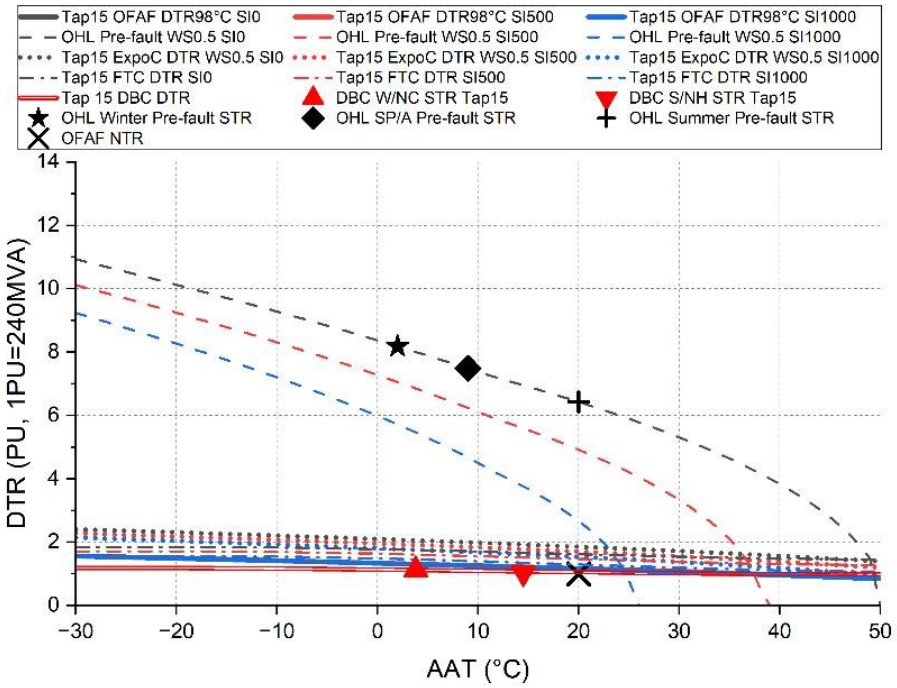

a) Joint circuit ratings full view

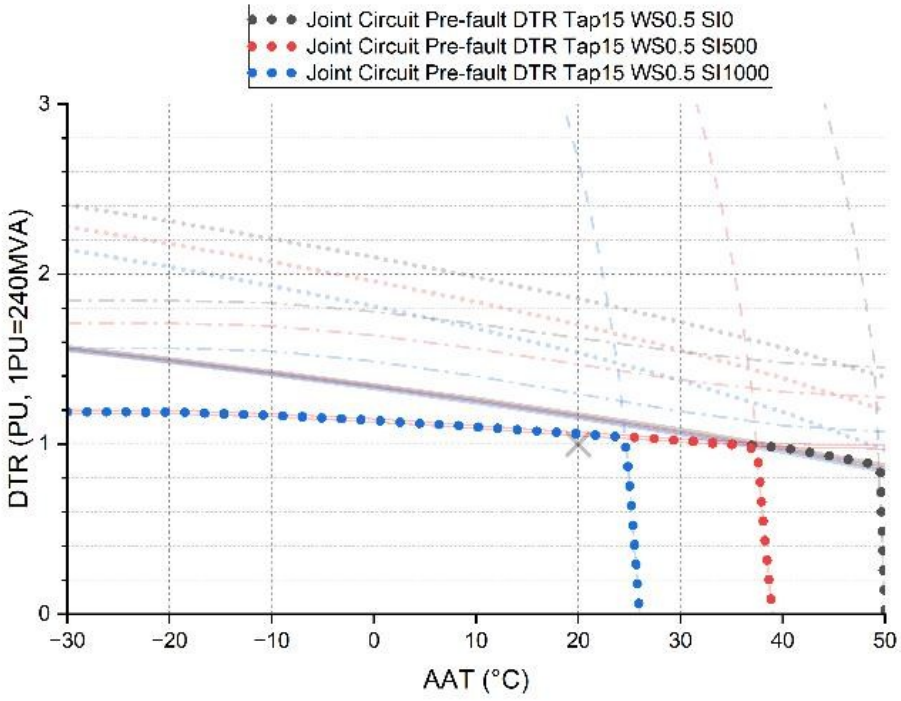

b) Joint circuit ratings detailed view

Figure 7.17: Joint circuit DTR of substation under pre-fault condition, tap position 15, 0.5m/s WS, full view and detailed.

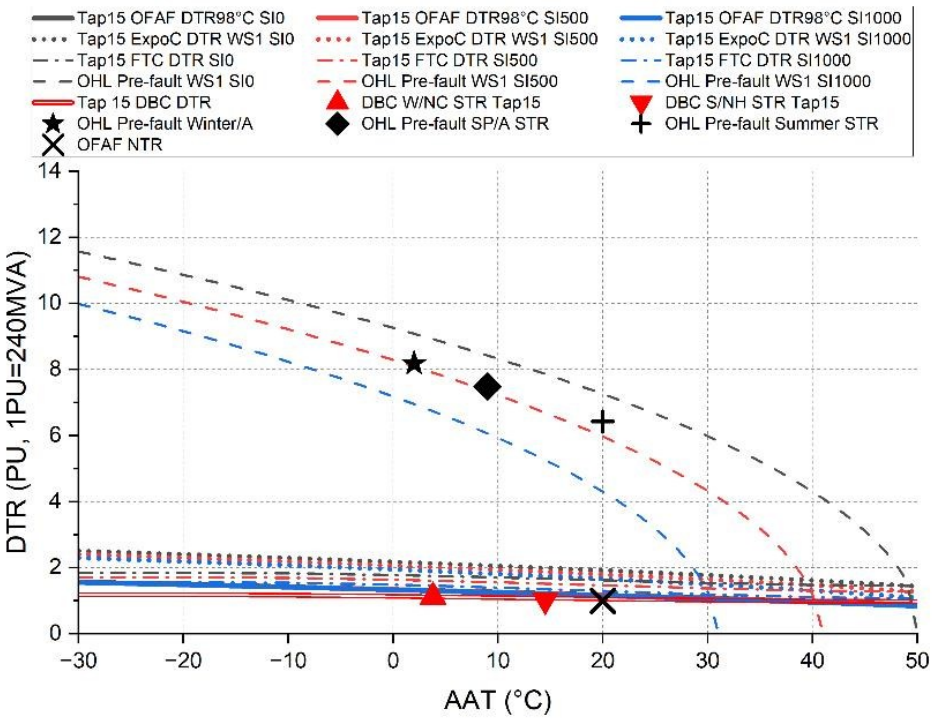

a) Joint circuit ratings full view

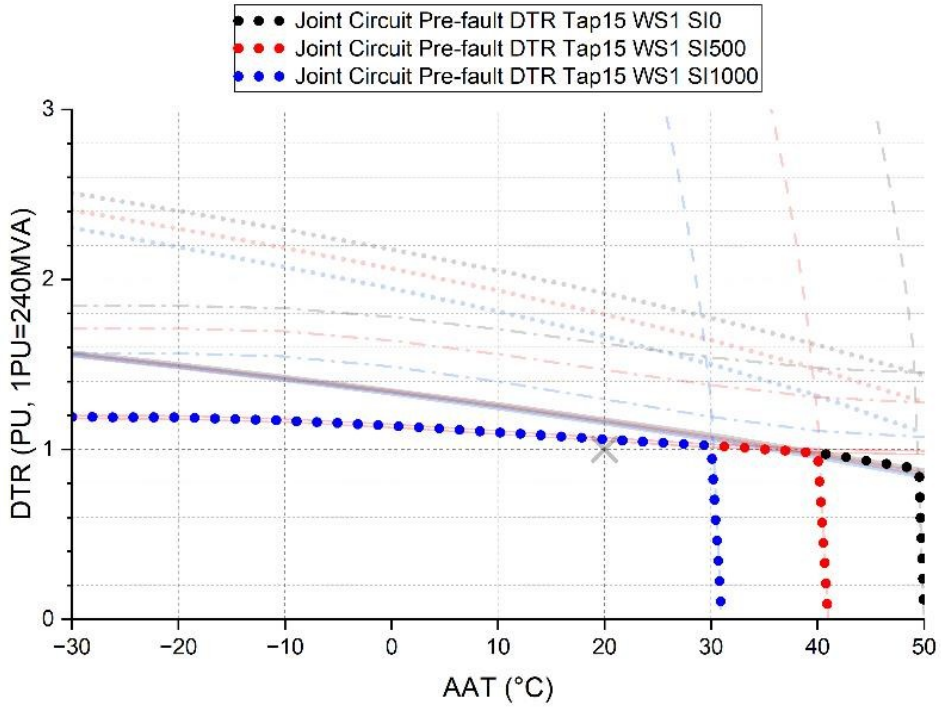

b) Joint circuit ratings detailed view

Figure 7.18: Joint circuit DTR of substation under pre-fault condition, tap position 15, 1m/s WS, full view and detailed.

In summary, moving to Tap 15 slightly reduces circuit capacity under hot, high-SI conditions. Although the general limiting sequence remains unchanged, the available margin above STR is reduced, leaving less headroom for overload at high ambient temperatures. This should be considered when operating the transformer at lower tap positions or when setting a conservative circuit limit.

Figure 7.18 present the joint circuit pre-fault DTR of the circuit at Tap 15 with a higher wind speed assumption of 1 m/s. At WS = 1 m/s, moving from Tap 11 (nominal) to Tap 15 trims the joint circuit pre-fault DTR slightly across the AAT range. At 20 °C, the Tap 15 curve sits about 2–3% lower than Tap 11, and the crossover to the OHL limit occurs a little earlier. For SI = 1000 W/m², the limiting point shifts from roughly ≈31 °C (Tap 11) to ≈30 °C (Tap 15). For SI = 500 W/m², it shifts from just over ≈41 °C to about ≈39–40 °C. The slope with AAT is essentially unchanged, so the effect of the tap change is a near-uniform downward offset. In short, Tap 15 provides slightly less headroom because the LV current is higher for the same MVA, pushing the LV cable sections closer to their limits and bringing the OHL limiting point forward by around 1–2 °C under high-SI conditions.

7.3.2.1.2 Joint Circuit Post-Fault Dynamic Thermal Rating of Substation

Under post-fault conditions, the OHL is restricted to operate at its 1 PU continuous rating, ensuring it is not thermally overstressed following a fault. The power transformer, however, is permitted to operate up to its emergency HST limit, with the corresponding emergency continuous rating derived from this limit as described in Section 4.2.2.

When comparing with the pre-fault case, several key observations can be made, as shown in Figure 7.19 and Figure 7.20:

- Higher transformer contribution: Because the transformer is allowed to use its emergency continuous rating, its thermal limit no longer constrains the joint circuit rating. This shifts the bottleneck to the cable sections and, at higher AAT, to the OHL.

- Slightly higher joint circuit rating: The overall DTR curve sits slightly above the pre-fault DTR curve across the AAT range, providing additional capacity margin during post-fault operation.
- Unchanged OHL limit at high AAT: The joint circuit rating still converges to the OHL limit (1 PU) at approximately the same temperature as in the pre-fault case for both 0.5 m/s and 1 m/s WS, because the OHL temperature limit remains unchanged.
- Improved resilience at low-to-medium AAT: The difference between pre-fault and post-fault ratings is most noticeable for AAT between -30 °C and 20 °C, where the emergency transformer rating allows higher loading to be carried through post-fault without exceeding temperature limits.

Overall, the post-fault DTR demonstrates increased loading limit thanks to the use of emergency transformer ratings, while still respecting the OHL continuous rating and cable thermal limit. By comparing Figure 7.19 and Figure 7.20, the OHL post-fault DTR is increased, similar to previous observations, due to higher wind cooling.

At WS = 0.5 m/s, Tap 15 shows a slightly lower joint circuit post-fault DTR across the entire AAT range compared with Tap 11 in Figure 7.21. The reduction is most noticeable in the cable-limited region (below ≈ 25 °C for SI = 1000 W/m²), where the blue dotted curve for Tap 15 lies consistently below that of Tap 11. The crossover to OHL-limited operation occurs marginally earlier for Tap 15, approximately 1–2 °C lower AAT, meaning the available headroom before reaching the OHL's 1 PU limit is slightly reduced.

At WS = 1 m/s and Tap 15 in Figure 7.22, the same trend is observed but with less operational impact. The increase in wind speed raises the thermal margin of the OHL, shifting the OHL-limited point to a higher AAT for both tap positions. Under these conditions, the difference between Tap 11 and Tap 15 becomes small but still visible: Tap 15 curves remain slightly lower, reflecting the reduced LV voltage and therefore slightly lower cable heating.

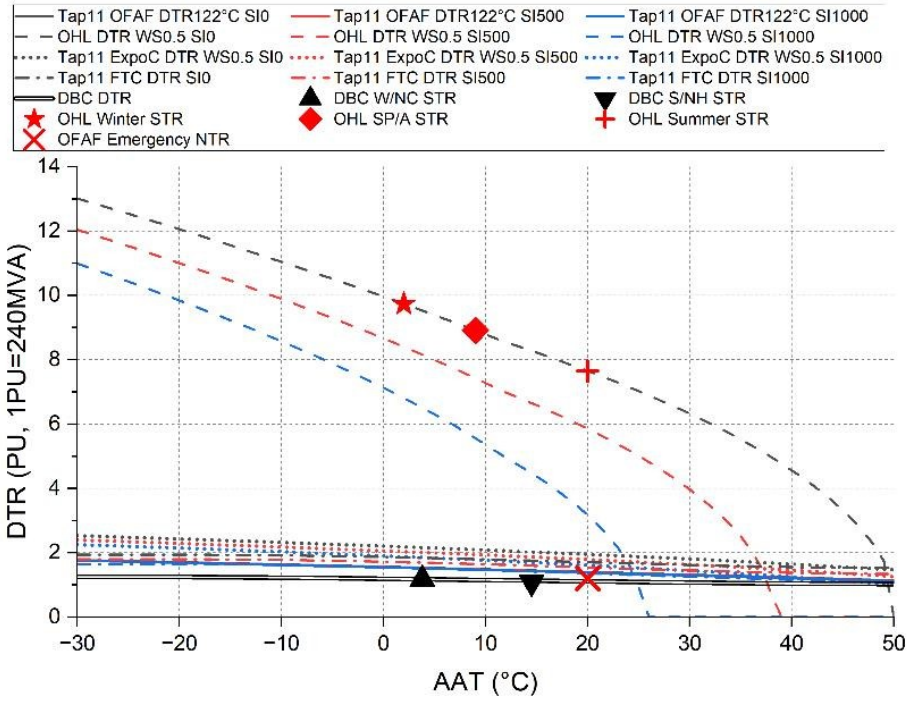

a) Joint circuit ratings, full view

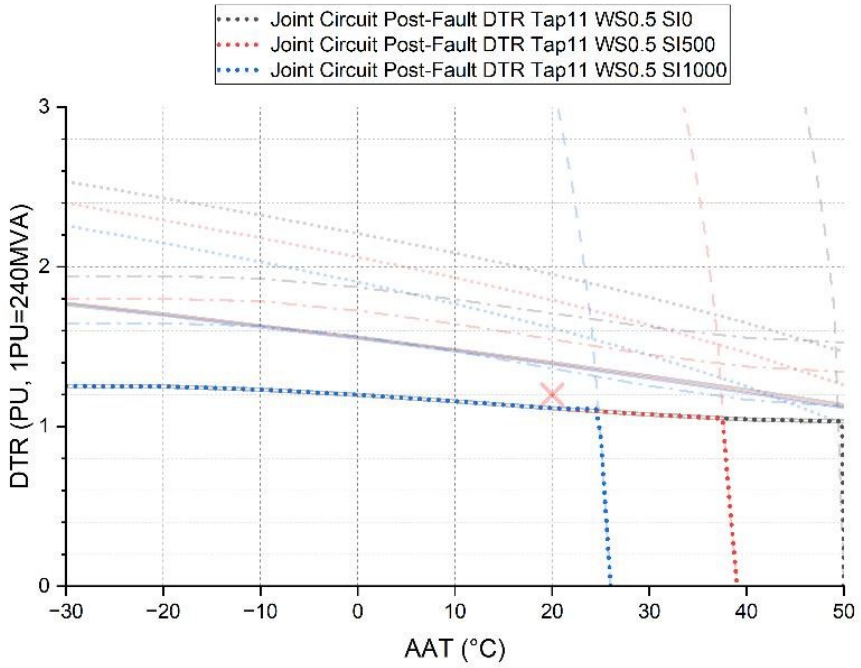

b) Joint circuit ratings, detailed view

Figure 7.19: Joint circuit DTR of substation under post-fault condition, tap position 11, 0.5m/s WS, full view and detailed.

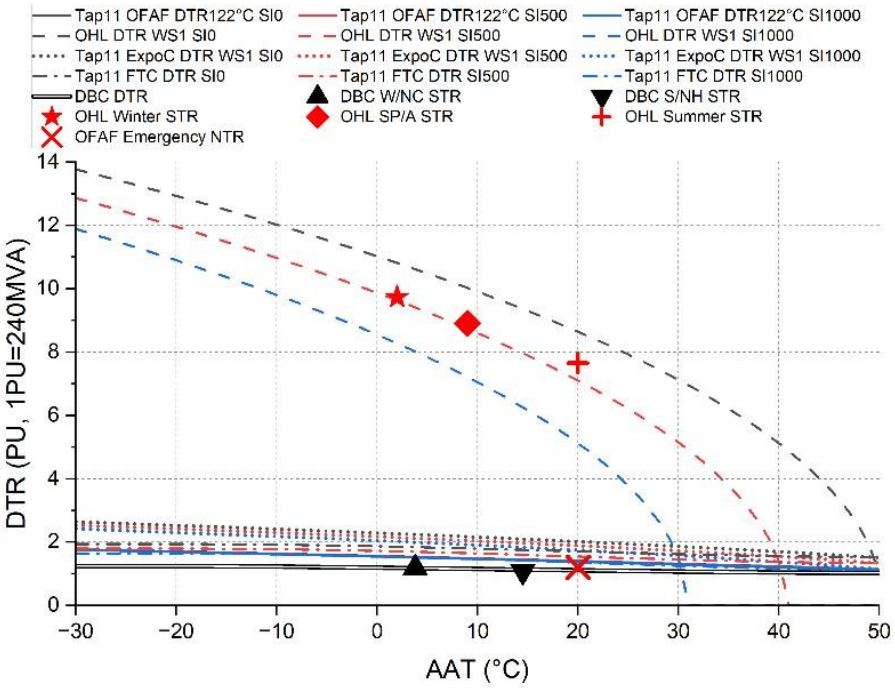

a) Joint circuit ratings full view

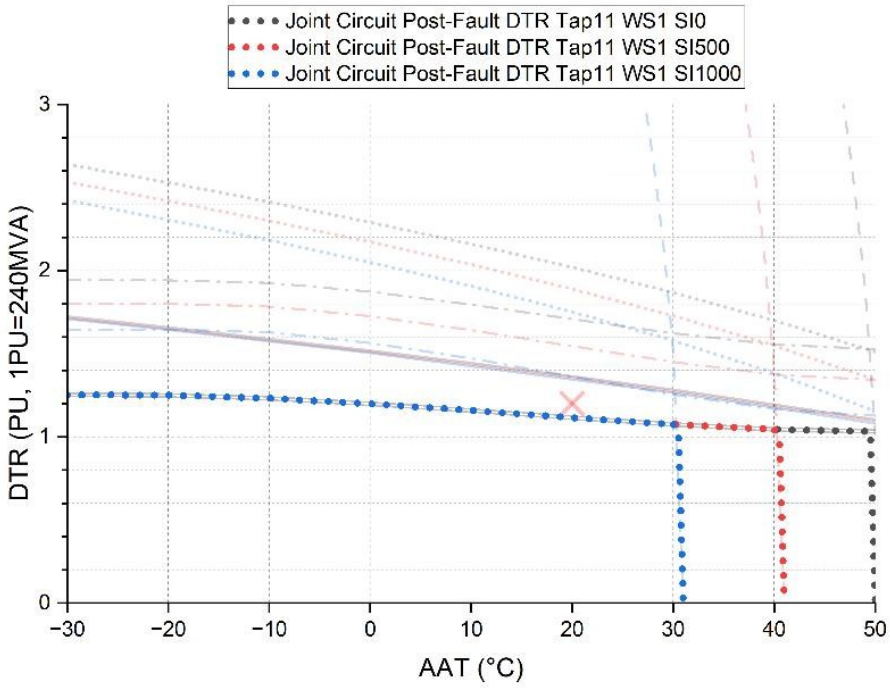

b) Joint circuit ratings detailed view

Figure 7.20: Joint circuit DTR of substation under post-fault condition, tap position 11, 1m/s WS, full view and detailed.

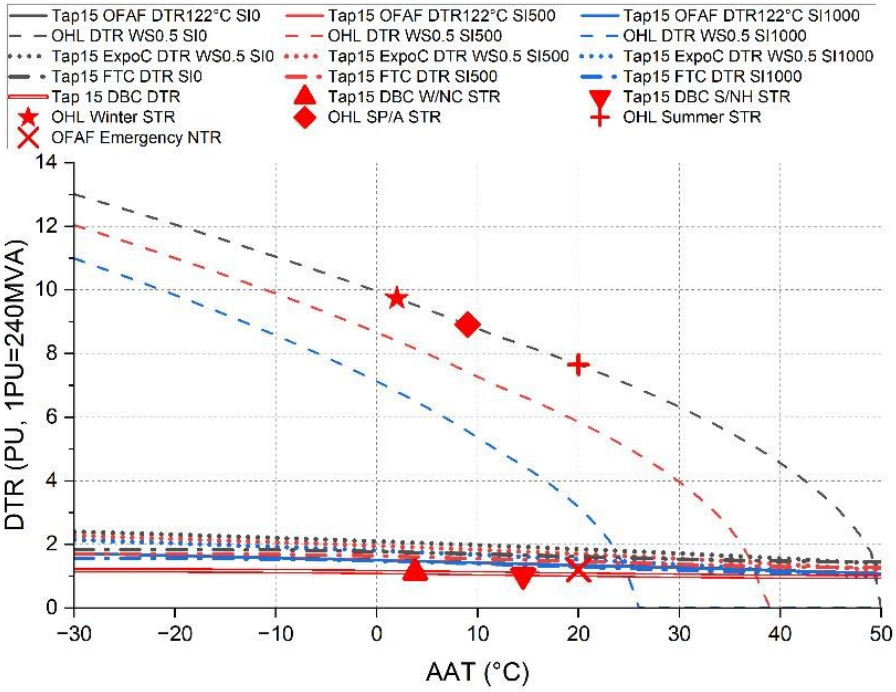

a) Joint circuit ratings, full view

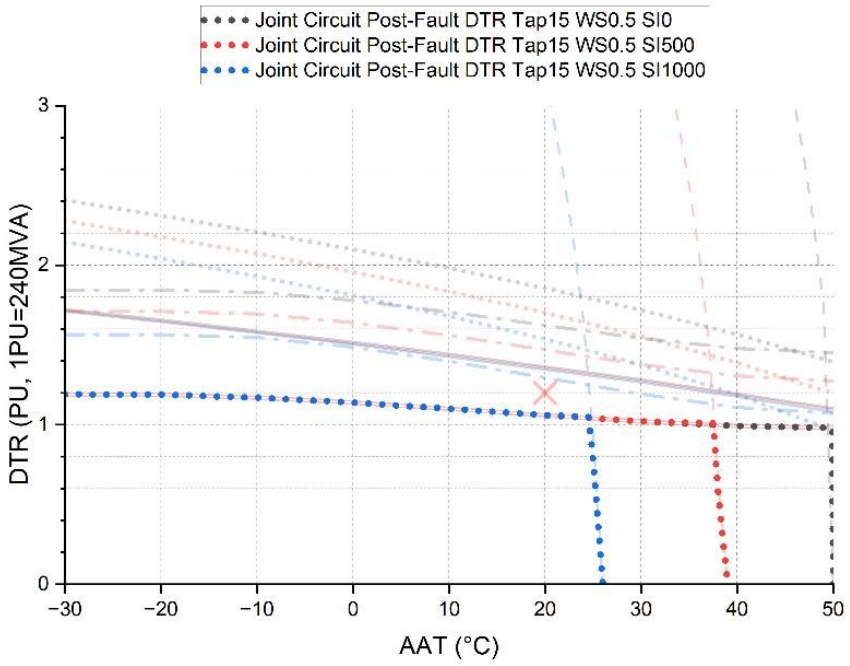

b) Joint circuit ratings detailed view

Figure 7.21: Joint circuit DTR of substation under post-fault condition, tap position 15, 0.5m/s WS, full view and detailed.

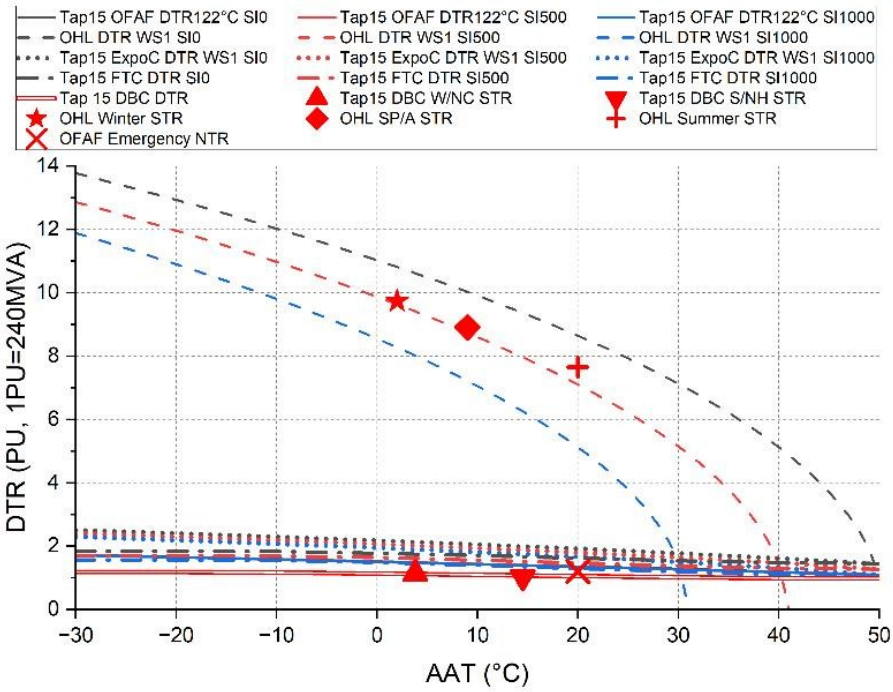

a) Joint circuit ratings, full view

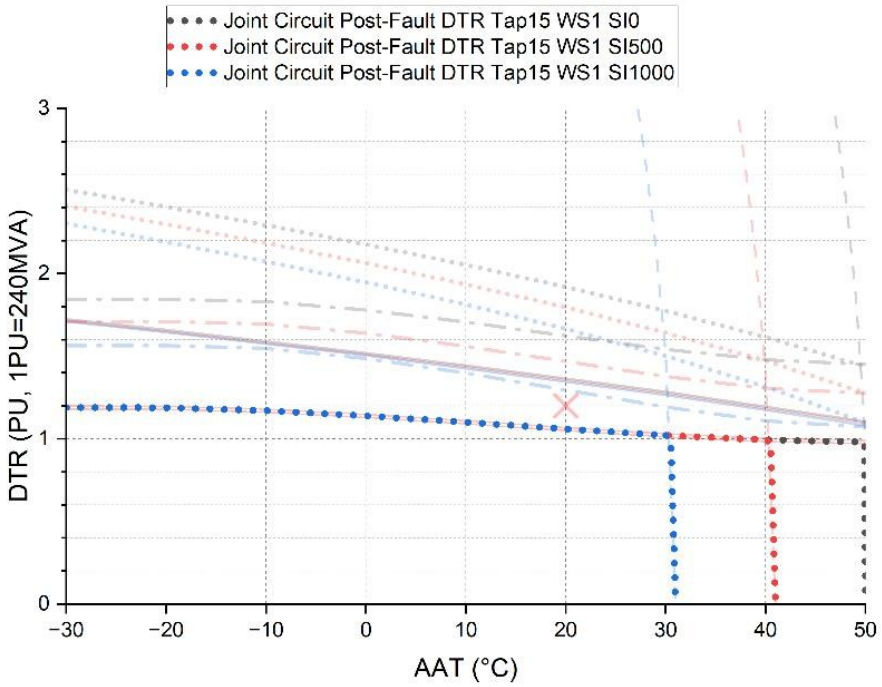

b) Joint circuit ratings, detailed view

Figure 7.22: Joint circuit DTR of substation under post-fault condition, tap position 15, 1m/s WS, full view and detailed.

Overall, tap position mainly introduces a near-uniform downward offset in DTR, with Tap 15 offering a slightly lower loading limit than Tap 11 under both wind speed scenarios. The effect is more relevant at lower wind speeds and high solar loading, where the margin to the OHL limit is already tight.

7.3.2.2 Joint Circuit Short-Term and Medium-Term Overloading Ratings of Substation Circuit

With the joint circuit pre-fault DTR of the substation circuit established, the S/MTOR are evaluated for selected pre-fault loading ratios of 0.85 PU, 0.75 PU, and 0.65 PU Because the circuit includes a power transformer, all S/MTOR values are expressed in PU, where 1 PU corresponds to 240 MVA at 400 kV on the transformer HV side. The HV side is also the primary side of the transformer, where the OLTC cannot influence the voltage.

On the LV side, 1 PU likewise corresponds to 240 MVA but at 132 kV. When the HV side is supplied at rated voltage, the OLTC can adjust the LV side voltage away from its nominal value for any tap position other than Tap 11. Importantly, the 1 PU base for S/MTOR calculations remains 240 MVA at 132 kV regardless of tap position, but the actual LV voltage must be determined from the applied HV voltage and the turn ratio of the selected tap.

The 100% pre-fault rating of the joint circuit is the same for OHL and cables as described above, but the 100% pre-fault rating for the transformer is based on the pre-fault DTR (DTR 98°C) of the transformer. The transformer post-fault rating is achieved by increasing the temperature limit from the maximum continuous limit (e.g., 98°C) to the maximum emergency limit (e.g., 122°C). Hence, the 100% pre-fault rating of the joint circuit has to be based on the pre-fault rating of the transformer. As a conclusion, the 100% pre-fault rating of the joint circuit is chosen from the minimum value of the post-fault rating of OHLs and cables, and the pre-fault rating of transformers.

Because the OHL section (ACSR Quad-Zebra) retains a non-zero CCC at its 50 °C temperature limit, the S/MTOR calculations are performed at 49.5 °C AAT. At exactly 50 °C AAT, results would default to zero. The CCC of Quad-Zebra at 49.5 °C AAT, 0.5 m/s wind speed, and no solar irradiance is 494.5 A, equivalent to 342.6 MVA

(1.43 PU) at 400 kV. This is sufficiently high that the OHL does not act as the limiting component in the S/MTOR calculations. The calculated S/MTOR values for the substation joint circuit, as a function of AAT, are presented in Table 7.5 and Table 7.6.

All S/MTOR results indicate that the OFAF-cooled transformer is the limiting component during post-fault short-term and medium-term overloading. The only exception occurs at 50 °C AAT, where the OHL cannot accept additional loading because it has already reached its temperature limit. To avoid this zero-capacity result and correctly identify the limiting element, calculations are instead performed at 49.5 °C AAT, which confirms that the transformer remains the governing constraint.

Table 7.6 below describes the results for Tap Position 15, which shows a general reduction in the joint circuit S/MTOR of the substation circuit. This outcome is expected, as the thermal performance at Tap 15 is inferior to that at Tap 11. Similar findings were presented in Section 4.2.4, confirming that the decrease in S/MTOR at Tap 15 is consistent with the higher current demand and reduced thermal margin associated with this tap setting.

7.3.2.3 Joint Circuit Cyclic Thermal Ratings of Substation

The results of joint circuit CTR of the substation at tap positions 11 and 15, with the variation of AAT, WS and SI, are shown in Figure 7.23 to Figure 7.26. The WS considered are the same as previous analyses, divided into 0.5m/s and 1m/s conditions. The SI considered are $500W/m^2$ and $1000W/m^2$ representing the medium and high SI conditions.

Also, as required by TGN [14], when using CTR in a joint circuit with the presence of OHL, the pre-fault rating of OHL must match the CTR of other components. So, the maximum pre-fault ratings of OHL are used in the assessment for the joint circuit CTR of the substation circuit to meet this requirement.

Table 7.5: Joint Circuit Short-Term and Medium-Term Overloading Ratings of Substation, 0.5m/s WS, 0 SI and Tap Position 11.

AAT (°C)		-30	-20	-10	0	10	20	30	40	49.5(50)
AST 0.3m (°C)		-0.5	-0.5	0.8	5.3	11.4	18.2	24.4	29.0	31.0
AST 1m (°C)		2.09	2.31	4.62	8.38	12.93	17.62	21.81	24.84	26.06
Pre-fault DTR (PU) /Limited by		1.253 /DBC	1.251 /DBC	1.232 /DBC	1.199 /DBC	1.159 /DBC	1.115 /DBC	1.075 /DBC	1.010 /OFAF	0.900 /OFAF
Post-fault DTR (PU)		1.253 /DBC	1.251 /DBC	1.232 /DBC	1.199 /DBC	1.159 /DBC	1.115 /DBC	1.075 /DBC	1.045 /DBC	1.033 /DBC
Pre-load%	**Duration (min)**	Pre-Fault Joint Circuit DTR S/MTOR in PU (1PU=240MVA at 400/132kV rated voltage at HV/LV side), 0.5m/s WS and 0 SI, Tap Position 11								
100% corresponds to		1.253 /DBC	1.251 /DBC	1.232 /DBC	1.199 /DBC	1.159 /DBC	1.115 /DBC	1.075 /DBC	1.010 /OFAF	0.900 /OFAF
-	**inf**	1.253 /DBC	1.251 /DBC	1.232 /DBC	1.199 /DBC	1.159 /DBC	1.115 /DBC	1.075 /DBC	1.045 /DBC	1.033 /DBC
85%	**360**	1.586 /DBC	1.585 /DBC	1.555 /DBC	1.514 /DBC	1.454 /DBC	1.392 /DBC	1.325 /OFAF	1.240 /OFAF	1.150 /OFAF
	60	1.945 /OFAF	1.885 /OFAF	1.810 /OFAF	1.730 /OFAF	1.655 /OFAF	1.570 /OFAF	1.475 /OFAF	1.380 /OFAF	1.300 /OFAF
	20	2.085 /OFAF	2.025 /OFAF	1.960 /OFAF	1.890 /OFAF	1.805 /OFAF	1.720 /OFAF	1.615 /OFAF	1.520 /OFAF	1.450 /OFAF
	10	2.125 /OFAF	2.085 /OFAF	2.020 /OFAF	1.960 /OFAF	1.875 /OFAF	1.790 /OFAF	1.695 /OFAF	1.590 /OFAF	1.520 /OFAF
	5	2.165 /OFAF	2.135 /OFAF	2.080 /OFAF	2.020 /OFAF	1.945 /OFAF	1.860 /OFAF	1.755 /OFAF	1.660 /OFAF	1.590 /OFAF
	3	2.265 /OFAF	2.215 /OFAF	2.160 /OFAF	2.090 /OFAF	2.015 /OFAF	1.920 /OFAF	1.815 /OFAF	1.720 /OFAF	1.650 /OFAF
75%	**360**	1.729 /DBC	1.705 /OFAF	1.640 /OFAF	1.570 /OFAF	1.485 /OFAF	1.410 /OFAF	1.325 /OFAF	1.240 /OFAF	1.150 /OFAF
	60	1.965 /OFAF	1.905 /OFAF	1.830 /OFAF	1.760 /OFAF	1.675 /OFAF	1.590 /OFAF	1.505 /OFAF	1.410 /OFAF	1.330 /OFAF
	20	2.105 /OFAF	2.055 /OFAF	2.000 /OFAF	1.930 /OFAF	1.845 /OFAF	1.760 /OFAF	1.665 /OFAF	1.570 /OFAF	1.490 /OFAF
	10	2.135 /OFAF	2.105 /OFAF	2.060 /OFAF	2.000 /OFAF	1.925 /OFAF	1.850 /OFAF	1.755 /OFAF	1.650 /OFAF	1.580 /OFAF
	5	2.175 /OFAF	2.155 /OFAF	2.120 /OFAF	2.070 /OFAF	1.995 /OFAF	1.920 /OFAF	1.825 /OFAF	1.730 /OFAF	1.660 /OFAF
	3	2.275 /OFAF	2.255 /OFAF	2.200 /OFAF	2.150 /OFAF	2.085 /OFAF	2.000 /OFAF	1.895 /OFAF	1.800 /OFAF	1.720 /OFAF
65%	**360**	1.775 /OFAF	1.715 /OFAF	1.640 /OFAF	1.570 /OFAF	1.495 /OFAF	1.410 /OFAF	1.325 /OFAF	1.240 /OFAF	1.150 /OFAF
	60	1.985 /OFAF	1.925 /OFAF	1.850 /OFAF	1.780 /OFAF	1.705 /OFAF	1.620 /OFAF	1.525 /OFAF	1.430 /OFAF	1.350 /OFAF
	20	2.125 /OFAF	2.075 /OFAF	2.020 /OFAF	1.960 /OFAF	1.885 /OFAF	1.810 /OFAF	1.715 /OFAF	1.620 /OFAF	1.530 /OFAF
	10	2.145 /OFAF	2.125 /OFAF	2.090 /OFAF	2.040 /OFAF	1.975 /OFAF	1.890 /OFAF	1.805 /OFAF	1.710 /OFAF	1.630 /OFAF
	5	2.175 /OFAF	2.175 /OFAF	2.140 /OFAF	2.100 /OFAF	2.045 /OFAF	1.970 /OFAF	1.885 /OFAF	1.790 /OFAF	1.710 /OFAF
	3	2.305 /OFAF	2.275 /OFAF	2.250 /OFAF	2.190 /OFAF	2.125 /OFAF	2.050 /OFAF	1.955 /OFAF	1.860 /OFAF	1.780 /OFAF

Table 7.6: Joint Circuit Short-Term and Medium-Term Overloading Ratings of Substation, 0.5m/s WS, 0 SI and Tap Position 15.

AAT (°C)		-30	-20	-10	0	10	20	30	40	49.5(50)
AST 0.3m (°C)		-0.5	-0.5	0.8	5.3	11.4	18.2	24.4	29.0	31.0
AST 1m (°C)		2.09	2.31	4.62	8.38	12.93	17.62	21.81	24.84	26.06
Pre-fault DTR (A) /Limited by		1.253 /DBC	1.251 /DBC	1.232 /DBC	1.199 /DBC	1.159 /DBC	1.115 /DBC	1.075 /DBC	0.980 /OFAF	0.875 /OFAF
Post-fault DTR		1.253 /DBC	1.251 /DBC	1.232 /DBC	1.199 /DBC	1.159 /DBC	1.115 /DBC	1.075 /DBC	1.045 /DBC	1.033 /DBC
Pre-load%	**Duration (min)**	Pre-Fault Joint Circuit DTR S/MTOR in PU (1PU=240MVA at 400/132kV rated voltage at HV/LV side), 0.5m/s WS and 0 SI, Tap Position 15								
100% corresponds to		1.253 /DBC	1.251 /DBC	1.232 /DBC	1.199 /DBC	1.159 /DBC	1.115 /DBC	1.075 /DBC	0.980 /OFAF	0.875 /OFAF
-	**inf**	1.253 /DBC	1.251 /DBC	1.232 /DBC	1.199 /DBC	1.159 /DBC	1.115 /DBC	1.075 /DBC	1.045 /DBC	1.033 /DBC
85%	**360**	1.507 /DBC	1.505 /DBC	1.478 /DBC	1.438 /DBC	1.381 /DBC	1.322 /DBC	1.275 /DBC	1.200 /OFAF	1.120 /OFAF
	60	1.895 /OFAF	1.835 /OFAF	1.760 /OFAF	1.690 /OFAF	1.605 /OFAF	1.530 /OFAF	1.435 /OFAF	1.340 /OFAF	1.260 /OFAF
	20	2.025 /OFAF	1.975 /OFAF	1.910 /OFAF	1.840 /OFAF	1.765 /OFAF	1.680 /OFAF	1.575 /OFAF	1.470 /OFAF	1.400 /OFAF
	10	2.065 /OFAF	2.025 /OFAF	1.970 /OFAF	1.910 /OFAF	1.835 /OFAF	1.750 /OFAF	1.655 /OFAF	1.550 /OFAF	1.480 /OFAF
	5	2.105 /OFAF	2.075 /OFAF	2.030 /OFAF	1.970 /OFAF	1.905 /OFAF	1.820 /OFAF	1.725 /OFAF	1.610 /OFAF	1.550 /OFAF
	3	2.205 /OFAF	2.155 /OFAF	2.110 /OFAF	2.040 /OFAF	1.965 /OFAF	1.880 /OFAF	1.785 /OFAF	1.670 /OFAF	1.600 /OFAF
75%	**360**	1.643 /DBC	1.641 /DBC	1.590 /OFAF	1.520 /OFAF	1.445 /OFAF	1.370 /OFAF	1.285 /OFAF	1.200 /OFAF	1.120 /OFAF
	60	1.915 /OFAF	1.855 /OFAF	1.780 /OFAF	1.710 /OFAF	1.635 /OFAF	1.550 /OFAF	1.465 /OFAF	1.370 /OFAF	1.290 /OFAF
	20	2.045 /OFAF	1.995 /OFAF	1.940 /OFAF	1.880 /OFAF	1.805 /OFAF	1.720 /OFAF	1.625 /OFAF	1.530 /OFAF	1.450 /OFAF
	10	2.075 /OFAF	2.055 /OFAF	2.010 /OFAF	1.950 /OFAF	1.875 /OFAF	1.800 /OFAF	1.705 /OFAF	1.610 /OFAF	1.530 /OFAF
	5	2.115 /OFAF	2.095 /OFAF	2.060 /OFAF	2.010 /OFAF	1.945 /OFAF	1.870 /OFAF	1.785 /OFAF	1.680 /OFAF	1.610 /OFAF
	3	2.215 /OFAF	2.185 /OFAF	2.150 /OFAF	2.090 /OFAF	2.025 /OFAF	1.950 /OFAF	1.845 /OFAF	1.740 /OFAF	1.670 /OFAF
65%	**360**	1.725 /OFAF	1.665 /OFAF	1.590 /OFAF	1.520 /OFAF	1.445 /OFAF	1.370 /OFAF	1.285 /OFAF	1.200 /OFAF	1.120 /OFAF
	60	1.925 /OFAF	1.865 /OFAF	1.800 /OFAF	1.730 /OFAF	1.655 /OFAF	1.570 /OFAF	1.485 /OFAF	1.390 /OFAF	1.310 /OFAF
	20	2.055 /OFAF	2.025 /OFAF	1.970 /OFAF	1.910 /OFAF	1.835 /OFAF	1.760 /OFAF	1.665 /OFAF	1.570 /OFAF	1.490 /OFAF
	10	2.085 /OFAF	2.065 /OFAF	2.030 /OFAF	1.980 /OFAF	1.915 /OFAF	1.840 /OFAF	1.755 /OFAF	1.660 /OFAF	1.580 /OFAF
	5	2.115 /OFAF	2.105 /OFAF	2.090 /OFAF	2.040 /OFAF	1.985 /OFAF	1.920 /OFAF	1.835 /OFAF	1.740 /OFAF	1.660 /OFAF
	3	2.225 /OFAF	2.215 /OFAF	2.180 /OFAF	2.130 /OFAF	2.075 /OFAF	1.990 /OFAF	1.905 /OFAF	1.810 /OFAF	1.730 /OFAF

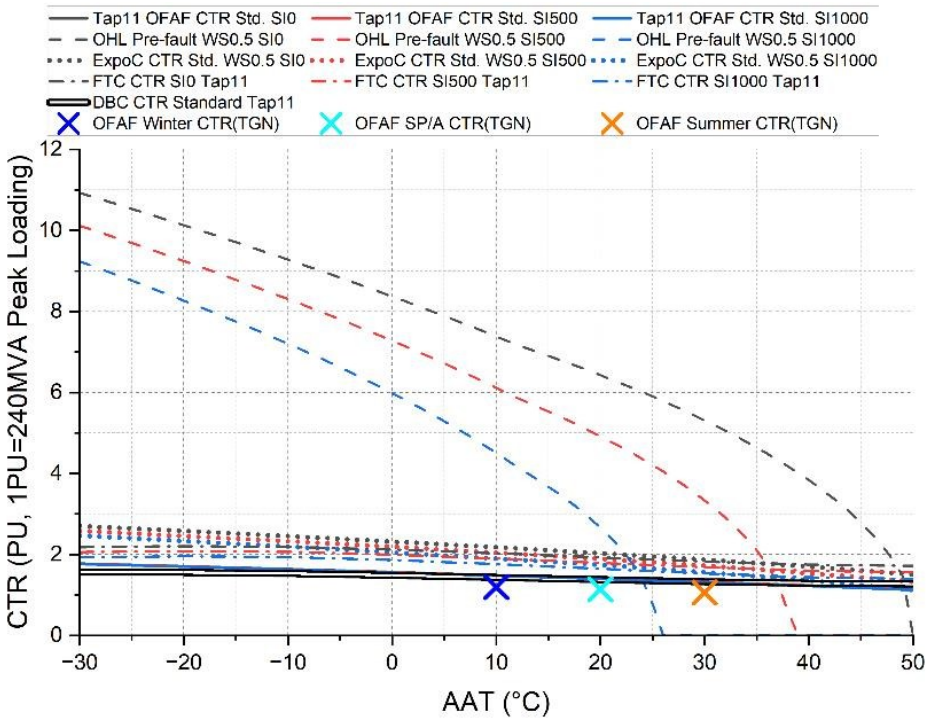

a) Joint circuit CTR full view

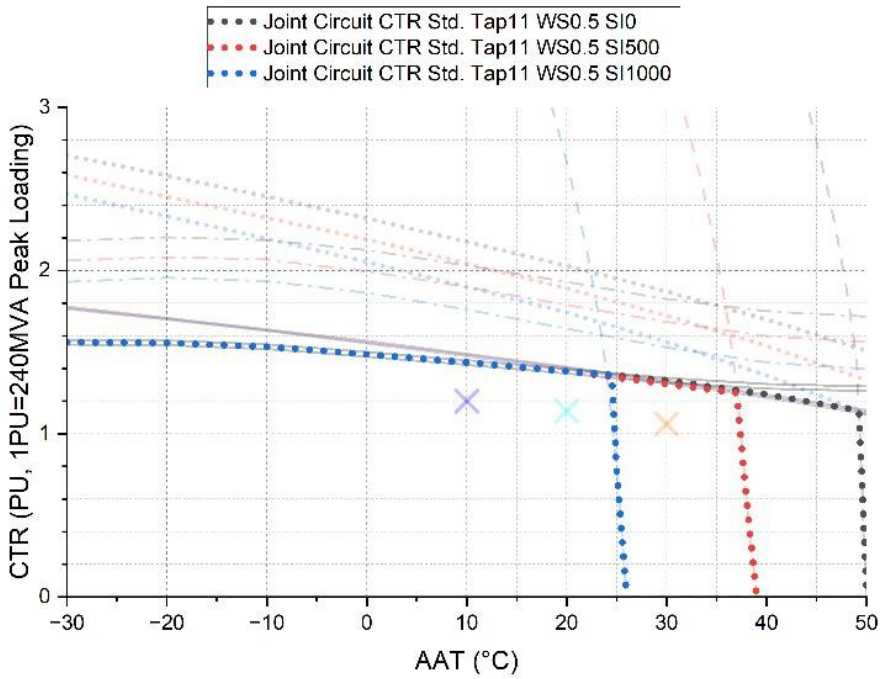

b) Joint circuit CTR detailed view

Figure 7.23: Comparison of joint circuit CTR of substation with the variation of AAT and SI under 0.5m/s WS at tap position 11, full background CTR view (a), detailed (b).

From the result at tap position 11, 0.5m/s WS and no SI, it can be seen that the DBC is the limit during lower AAT ranges, the power transformer becomes the limiting component at around 30℃ AAT until 50℃ AAT. At 50℃ AAT, due to the AAT increasing to the temperature limit of the OHL, the OHL is unable to take any loading without violating or exceeding the temperature limit, i.e., the rating of the OHL is zero. For a non-zero SI considered, such as the $500W/m^2$ and $1000W/m^2$ SI in this thesis, the zero rating of the OHL occurred at a lower AAT, at 39℃ and 26℃, respectively.

Figure 7.24 compares the results under 1m/s WS to 0.5m/s WS, where the zero rating of the OHL occurs at a higher AAT when non-zero SI are considered, at 41°C and 31°C AAT for the medium and high SI, respectively. However, as discussed in the DTR and exceedance rating of OHL, the OHL is allowed to exceed the set temperature limit, as long as the limit of exceedance is not violated. In this thesis, all temperature limit except during the evaluation of the exceedance rating is set as the hard limit of the component, or zero exceedance is allowed. So, the zero-rating of the OHL due to the low temperature limit setting is acknowledged and accepted as the result.

Figure 7.25 and Figure 7.26 describe the CTR at tap position 15 under 0.5 m/s and 1 m/s WS, respectively. Similar results are observed, with the DBC acting as the dominant limiting component at lower AATs up to around 30°C, after which the transformer becomes the governing constraint at higher temperatures, if OHL was not limiting.

At Tap Position 15, the CTR is generally lower compared to Tap Position 11, primarily due to the current limit for the DBC is the same, but the voltage on the LV side decreased due to the OLTC. Also, higher LV current for the same power transfer, which increases thermal loading on the power transformer. Nonetheless, the general trend remains the same for both figures compared to their counterparts, Figure 7.23 and Figure 7.24.

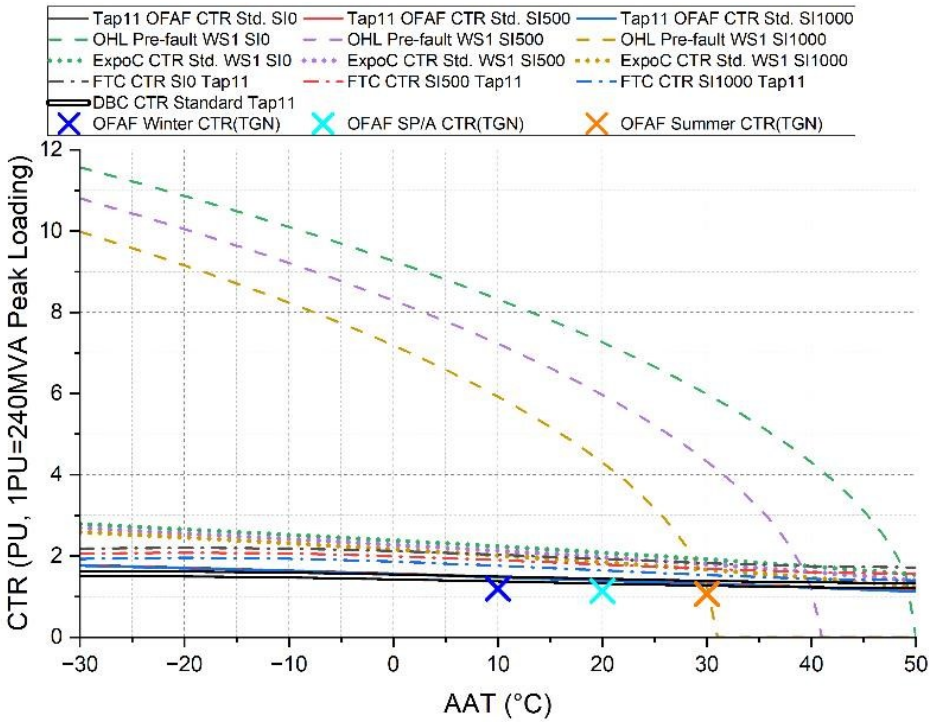

a) Joint circuit CTR full view

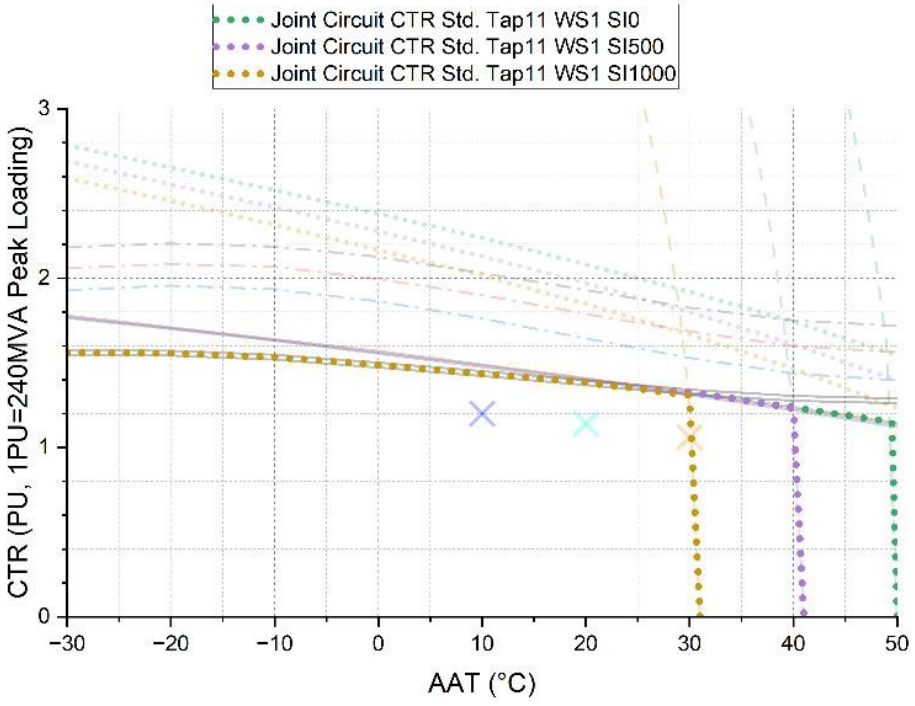

b) Joint circuit CTR detailed view

Figure 7.24 Comparison of joint circuit CTR of substation with the variation of AAT and SI under 1m/s WS at tap position 11, full background CTR view (a), detailed (b).

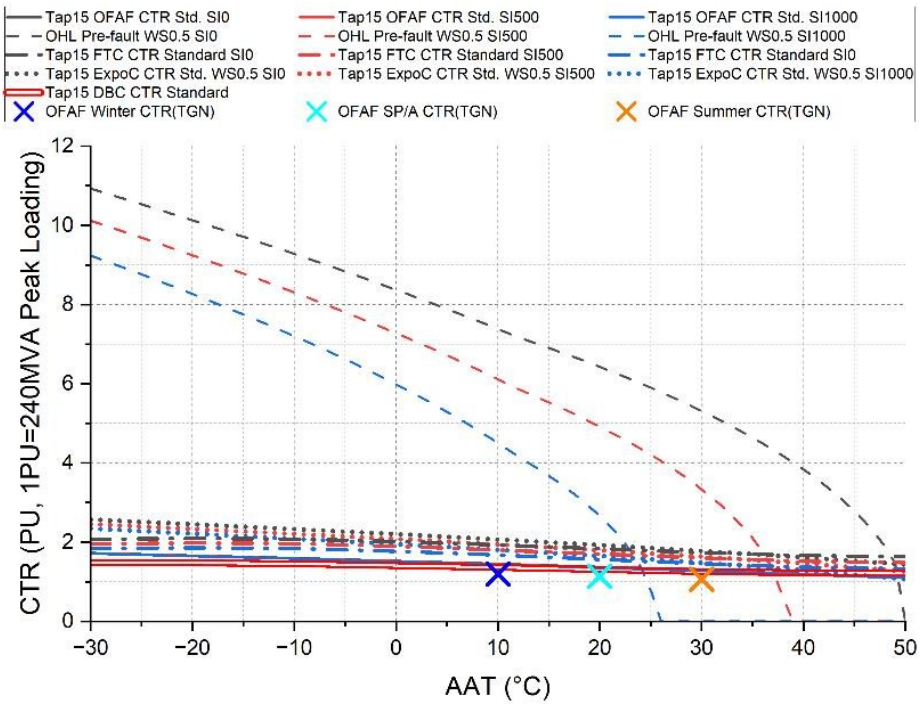

a) Joint circuit CTR, full view

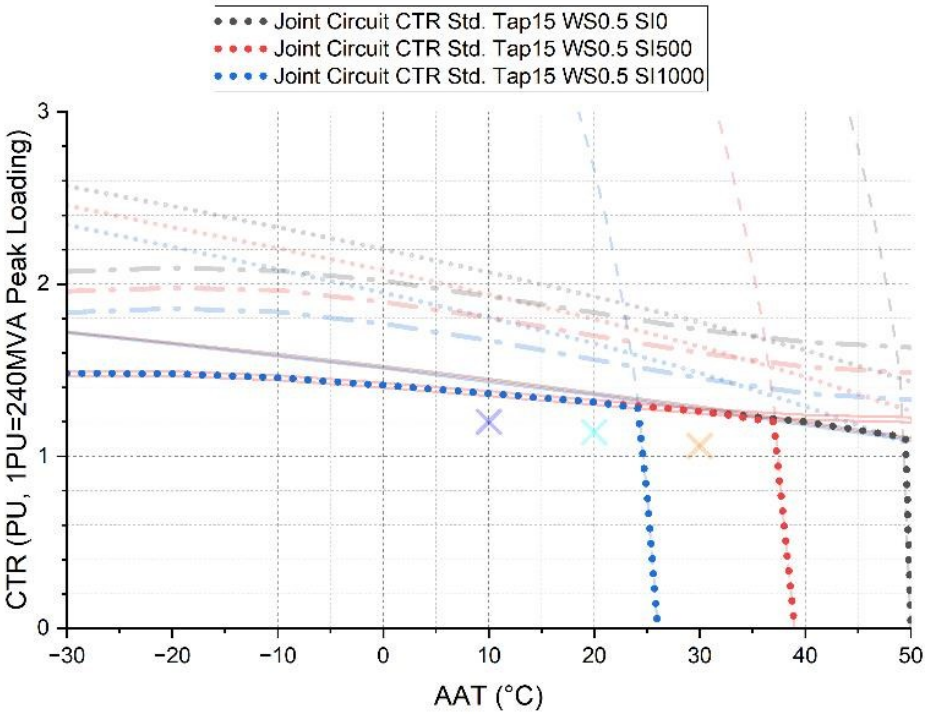

b) Joint circuit CTR, detailed view

Figure 7.25: Comparison of joint circuit CTR of substation with the variation of AAT and SI under 0.5m/s WS at tap position 15, full background CTR view (upper), detailed (lower).

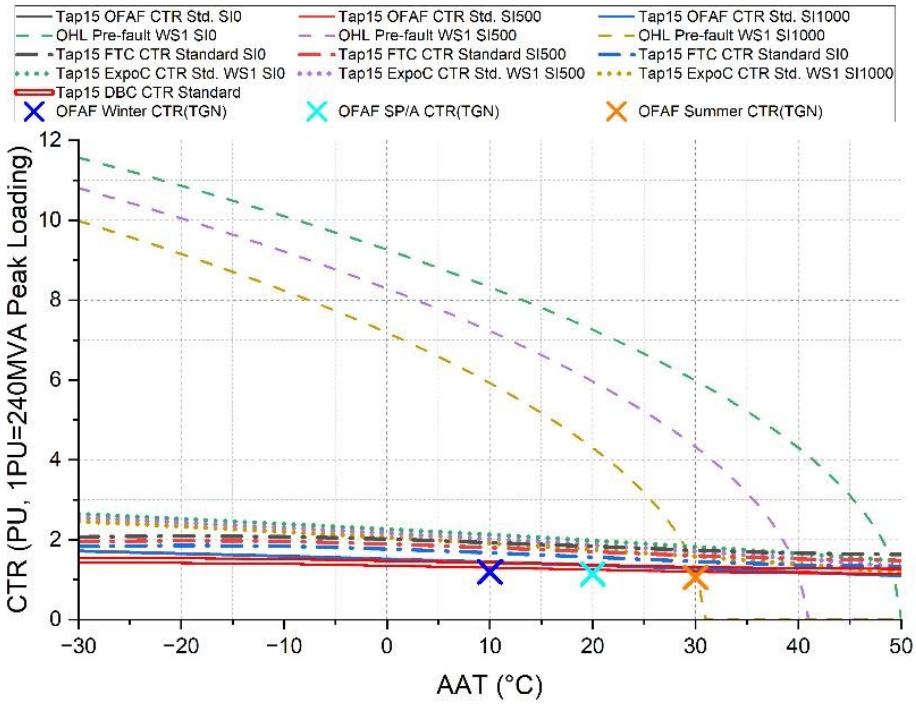

a) Joint circuit CTR, full view

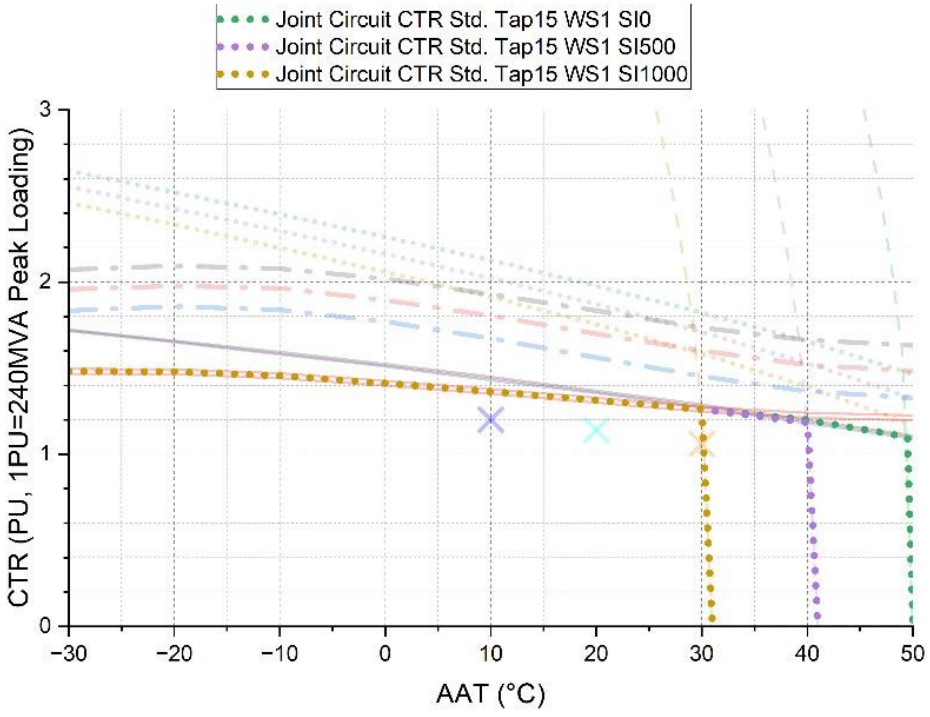

b) Joint circuit CTR, detailed view

Figure 7.26: Comparison of joint circuit CTR of substation with the variation of AAT and SI under 1m/s WS at tap position 15, full background CTR view (a), detailed (b).

Chapter 8

Conclusions and Future Work

This thesis establishes a consistent basis for joint-circuit ratings (MVA when a transformer changes voltage with a voltage output notification, amps with rated voltage otherwise), applies unified ambient assumptions, and uses DTR as the planning baseline. It also recognises real-time thermal response via S/MTOR and CTR, notes the dependence on the actual load profile, and emphasises coordination so cables and transformers are never pushed past firm limits. In a more detailed manner, the conclusions can be summarised as follows:

Units and reporting basis: Where a component can actively change voltage (e.g., the power transformer with OLTC), joint-circuit capacity should be expressed in MVA to ensure both sides of the transformer are represented consistently. However, the demand variation due to non-constant-power demands (constant impedance and current demands) should be handled with care. Then, where no element alters voltage, current (A) is sufficient because the circuit voltage is fixed by the supply voltage and branch drops. Nevertheless, if power is required, the circuit's rated voltage should be used to convert the current limit to a power limit. The OHLs and cables cannot alter the voltage on their own, and it is not the responsibility of such components to determine the voltage.

Consistent ambient exposure: Individual assets in a joint circuit are exposed to different environments (air with wind and sun, shallow trough, buried soil, oil-filled tank). This study adopts a conservative, unified set of ambient assumptions derived from measurements, so results for all assets can be combined without mixing incomparable exposure conditions.

Role of DTR as the planning reference: Continuous DTR are mapped across ambient drivers (air or soil temperature, wind speed, solar irradiance) under indefinite operation. These DTRs show how each driver limits each asset and the combined circuit

in the worst credible steady state. Under these conservative assumptions, DTR is the reference for both pre-fault and post-fault planning.

Thermal dynamics and time-limited headroom, recognising thermal time constant of each component, enable two complementary tools: Short- and Medium-Term Overload Ratings (S/MTOR) are duration-based emergency headroom above the post-fault continuous rating, parameterised by pre-fault loading, duration, and ambient. Cyclic Thermal Ratings (CTR) reflect realistic daily loading and solar cycles, using thermal capacitance and overnight cooling to increase sustainable capacity relative to DTR.

Importance of the loading profile: CTR depends on the shape of the daily load. As EV charging, heat pumps and demand-side management spread demand, peaks may lengthen and valleys rise, changing CTR materially. Because planners often specify load in MVA without explicit terminal voltage, translating those changes into ampere demand for each branch needs care.

Coordination across the joint circuit: Combined ratings are governed by the most restrictive element at each condition. Overhead lines use an exceedance level-based philosophy (small, quantified fractions of time above design temperature), but transformers and cables have hard limits set by protection and thermal damage. Therefore, any exceedance level-based uplift on the OHL must never force a transformer or cable to breach its limit. In practice, the OHL rating in a joint circuit is bounded by its own exceedance policy rather than the firm limits of the cable and transformer.

What remains to be added: OHLs, cables and the transformer. For a full substation view, joints, terminations, busbars, circuit breakers, instrument transformers and protection constraints should be incorporated next so that coordination holds for all essential components in the joint-circuit path. Additionally, evaluation of exceedance level ratings of joint circuits should be analysed, especially when OHLs are involved. This would provide an evidence check on whether joint circuit ratings derived from decades-old exceedance methods and legacy design ambient conditions still meet today’s TGN/standards requirements. With climate change and more frequent heatwaves, those assumptions may no longer hold, so both the ratings and the underlying

design ambient conditions should be revisited and, where needed, re-evaluated using present or future climate projections.

References

[1] "IEEE Guide for Loading Mineral-Oil-Immersed Transformers and Step-Voltage Regulators," Sep. 23, 2012, *IEEE Std C57.91*.

[2] "BSI Standards Publication Power transformers Part 7: Loading guide for mineral-oil-immersed power transformers," 2018, *BS IEC 60076-7*.

[3] "Transformer Loading Guide," Mar. 1994, *National Grid, TGN(T) 029*.

[4] "Electric cables — Calculation of the current rating. Part 1-1, Current rating equations (100 % load factor) and calculation of losses. General.," 2023, *BSI Standards Limited*.

[5] "Electric cables — Calculation of the current rating. Part 2-1, Thermal resistance. Calculation of thermal resistance.," 2023, *BSI Standards Limited*.

[6] "Electric cables — Calculation of the current rating Part 3-1: Operating conditions-Site reference conditions," 2020, *BSI Standards Limited*.

[7] "Calculation of the cyclic and emergency current rating of cables. Part 3, Cyclic rating factor for cables of all voltages, with partial drying of the soil.," BRITISH STANDARD, 2002.

[8] "Current Ratings for AC Cables," Sep. 2019, *National Grid, TGN(E) 067*.

[9] "IEEE Standard for Calculating the Current-Temperature Relationship of Bare Overhead Conductors," IEEE Std 738-2012, Sep. 2012.

[10] "Overhead electrical conductors — Calculation methods for stranded bare conductors," Jul. 30, 2021, *BSI PD IEC TR 61597:2021*.

[11] "Current Ratings for Overhead Lines," Feb. 2021, *National Grid, TGN(E) 026*.

[12] M. E. Baran and F. F. Wu, "Network Reconfiguration in Distribution Systems for Loss Reduction and Load Balancing," *IEEE Transactions on Power Delivery*, vol. 4, no. 2, pp. 1401–1407, 1989.

[13] "Transformer Thermal Modelling," 2016, *CIGRE 659*.

[14] "Co-ordination of Plant Thermal Ratings," Jan. 2019, *National Grid, TGN(E) 303*.

[15] "Loading guide for oil-immersed power transformers," Oct. 15, 1991, *IEC 60354:1991*.

[16] A. Doolgindachbaporn, “Data Driven Transformer Thermal Modelling for Identification of Thermal Issues,” Doctoral Thesis, University of Southampton, 2021.

[17] A. Doolgindachbaporn, G. Callender, P. L. Lewin, E. Simonson, and G. Wilson, “A Top-Oil Thermal Model for Power Transformers That Considers Weather Factors,” *IEEE Transactions on Power Delivery*, vol. 37, no. 3, pp. 2163–2171, Jun. 2022, [Online]. Available: https://ieeexplore.ieee.org/document/9516994/

[18] A. Doolgindachbaporn, G. Callender, P. Lewin, and G. Wilson, “Estimation on Degradation Rate of Insulating Paper in Power Transformers Using Historical Load and Thermal Data,” in *2021 IEEE Electrical Insulation Conference (EIC)*, IEEE, Jun. 2021, pp. 89–92.

[19] G. Wilson and E. Simonson, “Thermal Analysis of Transformers to Calculate Permissible Ratings,” in *84th International Conference of Doble Clients*, Doble Engineering Company, 2017.

[20] D. Susa, M. Lehtonen, and H. Nordman, “Dynamic thermal modelling of power transformers,” *IEEE Transactions on Power Delivery*, vol. 20, no. 1, pp. 197–204, Jan. 2005.

[21] N. Schmidt, S. Tenbohlen, R. Skrzypek, and B. Dolata, “Assessment of Overload Capabilities of Power Transformers by Thermal Modelling,” in *CIGRE SC A2 & D1 JOINT COLLOQUIUM 2011*, KYOTO, 2011.

[22] M. Djamali and S. Tenbohlen, “A New Top-Oil Temperature Model based on IEC 60076-7 for OFAF and ONAF Transformer,” in *Diagnostik Elektrischer Betriebsmittel 25*, VDE-Verl, 2014.

[23] V. Shiravand, J. Faiz, M. H. Samimi, and M. Djamali, “Improving the transformer thermal modeling by considering additional thermal points,” *International Journal of Electrical Power and Energy Systems*, vol. 128, Jun. 2021.

[24] L. Wang *et al.*, “Improved Dynamic Thermal Model with Pre-Physical Modeling for Transformers in ONAN Cooling Mode,” *IEEE Transactions on Power Delivery*, vol. 34, no. 4, pp. 1442–1450, Aug. 2019.

[25] A. Gamil, A. Al-Abadi, M. Schiessl, F. Schatzl, and E. Schlucker, “Improvements on Thermal Performance of Power Transformers: Modelling and Testing,” in *2019 6th International Advanced Research Workshop on Transformers (ARWtr)*, IEEE, Oct. 2019, pp. 13–18.

[26] D. Harrison, “Loading capabilities of large power transformers,” *Power Engineering Journal*, vol. 9, no. 5, pp. 225–230, Oct. 1995.

[27] P. White, “Standard Technique: SD8B/3 (Part3) Relating to 33kV Underground Cable Ratings,” Mar. 30, 2009, *Western Power Distribution*.

[28] K. Morozovska, R. Karlsson, and P. Hilber, “Dynamic rating of the wind farm transformer from the power system’s perspective,” in *2021 IEEE Madrid PowerTech*, IEEE, Jun. 2021, pp. 1–6.

[29] H. Yang, L. Xie, C. Guo, Y. Qin, and G. Liang, “Influence of New Energy Access to Power System on Curruent Transformer Aging,” in *2022 IEEE International Conference on High Voltage Engineering and Applications (ICHVE)*, IEEE, Sep. 2022, pp. 1–4.

[30] J. Marks, O. Krause, D. Martin, and D. McPhail, “Using power state estimation to calculate hotspot temperature of distribution transformers,” in *2015 IEEE PES Asia-Pacific Power and Energy Engineering Conference (APPEEC)*, IEEE, Nov. 2015, pp. 1–5.

[31] M. A. Ozcelik, “Experimental Investigation of Changes in Iron and Copper Losses in the Transformer,” in *2023 27th International Conference Electronics*, IEEE, Jun. 2023, pp. 1–4.

[32] S. Mousavi, M. Shamei, A. Siadatan, F. Nabizadeh, and S. H. Mirimani, “Calculation of Power Transformer Losses by Finite Element Method,” in *2018 IEEE Electrical Power and Energy Conference (EPEC)*, IEEE, Oct. 2018, pp. 1–5.

[33] G. U. Nnachi, A. O. Akumu, C. G. Richards, and D. V. Nicolae, “Estimation of no-Load Losses in Distribution Transformer Design Finite Element Analysis Techniques in Transformer Design,” in *2018 IEEE PES/IAS PowerAfrica*, IEEE, Jun. 2018, pp. 1–532.

[34] G. Upadhyay, A. Singh, S. K. Seth, and R. K. Jarial, “FEM based no-load loss calculation of triangular wound core transformer,” in *2016 IEEE 1st International Conference on Power Electronics, Intelligent Control and Energy Systems (ICPEICES)*, IEEE, Jul. 2016, pp. 1–4.

[35] T. Steinmetz, B. Cranganu-Cretu, and J. Smajic, “Investigations of no-load and load losses in amorphous core dry-type transformers,” in *The XIX International Conference on Electrical Machines - ICEM 2010*, IEEE, Sep. 2010, pp. 1–6.

[36] K. Dawood, G. Komurgoz, and F. Isik, “Modeling of Distribution Transformer for Analysis of Core Losses of Different Core Materials Using FEM,” in *2019*

8th International Conference on Modeling Simulation and Applied Optimization (ICMSAO), IEEE, Apr. 2019, pp. 1–5.

[37] K. Dawood and S. Tursun, "Effects of the Step-Lap Joints Configurations on the No-Load Losses of the Transformer," in *2023 12th International Conference on Power Science and Engineering (ICPSE)*, IEEE, Sep. 2023, pp. 60–64.

[38] K. Dawood and S. Tursun, "Effects of Gap Length of a Step Lap Joint on the No Load Losses of Transformers," in *2023 International Symposium on Fundamentals of Electrical Engineering (ISFEE)*, IEEE, Nov. 2023, pp. 1–5.

[39] J. Guo and S. Li, "Study on no-load loss of amorphous alloy control transformer based on the finite element analysis," in *2016 IEEE International Conference of Online Analysis and Computing Science (ICOACS)*, IEEE, May 2016, pp. 16–19.

[40] A. M. A. Haidar and M. Al-Dabbagh, "The Influences of T-Joint Core Design on No-Load Losses in Transformers," *IEEE Potentials*, vol. 32, no. 3, pp. 40–48, May 2013.

[41] M. Yazdani-Asrami, M. Mirzaie, and A. A. Shayegani Akmal, "No-load loss calculation of distribution transformers supplied by nonsinusoidal voltage using three-dimensional finite element analysis," *Energy*, vol. 50, no. 1, pp. 205–219, Feb. 2013.

[42] Z. Song *et al.*, "Tank losses and magnetic shunts in a three phase power transformer," in *2011 International Conference on Electrical Machines and Systems*, IEEE, Aug. 2011, pp. 1–4.

[43] T. Tanzer *et al.*, "Magnetic properties and their relation to the no-load noise and no-load losses of large power transformers," in *2017 IEEE International Electric Machines and Drives Conference (IEMDC)*, IEEE, May 2017, pp. 1–6.

[44] J. Wojtkun, B. Brodka, and D. Stachowiak, "The influence of core geometry on no-load losses of medium power transformers," in *2018 International Interdisciplinary PhD Workshop (IIPhDW)*, IEEE, May 2018, pp. 123–127.

[45] A. G. Lavrov, D. S. Ilyashov, and M. A. Sitnikov, "Analysis of Methods for Calculating No-Load Losses of Three-Phase Transformers and Assessment of the No-Load Current Active Component Asymmetry," in *2021 IEEE Conference of Russian Young Researchers in Electrical and Electronic Engineering (ElConRus)*, IEEE, Jan. 2021, pp. 985–988.

[46] J. C. Olivares-Galván, R. Escarela-Pérez, P. S. Georgilakis, and E. Campero-Littlewood, "Separation of no-load losses for distribution transformers using

experimental methods: two frequencies and two temperatures," in *7th Mediterranean Conference and Exhibition on Power Generation, Transmission, Distribution and Energy Conversion (MedPower 2010)*, IET, 2010, pp. 169–169.

[47] R. Minhaz, "Transformer Design & Design Parameters," *Transformer Consulting Services Inc.*

[48] S. C. Zhao *et al.*, "An Improved Analytical Method for Radiator Thermal Modelling of Natural Cooled Transformers," in *2022 IEEE International Conference on High Voltage Engineering and Applications (ICHVE)*, IEEE, Sep. 2022, pp. 1–4.

[49] S. Zhao, Q. Liu, M. Wilkinson, G. Wilson, and Z. Wang, "A Reduced Radiator Model for Simplification of ONAN Transformer CFD Simulation," *IEEE Transactions on Power Delivery*, vol. 37, no. 5, pp. 4007–4018, Oct. 2022.

[50] "IEEE Guide for the Application of Tertiary and Stabilizing Windings in Power Transformers," Apr. 27, 2018, *IEEE*.

[51] P. K. Preetha, S. Jacob, and P. S. C. Nair, "An equivalent circuit model for star-star-delta_utilized distribution transformer," in *TENCON 2014 - 2014 IEEE Region 10 Conference*, IEEE, Oct. 2014, pp. 1–6.

[52] "Electric cables - Calculation of the current rating Part 2-3: Thermal resistance - Cables installed in ventilated tunnels," 2017, *BSI Standards Limited 2017*.

[53] "IEEE Standard Power Cable Ampacity Tables," Sep. 30, 1994, *IEEE Std 835-1994*.

[54] "IEEE Standard Procedure for the Determination of the Ampacity Derating Factor for Fire-Protected Cable Systems," Feb. 16, 2015, *IEEE Std 848-2015, Piscataway, NJ, USA*: 848–1996. [Online]. Available: http://ieeexplore.ieee.org/document/7111195/

[55] "A Guide for Rating Calculations of Insulated Cables," Sep. 2015, *CIGRE 640*.

[56] "Cable Systems," Apr. 2022, *National Grid, TS 2.05*.

[57] R. J. Millar and M. Lehtonen, "A Robust Framework for Cable Rating and Temperature Monitoring," *IEEE Transactions on Power Delivery*, vol. 21, no. 1, pp. 313–321, Jan. 2006.

[58] M. Z. Degefa, "Real-time thermal state and component loading estimation in active distribution networks," Doctoral Dissertations, Aalto University, 2015.

[59] J. A. Pilgrim, P. L. Lewin, S. T. Larsen, F. Waite, and D. Payne, "Rating of Cables in Unfilled Surface Troughs," *IEEE Transactions on Power Delivery*, vol. 27, no. 2, pp. 993–1001, Apr. 2012.

[60] M. Terracciano, S. Purushothaman, F. de Leon, and A. V. Farahani, "Thermal Analysis of Cables in Unfilled Troughs: Investigation of the IEC Standard and a Methodical Approach for Cable Rating," *IEEE Transactions on Power Delivery*, vol. 27, no. 3, pp. 1423–1431, Jul. 2012, Accessed: Sep. 29, 2025. [Online]. Available: http://ieeexplore.ieee.org/document/6218216/

[61] "Guide for Thermal Rating Calculations of Overhead Lines," 2014, *CIGRE 601*.

[62] C. F. Price and R. R. Gibbon, "Statistical Approach To Thermal Rating of Overhead Lines for Power Transmission and Distribution.," *IEE Proceedings C: Generation Transmission and Distribution*, vol. 130, no. 5, pp. 245–256, 1983.

[63] R. Adapa and D. Doulgass, "Dynamic Thermal Rating of Substation Terminal Equipment," *CIGRÉ*, Jan. 2004.

[64] "EPRI Research Collaboration on Substations ." Accessed: Jan. 18, 2025. [Online]. Available: https://smarter.energynetworks.org/projects/nia_nget0210/

[65] R. Adapa and D. A. Douglass, "Dynamic thermal ratings: monitors and calculation methods," in *Proceedings of the Inaugural IEEE PES 2005 Conference and Exposition in Africa*, IEEE, 2005, pp. 163–167.

[66] "Lower Cost Underground Transmission Cable," Palo Alto, CA, 2004.

[67] "Improved Thermal Modeling Tools for Substation Equipment," Palo Alto, CA; CenterPoint Energy, Houston, TX; KeySpan Energy, Hicksville, NY; PSE&G, Newark, NJ; PNM, Albuquerque, NM; Georgia Power, Forest Park, GA; and American Transmission Company, Waukesha, 2007. [Online]. Available: www.epri.com

[68] D. A. Douglass and A.-A. Edris, "Real-time monitoring and dynamic thermal rating of power transmission circuits," *IEEE Transactions on Power Delivery*, vol. 11, no. 3, pp. 1407–1418, Jul. 1996.

[69] "Loading guide for oil-immersed transformers," Mar. 27, 1975, *BSI CP 1010:1975*.

[70] "MATLAB," 2019, *The MathWorks Inc., Massachusetts*: 9.6.0.1472908 (R2019a).

[71] "acsr-astm-b-aluminium-conductor-steel-reinforced," Eland Cables. Accessed: Feb. 07, 2022. [Online]. Available: https://www.elandcables.com/media/38193/acsr-astm-b-aluminium-conductor-steel-reinforced.pdf.

[72] H. J. Li, "Estimation of thermal parameters and prediction of temperature rise in crane power cables," in *IEE Proceedings: Generation, Transmission and Distribution*, May 2004, pp. 355–360.

[73] "Technical Data Sheet Medium Voltage Cables," *AEI Cables*. [Online]. Available: www.aeicables.co.uksales@aeicables.co.uk

[74] "Technical specification SZ13-6300/35," *ABB Zhongshan Transformer Company Ltd., Zhongshan*.

[75] "Transformer Type Test Report, Three Phase Auto Transformer, TAQ-185R44U9L-99, ser.no.:1,724.430, National Grid / Braintree, 240MVA 400/132/33 kV," May 2006, *VA TECH ELIN Transformatoren*.

[76] "Rating and Diagram Plate for 240MVA 400/132kV Autotransformer," *National Grid Drawing NO. 81/VA/0151, ELIN 5971888*.

[77] "Current Rating Guide for High Voltage Overhead Lines Operating in the UK Distribution System," 1986, *Electricity Association*.

[78] "Code of Practice for Overhead Line Ratings and Parameters," 2017.

[79] MET Office, "MIDAS Open: UK hourly weather observation data, v202507. NERC EDS Centre for Environmental Data Analysis." [Online]. Available: https://catalogue.ceda.ac.uk/

[80] MET - Office, "UK Met Office, UKCP18 Probabilistic Projections of UK Climate: Data Release Notes. Exeter, UK: Met Office." [Online]. Available: https://www.metoffice.gov.uk/research/approach/collaboration/ukcp/index

[81] S. Hoffmann, "Company Directive Relating to Revision of Overhead Line Ratings," 2020.

[82] "Historic Demand Data," *National Energy System Operator*. Accessed: Jul. 06, 2025. [Online]. Available: https://www.neso.energy/data-portal/historic-demand-data?page=0

[83] "Met Office (2024): MIDAS Open: UK hourly weather observation data, v202407," Aug. 06, 2024, *NERC EDS Centre for Environmental Data Analysis*.

[84] "Historical Demand Data," *Elexon*.

[85] A. Zakaria, C. Duan, and S. Z. Djokic, “Hosting capacity of distribution networks for controlled and uncontrolled residential EV charging with static and dynamic thermal ratings of network components,” *IET Generation, Transmission & Distribution*, vol. 18, no. 6, pp. 1283–1301, Mar. 2024.

[86] B. Kozanoglu and F. Rubio, “The characteristic length on natural convection from a horizontal heated plate facing downwards,” *Thermal Science*, vol. 18, no. 2, pp. 555–561, 2014.

[87] T. Fujii and H. Imura, “Natural-convection heat transfer from a plate with arbitrary inclination,” *Int. J. Heat Mass Transf.*, vol. 15, no. 4, pp. 755–767, Apr. 1972.

[88] S. Fathi, A. Ghahremani, M. B. Shafii, M. Sadr, and A. Salehzehi, “Improving transformer cooling performance through advanced heat pipes integration,” *Appl. Therm. Eng.*, vol. 267, p. 125775, May 2025.

[89] Y. Feng, N. Zhao, B. Wang, and Q. Li, “A method for monitoring internal temperature field distribution of transformers based on heat transfer coefficient under different operating conditions,” *Case Studies in Thermal Engineering*, vol. 75, p. 107094, Nov. 2025.

[90] S. Zhao, Q. Liu, M. Wilkinson, G. Wilson, and Z. Wang, “A Reduced Radiator Model for Simplification of ONAN Transformer CFD Simulation,” *IEEE Transactions on Power Delivery*, vol. 37, no. 5, pp. 4007–4018, Oct. 2022.

[91] Y. J. Kim and M. Y. Ha, “A study on the performance of different radiator cooling systems in large-scale electric power transformer,” *Journal of Mechanical Science and Technology*, vol. 31, no. 7, pp. 3317–3328, Jul. 2017.

[92] A. C. Franklin and D. P. Franklin, *The J & P Transformer Book*, 11th ed. Elsevier, 1983.

[93] J. H. Dellinger, “The temperature coefficient of resistance of copper,” *J. Franklin Inst.*, vol. 170, no. 3, pp. 213–216, Sep. 1910.

[94] Sumaryadi, B. Cahyono, and I. Arifianto, “Diagnostic degradation process of power transformer insulation system: Harmonic current impact to capability of transformer #7 Pulogadung s/s,” in *2009 IEEE 9th International Conference on the Properties and Applications of Dielectric Materials*, IEEE, Jul. 2009, pp. 216–219.

[95] P. Penabad-Duran, C. Alvarez-Marino, and X. M. Lopez-Fernandez, “Transformer Tertiary Stabilizing Windings. Part II: Overheating hazard on tank walls,” in *2012 XXth International Conference on Electrical Machines*, IEEE, Sep. 2012, pp. 2369–2374.

[96] P. Penabad-Duran, X. M. Lopez-Fernandez, and C. Alvarez-Marino, "Transformer Tertiary Stabilizing Windings. Part I: Apparent power rating," in *2012 XXth International Conference on Electrical Machines*, IEEE, Sep. 2012, pp. 2362–2368.

[97] "Instruction Manual No. 1283," Feb. 28, 2007, *VA TECH ELIN Transformatoren GmbH & Co*.

[98] "National Grid Drawing No. 50/VA/0067," Feb. 24, 2006, *ELIN*.

[99] "AISI 310 Stainless Steel - Properties," 2019. Accessed: Jun. 02, 2024. [Online]. Available: https://www.engineeringtoolbox.com/stainless-steel-310-properties-d_2167.html

[100] "High Voltage XLPE Cables," *Tele-Fonika Kable S.A.*

[101] "High Voltage Cable Systems-Cables and Accessories up to 550 kV," *nkt cables*.

[102] M. L. Marceau and M. G. Vangeem, "Solar Reflectance Values for Concrete," *Concrete International*, pp. 52–58, Aug. 2008.

[103] "AAAC CONDUCTOR," *DEMKA*.

[104] E. Morresi, "M20 traffic expected as two massive 'house-sized' transformers to move from Dover to Sellindge," KentLive. Accessed: Jul. 22, 2025. [Online]. Available: https://www.kentlive.news/news/kent-news/m20-traffic-expected-two-massive-2368885